Study of the Josephson effect in graphene-based moiré superlattices

Andrés Díez Carlón

München 2025

Study of the Josephson effect in graphene-based moiré superlattices

Andrés Díez Carlón

Dissertation
an der Fakultät für Physik
der Ludwig–Maximilians–Universität
München

vorgelegt von
Andrés Díez Carlón
aus Oviedo

München, den 3. Juli 2025

Erstgutachter: Prof. Dr. Dmitri K. Efetov
Zweitgutachter: Prof. Dr. Milan Allan
Abgabedatum: 3. Juli 2025
Tag der mündlichen Prüfung: 14. August 2025

A mis abuelos,
a mis padres,
a Marina,
a Marta

Contents

Zusammenfassung **ix**

Summary **xi**

Acknowledgements **xiii**

Author's publications **xv**

Introduction **1**

1 Graphene-based moiré superlattices and Josephson junctions **5**

1.1 Monolayer Graphene 5

1.2 Heterobilayer moiré superlattices: Graphene/hBN 8

1.2.1 Moiré potential and satellite Dirac points 9

1.2.2 Hofstadter butterfly in the magnetic field phase diagram 11

1.3 Homobilayer moiré superlattices: Twisted Bilayer Graphene 15

1.3.1 Continuum model and flat bands in TBG 15

1.3.2 Many body correlated phases in TBG 19

1.4 Josephson junctions 24

1.4.1 Tunneling junctions and weak links 25

1.4.2 The washboard potential and IV characteristics 30

1.4.3 Superconducting interference under a magnetic field 32

2 Experimental Methods **39**

2.1 vdW heterostructures fabrication 40

2.1.1 Exfoliation 40

2.1.2 Flake identification 43

2.1.3 Stamp preparation 43

2.1.4 Transfer method: stacking 46
2.1.5 Graphene-cutting techniques 50
2.1.6 Nanofabrication: lithography, etching and evaporation 52
2.2 Josephson junctions fabrication 57
2.2.1 Sputtering of superconducting Molybdenum-Rhenium 57
2.2.2 Superconducting contact engineering to graphene 60
2.2.3 Minimizing stress with a Peltier device 66
2.2.4 Thermal evaporation of Aluminum 70
2.3 Low-temperature transport measurements 71
2.3.1 Cryogenics and electronic filtering 71
2.3.2 Low-frequency transport measurements 77

3 High-field superconductivity in a ballistic moiré superlattice JJ 81
3.1 Ballistic moiré-graphene Josephson junctions 82
3.1.1 Fabry-Pérot oscillations 84
3.1.2 Length dependence of the long-ballistic regime 88
3.2 High-field superconductivity and cyclotron breakdown 90
3.2.1 The superconducting proximity effect for increasing magnetic fields 90
3.2.2 Proximity effect at high magnetic fields in the moiré bands 92
3.2.3 Comparison with a ballistic monolayer graphene JJ 95

4 Flat band limit of the SC proximity effect in TBG Josephson junctions 97
4.1 Quantum Geometry and superconductivity in the flat band limit 98
4.1.1 The quantum metric 98
4.1.2 Superfluidity in the BCS theory 99
4.1.3 Quantum geometric contribution to the superfluidity 100
4.2 A Josephson junction with a TBG weak link 101
4.3 Unconventional scaling between I_c and G_N 104
4.3.1 Estimation of the expected decrease of I_cR_N in the flat bands . . . 107
4.3.2 Interaction-driven critical current 109
4.4 Quantum geometric and multiband contributions to the proximity effect . . 111
4.5 The Josephson diode effect 118
4.5.1 Interference patterns with broken inversion symmetry 120
4.5.2 Symmetry-breaking across a large range of filling 122

4.5.3 Supercurrent dominated by edge states 124

5 Gate-defined junctions of monolithic twisted bilayer graphene 129

5.1 Fabrication and characterization of gate-defined devices 130

5.2 Gate-defined Josephson junctions in TBG 135

5.2.1 Symmetry-breaking and edge states 135

5.2.2 Orbital magnetism and valley polarization 138

5.3 Gate-defined p-n junctions in TBG 142

5.3.1 Cooling dynamics and Umklapp scattering 142

5.3.2 Thermoelectric transport and heavy-fermion physics 145

Conclusions and Outlook 149

Bibliography 155

List of Abbreviations and Symbols 175

List of Figures

1 Investigating Josephson junctions with moiré superlattice weak links 2

1.1 Graphene lattice and band structure 6
1.2 Graphene transport and spin/valley degeneracy 7
1.3 Graphene/hBN moiré superlattice and satellite Dirac points 10
1.4 Hofstadter butterfly in the Landau fan of a Gr/hBN moiré superlattice . . 13
1.5 Twisted bilayer graphene moiré superlattice and mini-Brillouin zone 16
1.6 Electronic band structure of TBG and flat bands at the first magic angle . 18
1.7 Temperature phase diagram of TBG 20
1.8 Magnetic field phase diagram of TBG 22
1.9 Superconducting proximity effect in SNS junctions and Andreev reflection . 26
1.10 Andreev Bound States in SNS junctions 28
1.11 RCSJ model, washboard potential and IV characteristics 31
1.12 Superconducting interference under a magnetic field 34
1.13 Critical current density profile extraction 37

2.1 Cleaning of Si/SiO_2 chips 40
2.2 Exfoliation of graphene 42
2.3 Exfoliation of hBN 42
2.4 Graphene and hBN flakes identification 43
2.5 Dry-transfer technique 44
2.6 PC film making for stamps 44
2.7 Preparation of PDMS/PC stamps 45
2.8 Transfer stage 46
2.9 Stacking twisted bilayer graphene 47
2.10 Stacking going wrong 48
2.11 Graphene flakes selection 49
2.12 hBN flakes selection 50
2.13 Graphene cutting techniques 51
2.14 Nanofabrication steps and 1D contact to graphene 52
2.15 Lithography with MLA and EBL 53
2.16 Reactive ion etching to shape a device 54
2.17 Etching rate of hBN and graphite 55
2.18 Metallic deposition to contact a device 56
2.19 Sputtering process 58

2.20 Superconducting sputtered MoRe . . . 59
2.21 Electron beam optimization of a JJ design . . . 61
2.22 MoRe-graphene JJs sputtered at high power . . . 62
2.23 Sputtering with varying DC power and Ar pressure in a JJ design . . . 63
2.24 MoRe leads in a JJ design sputtered at low power . . . 64
2.25 MoRe superconducting transition dependent on sputtering power . . . 65
2.26 Peltier device for sputtering and active cooling . . . 67
2.27 MoRe-graphene JJs sputtered at high power with active cooling . . . 68
2.28 Transfer-length method and contact resistance of MoRe-graphene . . . 69
2.29 Example of a uniform ballistic graphene Josephson junction . . . 70
2.30 Example of Ti/Al graphene JJs . . . 71
2.31 Pulse tube cooling and superfluid ^{4}He . . . 72
2.32 ^{3}He/^{4}He mixture cooling and dilution refrigerator . . . 75
2.33 Current-voltage and differential resistance characteristics measurements . . . 79

3.1 Josephson junction with a graphene/hBN moiré superlattice weak link . . . 83
3.2 Fabry-Pérot oscillations over several moiré bands . . . 85
3.3 Fabry-Pérot oscillations in the normal state . . . 87
3.4 Long-ballistic regime evidence in the length dependence of $I_c(T)$ and I_cR_N 89
3.5 Interference patterns at increasing magnetic fields . . . 91
3.6 High-field superconductivity in the moiré bands . . . 93
3.7 Fabry-Pérots and high-field superconductivity in a ballistic graphene JJ . . . 96

4.1 Superconducting proximity effect in a TBG Josephson junction . . . 103
4.2 Strength of the proximity effect and I_c vs G_N scaling . . . 104
4.3 Proximitized flat bands with varying twist-angle . . . 106
4.4 Scaling of the proximity effect according to the theory of long-diffusive JJs 108
4.5 Interaction-induced critical current in the TBG flat bands . . . 111
4.6 Proximity effect with decreasing bandwidth in the flat bands . . . 114
4.7 Quantum geometric and multiband contributions to the induced superconductivity in the flat bands . . . 116
4.8 Proximity effect in the dispersive bands. . . . 117
4.9 Asymmetric critical current oscillations and reversible Josephson diode effect 121
4.10 Inversion symmetry breaking and TRS conservation across the whole dome 123
4.11 Supercurrent density profile and node-lifting . . . 125
4.12 Supercurrent density profile in the Josephson diode: Bulk vs Edge . . . 126
4.13 Temperature dependence of the asymmetric oscillations . . . 127

5.1 Fabrication of gate-defined TBG devices . . . 131
5.2 Gate-defined TBG junctions . . . 133
5.3 Gate-defined TBG Josephson junction . . . 136
5.4 Supercurrent carried by edge states in the symmetry-broken phase . . . 138
5.5 JJ with orbital magnetism . . . 140

5.6 Zero-field programmable Josephson diode 141
5.7 Ultrafast Umklapp-assisted cooling in TBG p-n junctions 144
5.8 Photo-thermoelectric effect in TBG with gate-defined p-n junctions 147

List of Tables

1.1 Ballistic and diffusive regimes in an SNS junction 26
1.2 Short and long regimes in an SNS junction 27

2.1 MoRe sputtering rate vs DC power 65

3.1 Summary of all graphene/hBN moiré Josephson junction devices 88

4.1 Summary of all TBG and graphene Josephson junctions devices 105

Zusammenfassung

Graphen-basierte Moiré-Übergitter, insbesondere im magischen Winkel verdrehtes Doppellagen Graphen (TBG), haben sich als vielversprechende Plattform zur Erforschung unkonventioneller Supraleitung in elektronischen Flachbändern erwiesen, in denen das Zusammenspiel von starken Korrelationen, nichttrivialer Topologie und quantengeometrischen Effekten eine zentrale Rolle spielt. Der Josephson-Effekt bietet ein vielseitiges Mittel, um die fundamentalen Eigenschaften supraleitender Zustände und deren Wechselwirkungen mit anderen korrelierten Phasen zu untersuchen. Dennoch blieb dessen Einwirkung auf Moiré-Systemen bislang weitgehend unerforscht.

In dieser Dissertation schließen wir diese Lücke, indem wir Techniken zum Stapeln von Van-der-Waals-Kristallen mit transparenten supraleitenden Kontakten und Tieftemperatur-Transportmessungen kombinieren. Unser Ansatz umfasst zwei Nanoarchitekturen: extrinsische Josephson-Kontakte mit externen s-Wellen-Supraleitern sowie intrinsische, Gate-definierte Josephson-Kontakte, die innerhalb eines einzigen, monolithischen TBG-Kristalls realisiert werden.

Zunächst untersuchen wir ein Graphen/hBN-Moiré-Pontetial im ballistischen Regime, in dem sich Fabry-Pérot-Oszillationen und Supraleitung bei hohen Magnetfeldern als direkte Signaturen der Minibandstruktur zeigen. Der Schwerpunkt dieser Arbeit liegt auf TBG im magischen Winkel, dessen flache Bänder aufgrund ihrer verschwindenden Fermi-Geschwindigkeit nur schwache, induzierte Supraleitung erwarten lassen. Entgegen dieser Erwartung beobachten wir einen starken Josephson-Effekt sowohl in den flachen als auch in den dispersiven Bändern, sowie eine deutliche Verletzung der konventionellen Skalierung zwischen kritischem Strom und Normalleitwert – ein Hinweis auf unkonventionelle Mechanismen, die durch starke Wechselwirkungen, Quantengeometrie und Mehrband-Paarung getragen werden. Schließlich realisieren wir durch Ausnutzung des intrinsischen supraleitenden Zustands von TBG Gate-definierte JJs mit symmetriegebrochenem Josephson-Effekt und einer programmierbaren Nullfeld-Josephson-Diode.

Diese Arbeit ebnet den Weg für zukünftige experimentelle und theoretische Untersuchungen des supraleitenden Proximity-Effekts in Moiré-Materialien, insbesondere in Flachbandsystemen. In Zukunft könnte die Kopplung externer Supraleiter an den intrinsischen

supraleitenden Zustand von TBG entscheidende Einblicke in die Symmetrie seines Ordnungsparameters ermöglichen. Andere hier noch nicht untersuchte graphen-basierte Moiré-Übergitter, wie beispielsweise rhomboedrisches Graphen mit paraleller hBN-Ausrichtung, werden von der Erforschung ihrer topologischen Phasen mit dem Josephson-Effekt erheblich profitieren und möglicherweise zur Entwicklung hybrider JJs für topologische Quantentechnologien führen.

Summary

Graphene-based moiré superlattices, and in particular magic-angle twisted bilayer graphene (TBG), have emerged as a promising platform for studying unconventional superconductivity in electronic flat bands, where the interplay between strong correlations, nontrivial topology and quantum geometry plays a central role. The Josephson effect provides a powerful tool to probe the fundamental properties of superconducting states and how they interact with other correlated phases of matter. And yet, it has remained largely unexplored in these moiré systems.

In this dissertation, we demonstrate various experimental efforts to address this gap by combining van der Waals stacking techniques with transparent superconducting contacts and low-temperature transport measurements. Our approach spans two device architectures: extrinsic Josephson junctions (JJs) incorporating external s-wave superconducting leads, and intrinsic gate-defined JJs realized within a single monolithic TBG device.

We first investigate a graphene/hBN moiré superlattice in the ballistic regime, where Fabry-Pérot oscillations and high-field superconductivity reflect the underlying miniband structure. The core of this thesis work focuses on magic-angle TBG, whose flat bands are expected to suppress the proximity-induced superconductivity due to their vanishing Fermi velocity. Surprisingly, we observe a strong Josephson effect in both its flat and dispersive bands, along with a clear violation of the conventional scaling between critical current and normal-state conductance—pointing to unconventional mechanisms involving strong correlations, quantum geometry, and multiband pairing. Finally, by leveraging the intrinsic superconducting state of TBG, we realize gate-defined JJs that display a symmetry-broken Josephson effect and a programmable, zero-field Josephson diode.

This research paves the way for future experimental and theoretical studies of the superconducting proximity effect in moiré materials and especially in flat band systems. Looking forward, coupling external superconductors to the intrinsic superconducting state of TBG will prove a key experiment in unraveling its pairing symmetry. Other graphene-based moiré superlattices not studied here, such as rhombohedral graphene aligned with hBN, will greatly benefit from the exploration of their topological phases with the Josephson effect, potentially leading to the creation of hybrid JJs for topological quantum technologies.

Acknowledgements

As I start to reflect on these five years of PhD, I realize it started in Barcelona amid curfews and lockdowns due to the pandemic, and now it's concluding in Munich. There's way too many people to thank for all the support during this time. First and foremost, I'd like to start with my supervisor, Dima Efetov. Thank you for giving me the great opportunity to be part of the two fantastic research groups we had in ICFO and LMU, for trusting me with such ambitious and important research projects, as well as for the guidance throughout the whole journey.

I'd also like to thank Prof. Milan Allan, Prof. Mathias Scheurer, Prof. Joachim Rädler and Prof. Otmar Biebel for being part of my PhD committee. Special thanks to Mathias for the endless physics discussions in our collaborations.

To all of my colleagues who were a big part of my life both in Barcelona and Munich: Ipsita, Rafa, Jaime, Giorgio, Roop, Alex and Martin. To Ipsita, for going from "where is Ipsita?!", to enjoying so much a fabada, being our bouldering buddy and a big friend. To Rafa, whom I met during a videogame scam and who almost left Munich amid an apartment scam. Thank you for always checking on me, for your endless enthusiasm and for being the best friend I could hope for. To Jaime, for the Díez team, the JJ team. As the time has passed by, I realize now the incredible work that you did that first year by teaching me everything in the lab. I am so grateful for that, but foremost, for having shared, learned and accomplished together so many things, and for ultimately, making it work. To Giorgio, for cooking me the best pasta I've ever eaten. To Roop, for Thursdays no breaks. To Alex, for sticking with me since our first day in ICFO, closing many boxes together during the move, and being the most genuinely interested person in physics that I know, which still inspires me to date. To Martin, for his kindness and support, and for always bringing solutions to my problems in the cleanroom after a whole night of work.

And then with the new generation, the Mensa guys came: Jiazhuo, Janos, Daniil, Leon, Marc, Hajar, Lorenzo, Majid, Joshua, Mudit, Soumya, Ashwin, Ylvi, Egor, Gabriela, Carl, LeonB, Quentin and Bihn. Ever since day one I have admired your clear sightedness in what is important in life, and I really wanna thank you all for that. A special thanks to Daniil, who worked day and night to get the superconducting sputtering working again,

and from whom I have learned a lot, even though he'll probably deny it. To all current and especially previous group members for all their help: Cheng, Elisa and Prasanna. And to Hadrien, for his short yet powerful mentorship in Grenoble.

Thanks to all the people that have made our lives easier in the lab and in the cleanroom, who many times go unnoticed. In ICFO, thanks to Paula and Javi, and to Carlos for helping us out with the move and giving us the drill after days of manually screwing tens of wooden boxes. In LMU, I'd like to thank Christian for his endless good mood and support, to Philipp for all his invaluable help with the sputtering and the Peltier device, to Dayse and Bert for helping us with the transition and all the paperwork, and to Anton for always being willing to help.

Nunca me habría quedado encandilado de la Física si no hubiera sido por mis profesores, de los que aspiro a ser la mitad de lo que ellos supusieron para mí. Gracias a Agustín y a Manolo del Fleming. Gracias a Osorio, Andrés Viña y Jesús Blanco, por hacerme ver que aunque por imposible que me pareciera de aquella, se podían descubrir cosas nuevas en Física, y siempre con rigor.

A los mejores, la gente de Afincados y Onfire: Paula, Berto, Mendo, Lucía, Sara, Elena, Claudia, y Fonso. Disfrutones, siempre listos para celebrar todo lo bueno, y en los que me he refugiado cuando las cosas no iban tan bien. A Irene y a Gaia, por esa relación amor-odio con los paseos en Rambla de Brasil, y los buenos momentos en Barcelona. A Laura, por haber formado parte de la expatriación de su querida Cataluña, por sus cero rayadas, y por haber sido una gran amiga y resistido aquí con nosotros en Munich hasta (casi) el final. A los Joans, Carla, María y Buggy, por esas tardes de hitster y hacer una cuenta atrás para volvernos todos a España. Al golfus team, Xavi y Chaco, por esas fozadas que aunque ellos no lo sepan, más de una vez me han sacado de un agujero y me han hecho recordar por qué quiero seguir haciendo Física. Y a todas esas personas que han hecho de ICFO, Barcelona, LMU, Munich y todos los viajes y conferencias algo que no olvidaré!

La dedicatoria de esta tesis es para mi familia. Empieza con mis abuelos, Angelines, Felisa, Julián y Miguel. Gracias a su sacrificio para sacar a sus familias adelante, yo puedo estar hoy aquí ganándome la vida haciendo un doctorado y trabajando en investigación. Abuelo, recuerdo todas las veces que me preguntabas por el grafeno, y te echaré mucho de menos. A mis padres, por quererme incondicionalmente y por dedicar una vida plena a cuidarnos. A Marina, por haber sido la persona que más me ha venido a ver tanto en Barcelona como en Munich, y por estar siempre ahí. A mi tia Angelines por todo su cariño, a Benjamín, y a toda mi familia.

Marta, el último autor en aparecer puede haber hecho entre nada y todo. En este caso, esta tesis es tanto mía como tuya. Pasando por exponerte cada asignatura de la carrera por Fuertes Acevedo, a no parar de hablar de JJs y magic angles, has aguantado unas chapas monumentales sobre Física, y de alguna manera nunca me has hecho sentir que te las estuviera dando. Desde Barcelona a Munich, has hecho que esto haya merecido la pena, y todo lo que hemos conseguido en estos 5 años, lo hemos conseguido juntos.

Author's publications

[P1] A. Díez-Carlón, et al. "High-field superconductivity in a moiré superlattice ballistic Josephson junction". *In preparation* (2025).
Contributions: Sample fabrication, measurements, data analysis, discussion and paper writing.

[P2] A. Díez-Carlón, J. Díez-Mérida, P. Rout, D. Sedov, P. Virtanen, S. Banerjee, R. Penttilä, P. Altpeter, K. Watanabe, T. Taniguchi, S.-Y. Yang, T.T. Heikkilä, P. Törmä, M.S. Scheurer, D.K. Efetov. "Probing the flat-band limit of the superconducting proximity effect in twisted bilayer graphene Josephson junctions". *arXiv:2502.04785* (2025). Under review in *Physical Review X*. `http://arxiv.org/abs/2502.04785`
Contributions: Sample fabrication, measurements, data analysis, discussion and paper writing.

[P3] J. Díez-Mérida, A. Díez-Carlón, S.Y. Yang, Y. Xie, X. Gao, J. Senior, K. Watanabe, T. Taniguchi, X. Lu, A.P. Higginbotham, K.T. Law, D.K. Efetov. "Symmetry-broken Josephson junctions and superconducting diodes in magic-angle twisted bilayer graphene". *Nature Communications* 14, 2396 (2023). `https://doi.org/10.1038/s41467-023-38005-7`.
Contributions: Sample fabrication, measurements, data analysis, discussion and paper writing.

[P4] P. Virtanen, R.P.S. Penttilä, P. Törmä, A. Díez-Carlón, D.K. Efetov, T.T. Heikkilä. "Superconducting junctions with flat bands", *arXiv:2410.23121* (2025). Under review in *Physical Review B*. `https://arxiv.org/abs/2410.23121`
Contributions: Insight into the theoretical modelling and discussion.

[P5] R. Luque-Merino, D. Călugăru, H. Hu, J. Díez-Mérida, A. Díez-Carlón, T. Taniguchi, K. Watanabe, P. Seifert, B.A. Bernevig and D.K. Efetov. "Interplay between light and heavy electron bands in magic-angle twisted bilayer graphene", *Nature Physics* (2025). `https://doi.org/10.1038/s41567-025-02912-x`
Contributions: Sample fabrication, transport measurements and discussion.

[P6] J. Díez-Mérida, I. Das, G. Di Battista, A. Díez-Carlón, M. Lee, L. Zeng, K. Watanabe, T. Taniguchi, E. Olsson, D.K. Efetov. "High-yield fabrication of bubble-free magic-angle twisted bilayer graphene devices with high twist-angle homogeneity". *Newton* 1, 1 (2025). https://doi.org/10.1016/j.newton.2024.100007
Contributions: Sample fabrication, transport measurements and discussion.

[P7] G. Di Battista, K.C. Fong, A. Díez-Carlón, K. Watanabe, T. Taniguchi, D.K. Efetov. "Infrared single-photon detection with superconducting magic-angle twisted bilayer graphene", *Science Advances* 10, eadp3725 (2024). https://doi.org/10.1126/sciadv.adp3725
Contributions: Sample fabrication, transport measurements and discussion.

[P8] J.D. Mehew, R. Luque-Merino, H. Ishizuka, A. Block, J. Díez-Mérida, A. Díez-Carlón, K. Watanabe, T. Taniguchi, L.S. Levitov, D.K. Efetov, K.-J. Tielrooij. "Ultrafast Umklapp-assisted electron-phonon cooling in magic-angle twisted bilayer graphene", *Science Advances* 10, adj136 (2024). https://doi.org/10.1126/sciadv.adj1361
Contributions: Sample fabrication and transport measurements.

[P9] S.Y. Yang, A. Díez-Carlón, J. Díez-Mérida, A. Jaoui, I. Das, G. Di Battista, R. Luque-Merino, R. Mech, D.K. Efetov. "Plethora of many body ground states in magic angle twisted bilayer graphene", *Low Temperature Physics* 49, 631–639 (2023). https://doi.org/10.1063/10.0019420
Contributions: Sample fabrication, measurements and discussion.

Introduction

For many decades during the 20th century, two-dimensional (2D) materials were believed to be thermodynamically unstable in nature [1]. This notion came from theoretical arguments, such as the demonstration by Mermin on how thermal fluctuations can displace the atoms in the order of their interatomic distances in lower dimensions, thus destroying long-range crystalline order [2]. Additionally, Anderson localization suggested that for non-interacting electrons, even the smallest disorder localizes all states in two dimensions at zero temperature, suppressing metallic transport [3]. The isolation of monolayer graphene in 2004 challenged these long held assumptions, demonstrating that atomically thin crystals could indeed exist as stable, free-standing materials [4]. As this 2D material is exfoliated from a bulkier 3D material, the strong interatomic bonds confers it an exceptional in-plane stiffness, which along with a gentle corrugation that adds small ripples in the third dimension, suppress thermal fluctuations and stabilize long-range crystalline order [1]. Furthermore, as its charge carriers obey a massless Dirac dispersion, even weak localization is often absent in graphene, allowing for extremely high mobilities and rendering it an excellent conductor [5, 6]. This discovery not only opened a new realm of material science but also provided a tunable platform to explore quantum transport in two dimensions.

Following the discovery of graphene, a variety of atomically thin materials with a wide range of physical properties were exfoliated and studied, including insulators (hBN), semiconductors (MoS_2, WSe_2), superconductors ($NbSe_2$, $MoTe_2$), magnets (CrI_3) and topological insulators (WTe_2) [7]. More importantly, these atomically thin crystals can be stacked on top of each other due to the weak van der Waals forces between layers. This stacking, which does not rely on chemical bonding, preserves the integrity of each individual layer while allowing novel interlayer coupling. The resulting vertical assembly thus constitutes a van der Waals heterostructure in which the quantum phases of each layer can coexist and interact, engineering a new material altogether.

An even more striking degree of freedom arises when these stacked layers are rotated with respect to one another. A small relative twist between two periodic lattices generates a moiré superlattice, a much larger lattice that the two constituent ones, whose long-wavelength periodic potential can reshape the electronic band structure completely.

The most notable example is twisted bilayer graphene (TBG), in which if two graphene sheets are overlaid and twisted by an angle 1.1°, the so-called magic angle, the low-energy bands become remarkably flat, quenching the kinetic energy and amplifying the effects of electron-electron interactions [8–12]. From 2018, experiments showed that these flat bands host a strongly correlated phase diagram that includes correlated insulators [11], superconductivity [12, 13], orbital ferromagnetism [14], Chern insulating states [14–16]; and many others [17]. Beyond TBG, similar strategies have been applied to twisted TMD bilayers, where correlated and topological phases have also been observed [18]. That such a rich many body phase diagram can arise simply by rotating one atomic layer with respect to another is one of the most profound findings in condensed matter physics in recent years, which has created an entire new field of research, coined Twistronics.

In this rapidly evolving field, the Josephson effect offers a unique and powerful probe of the underlying quantum phases. A Josephson junction (JJ) comprises two superconductors separated by a non-superconducting weak link, across which Cooper pairs can travel via the proximity effect, creating a dissipationless supercurrent. The dependence of this supercurrent on the carrier density, temperature and magnetic field can encode detailed information about the proximitized material, such as the symmetries of its ground state and the electronic and topological structure of its underlying bands. In the last two decades,

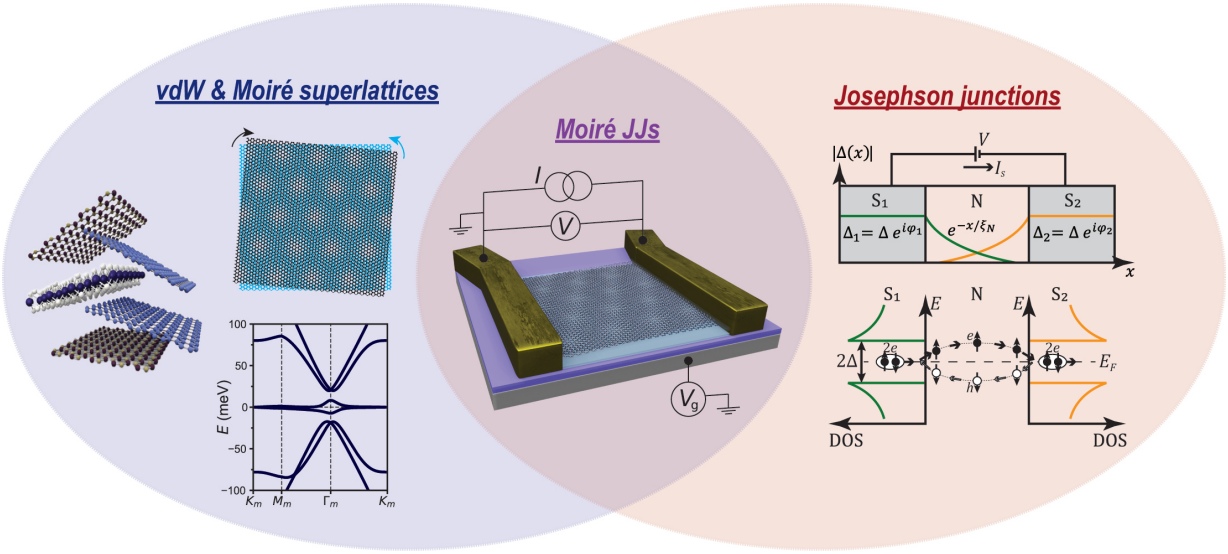

Fig. 1: Investigating Josephson junctions with moiré superlattice weak links. On the left, the vertical assembly of vdW heterostructures (partially adapted from [7]), along with the relative twist-angle between each atomic layer, enable the formation of moiré superlattices with exotic quantum phases and flat electronic band structure. On the right, research with Josephson junctions explores how the superconducting proximity effect in a weak link, described by the creation of Andreev Bound states, is affected by its electronic and topological properties. The intersection represents the scope of this thesis, which is to explore Josephson junctions with graphene-based moiré superlattices as the weak link.

JJs with monolayer graphene as the weak link have been used to study superconducting ballistic transport [19], Fabry-Pérot oscillations [20], Andreev bound states [21], and supercurrents through Quantum Hall edge states [22–24]. Yet, the exploration of the Josephson effect in moiré superlattices remains largely unexplored.

This thesis aims to bridge that gap by investigating the Josephson effect in graphene-based moiré superlattices, with a particular focus on twisted bilayer graphene near the magic angle. Through high-precision van der Waals assembly and low-temperature transport measurements, we study how the superconducting proximity effect manifests in systems with strongly renormalized band structures, and how phenomena such as flat bands, quantum geometry, and symmetry-broken phases affect the Josephson response. In doing so, we demonstrate not only how the Josephson effect can deepen our understanding of how superconductivity behaves in moiré superlattices, but also how they may enable novel device functionalities such as Josephson diodes.

Outline of the thesis

This doctoral thesis is structured in five Chapters, which provide the necessary background, experimental context, and detailed analysis of the results obtained in several classes of graphene-based moiré Josephson junctions. Chapter 1 is purely introductory, while Chapter 2 focus on the fabrication and experimental techniques used in this thesis work, and Chapters 3, 4 and 5 concentrate on the results obtained.

Chapter 1 provides a theoretical background on graphene moiré superlattices and Josephson junctions. We start from the analytical calculation of the band structure of single-layer graphene (Section 1.1), following with the description of its band structure reconstruction under a moiré potential with an aligned hexagonal boron nitride substrate (Section 1.2), or with another graphene with a relative twist-angle (Section 1.3). For the latter system, we discuss the emergence of flat bands when the two graphene layers are rotated at the magic angle 1.1° and show quantum transport experimental data of its strongly correlated phase diagram. In the last Section 1.4, we introduce the concept of Josephson junctions and discuss how the superconducting proximity effect behaves when proximitizing normal metal weak links such as monolayer graphene.

In Chapter 2, we extensively describe the experimental methods used to produce our results. Section 2.1 outlines the fabrication protocol developed during this thesis work to achieve vertical assembling of high-quality two-dimensional materials, in especial twisted bilayer graphene. We then narrate our efforts and eventual success in producing superconducting contacts to graphene-based van der Waals heterostructures in order to engineer Josephson junctions with them (Section 2.2). In Section 2.3 we describe the working principles of low-temperature cryostats employed to perform our experiments, as well as the electronic setup used for the low-frequency transport measurements.

In Chapter 3, we present our results on the study of the ballistic Josephson effect in a graphene/hBN moiré superlattice weak link. Through the observation of Fabry-Pérot oscillations and their dependence on the carrier density, in Section 3.1 we can gain information about the moiré bands. In Section 3.2, the ballistic regime also allows us to explore for the first time the superconducting proximity effect at high magnetic fields in the moiré minibands once the superlattice density is reached, which we find to differ from the Dirac cone band due to the presence of saddle-point van Hove singularities.

Chapter 4 consists of the main piece of work in this thesis, where for the first time we explore the superconducting proximity effect in the flat bands of twisted bilayer graphene with external superconducting leads. In Section 4.1 we introduce the concept of quantum geometry and its importance in describing superconductivity in flat band systems. Section 4.2 presents the proximity effect in the flat and dispersive bands of TBG, demonstrating an unconventional Josephson effect in the former, which is evidenced by the violation in the scaling of the critical current with the normal state conductance (Section 4.3). The dependence of the critical current with the filling of the flat bands is further explored in Section 4.4, where we discuss the importance of the contributions from the quantum geometry and multiband pairing to the proximity effect. Finally, Section 4.5 gathers our study of the Josephson diode effect and gives insights into the broken symmetries of the ground states of TBG.

Chapter 5 shows our efforts to exploit the gate-tunability and correlated phase diagram of twisted bilayer graphene to engineer hybrid gate-defined junctions. Section 5.1 shows the nanofabrication methods we developed to engineer these devices, as well as their quantum transport characterization. By gating the sides of the junctions to the intrinsic superconducting state of TBG, in Section 5.2 we are able to create gate-defined Josephson junctions. Here we present our findings of a symmetry-broken Josephson effect close to half-filling of the flat bands, which enables us to create a Josephson diode, and explain how the results agree with a ground state dominated by orbital magnetism and valley polarization. Finally, in Section 5.3 we show how this versatile platform allows us to engineer gate-defined p-n junctions, and summarize how they enable us to study the cooling dynamics and thermoelectric transport of TBG through optoelectronic measurements.

Chapter 1

Graphene-based moiré superlattices and Josephson junctions

1.1 Monolayer Graphene

The electronic structure of carbon is $1s^2 2s^2 2p^2$, with 4 valence electrons. Due to the sp^2-hybridization between the first s-, p_x- and p_y-orbitals, the carbon atoms in graphene are bonded through in-plane σ-bonds with an average distance of $d \approx 0.142$ nm (see Fig. 1.1a). In this honeycomb lattice, which is a triangular Bravais lattice with a two-atom basis A and B, the lattice parameter is $a = \sqrt{3}d \approx 0.246$ nm and the primitive unit-cell vectors are

$$\boldsymbol{a_1} = a\left(\frac{\sqrt{3}}{2}, \frac{1}{2}\right) \quad , \quad \boldsymbol{a_2} = a\left(\frac{\sqrt{3}}{2}, -\frac{1}{2}\right). \tag{1.1}$$

The remaining perpendicular p_z-orbitals form two covalent π-bonds with its neighbors, providing the free electrons that contribute to the electronic transport [25]. By considering only nearest-neighbor hopping, we can estimate the energy dispersion relation for the π-electrons of graphene with the tight-binding approximation. Taking the Fourier transform of the creation (annihilation) operators $c_\alpha^\dagger$ (c_α) for the sites $\alpha = \mathrm{A}, \mathrm{B}$ to work in the momentum-space basis, the Hamiltonian reads:

$$\mathcal{H} = -t \sum_{\langle i,j \rangle} \left(c_i^\dagger c_j + \mathrm{h.c.} \right) = -t \sum_{\mathbf{k}} \left(c_{\mathrm{A}}^\dagger(\mathbf{k}) \sum_{j=1}^{3} e^{i\mathbf{k}\cdot\boldsymbol{\delta}_\mathbf{j}} \; c_{\mathrm{B}}(\mathbf{k}) + \mathrm{h.c.} \right). \tag{1.2}$$

Here $t \approx 2.7$ eV is the hopping amplitude and $\boldsymbol{\delta_j}$ are the vectors which connect the A-sites with its three nearest B-sites (see Fig. 1.1a), given by:

$$\boldsymbol{\delta_1} = d\,(1,0) \quad , \quad \boldsymbol{\delta_2} = d\left(-\frac{1}{2}, \frac{\sqrt{3}}{2}\right) \quad , \quad \boldsymbol{\delta_3} = d\left(-\frac{1}{2}, -\frac{\sqrt{3}}{2}\right). \tag{1.3}$$

In this basis, diagonalizing the matrix Eq. (1.2) simply gives $E_{\pm}(\mathbf{k}) = \pm t|\sum_{j=1}^{3} e^{i\mathbf{k}\cdot\boldsymbol{\delta}_\mathbf{j}}|$, where $|z| = \sqrt{zz^*}$ denotes the complex modulus of $z \in \mathbb{C}$. The full-written expression of these eigenvalues is

$$E_{\pm}(\mathbf{k}) = \pm t\left|1 + 2e^{i\sqrt{3}ak_x/2}\cos\left(ak_y/2\right)\right| \tag{1.4}$$

and Fig. 1.1b shows the corresponding energy bands. From Eq. (1.4) we can deduce that there are two inequivalent points $\mathbf{K} = (4\pi/\sqrt{3}a,\ 4\pi/3a)$ and $\mathbf{K}' = (4\pi/\sqrt{3}a,\ -4\pi/3a)$ in the first Brillouin zone where the valence (E_-) and conduction (E_+) bands touch, i.e. points where $E_{\pm}(\mathbf{k}) = 0$; as also visualized in Fig. 1.1b-c. Because three of the four valence electrons in graphene are completely filling the σ bands, the remaining one has to be shared in the perpendicular p_z-orbital, which fills the π valence band, i.e. the E_- band in Eq. (1.4). Thus, the intrinsic Fermi level of graphene has to be placed at $E_F = 0$ where the valence and conduction bands meet; the so-called Dirac points $\mathbf{K}$ and $\mathbf{K}'$.

Expanding around these high-symmetry points, $\mathbf{k} = \mathbf{K}^{(\prime)} + \mathbf{q}$ such that $|\mathbf{q}| << |\mathbf{K}^{(\prime)}|$, the low-energy dispersion of graphene becomes linear:

$$E_{\pm}(\mathbf{q}) = \pm\hbar v_F|\mathbf{q}| + \mathcal{O}[(|\mathbf{q}|/|\mathbf{K}^{(\prime)}|)^2], \tag{1.5}$$

where $v_F = \sqrt{3}at/2 \approx 10^6$ m/s is the Fermi velocity. Similarly, the Hamiltonian reduces to the Dirac Hamiltonian for massless electrons: $\mathcal{H} = \pm\hbar v_F\,\boldsymbol{\sigma}\cdot\mathbf{q}$, with $\boldsymbol{\sigma} = (\sigma_x, \sigma_y)$ the Pauli matrices [25]. This Dirac-like dispersion, accessible in quantum transport experiments, highlights the vanishing effective mass of electrons in graphene, which has been extensively studied over the last two decades [4, 5, 25].

While $\mathbf{K}$ and $\mathbf{K}'$ are inequivalent sites in the Brillouin zone, since they belong to the two different A and B sublattices, the low-energy states are degenerate at these points (see

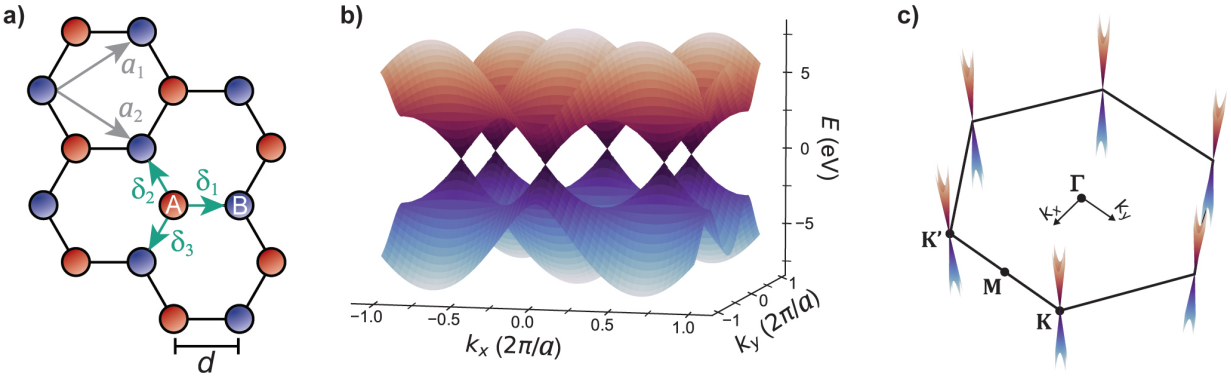

Fig. 1.1: Graphene lattice and band structure. a) Honeycomb lattice of graphene, where the A (resp. B) sites are indicated by red (blue) colors. The vectors $\boldsymbol{a_1}$, $\boldsymbol{a_2}$ form the triangular Bravais lattice of the B-sublattice. Vectors $\boldsymbol{\delta_1}$, $\boldsymbol{\delta_2}$ and $\boldsymbol{\delta_3}$ denote the positions of the first nearest-neighbors. **b)** Graphene band structure obtained from the tight-binding model derived in the text. **c)** Zoom-in of **b**, where the low-energy dispersion shows Dirac cones that cross at zero-energy at the inequivalent high-symmetry points $\mathbf{K}$ and $\mathbf{K}'$.

Fig. 1.1c). This degeneracy is the so-called valley quantum number, which along with the spin symmetry, gives a four-fold degeneracy to the graphene Dirac cones.

The two valleys in graphene are related by the two-fold rotation or inversion symmetry $C_2 : (x, y) \to (-x, -y)$ and by the time-reversal symmetry operation $\mathcal{T} : H \to H^\dagger$. When working with the one-valley representation however, these two symmetries are no longer individually valid, but the product of them is: $C_2\mathcal{T}$. This is a key concept, as the breaking of the C_2 or $\mathcal{T}$ symmetries splits the valley and creates a gap in graphene, with the electrons acquiring some finite effective mass. This is the case of hexagonal Boron Nitride (hBN) for example, with the same honeycomb lattice as graphene but C_2 here is broken because the two on-site energies of B and N are different. hBN is indeed an insulator with a ~ 6 eV indirect bandgap [26, 27].

In low-temperature transport experiments, the electrical resistance of graphene can be measured in a 4-terminal Hallbar geometry, where its low carrier density n can be tuned by applying an electric field with a gate voltage [4]. Fig. 1.2a shows the longitudinal resistance R_{xx} measured at the conduction ($n > 0$) and valence ($n < 0$) bands, with a peak at zero density corresponding to the Dirac point or charge-neutrality point (CNP). The higher resistance at the valence band is explained by the n-doping of graphene from the Cr metallic contacts in our experiment. As the Fermi level of graphene is lowered to the valence band (p doping), a n-p-n junction is formed, which raises the resistance due to the carriers undergoing multiple partial reflections at the two n-p interfaces.

By studying the Quantum Hall effect of graphene, its spin-valley degeneracy $g = g_s g_v$ can be observed [28]. Under a perpendicular magnetic field B, the Dirac spectrum quantizes

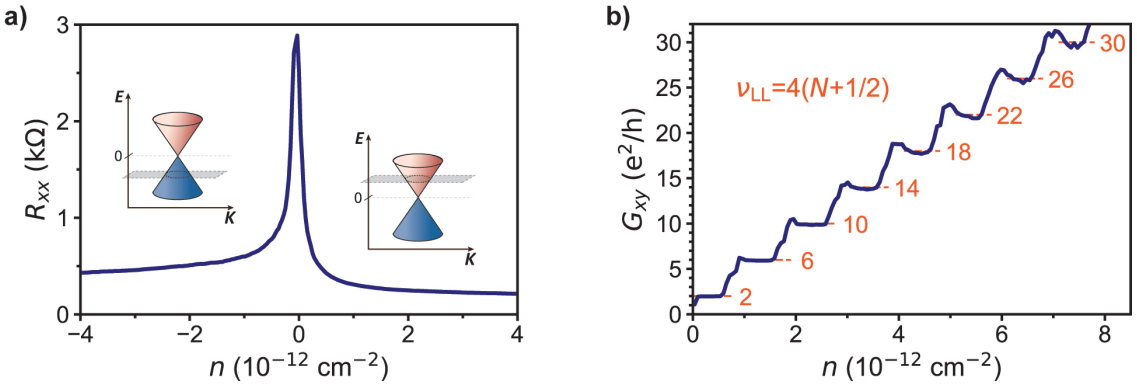

Fig. 1.2: Graphene transport and spin/valley degeneracy. a) Measured 4-terminal longitudinal resistance R_{xx} of a graphene sample as a function of carrier density n. It shows a peak at the CNP of the Dirac cone and higher values at the hole side due to the n-doping from the electrical contacts. **b)** Measured 4-terminal transversal conductance $G_{xy} = 1/R_{xy}$ of the same sample as in **a**, at a magnetic field of 6 T, in units of the quantum of conductance e^2/h. The LLs clearly follow the quantized sequence of Eq. (1.6). All measurements are done at 35 mK.

into relativistic Landau levels (LLs) $E_N = \mathrm{sgn}(N)\, v_F \sqrt{2e\hbar|N|B}$, where $N \in \mathbb{Z}$. Given the filling factor of a LL $\nu_{\mathrm{LL}} = nh/eB$ is proportional to the number of electron or hole channels, i.e. the degeneracy g; the expected sequence of LLs for graphene is [29]:

$$\nu_{\mathrm{LL}} = g\,(N + 1/2), \tag{1.6}$$

since $N = 0$ corresponds to a half-filled LL. Fig. 1.2b shows the transport experiment, where the Hall conductance $G_{xy} = \nu_{\mathrm{LL}} e^2/h$ is measured, and the sequence $\nu_{\mathrm{LL}} = 2, 6, 10, 14, ...$ is found, corresponding to a spin-valley degeneracy of $g = g_s g_v = 4$.

1.2 Heterobilayer moiré superlattices: Graphene/hBN

When vertically assembling two equal two-dimensional lattices on top of one another, a new material is created. In the case of graphene, this process creates AB Bernal bilayer graphene, where the only stable, energetically favorable arrangement of the two layers occurs when the A and B sublattices are aligned in the vertical axis.

In general, if one of the two assembled lattices has a small lattice mismatch δ, a new superlattice—called moiré superlattice—with a much bigger periodicity than the two composing ones is created. If a relative angle θ is further set between each layer, the resulting period of the moiré changes. This is shown in Fig. 1.3a-b.

The size of the superlattice unit cell in real space, called moiré wavelength λ_m, can be deduced from the two composing lattices [30]. First, let $\mathbf{g} = \frac{2\pi}{a}(1,0)$ be the reciprocal lattice vector of the first lattice along the k_x direction. Then, for a second lattice with a lattice mismatch δ and rotated an angle θ with respect to the first, this same vector is $\mathbf{h} = \frac{2\pi}{(1+\delta)a}(\cos\theta, \sin\theta)$. The unit cell vector of the superlattice in the reciprocal space, $\mathbf{b}$, will then connect the two previous reciprocal lattice vectors $\mathbf{g}$ and $\mathbf{h}$, such that:

$$\mathbf{b} = \mathbf{g} - \mathbf{h} = \frac{2\pi}{a}\left(1 - \frac{\cos\theta}{1+\delta}, -\frac{\sin\theta}{1+\delta}\right). \tag{1.7}$$

The moiré wavelength will be then $\lambda_m = 2\pi/|\mathbf{b}|$. By having

$$|\mathbf{b}| = \frac{2\pi}{(1+\delta)a}\sqrt{(1+\delta)^2 + 1 - 2(1+\delta)\cos\theta} \tag{1.8}$$

and doing a little of algebra, we finally get to

$$\lambda_m = \frac{(1+\delta)\,a}{\sqrt{2(1+\delta)(1-\cos\theta) + \delta^2}}. \tag{1.9}$$

We note that in this derivation, we have not assumed the two composing lattices to be of any kind. Thus, Eq. (1.9) holds in general for any two-dimensional lattice [30].

In our case we are especially interested in graphene, a honeycomb lattice with a lattice constant $a = 0.246$ nm. It turns out that hBN, a vdW insulating crystal that is generally used as a substrate to encapsulate graphene, also is a honeycomb lattice where the B and N atoms are intercalated. Because the bonds between these two species of atoms have a different distance that the C–C bonds in graphene, hBN has a lattice constant of $a = 0.250$ nm [30]. This results in a $\delta = 0.018$ lattice mismatch between hBN and graphene; sufficiently small to create a moiré potential at low relative twist-angles (see Fig. 1.3a-b). Indeed, taking this $\delta = 0.018$ and $\theta = 0$ into Eq. (1.9) gives us $\lambda_m = 13.9$ nm. This value, about sixty times bigger than the graphene lattice constant, has been confirmed experimentally by local probe measurements such as STM [30] or AFM [31].

1.2.1 Moiré potential and satellite Dirac points

To describe the effect of the periodic potential from the hBN substrate on the electrons of graphene, we use a continuum description, first implemented in twisted bilayer graphene [9, 10], as we will see in Section 1.3. The idea lies in that, because the moiré distance λ_m is much larger than the atomic lattice a, the in-plane variation of the wavefunctions of the p_z graphene orbitals is smooth. This means that the moiré potential is periodic under translations of the moiré lattice, and thus can be expanded in a Fourier series by the six smallest reciprocal lattice vectors $\mathbf{b}_j$ [32, 33]:

$$V(\mathbf{r}) = \sum_{j=0}^{5} V_j \, e^{i\mathbf{b}_j \cdot \mathbf{r}}, \qquad \mathbf{b}_j = R_{j\pi/3}\mathbf{b}_0, \tag{1.10}$$

where $\mathbf{b}_0$ is the same moiré wave-vector as in Eq. (1.7) and R_ϕ is a ϕ-angle rotation matrix. The full continuum Hamiltonian is then

$$\mathcal{H}(\mathbf{r}) = \mathcal{H}_0 + \sum_{j=0}^{5} V_j \, e^{i\mathbf{b}_j \cdot \mathbf{r}}, \tag{1.11}$$

where $\mathcal{H}_0 = v_F \, \boldsymbol{\sigma} \cdot \boldsymbol{p}$ is the graphene Dirac Hamiltonian describing the low-energy carriers near a single valley. Although hBN is formed by a honeycomb lattice, the different on-site energies of the B and N atoms break the inversion symmetry and introduce a mass term. Thus, the moiré potential can be phenomenologically modeled as a combination of a dominant three inversion-symmetric terms (u_0, u_1, u_3), with the addition of a small inversion-asymmetric perturbation $(\tilde{u}_0, \tilde{u}_1, \tilde{u}_3)$ [34]:

$$\begin{aligned} V_j = \; & u_0 + i(-1)^j u_1 \Big[-\sin(\phi_j)\,\sigma_x + \cos(\phi_j)\,\sigma_y \Big] + i(-1)^j u_3 \sigma_z \\ & + i(-1)^j \tilde{u}_0 + i\tilde{u}_1 \Big[-\sin(\phi_j)\,\sigma_x + \cos(\phi_j)\,\sigma_y \Big] + \tilde{u}_3 \sigma_z, \end{aligned} \tag{1.12}$$

where $\phi_j = \pi j/3$. Here, u_0 just describes a potential modulation over the superlattice, u_1 a modulation of the A-B sublattice hopping, and u_3 the A-B sublattice asymmetry imposed by the hBN substrate, i.e. the sublattice mass term [32].

In Fig. 1.3c we show a band structure calculated by numerically diagonalizing the Hamiltonian in Eq.(1.11). Since the superlattice is much bigger than the atomic lattice, the superlattice Brillouin zone is much smaller than the atomic Brillouin zone, and is called mini Brillouin zone (mBZ). As such, a band-folding process occurs, where the states at linear combinations of the reciprocal vectors $\mathbf{b}_1, \mathbf{b}_2$, are brought to the same point in the mBZ [32, 33].

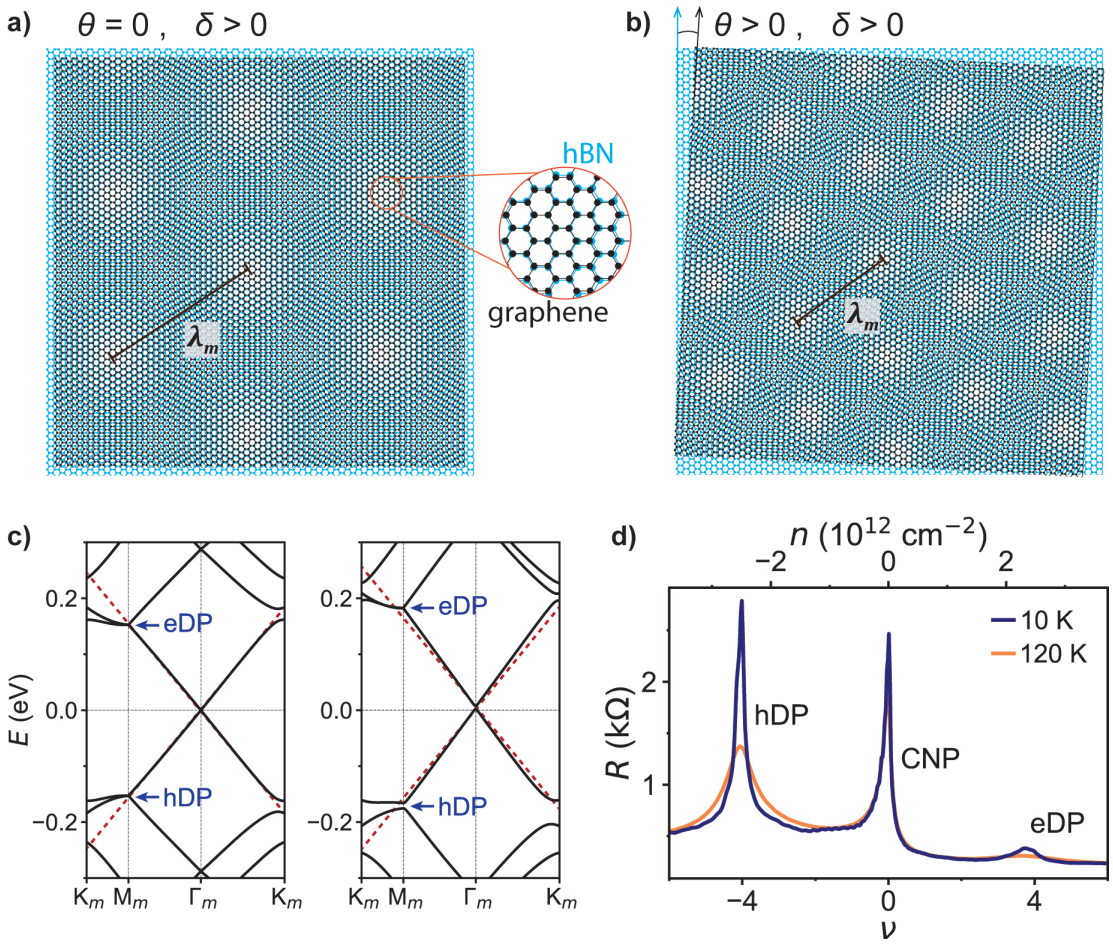

Fig. 1.3: Graphene/hBN moiré superlattice and satellite Dirac points. a) A graphene (black) and an hBN lattice (blue) on top of one another perfectly aligned ($\theta = 0$) forms a moiré superlattice with period λ_m thanks to their atomic lattice mismatch δ, as shown in the inset. **b)** When they are rotated a finite twist-angle between each other ($\theta > 0$), the moiré period decreases. **c)** Band structure of graphene/hBN moiré for $\theta = 0.2°$, for two different sets of the phenomenological parameters $(u_{0,1,3}, \tilde{u}_{0,1,3})$ described in the text. The right panel predicts a finite gap in the hDP and CNP, whereas the left panel does not. In both cases, the red-dashed lines indicate the Dirac dispersion of monolayer graphene. **d)** Transport measurement of resistance R vs filling factor ν (bottom) and carrier density n (top), for a graphene/hBN moiré device with $\theta = 0.2°$.

As we can see in any of the two panels in Fig. 1.3c, the resulting band structure at very low energies consists of a Dirac cone with practically the same Fermi velocity as graphene $v_F \sim 10^6$ m/s. As we approach the end of that first miniband though, due to the band-folding, another set of satellite Dirac points (sDP) appear; both at the electron (eDP) and hole (hDP) sides. This occurs at the $\mathbf{M}_m$ BZ point and at energies $\sim \pm 0.17$ eV. Importantly, these sDP have a renormalized Fermi velocity in one direction of the BZ towards $\mathbf{K}_m$, about half of monolayer graphene ($v_F \sim 0.5 \times 10^6$ m/s) [32].

The difference between the left and right panels are the phenomenological parameters used. The left panel uses $u_{0,1,3} = (-52, 0, 0)$ meV and $\tilde{u}_{0,1,3} = (0, 0, 0)$, which corresponds to setting a rigid potential modulation from the hBN, and yields a particle-hole symmetric band structure [32]. The right panel uses $u_{0,1,3} = (-25, 14, 14)$ meV and $\tilde{u}_{0,1,3} = (-5, 3, 3)$ meV. The nonzero u_1 and u_3 values produce an electron-hole asymmetric band structure, which is always present in STM and transport experiments [30, 35–38]. Fig. 1.3d brings an example, where we measure the resistance of a graphene/hBN moiré sample with a twist-angle $\theta = 0.2°$, as a function of carrier density n (top) and the filling factor ν of the moiré minibands (bottom). Here $\nu = \pm 4$ corresponds to 4 electrons/holes per moiré unit cell, i.e. to a fully-filled miniband due to the 4-fold spin-valley degeneracy of graphene, which is still present in the graphene/hBN Hamiltonian of Eq. (1.11). In Fig. 1.3d we see how the CNP is still present at $n = 0$ compared to bare monolayer graphene (Fig. 1.2a), with the difference that two resistive peaks at exactly $\nu = \pm 4$ occur, corresponding to the sDP. The electron-hole asymmetry is evident from the difference in the height of the peaks.

Furthermore, the inversion-asymmetric tilde terms $\tilde{u}_i$ are able to open a minigap at the Dirac point (CNP) and at the sDP. Indeed, in the right panel of Fig. 1.3c we have a small gap of ~ 4 meV (~ 45 K) at the CNP, and a more significant ~ 10 meV (~ 115 K) for the hDP, while the eDP is obscured by overlapping bands [32]. These gaps are also seen in spectroscopy experiments [30]. In transport, as in the case for our $\theta = 0.2°$ sample, the gaps are detected by thermal activation, where the resistance increases with decreasing temperature (see Fig. 1.3d). In the next Subsection 1.2.2 we will show how this twist-angle can be extracted with precision from the magnetic field phase diagram.

1.2.2 Hofstadter butterfly in the magnetic field phase diagram

An electron moving in a two-dimensional crystal has two competing length-scales when a perpendicular magnetic field B is applied: the lattice constant a that builds Bloch bands and the magnetic length $l_B = \sqrt{\hbar/eB}$ that quantizes Landau levels. In 1955, Harper studied the Bloch problem for a square lattice with dispersion $E(\boldsymbol{k}) = t_0(\cos k_x a + \cos k_y a)$, when subjected under a perpendicular magnetic flux $\Phi = B\,A$, where $A = a^2$ is the area of the lattice, and $\Phi_0 = h/e$ the magnetic flux quanta in the QHE. He demonstrated that solving for the wavefunction $\psi(x, y)$ reduced to solving a one-dimensional discrete equation, called the Harper equation [39]: $\psi_{m+1} + \psi_{m-1} + 2\cos(2\pi m\,\Phi/\Phi_0 - \tilde{q})\psi_m = 2E/t_0\psi_m$, where

$m \in \mathbb{Z}$ marks the m-th unit cell and $\tilde{q}$ is a dimensionless parameter depending on the energy dispersion.

Two decades later, Hofstadter solved this equation for rational flux fractions $\Phi/\Phi_0 = p/q$, whose E/t_0 vs Φ/Φ_0 diagram is now known as the Hofstadter butterfly fractal [40] (see Fig. 1.4c). Here, each band is determined by two integers (s,t) that satisfy the Diophantine relation derived by Wannier [41]:

$$\frac{n}{n_0} = t\,\frac{\Phi}{\Phi_0} + s, \tag{1.13}$$

where n is the electron density and $n_0 = 1/A$ the number of primitive cells per unit area, so that $\nu = n/n_0$ is the electron filling factor of the bands. We note that Eq. (1.13) is valid for any 2D lattice. The integer numbers defining the physics of the 2DEG gained meaning when the TKNN theory later showed that the slope $t \in \mathbb{Z}$ is the Chern number C of the band, so each gap carries a quantized Hall conductance $\sigma_{xy} = t\,e^2/h$ [42]. In the case of a Landau level, $t = \nu_{\mathrm{LL}}$. As for the intercept $s \in \mathbb{Z}$, it just shows that at each integer filling of the band, a set of Chern bands or LLs disperse with the magnetic field.

The experimental confirmation of these predicted fractal minibands was not possible with available 2D electron gases, as the magnetic field required to get to a single flux quanta per unit cell, $B_0 = \Phi_0\,A$, or a significant fraction of it, was far too big to be generated in lab conditions. As an example, if one takes graphene with a lattice constant $a = 0.246$ nm, its corresponding unit-cell area is $A = 5.2 \times 10^{-2}$ nm^2, so that $B_0 \sim 8 \times 10^6$ T. So for these atomic lattices, even smaller fractions such as $\Phi/\Phi_0 = 1/10$ lie well beyond what can be achieved with coil magnets. Early attempts to tackle this problem turned to artificial superlattices whose larger period significantly lowers the required field by a square factor. This was achieved in high-mobility GaAs 2DEG, on top of a Au film with a hole-array of 100 nm periodic length, which were fabricated with lithography techniques [43]. This brought down Φ/Φ_0 to only 0.3 T and provided the first evidence of fractal LLs, but could only scan at a fixed point in n/n_0, since these semiconducting 2DEGs can only be doped chemically.

Van der Waals heterostructures offered a cleaner and more tunable route. The first moiré superlattice with these materials was done by aligning monolayer graphene with hBN. For a perfectly aligned stack, the corresponding moiré period is $\lambda_m = 13.8$ nm, so that $A = 1.6 \times 10^2$ nm^2 and $B_0 \sim 25$ T, which was under experimental reach in high-magnetic field facilities [35–37]. Importantly, thanks to graphene's high mobility and electrostatic gating, the in-situ tuning of both n and B enable a full mapping of the Diophantine Eq. (1.13). This can be visualized in Fig. 1.4a, where we show a measurement of a Landau fan diagram. The graphene/hBN sample is shaped into a Hallbar geometry and the measured longitudinal resistance R_{xx} reveals the formation of LLs when it vanishes. Apart from the fan emanating from the CNP, corresponding to $(t, s = 0)$, another set of LLs is registered from the sDP at $s = \pm 4$ and some less obvious at $s = 2, 6$ (see also Fig. 1.4b). There we can also see that the degeneracy of the LLs in the sDP is 4, just like at the CNP. Due to the fractal nature of the Diophantine equation, the LLs from different s cross each other at every rational p/q

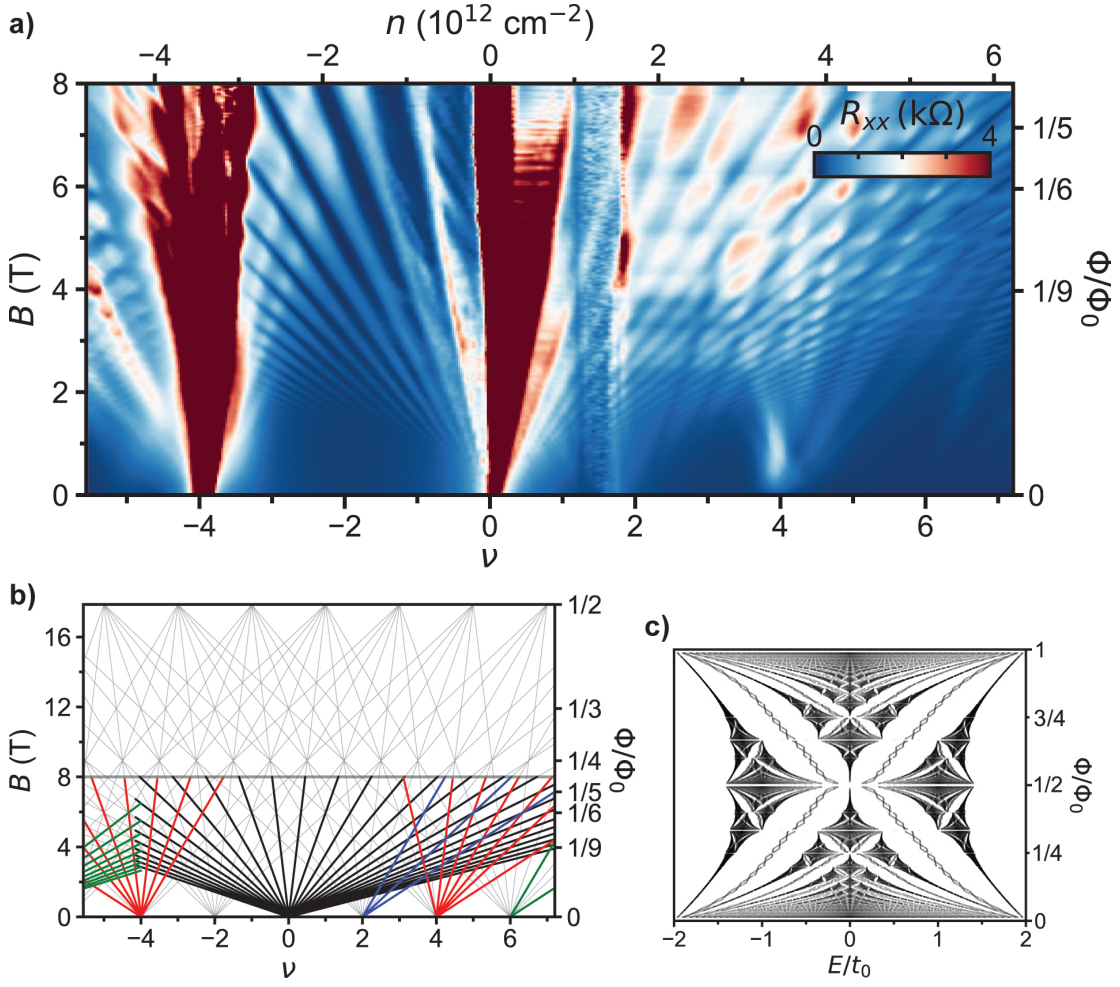

Fig. 1.4: Hofstadter butterfly in the Landau fan of a Gr/hBN moiré superlattice. a) Landau fan diagram of a Gr/hBN sample with $\theta \sim 0.68°$, where the longitudinal resistance R_{xx} is measured vs filling $\nu = 4n/n_s$ of the moiré bands (top), carrier density n (bottom), and vs magnetic field B. The right axis converts B into a fraction of the magnetic flux quanta Φ/Φ_0, where we indicate the values at which some LL crossing occur. **b)** Expected Landau fan in gray lines, along with the observed LLs from **a** in colour lines. The solid horizontal line at 8 T indicates the limit of our experimental measurement in **a**. **c)** Hofstadter butterfly fractal in the energy vs flux diagram, where the bands are coloured in black and the white areas indicate gaps.

fraction of Φ/Φ_0, which we show in the ticks of the right axis in Fig. 1.4a-b. Finally, by looking at Fig. 1.4a, the electron-hole asymmetry of the band structure showed in Fig. 1.3c for zero field, is also very evident here at high magnetic fields.

During the stacking process of a vdW heterostructure, which will be described in detail in Chapter 2, the aimed twist-angle between the different crystals can differ from the final one. However, from the study of these Landau fan diagrams, one can extract with high

precision the twist-angle of the sample. To estimate θ, we need to know the carrier density n_s corresponding to a fully filled moiré superlattice band, since $n_s = g/A$, where g is the degeneracy. For graphene $g = 4$ and the hexagonal moiré superlattice has $A = \sqrt{3}\lambda_m^2/2$. From Eq (1.9) we then arrive to:

$$\theta = \arccos\left(1 - \frac{\sqrt{3}n_s(1+\delta)^2a^2/8 - \delta^2}{2(1+\delta)}\right) \tag{1.14}$$

To estimate n_s, we first need to convert the gate voltage V_g we use to dope our material by accumulation of electrostatic charges, to carrier density n. This is done by knowing the gate capacitance of the dielectric per unit area C_g:

$$n = C_g V_g/e. \tag{1.15}$$

The calculation of the capacitance can be done geometrically by knowing the dielectric constant ϵ and its thickness d, since $C_g = \epsilon/d$. A more accurate estimation of C_g can nevertheless be achieved by fitting the slopes of the LLs in the V_g–B diagram, as we explain next.

A LL is labeled by its filling factor ν_{LL}, which indicates the number of electron/hole edge channels in the 2DEG. For monolayer graphene, due to the spin-valley degeneracy, the sequence of LLs is $\nu_{\mathrm{LL}} = 4(N + 1/2)$. In general, these topological states follow the Streda Formula:

$$n = \nu_{\mathrm{LL}} B/\Phi_0, \tag{1.16}$$

which states that the LLs evolve linearly in field and density, as seen in Fig. 1.4a. Combining Eqs. (1.15) and (1.16), we get an expression to calculate C_g:

$$C_g = \frac{\nu_{\mathrm{LL}} e}{\Phi_0}\frac{B}{V_g}. \tag{1.17}$$

Thus, with Eq. (1.17) and by following the slope of a certain LL, dB/dV_g, we can estimate C_g, but by first knowing the corresponding ν_{LL}. This can be obtained by measuring the Hall resistance R_{xy} in the Landau fan diagram (as we showed in Fig. 1.2b), since $R_{xy} = h/e^2\nu_{\mathrm{LL}}$. Otherwise, one can guess ν_{LL} and verify that the rest of measured LLs can be fitted too. Once C_g is estimated, the V_g axis is converted into n, and from there we can known n_s. This is done by extracting the n value where the resistance peak corresponding to the fully filled superlattice band lies, i.e. to the sDP. An even more accurate method is to extrapolate the LLs emerging from that sDP down to zero field.

Following this method and using Eq. (1.14), we estimate $\theta = 0.68° \pm 0.01°$ for the sample presented in Fig. 1.4. For this twist-angle, we have $\lambda_m = 11.6 \pm 0.2$ nm, so that $A = 1.1 \times 10^2$ nm and $B_0 \sim 35$ T. In our dilution fridge the maximum magnetic field we can reach with our superconducting coils is 8 T, which lies in between $\Phi/\Phi_0 = 1/5$ and $1/4$. At $\Phi/\Phi_0 = 1/5$ we can indeed see some LLs crossings (see Fig. 1.4a-b).

1.3 Homobilayer moiré superlattices: Twisted Bilayer Graphene

A moiré superlattice can also be formed by assembling two exactly equal lattices on top of one another and by rotating them at a relative non-zero twist-angle θ, as shown in Fig. 1.5a. The size of the superlattice in this case can be deduced from Eq. (1.9) by setting $\delta = 0$. Doing so we get

$$\lambda_m = \frac{a}{2\sin(\theta/2)}. \tag{1.18}$$

The key difference between this homobilayer moiré in Eq. (1.18) and the heterobilayer moiré in Eq. (1.9) is that its superlattice grows exponentially as θ approaches zero. The comparison between the two can be seen in Fig. 1.5c. This exponential behavior (red curve), in contrast to the rather constant value of the moiré heterobilayers (green curve), has implications for the study of homobilayer systems at low twist-angles.

For the case that interests us of two graphene layers forming this moiré superlattice, the resulting material is called twisted bilayer graphene (TBG). Because the superlattice period λ_m exceeds the atomic periodicity a at low twist-angles θ, the Brillouin zone of TBG is much smaller; often referred as the mini-Brillouin zone (mBZ). Its size $k_\theta = 2|K|\sin(\theta/2)$, where $|K| = 4\pi/3a$, is determined by the distance between the $\mathbf{K}$ points of each layer, as pictured in Fig. 1.5b. The vertices of the hexagonal mBZ are thus the valleys of the moiré $\mathbf{K}_m$, $\mathbf{K}_m^{'}$, and its center the gamma point $\mathbf{\Gamma}_m$.

Contrary to Gr/hBN, the electronic band structure of TBG varies strongly compared to that of monolayer graphene. At large twist-angles ($\theta \gtrsim 3°$) the two Dirac cones of each graphene layer are far from each other in k-space, and thus the resulting system can be treated as individual decoupled graphene layers (see Fig. 1.6a). However, at low twist-angles ($\theta \lesssim 3°$) the Dirac cones overlap and create new moiré bands (see Fig. 1.6b-c).

Motivated by the key observation of van-Hove-singularities (vHs) in STM experiments on TBG samples with $0.8° \lesssim \theta \lesssim 1.3°$ in 2009 [8], follow-up theoretical work predicted the existence of a pair of flat bands to be responsible for these vHs, featuring a vanishing Fermi velocity at a series of so-called magic angles θ_m [9, 10, 44]. In the following we derive the main aspects of this Bistritzer-MacDonald (BM) single-particle continuum model and show its predictions of flat bands at the first magic angle $\theta_m \sim 1.1°$.

1.3.1 Continuum model and flat bands in TBG

At small twist-angles $\theta \lesssim 3°$ the moiré superlattice period λ_m exceeds the atomic scale by an order of magnitude, resulting in a supercell of $\sim 10^4$ atoms. The exact tight binding model of such material cannot be then calculated with classical computation. This separation between the atomic scale and the moiré scale can nevertheless be exploited: instead of

tracking every carbon orbital, we can treat each graphene layer as a smooth rotated Dirac cone centered on their valley points $\mathbf{K}$ and $\mathbf{K}'$, and couple the layers through a long-wavelength tunneling potential that carries only the three shortest moiré wave-vectors [9]. In this continuum model, for each valley $\xi = \pm 1$ and each layer $\ell = 1, 2$, the intralayer Hamiltonian reads

$$h_\xi^{(\ell)}(\mathbf{k}) = \hbar v_F \, \boldsymbol{\sigma}_\xi \cdot \left[\mathcal{R}(\pm\theta/2)\left(\mathbf{k} - \mathbf{K}_\xi^{(\ell)}\right)\right], \tag{1.19}$$

where $\boldsymbol{\sigma}_\xi = (\xi\sigma_x, \sigma_y)$ acts on the sublattice and $\mathcal{R}$ is the SO(2) rotation matrix, which acts on the wave-vectors centered at the $\mathbf{K}_\xi$ points. Since the crystal momentum is only conserved up to an integer combination of the moiré reciprocal vectors $\mathbf{b}^m_{1,2} = k_\theta\,(1/2, \mp\sqrt{3}/2)$ (see Fig. 1.5a), any plane wave at momentum $\boldsymbol{k}$ mixes only with momenta $\mathbf{k} + i\,\mathbf{b}^m_1 + j\,\mathbf{b}^m_2$, whose integers (i, j) lie inside an hexagonal momentum shell. Cutting this shell at $|i|, |j|, |i+j| \leq 2$ yields 19 momenta in layer 1 and 12 in layer 2, which (together with the two sublattice components) produce a 62-dimensional Hilbert space per spin and valley, sufficiently small to converge at low energies [9, 45].

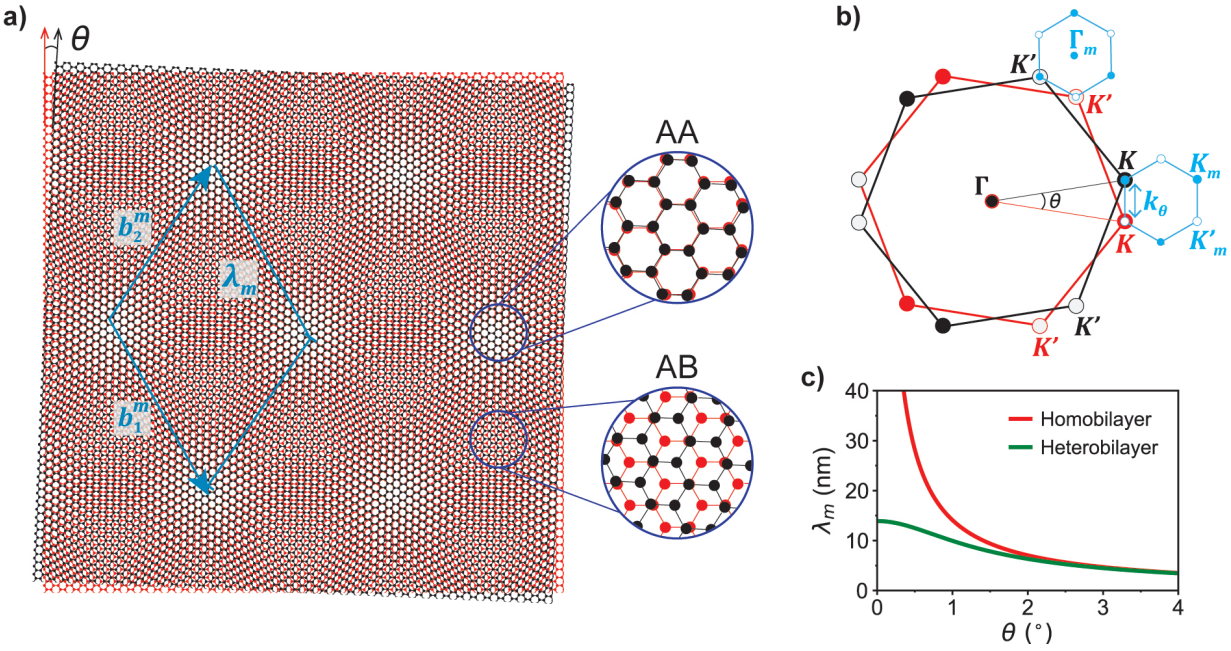

Fig. 1.5: Twisted bilayer graphene moiré superlattice and mini-Brillouin zone. **a)** Two graphene lattices (black and red) on top of one another and twisted by a relative angle θ, resulting in a moiré superlattice with period λ_m, known as twisted bilayer graphene. Zoom-ins show the AA and AB stacking orders of the superlattice. **b)** Brillouin zone of the two graphene layers in red and black, and the mini-Brillouin zone corresponding to TBG in blue. The Dirac points $\mathbf{K}$ and $\mathbf{K}'$ corresponding to each system are shown with the same color code. **c)** λ_m vs θ for a homobilayer (e.g. TBG) and a heterobilayer (e.g. Gr/hBN) moiré superlattice. In the case of TBG (red) the period diverges at low angles, whereas for Gr/hBN (green) it does not.

Because the interlayer separation (~ 3.35 Å) is much smaller than λ_m, the interlayer tunneling amplitude varies smoothly in the plane and can be considered a periodic function. By doing a Fourier expansion and retaining only the three shortest wave-vectors $\mathbf{Q}_0 = 0$, $\mathbf{Q}_+ = +\mathbf{b}_2^m$ and $\mathbf{Q}_- = -\mathbf{b}_1^m$, the interlayer tunneling matrices are:

$$T_0 = \begin{pmatrix} w_{AA} & w_{AB} \\ w_{AB} & w_{AA} \end{pmatrix}, \qquad T_\pm = \begin{pmatrix} w_{AA}e^{\pm 2\pi i/3} & w_{AB} \\ w_{AB}e^{\mp 2\pi i/3} & w_{AA}e^{\pm 2\pi i/3} \end{pmatrix}, \tag{1.20}$$

reflecting the C_{3z} symmetry of AA, AB, and BA local stacking orders (see insets of Fig. 1.5a). In this formulation, we have included lattice relaxation effects, which increase the AB regions at the expense of AA, yielding $w_{AA} < w_{AB}$ [45, 46]. This part was not included in the original BM model [9], but is key to reproduce experimentally observed features such as a bandgap separating the flat and dispersive bands. Based on STM experiments and density-functional calculations, $w_{AA}/w_{AB} \approx 0.75$ appears to be a good estimation at low angles θ [45–47].

Combining Eqs. (1.19) and (1.20), the Bistritzer-McDonald (BM) Hamiltonian for a single valley takes the form

$$\mathcal{H}_\xi(\mathbf{k}) = \begin{pmatrix} h_\xi^{(1)}(\mathbf{k}) & T(\mathbf{r}) \\ T^\dagger(\mathbf{r}) & h_\xi^{(2)}(\mathbf{k}) \end{pmatrix}, \quad T(\mathbf{r}) = \sum_{j=0,\pm} T_j\, e^{i\mathbf{Q}_j\cdot\mathbf{r}}, \tag{1.21}$$

which couples each Dirac block in layer 1 to the three symmetry-related neighbors in layer 2. We note that $\mathcal{H}_\xi$ is written in one valley, but as the time-reversal symmetry relates the two valleys, one may diagonalize the Hamiltonian only for one of them. By doing so numerically for the parameters $\theta = 1.05$, $w_{AA} = 88$ meV and $w_{AB} = 110$ meV, in Fig. 1.6d we find a pair of flat bands with bandwidth ~ 15 meV and a renormalized Fermi velocity of $v_F/v_F^0 \approx 6 \times 10^{-3}$, with $v_F^0 \sim 10^6$ m/s. Separated by band gaps of ~ 12 meV lie the dispersive bands, whose DOS is much smaller than that of the flat bands.

Furthermore, by calculating the band structure at different θ, as shown in Fig. 1.6f, we can find that the bandwidth of the flat bands is minimal at a magic angle $\theta_m \sim 1.12°$. Analytically, one may also derive such a result in terms of a vanishing renormalized Fermi velocity, as we explain next. The interlayer hopping amplitude is described by the dimensionless parameter

$$\alpha = \frac{w}{\hbar v_F^0 |K| \theta}, \tag{1.22}$$

where $2w$ is the hybridization energy between the two layers. Before, we have introduced this value as site-dependent with w_{AA} and w_{AB}. From here one can learn that α is vanishing small for very large θ, i.e. the two graphene layers are decoupled for large twist-angles (see Fig. 1.6a). For relatively small twist-angles $\theta \sim 3°$, the cones start to overlap and create new hybridized moiré bands, although $2w$ is still much lower than the kinetic energy: $2w \ll \hbar v_F^0 |K|\theta$ (see Fig. 1.6b, where $k_\theta \approx |K|\theta$). If however, θ decreases further such that α increases, it comes a point when $2w$ and $v_F^0|K|\theta$ are comparable, so that the lowest of

the hybridized bands is pushed to zero energy, creating a pair of flat bands (Fig. 1.6c). In Ref.[9] it was shown that for these low α values, the Fermi velocity of the hybridized moiré bands decreases continuously as:

$$v_F(\alpha) = v_F^0 \frac{1-3\alpha^2}{1+6\alpha^2}. \tag{1.23}$$

Indeed, a solution of Eq. (1.23) with $\alpha_m = 1/\sqrt{3}$ corresponds to bands with zero Fermi velocity. Using Eq. (1.22), the twist-angle necessary to achieve this solution is

$$\theta_m = \frac{\sqrt{3}w}{\hbar v_F^0 |K|}, \tag{1.24}$$

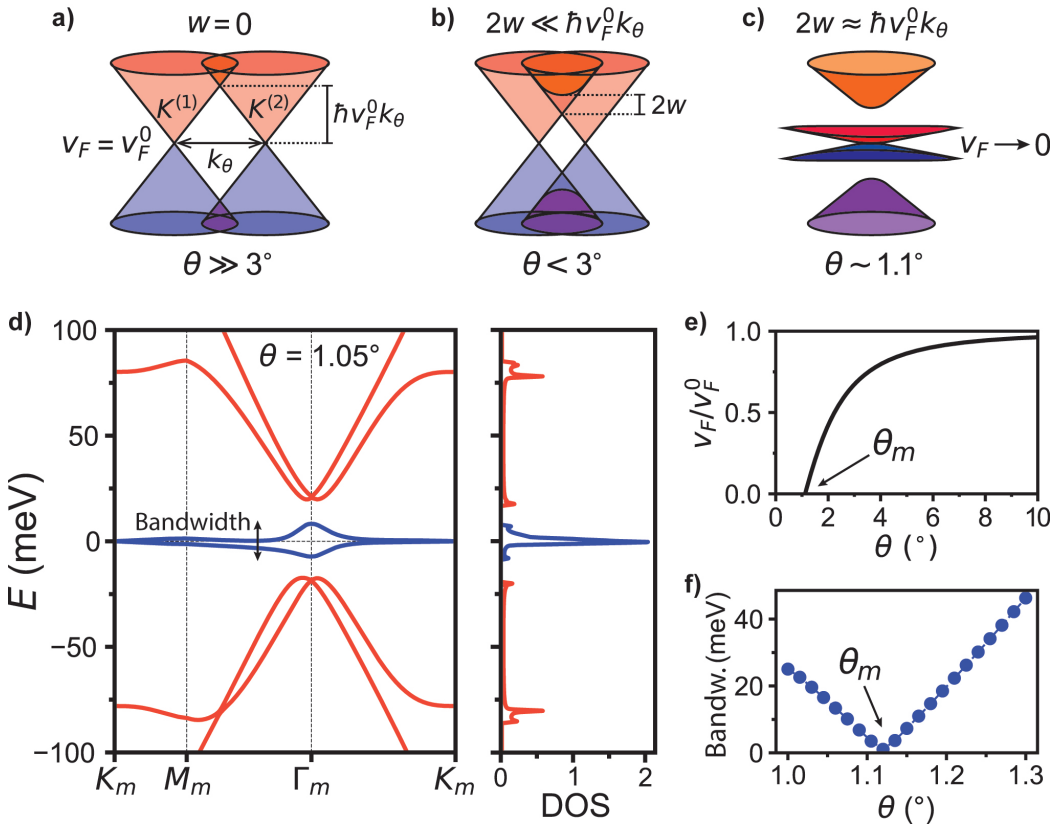

Fig. 1.6: Electronic band structure of TBG and flat bands at the first magic angle. a-c) Hybridization of the Dirac cones $K^{(1)}$ and $K^{(2)}$ of the two graphene layers forming TBG, for different regimes of twist-angle θ. As it approaches the magic angle θ_m, a pair of flat bands are created at the Fermi level with vanishing Fermi velocity. **d)** Band structure along the high-symmetry points and DOS (in arbitrary units) of TBG at $\theta = 1.05°$, calculated from the continuum model with $v_F^0 = 0.87 \times 10^6$ m/s, $w_{AA} = 88$ meV and $w_{AB} = 110$ meV. **e)** Renormalized Fermi velocity v_F/v_F^0 of TBG, according to Eq. (1.23), showing a vanishing value at $\theta_m \sim 1.1°$. **f)** Bandwidth of the flat bands from **c**, which has a minimum at $\theta_m \approx 1.12°$ and scales linearly around it.

which is called the first magic angle and corresponds to the formation of almost perfect flat bands. Setting $w = 110$ meV and $v_F^0 = 0.87 \times 10^6$ m/s, we get $\theta_m \approx 1.1°$. In Ref. [9] a series of several magic angles was numerically derived too, with lower values that the first magic angle.

The prediction of flat bands by the single-particle Hamiltonian of the continuum model of TBG turned out to be successful, as 15 years later it was confirmed experimentally. As we will see next though, the many body quantum phases that were found inside the flat bands are not described by this single-particle model, highlighting the need to account for electron-electron interactions in order to correctly describe the physics of TBG.

1.3.2 Many body correlated phases in TBG

The experimental breakthrough that reveled the many body physics of magic-angle twisted bilayer graphene came in 2018, with the observation of two hallmark signatures of strong electronic correlations: Mott-like insulating states at half-filling of the electron and hole flat bands [11], as well as adjacent domes featuring superconducting phases with critical temperatures of $T_c \sim 1$ K [12]. The presence of these exotic phases within the flat bands, not predicted by the single-particle continuum model [9, 10], suggests that in order to describe the band structure of this system correctly, dominating electron-electron interactions need to be incorporated into new theoretical models [11, 12, 48].

Furthermore, compared to other correlated systems such as the cuprates, the low carrier concentration of the TBG flat bands enables to vary in-situ the electron density and displacement field through the application of gate voltages. Later discoveries of more correlated phases, such as strange metallicity or topological Chern insulators, turned TBG into an exceptionally high-tunable platform for exploring many body physics in two dimensions [P9]. Here we dwell into each of these phases and present some of the transport measurements that help us study them.

The presence of correlated states at every integer filling of the flat bands, not just half-filling ($\nu = \pm 2$), was soon after reported in magneto-transport experiments of TBG samples closer to the magic angle $\theta_m \sim 1.1°$ [13, 14]. Here ν is the filling factor of the TBG bands, which represents the number of electrons per moiré. Since the spin-valley degeneracy of the system is 4 and n_s is the carrier density corresponding to a fully filled moiré band, we have $\nu = 4n/n_s$. Fig. 1.7a shows a 4-probe longitudinal resistance measurement R_{xx} of a TBG sample with $\theta \sim 1.14° \pm 0.02°$, where the peaks mark the position of the integer filling correlated states. Of all these, $\nu = \pm 2, \pm 3$ are insulators, often called thus correlated insulators (CIs), with thermal activation gaps up to $\Delta \sim 2$ meV (see Fig. 1.7c). In transport, these gaps are extracted by the Arrhenius formula $G_{xx} \propto e^{-k_B T/\Delta}$, which generally underestimates their values by an order of magnitude when compared to spectroscopy STM measurements [49, 50]. An exception happens at $\nu = \pm 1$, where a metallic behavior in the resistance is found. Of these correlated metal (CM) phases, the resis-

tance of $\nu = 1$ saturates at low temperatures, whereas at $\nu = -1$ the resistance peak state does not nucleate and appears to fade (see Fig. 1.7a). When studied with thermodynamic probes, such states reveal the ^{3}He Pomeranchuk effect, where the Fermi liquid transits to a solid upon increasing the temperature. In the case of TBG, this transition occurs from a disordered isospin liquid into an isospin-polarized ordered metallic state [51, 52].

For dopings $|\nu| \gtrsim 1$ it was found that the resistivity ρ of TBG grows linearly with temperature, from 30 K down to mK temperatures [53–55]. An example can be found in Fig. 1.7e. This so-called strange metal (SM) phase violates the expected Fermi liquid (FL) behavior, where $\rho \propto T^2$. The FL phase is rather formed near the CNP of the flat bands and when the twist-angle of TBG is turned away from the magic angle [55]. The linear-temperature dependence in strange metals is associated with a carrier scattering

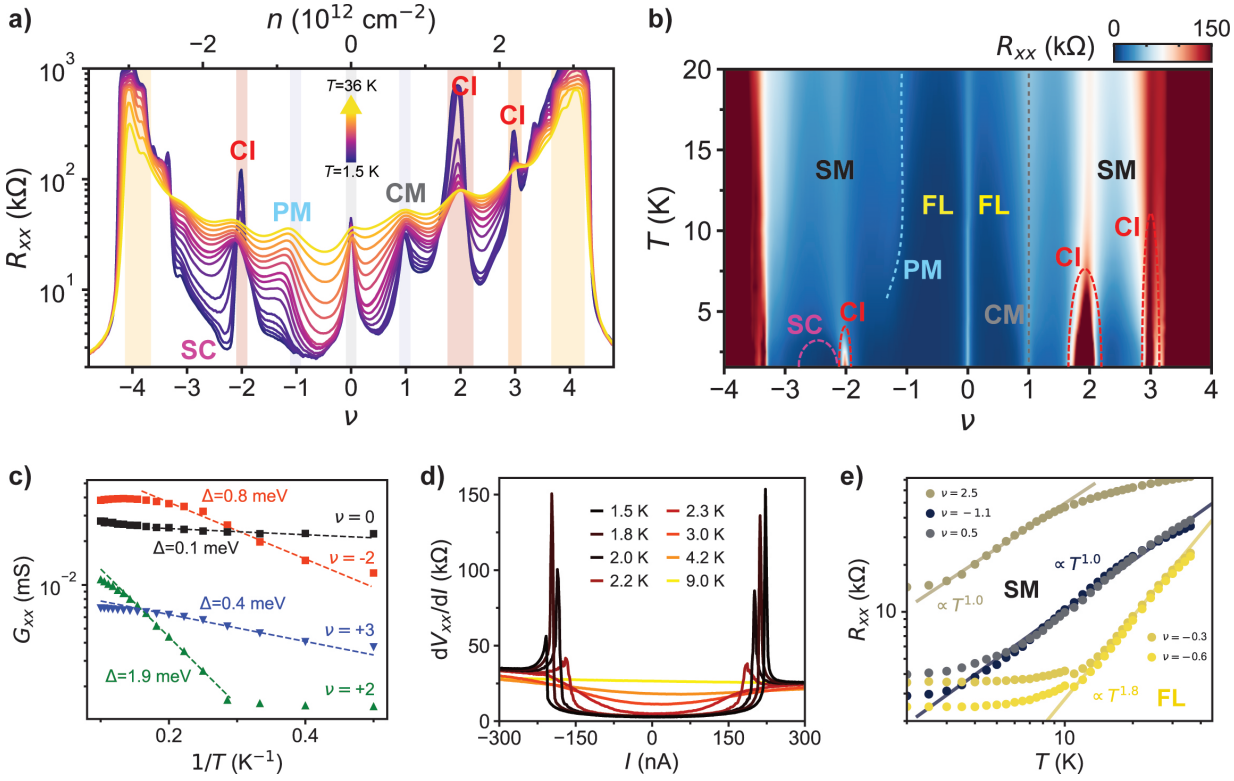

Fig. 1.7: Temperature phase diagram of TBG. a) Resistance R_{xx} measured as a function of filling ν (bottom) and carrier density n (top) for different temperatures T. **b)** Colormap of R_{xx} vs ν and vs T. In **a-b** the abbreviations correspond to: CI=Correlated Insulator, CM=Correlated Metal, SC=Superconductor, SM=Strange Metal, FL=Fermi Liquid, PM=Pomeranchuk. **c)** Arrhenius plot where from the conductance G_{xx} of the integer fillings, a finite thermal activation gap Δ is extracted. **d)** Differential resistance dV_{xx}/dI vs d.c. current I, where the nonlinearities reveal a superconducting state with $I_c \sim 200$ nA and $T_c \sim 2.2$ K, measured at $\nu = -2.2$. **e)** Resistance vs temperature where a strange metal phase with $R \propto T$ or a Fermi liquid phase with $R \propto T^2$ are identified.

rate defined by the Planckian limit $\tau^{-1} = k_B T/\hbar$, which does not depend on the type of scattering in the system, indicating that quantum fluctuations dominate the metallic ground state. The SM phase is very reminiscent of the cuprates, where a crossover to the FL is also observed at high dopings [56], and forms the parent state of the superconducting phase, which could have implications for the superconducting state of TBG (see Fig. 1.7b).

Of special interest is the superconducting phase of TBG, whose electron pairing mechanism and order parameter, even though many experiments have been conducted, is still unknown. As TBG is a 2D material, the superconducting condensate is governed by a Berezinskii–Kosterlitz–Thouless (BKT) transition, which is often experimentally observed in broad R vs T curves and in the V^2 decaying power law of the non-linear differential resistance $\mathrm{d}V/\mathrm{d}I$ curves (see Fig. 1.7d). The surprising diluted phase diagram of TBG, with a carrier density of 10^{12} cm^{-2}, sets a Fermi velocity $T_F \sim 20$ K for the superconducting state (from quantum oscillation measurements). This gives a rather high T_c/T_F ratio that cannot be explained by the weak-coupling BCS theory, but rather sits at an intermediate regime between the BCS and BEC limits, pointing towards electron-electron Coulomb correlations driving the pairing mechanism instead of the conventional electron-phonon [12]. Further unconventional properties have been uncovered, from a nematic order [57], to evidences of a nodal superconducting gap from thermal transport [58], STM spectroscopy [50] and kinetic inductance measurements [59].

The superconducting phase seems to be ubiquitous in graphene-based moiré superlattices. Apart from TBG, other mirror-symmetric twisted multilayers were found to have magic angles that lead to the formation of flat bands. As an example, twisted trilayer graphene has a magic angle of $\sqrt{2}\theta_m \approx 1.5°$. So far, robust superconducting phases have been observed in 3-, 4-, and 5-layer twisted graphene [60–63], where the T_c slowly increases with the number of layers and the carrier density range where the condensate nucleates grows much larger. Other systems with a broken $C_{2z}\mathcal{T}$ symmetry where superconductivity has been observed include twisted double-bilayer graphene [64], rhombohedral multilayer graphene aligned with hBN [65, 66], as well as twisted bilayer WSe_2 [67, 68]. This suggest moiré superlattices to be a key ingredient for driving superconducting phases. Nevertheless, the striking detection of superconductivity in previously well-studied systems such as pristine AB bilayer graphene [69] and ABC rhombohedral trilayer graphene [70], poses the question whether a moiré superlattice is just a means to create flat bands, which ultimately set the electronic structure of the system and drive correlations.

When a perpendicular magnetic field is applied, the phase diagram of TBG is not less complex. As the twist-angle approaches the magic angle, the Landau levels stemming from the CNP are found to reduce its degeneracy from eight- to four-fold [11, 71]. Furthermore, when the filling factor ν reaches an integer value, a new set of LLs appear with a decreased degeneracy: 3-fold for $\nu = \pm 1$, 2-fold for $\nu = \pm 2$ and 1-fold for $\nu = \pm 3$ [13]. This can be clearly seen in Fig. 1.8a-b. Importantly, the LLs only evolve towards higher $|\nu|$, indicating that when the Fermi level reaches an integer filling, a new Fermi surface is formed due to a reconstruction of the flat bands. These sequences of LLs are in principle reminiscent of

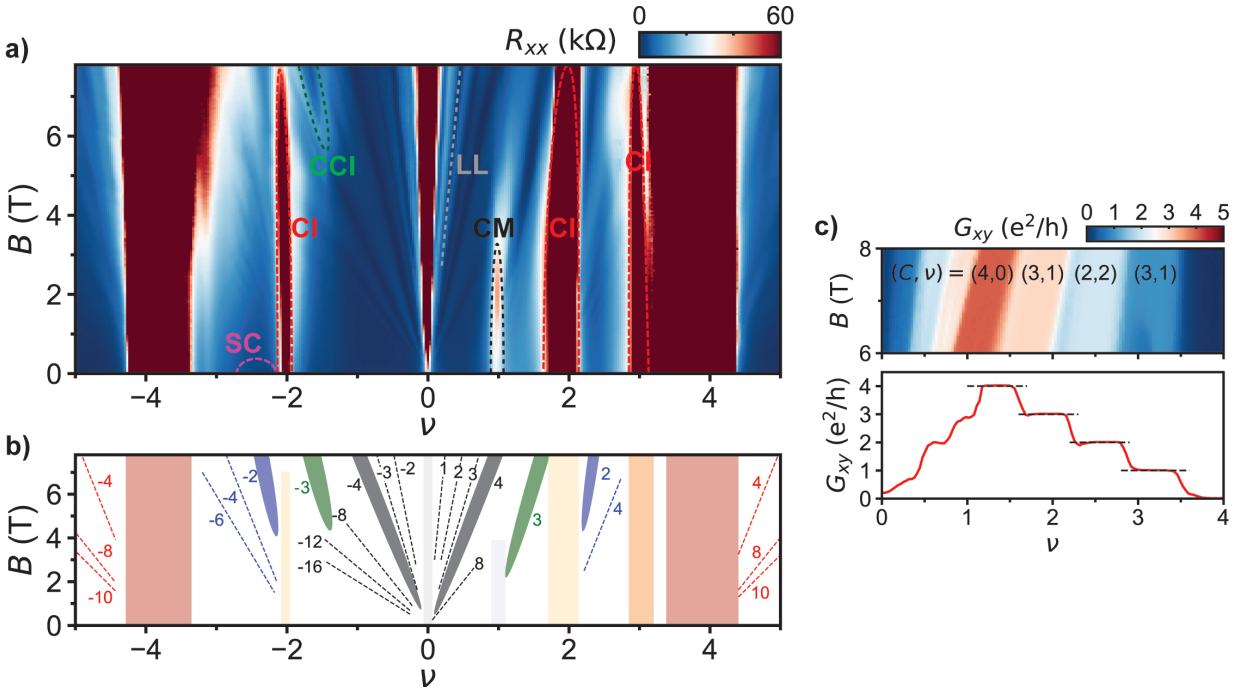

Fig. 1.8: Magnetic field phase diagram of TBG. a) Landau fan diagram of a TBG samples with $\theta \sim 1.14°$, where the longitudinal resistance R_{xx} is measured as a function of magnetic field B and filling ν. The abbreviations correspond to: CI=Correlated Insulator, CM=Correlated Metal, SC=Superconductor, LL=Landau Level, CCI=Correlated Chern Insulator. **b)** Extracted Landau levels in dashed lines with their filling factor annotated. The shaded regions correspond to the observed correlated Chern insulators along with their Chern number. **c)** Top panel shows the transverse conductance G_{xy} of another TBG sample with $\theta \sim 0.98°$ at high field and in units of quantum of conductance. The bottom panel shows a line-cut at 8 T, with the quantization of the Chern insulators indicated by dashed horizontal lines and their sequence $(C, \nu) = (4 - \nu, \nu)$ shown in the top panel.

the SU(4) quantum-Hall ferromagnetism of graphene, where the Zeeman and valley gaps lift the spin–valley degeneracy, polarizing the flavor of the state [72].

Inverse compressibility measurements [73] showing a sawtooth pattern in the chemical potential, with positive jumps at every integer ν, have also been interpreted as evidence of a hierarchy of flavour-polarized, symmetry-broken ground states. This simple picture of assigning a flavor occupancy with the spin and valley quantum numbers at every integer ν in TBG has proven to be nevertheless too simple. More complicated mixed orders have since then been proposed as candidate ground states, such as intervalley coherent (IVC) or incommensurate Kelulé spiral (IKS) states, which have been recently confirmed by STM experiments [74]. Furthermore, recent thermoelectric measurements have instead interpreted the resets of the inverse compressibility as a reconstruction of the flat bands due to two types of carriers driving the physics of TBG: correlated localized 'heavy' f-

electrons and dispersive 'light' c-electrons [P5]. This is done under the framework of the Topological Heavy Fermion model [75], which providing a unifying theory for explaining the apparent dichotomy of TBG displaying both heavy-like correlated behavior in its insulating states, and dispersive-like states such as superconductivity and topological states (see Subsection 5.3.2 for more details).

Apart from these LLs, another set of states with a quantized transversal resistance that also follows the Streda formula

$$\sigma_{xy} = \frac{Ce^2}{h}, \qquad \frac{dn}{dB} = \frac{Ce}{h}, \tag{1.25}$$

were uncovered by STM and magneto-transport experiments [15, 16, 76–79]. These topological states with Chern number C following the sequence $C = 4 - \nu$ at every integer ν (see Fig. 1.8c), have a larger gap (~ 1 meV) than usual LLs (~ 0.1 meV) [16]. The theoretical understanding is that they are formed when the $C_{2z}\mathcal{T}$ symmetry of TBG is lifted, and were thus named symmetry-broken Correlated Chern Insulators (CCIs). The symmetry-breaking can be done by either breaking $\mathcal{T}$ with an applied external magnetic field, or by breaking C_{2z} with a substrate potential or due to interactions, as we explain next.

During the first transport experiments in TBG, two samples allegedly aligned with hBN were reported to show a (Quantum) Anomalous Hall Effect at the integer filling $\nu = 3$ [80, 81]. Because these phases emerge from a purely carbon lattice with negligible intrinsic spin-orbit coupling, their appearance pointed towards an orbital magnetism origin driven by interactions [14, 82, 83]. These states were later identified as the same Correlated Chern Insulators, but nucleating down at zero magnetic field. The alignment of TBG with hBN is still an open problem in the community, as the reproducibility of the QAHE is yet to be demonstrated, and especially because other signatures often found in other multilayer graphene systems aligned with hBN, such as the Hofstadter butterfly and a gap-opening at the CNP, seem to be lacking in the flat bands of TBG.

From the Landau fan diagram in Fig. 1.8a, and by using Eqs. (1.15) and (1.17), we can convert the gate-voltage to carrier density, and estimate the twist-angle of the measured TBG sample. By taking the moiré period from Eq (1.18), and since in this case $n_s = 4/A$, we arrive to:

$$\theta^2 \approx \frac{\sqrt{3}a^2 n_s}{8}, \tag{1.26}$$

where we have made the approximation $\sin(\theta) \approx \theta$ for low angles. In the case of TBG, estimating n_s can be more difficult, as the band insulators at $\nu = \pm 4$ can be very broad in carrier density due to twist-angle disorder (see Fig. 1.7a-b and Fig. 1.8a). The most accurate method is then to fit the LLs emanating from the band insulators and extrapolating them to zero field.

1.4 Josephson junctions

The phenomenon of superconductivity, first discovered by Onnes in 1911 after cooling Hg below 4 K, is a phase transition between a metallic state, often well described by a Fermi liquid, and a collective quantum phase that conducts electricity without dissipation below a critical temperature T_c. Maxwell's equations, along with London's postulate that the dissipationless current is accelerated by an electrical field [84], dictate that such zero-resistance state must also be a perfect diamagnet, obeying what is known as the Meissner effect [85]. The most successful microscopic description of superconductivity was developed in 1957 by Bardeen, Cooper and Schrieffer (BCS) [86, 87], where it was proposed that an attractive phonon-mediated interaction can bind electrons into pairs, known as Cooper pairs. This process opens up a gap Δ at the Fermi level, which the BCS theory predicts to be exactly $1.764 k_B T_c$. Such relation has been experimentally corroborated in many different superconductors, such as Al, Pb, Nb, In, or Ti; which have critical temperatures of just a few kelvin [88]. Yet, since the discovery of high-temperature superconductors in 1986 [89], with a T_c far above liquid-nitrogen temperatures, a considerable amount of "unconventional" superconductors that the BCS theory fails to describe have been reported. To understand their exact mechanism has proven to be one of the biggest open problems of the 21st century in Condensed Matter Physics.

In conventional BCS superconductors with s-wave pairing, Cooper pairs are formed by two electrons with opposite momenta and opposite spin. These quasi-particles with zero total spin obey the Bose-Einstein statistics, so that they form a condensate that can be described by a single macroscopic wavefunction. Such wavefunction is often called the (complex) order parameter $\Delta(\mathbf{k}) = \Delta_0(\mathbf{k}) e^{i\varphi(\mathbf{k})}$ of the superconductor, where $\Delta_0(\mathbf{k})$ is the superconducting gap and $\varphi(k)$ the macroscopic phase. For BCS superconductors, the s-wave pairing imposes both quantities to be constants: $\Delta_0(\mathbf{k}) = \Delta_0$ and $\varphi(\mathbf{k}) = \varphi$; whereas for other unconventional superconductors the order parameters can vary in k-space, such as those with d-wave or p-wave pairing [90].

In 1962, Brian D. Josephson theoretically demonstrated that a supercurrent can flow between two superconductors separated by a thin insulating barrier, even in the absence of a voltage bias [91]. This prediction, soon confirmed experimentally [92], became known as the Josephson effect and has been recognized ever since as a key signature of superconductivity, given its manifestation of macroscopic phase coherence. While Josephson initially considered a superconductor-insulator-superconductor (SIS) configuration, the effect is a more general property of any system consisting of two weakly coupled superconductors, called Josephson junction. The weak link can be realized using various geometries and materials, such as normal metals, semiconductors, ferromagnets, topological insulators, etc. Today, Josephson junctions (JJs) are fundamental components in a broad range of superconducting technologies, including ultra-sensitive detectors, high-frequency electronics, and building blocks of quantum computing superconducting circuits. More importantly to us, they serve as an important platform for exploring macroscopic quantum coherence and its influence in other fundamental condensed matter systems.

1.4.1 Tunneling junctions and weak links

SIS tunneling junctions

In his derivation, Josephson considered two superconductors $S_{1,2}$ with one-dimensional superconducting wavefunctions $\Delta_{1,2} = |\Delta_{1,2}|e^{i\varphi_{1,2}}$. When put in sufficiently close proximity to one another, he demonstrated that the wavefunctions of the Cooper pairs have a non-zero probability of tunneling through an insulating barrier. The supercurrent I_s generated through the junction by these quasiparticles is the first Josephson equation:

$$I_s = I_c \sin(\varphi), \tag{1.27}$$

where $\varphi = \varphi_1 - \varphi_2$ is the phase difference between the two superconductors and I_c is the critical current of the JJ, i.e. the maximum supercurrent that it can support. Eq. (1.27) describes what is known as the d.c. Josephson effect, where even in the absence of an applied voltage V between the two superconductors, a supercurrent can still flow. If nevertheless such a voltage is applied, the phase difference φ evolves with time, which is described by the second Josephson equation:

$$\frac{d\varphi}{dt} = \frac{2eV}{\hbar}. \tag{1.28}$$

This can be interpreted as a supercurrent traversing the JJ with a frequency $2eV/\hbar$, and is thus known as the a.c. Josephson effect [93].

Combining Eqs. (1.27) and (1.28), one can derive the free energy stored in the junction by integrating over the work I_sV done on it [93]:

$$\Delta F = \int_0^t dt\ I_s V = \int_0^\varphi d\varphi\ I_c \sin(\varphi)\frac{\hbar}{2e} = \frac{\hbar I_c}{2e}[1-\cos(\varphi)] = E_J[1-\cos(\varphi)] \tag{1.29}$$

where $E_J = \hbar I_c/2e$ is the Josephson energy, an important characteristic energy for the Josephson effect. For instance, a critical current of 10 nA gives $E_J \sim 20$ µeV ~ 0.25 K, so that if thermal fluctuations k_BT are bigger than E_J, the phase-coherent supercurrent smears out. For this reason, resolving small critical currents remains experimentally challenging, as it needs to be done under sufficiently low temperatures and low electronic noise conditions.

SNS weak link junctions

While the original prediction by Josephson was based on the Cooper pairs tunneling between two superconductors producing a supercurrent, soon it was discovered that this phenomena also applied to weak links, where the supercurrent would flow across a normal metal (N) or a weaker superconducting material (S') [94–97]. Here we focus on the former,

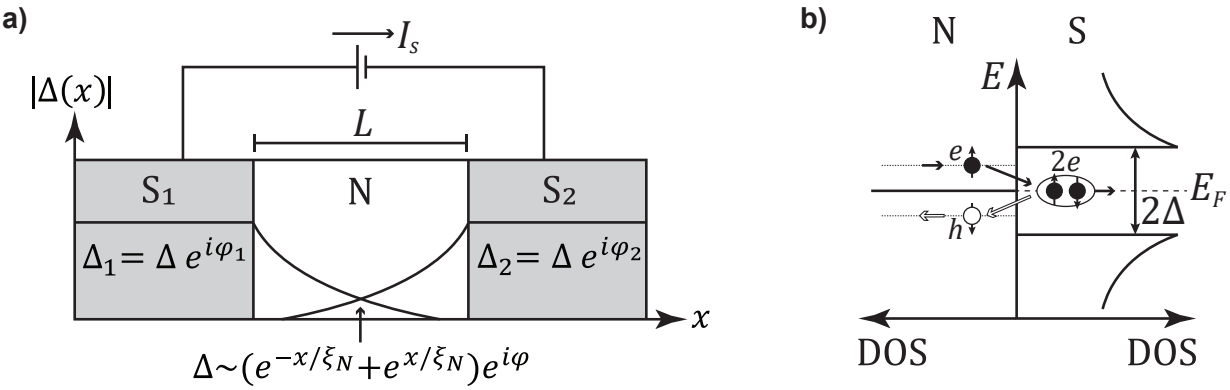

Fig. 1.9: Superconducting proximity effect in SNS junctions and Andreev reflection. a) Sketch of the superconducting proximity effect in an SNS junction of length L, where the two order parameters decay exponentially according to the coherence length in the weak link ξ_N, and overlap, giving rise to a supercurrent and the Josephson effect. **b)** Sketch of the Andreev reflection mechanism, where the incident electron cannot penetrate the superconductor alone, so a retro-reflected hole with opposite spin is created in order to form a Cooper pair, thus conserving the charge, spin and momentum of the process.

also known as SNS junctions. This is the so-called superconducting proximity effect (see Fig. 1.9a), where the superconducting order parameters of the electrodes $\Delta_{1,2} = |\Delta_{1,2}|e^{i\varphi_{1,2}}$ penetrate into the weak link, exponentially decreasing within the metal over a distance ξ_N. This decoherence happens because the normal metal does not support attractive interactions anymore as in the superconductors, so the injected Cooper pairs are no longer bound. If sufficiently close to one another however, Δ_1 and Δ_2 interfere, such that their superposition creates a finite induced order parameter in the weak link, so the Cooper pairs do not decohere completely and give rise to a finite supercurrent.

Mesoscopic SNS junctions are generally classified by comparing their junction length, L, with relevant length scales. The mean free path l_{mfp} of the normal metal is the criterion for defining the ballistic and diffusive junction regimes (see Table 1.1), while the coherence length in the weak link ξ_N separates the short and long junction regimes (see Table 1.2). Therefore, there are four different possible junction regimes: short-ballistic, short-diffusive, long-ballistic, and long-diffusive [98].

Regime	Criteria	Coherence length	Thouless energy
Ballistic	$L < l_{\mathrm{mfp}}$	$\xi_N = \hbar v_F / L$	$E_{Th} = \hbar v_F / L$
Diffusive	$L > l_{\mathrm{mfp}}$	$\xi_N = \sqrt{\hbar D / \Delta}$	$E_{Th} = \hbar D / L^2$

Table 1.1: Ballistic and diffusive regimes in an SNS junction. Sorting criteria for the two regimes, along with the different expressions for the coherence length ξ_N and the Thouless energy E_{Th} in each of them.

For a metal with ballistic transport, $\xi_N = \hbar v_F/\Delta$, where Δ is the superconducting gap of the electrodes. This expression is an analogy to the coherence length in a superconductor in the clean limit, where here the Fermi velocity v_F is instead that of the normal metal. In the case where diffusive transport is dominant, $\xi_N = \sqrt{\hbar D/\Delta}$, with $D = v_F l_{\mathrm{mfp}}/2$ the diffusion constant in the normal region (in two dimensions in this case). The ballistic and diffusive regimes then set the values of the coherence length ξ_N (see Table 1.1), which need to be compared with the length of the junction L so that it can be sorted in the short or long regimes (see Table 1.2).

It is also possible to compare the energy scales of the system instead of considering the length scales. The relevant energy scale is the Thouless energy, E_{Th}, which is related to the dwell time τ of the induced Cooper pair in the junction, i.e. $E_{Th} = \hbar/\tau$. Thus, in a ballistic system $E_{Th} = \hbar v_F/L$, whereas $E_{Th} = \hbar D/L^2$ for diffusive systems [98]. Comparing this quantity with Δ gives the smallest energy scale, which determines the short ($\Delta < E_{Th}$) and long ($\Delta > E_{Th}$) regimes. Furthermore, these quantities limit the $I_c R_N$ product of the junction, such that for a short JJ it remains approximately constant, as it is ruled by the superconducting gap Δ, whereas for a long JJ it can vary according to the Thouless energy E_{Th}, which depends on the Fermi velocity and the density of states on the Fermi surface.

Regime	**Length criteria**	**Energy criteria**
Short	$L < \xi_N$	$\Delta < E_{Th}$
Long	$L > \xi_N$	$\Delta > E_{Th}$

Table 1.2: Short and long regimes in an SNS junction. Sorting criteria for the two regimes, along with the different expressions for the coherence length ξ_N and the Thouless energy E_{Th} in each of them.

The microscopic mechanism underlying the superconducting proximity is described by a process known as Andreev reflection, named after the physicist who first proposed it in 1964 [99]. When a low-energy electron ($|E| < \Delta$) from the normal metal reaches the N/S interface, its transmission into the gaped superconductor is forbidden, where only Cooper pairs reside. Instead, the electron is retro-reflected as a hole with opposite spin and momentum, while a Cooper pair is simultaneously transmitted into the S region. Fig. 1.9b shows this process, which conserves both charge, spin and momentum. The resulting coherent superposition of the incident electron and the reflected hole is usually referred to as an Andreev pair.

If we now extend this to two interfaces forming an SNS junction, the Andreev pair is created in the N region at the first S/N interface. If the next N/S interface is sufficiently close, this time-reversal electron-hole pair reaches it, undergoing another Andreev reflection and thus creating another Cooper pair in the second superconductor. As a result, a Cooper pair has traversed the junction and a supercurrent can flow, which proximitizes the normal

metal. This process of successive Andreev reflections, illustrated in Fig. 1.10a, leads to the formation of discrete energy levels within the normal region, known as Andreev Bound States (ABS). These states are confined within the normal metal and have energies less than the superconducting gap.

In the Blonder-Tinkham-Klapwijk (BTK) model an interface is described by a dimensionless transparency parameter τ, which quantifies the transmission of a single transverse mode. For an incoming sub-gap electron ($|E| < \Delta$), the BTK model gives the probability amplitude of an Andreev reflection taking place [100]:

$$A(E) = \frac{\Delta^2}{E^2 + (\Delta^2 - E^2)(2\tau^{-1} - 1)^2}. \tag{1.30}$$

At zero energy, where the ABS lie, this simplifies to $A(0) = \tau^2/(2-\tau)^2$, such that a perfectly transparent interface ($\tau = 1$) retro-reflects every electron ($A(0) = 1$).

The energies of these bound states mainly depend on the phase difference φ between the two superconductors and the transparency τ of the interfaces. For a short-ballistic SNS junction, from Eq. (1.30) it can be derived that each transverse conduction channel with transmission probability τ_n supports a pair of ABS with energies:

$$E_n(\varphi) = \pm\Delta\sqrt{1 - \tau_n \sin^2(\varphi/2)} \tag{1.31}$$

At zero temperature the supercurrent carried by each channel is $I_{s_n} = \frac{2e}{\hbar}\frac{\partial E_n}{\partial \varphi}$. Considering that only the negative brach is occupied at zero temperature (see Fig. 1.10b), we only use

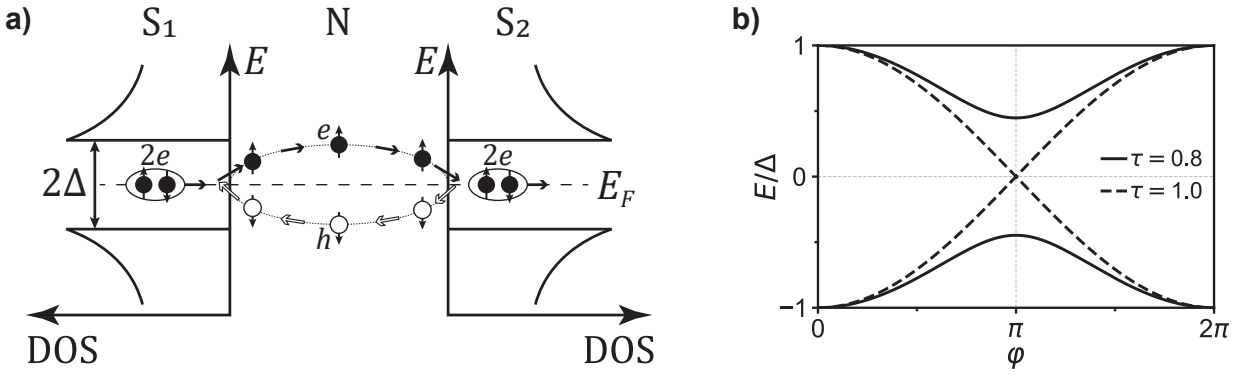

Fig. 1.10: Andreev Bound States in SNS junctions. a) Sketch of the microscopic mechanism of the superconducting proximity effect in an SNS junction, where an ABS is formed in the N region after two coherent Andreev reflections take place in the S_1/N and N/S_2 interfaces. **b)** In the short-ballistic limit, energy spectra of a gapless ABS for a perfect transmission ($\tau = 1$) and of a gaped ABS for an imperfect one ($\tau < 1$), as a function of the phase difference φ.

the negative solution in Eq. (1.31), from where we get the total supercurrent of the system:

$$I_s(\varphi) = \frac{e\Delta}{2\hbar} \sum_n \frac{\tau_n \sin(\varphi)}{\sqrt{1 - \tau_n^2 \sin^2(\varphi/2)}} \tag{1.32}$$

Because each transverse mode contributes independently, the total critical current in the short-ballistic limit will be the sum of each $I_c(\tau_n)$. Finding the minima of this expression gives us the critical current:

$$I_c = \frac{e\Delta}{\hbar} \sum_n \frac{\tau_n}{1 + \sqrt{1 - \tau_n}}. \tag{1.33}$$

Now, knowing from the Landauer-Büttiker formalism that for a spin-degenerate metal the conductance is $G_N = \frac{2e^2}{h} \sum_n \tau_n$, and expanding Eq. (1.31) for small transparencies $\tau_n \ll 1$, we find:

$$I_c = \frac{\pi\Delta}{2e} G_N, \tag{1.34}$$

which is the Ambegaokar-Baratoff relation for tunnel junctions [97, 101, 102]. If we instead consider a very transparent SNS junction with a single mode ($\tau \sim 1$), i.e. the so-called quantum-point-contact limit [103], we get:

$$I_c = \frac{\pi\Delta}{e} G_N. \tag{1.35}$$

These results emphasize that for the short-ballistic regime, $I_c \propto G_N$. In intermediate regimes of SNS junctions with finite temperature, this relation is not linear anymore, but follows much more complicated expressions [97]. One very important note is that, still, I_c remains a monotonically increasing function of G_N: if one increases so does the other and vice-versa. This is known as the I_c vs G_N scaling. Another conclusion from these expressions is that, for short-ballistic JJs, $I_c R_N \sim \Delta$. This means that the $I_c R_N$ product is only limited by the superconducting gap, and since no band structure or material-dependent properties have been considered in this general derivation, this quantity is thus often used as a measure of how strong the proximity effect compares to the theoretical limit of Eqs. (1.34) and (1.35) [93]. Finally, it can be experimentally checked if a JJ falls in this regime by measuring the temperature dependence of the I_c, which in this case is set by the superconducting gap:

$$I_c(T) = \frac{\pi\Delta(T)}{2eR_N} \tanh\left(\frac{\Delta(T)}{2k_B T}\right), \tag{1.36}$$

where $\Delta(T) \approx \Delta\sqrt{1 - (T/T_c)^2}$ [98, 104].

For diffusive or long SNS junctions the Andreev levels broaden into a quasi-continuum and the Thouless energy $E_{Th} = \hbar D/L^2$ replaces Δ as the controlling scale. Solving the Usadel equations [105] with transparent S/N interfaces gives $I_c = \alpha E_{Th} G_N$, where $\alpha \approx 10.82$ at $T = 0$ in the long-diffusive theoretical limit ($\Delta \gg E_{Th}$ or $L \gg \xi_N$) [106]. Since E_{Th} also

depends on the conductance through the diffusion coefficient, we can conclude that I_c also scales with G_N in this regime. The temperature dependence for long junctions is governed by an exponential scaling $I_c \propto e^{-k_B T/\delta E}$, where $\delta E \approx \hbar v_F/2\pi L$ [104]. In the case of the long-diffusive limit, the expression is [106]:

$$I_c(T) = \frac{10.82 E_{Th}}{eR_N}\left(1 - 1.3e^{-10.82E_{Th}/3.2k_BT}\right) \tag{1.37}$$

These derivations demonstrate that the Josephson equations approximately hold for SNS junctions too. While Eq. (1.27), which describes a sinusoidal CPR, holds exactly at $T \approx T_c$ and in the long-diffusive limit for any temperature [102], it is known that the CPR is modified for extremely transparent ballistic SNS JJs [97, 107]. In general, the study of the CPR in real imperfect SNS junctions shows that it approximately follows a sinusoidal relation [102, 108]. From a theoretical perspective, an accurate derivation of a general CPR in these imperfect systems is complicated, as the supercurrent carried by the Andreev Bound States depends on the length L, coherence length ξ_N and decoheres through multiple scattering processes with the normal carriers in the metal.

1.4.2 The washboard potential and IV characteristics

A more complete model of a realistic Josephson junction is the RCSJ (Resistively and Capacitively Shunted Junction) model, which enables to explain the current-voltage characteristic for example. It consists of incorporating in parallel to the JJ: a capacitor, which provides the geometric capacitance C of the normal region between the two superconducting leads, and a resistor, which provides the dissipative resistance R of the junction in its normal state (equivalent to R_N) [93]. The total current I in the system will then be divided through the three different elements (see also Fig. 1.11a): $I = I_c \sin(\varphi) + V/R + CdV/dt$. By applying Eq. (1.28) we then get:

$$I = I_c \sin(\varphi) + \frac{\hbar}{2eR}\frac{d\varphi}{dt} + \frac{\hbar C}{2e}\frac{d^2\varphi}{dt^2}. \tag{1.38}$$

The dynamics of this differential equation can be understood by analogy to the same differential equation describing the motion $x(t)$ of a classical particle:

$$F = U_o \sin(x) + \eta\frac{dx}{dt} + m\frac{d^2x}{dt^2}, \tag{1.39}$$

where $F = \hbar I/2e$ is the external force, $U_o = \hbar I_c/2e = E_J$ is the effective potential energy, $\eta = \hbar^2/4e^2R$ is the viscosity and $m = \hbar^2 C/4e^2$ the mass of the particle providing the inertia. The potential in which this particle moves is $U(x) = U_o(1 - \cos(x)) - Fx$. For the RCSJ model in Eq. (1.38), this potential is then:

$$U(\varphi) = E_J\left(1 - \cos(\varphi) - \frac{I}{I_c}\varphi\right), \tag{1.40}$$

which is called a washboard potential [93], whose characteristic energy is the Josephson energy E_J. Fig. 1.11b shows it for different I/I_c values, where we can see that it tilts as I/I_c increases. Furthermore, as $I = I_c$, the potential no longer has stable equilibrium minima, but rather unstable points, meaning the particle never gets to a stable position (analogous to a fixed φ) and therefore the system has no solution (superconductivity in the JJ is lost). If, on the other hand, $I \lesssim I_c$, fluctuations can make the system escape from the shallow minima, such as thermal fluctuations $k_B T$ or quantum tunneling.

This means that, in general, there is a certain probability that the current needed to switch from the superconducting to the normal state is smaller than the true critical current. In experiments, this measured transition in current is thus often called switching

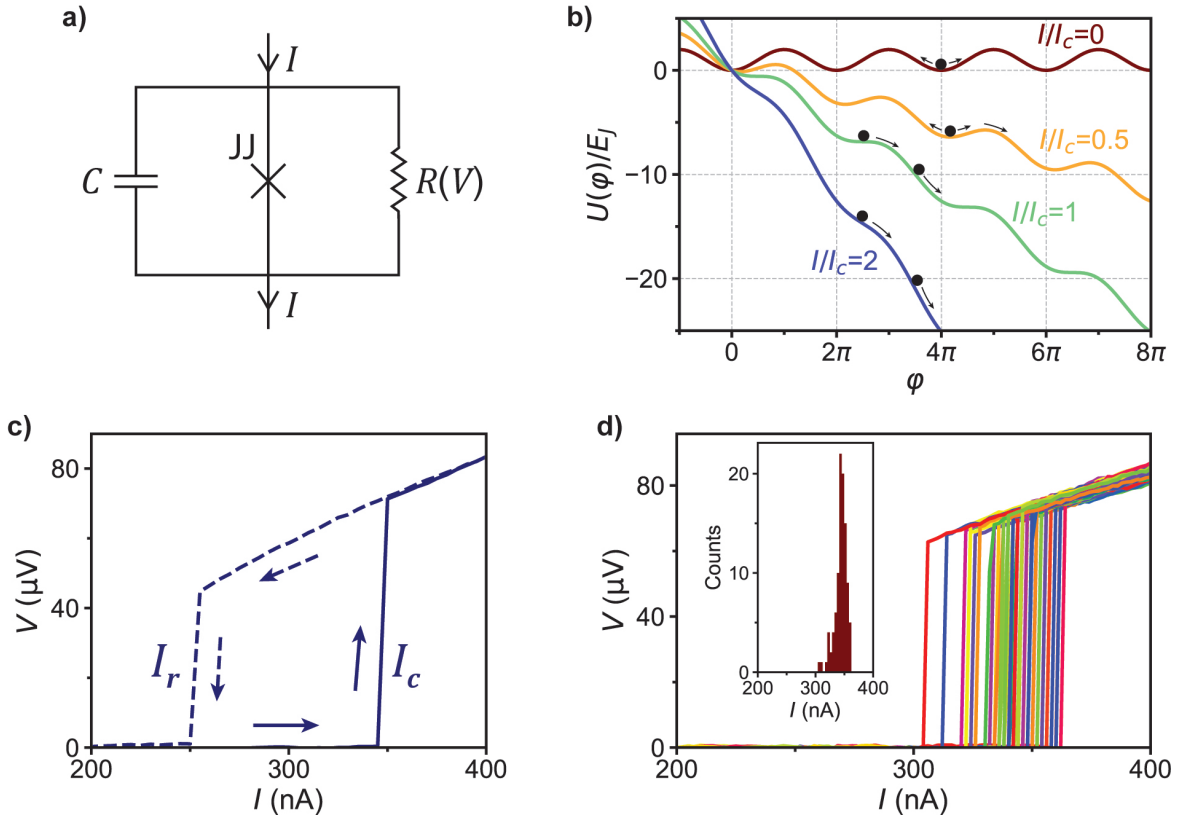

Fig. 1.11: RCSJ model, washboard potential and IV characteristics. a) Circuit of the RCSJ model. **b)** Normalized tilted-washboard potential $U(\varphi)/E_J$ according to Eq. (1.40), plotted for several values of I/I_c; the analogous to the driving force. For $I < I_c$ the potential has local minima, whereas for $I > I_c$ it does not. **c)** Hysteresis of a measured current-voltage (IV) curve. The solid-line data is acquired while sweeping the d.c. current I away from zero, and the dashed-line while sweeping towards zero. **d)** Same measured IV curve as in **c**, always sweeping away from zero. The repetition of the measurements shows an evident stochastic switching. Inset shows the distribution of this switching, revealing I_c is not well defined experimentally.

current. Fig. 1.11d shows an example of an IV measurement repeated over time, where the transition is seen to be non-deterministic. One can then take the average of the distribution as an approximation to the "true" I_c.

According to the quality factor $Q = w_J RC$, where $w_J = \sqrt{2eI_c/\hbar C}$, there are two JJ regimes one can consider: the overdamped regime (C small such that $Q \ll 1$) and the underdamped regime (C finite such that $Q > 1$). The underdamped junctions are especially interesting, as this model explains the hysteresis found in the IV curves of such JJs.

When the junction transits from the superconducting state ($I < I_c$) to the normal state ($I > I_c$), the associated voltage V goes from zero to a finite value $V = IR$, yielding a non-linear IV curve, also called IV characteristic (see Fig. 1.11c-d). In Eq. (1.40) and Fig. 1.11b this corresponds to the phase φ increasing at a rate $d\varphi/dt = 2eV/\hbar$, meaning the system slides down the tilted washboard. If now, from this situation and in the underdamped regime, I is reduced back to $I < I_c$, because C is finite, the particle has big enough inertia such that the viscosity does not slow it down, so we still have $V \neq 0$. This means that, although $U(\varphi)$ has well-defined minima, the particle carries up and over the barriers. This process continues until the so-called retrapping current I_r is reached. With a finite damping ($Q > 1$), $I_r \neq 0$ is fixed by the current at which its work on the system exactly equals the energy required in advancing φ from one minima to the next. From here, one can derive that $I \leq I_r = 4e/\pi Q$ [93]. An example of such hysteretic IV curve can be seen in Fig. 1.11c.

It is worth noting that this hysteresis can also be due to overheating effects in the junction, such that it also occurs in overdamped JJs [109]. As the JJ switches to its normal state at $I = I_c$, its finite resistance increases the electron temperature due to Joule heating. By now decreasing I, the transition back to the superconducting state can happen at a $I < I_c$, since I_c decreases for increasing temperatures.

1.4.3 Superconducting interference under a magnetic field

For a complex superconducting order parameter with spatial variation $\Delta(\boldsymbol{r}) = |\Delta(\boldsymbol{r})|e^{i\varphi(\boldsymbol{r})}$, the second Ginzburg-Landau equation reads

$$\boldsymbol{J_s} = \frac{q}{m}|\Delta|^2 \left(\hbar\nabla\varphi(\boldsymbol{r}) - q\boldsymbol{A}\right), \tag{1.41}$$

where $q = 2e$ is the charge of the Cooper pairs and $\boldsymbol{A}$ is the magnetic vector potential. Deep inside the superconductor, where no external magnetic field penetrates and thus no screening currents are being generated, $\boldsymbol{J_s} = 0$. From here, by integrating over a contour $\mathcal{C}$, we get:

$$\varphi(\boldsymbol{r}) = \varphi_0 + \frac{2\pi}{\Phi_0}\int_{\mathcal{C}} \boldsymbol{A}\cdot d\boldsymbol{l}. \tag{1.42}$$

This expression manifests how an external magnetic field adds on the phase φ. For a closed contour, i.e. a superconducting ring, it follows from Eq. (1.42) that the phase is periodically modulated by units of the superconducting flux quantum $\Phi_0 = h/q$ [93].

Interference in a Josephson junction

If we now consider a coplanar Josephson junction over the xy plane and an applied perpendicular magnetic field $\boldsymbol{B} = B\boldsymbol{e_z}$, as depicted in Fig. 1.12a, we can calculate how the phase difference φ between the two superconductors is modulated in the x axis. For this, we choose the Landau gauge $\boldsymbol{A} = Bx\boldsymbol{e_y}$, yielding:

$$\varphi(x) = \varphi_0 + \frac{2\pi}{\Phi_0}\int_{-L/2-\lambda_L}^{+L/2+\lambda_L} A_y \, dy = \varphi_0 + \frac{2\pi}{\Phi_0} Bx(L+2\lambda_L). \tag{1.43}$$

From here and Eq. (1.27) we know the supercurrent density $J_s(x)$ in the junction must be $J_s(x) = J_c \sin[\varphi_0 + \frac{2\pi}{\Phi_0} Bx(L+2\lambda_L)]$. This behavior is shown in Fig. 1.12b. The total supercurrent I_s in the Josephson junction will then be:

$$I_s(B) = \int_{-W/2}^{W/2} J_s(x)dx = J_c W \sin(\varphi_0) \frac{\sin[\pi BW(L+2\lambda_L)/\Phi_0]}{\pi BW(L+2\lambda_L)/\Phi_0}. \tag{1.44}$$

In the experiment, the observable quantity is the critical current $I_c(B)$, which is the maximum supercurrent flowing in the junction, i.e. where φ_0 maximizes Eq. (1.44) at zero magnetic field. From there it follows:

$$I_c(B) = I_c(0)\left|\frac{\sin(\pi\Phi/\Phi_0)}{\pi\Phi/\Phi_0}\right|, \tag{1.45}$$

where $\Phi = BW(L+2\lambda_L)$ is the magnetic flux threading through the junction. The addition of twice the London penetration length $2\lambda_L$ is done because the magnetic field can penetrate into the superconducting electrodes up to that distance, which is called flux-focusing effect.

Importantly, Eq. (1.45) manifests the quantum interference of the supercurrents inside a Josephson junction under a perpendicular magnetic field, which is identical to a single-slit optical diffraction pattern, also called Fraunhofer pattern. Indeed, in Fig. 1.12c we show an experiment where the critical current decays according to Eq. (1.45). The periodicity of the oscillations $\Delta B \sim 2.1 \pm 0.1$ mT coincides with the value from the physical area of the junction $\Delta B_o \sim 2.0 \pm 0.2$ mT when flux-focusing effects are taken into account. Historically, these type of interference experiments, first done by Little and Parks [110], served to prove that the charge of the quasiparticles driving the superconducting phase (Cooper pairs) had a charge $q = 2e$, since the I_c vanishes at every integer $\Phi_0 = h/q$ [111].

Interference in a SQUID

Let's consider now two JJs placed in parallel, such that the magnetic flux penetrates through the enclosing area $\mathcal{S}$ between them. One can imagine this as a modification of the sketch in Fig. 1.12a with two JJs at the edges and empty space in the middle, such as

the inset in Fig. 1.12d. Starting again from Eq. (1.41) and choosing a contour $\mathcal{C}$ along this structure such that $\boldsymbol{J_s} = 0$, we get:

$$\int_{\mathcal{C}} \nabla\varphi \cdot d\boldsymbol{l} = \frac{2\pi}{\Phi_0} \int_{\mathcal{C}} \boldsymbol{A} \cdot d\boldsymbol{l}. \tag{1.46}$$

Letting $\varphi_{1,2}$ be the phase differences in each JJ, and since the phase will be 2π for each winding loop $n \in \mathbb{Z}$, the left integral gives $2\pi n - (\varphi_1 - \varphi_2)$. By now using Stokes theorem,

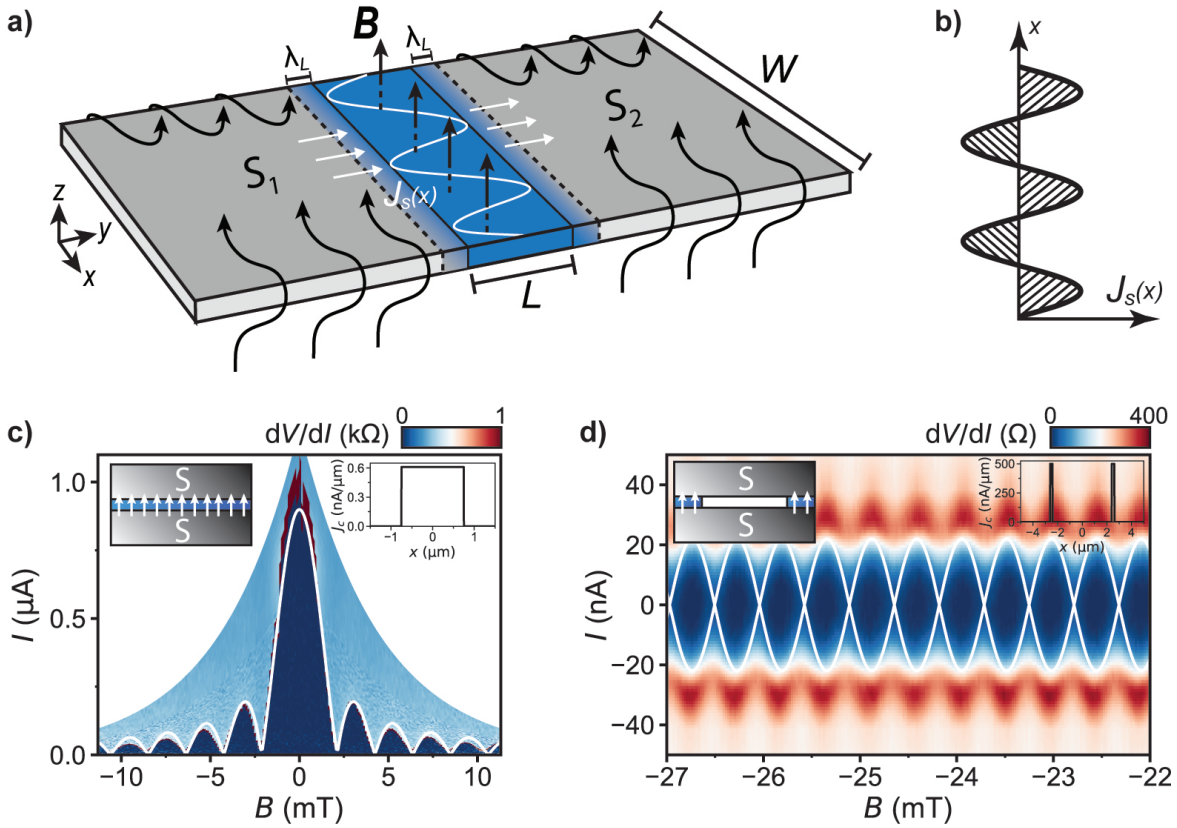

Fig. 1.12: Superconducting interference under a magnetic field. **a)** Sketch of a coplanar Josephson junction, where the weak link (blue color) is trespassed by an external perpendicular magnetic field B (black arrows), as opposed to the superconducting leads (grey color) which screen the field due to the Meissner effect. Such field creates an interference in the supercurrent density profile $J_s(x)$ in the weak link (white color). **b)** Example of a sinusoidal $J_s(x)$ in a JJ, according to Eq. (1.49), which corresponds to a flux $\Phi = 5\Phi_0/2$, i.e. to the maxima of the third lobe in **c**. **c)** Example of a measured JJ, where the experimental differential resistance $\mathrm{d}V/\mathrm{d}I$ is plotted vs d.c. current I and a field B. The I_c, obtained as the transition in I from the zero-resistance state (dark blue) to the finite-resistance state, follows well the theoretical prediction of Eq. (1.45) (white line). **d)** Example of a measured SQUID, where the experimental I_c follows well the theoretical prediction of Eq. (1.48) (white line). The insets of **c** and **d** include a sketch and the calculation of the precise critical current profiles $J_c(x)$ that generate the theoretical $I_c(B)$ fits.

the right integral results in $\frac{2\pi}{\Phi_0}\iint_{\mathcal{S}} \nabla \times \boldsymbol{A} \cdot d\boldsymbol{s} = 2\pi\Phi/\Phi_0$. Thus, the relative phase of the two junctions is related to the flux Φ through the ring by [93]:

$$\varphi_1 - \varphi_2 = \frac{2\pi\Phi}{\Phi_0} mod(2\pi). \tag{1.47}$$

The total supercurrent I_s of the device will be divided in two. Assuming each junction has the same critical current I_{c_0} this yields $I_s = I_{c_0}\sin(\varphi_1) + I_{c_0}\sin(\varphi_2)$. Now taking into account Eq. (1.47) we rewrite this as $I_s = I_{c_0}\sin(\varphi_1 - \pi\Phi/\Phi_0)\cos(\pi\Phi/\Phi_0)$. Thus, choosing φ_1 such that it maximizes I_s, the total critical current I_c of the device will be:

$$I_c(B) = I_c(0)\left|\cos(\pi\Phi/\Phi_0)\right|. \tag{1.48}$$

As opposed to a single junction, where the critical current exponentially decays with field, Eq. (1.48) creates constant oscillations, just like a double-slit interference pattern in optics. An experimental example of this structure, known as a superconducting quantum interference device (SQUID) [112], is shown in Fig. 1.12d. These devices are commonly used as highly sensitive magnetometers, as they can detect a change in their I_c down to a field variation of ~ 150 aT$/\sqrt{\text{Hz}}$ [113].

Interference for any critical current density profile

The analogy with the optics interference phenomena should not be surprising. As the Cooper pairs in a superconductor follow Bose-Einstein statistics, they are all described by the same macroscopic wavefunction and thus all have the same phase, exactly as with light waves. With this in mind, one can derive a more general expression between the critical current density profile $J_c(x)$ and the measured critical current $I_c(B)$ through the Fourier transform, as we show in the following.

From Eq. (1.43) we can define the normalized magnetic field unit as $\beta = 2\pi(L + 2\lambda_L)B/\Phi_0$, and from Eq. (1.27) we know the supercurrent density in the junction is

$$J_s(x) = J_c(x)\sin(\varphi_0 + \beta x) = J_c(x)\ \mathrm{Im}\left[e^{i(\beta x + \varphi_0)}\right], \tag{1.49}$$

where $J_c(x)$ is a function of the lateral dimension x along the width of the junction W. By setting the cutoff with a vanishing $J_c(x)$ beyond W, the integration to calculate the total current I_s in the Josephson junction is then done over the whole real space:

$$I_s(\beta) = \int_{-\infty}^{+\infty} J_c(x)\frac{1}{2i}\left(e^{i(\beta x+\varphi_0)} - e^{-i(\beta x+\varphi_0)}\right)dx \tag{1.50}$$

Defining now the complex function $\mathcal{J}(\beta) = \int_{-\infty}^{+\infty} J_c(x)e^{i(\beta x+\varphi_0)}dx$, we get

$$I_s(\beta) = \frac{1}{2i}\left[\mathcal{J}(\beta) - \mathcal{J}^*(\beta)\right] = \mathcal{FT}[\mathcal{J}(\beta)], \tag{1.51}$$

where $\mathcal{FT}$ marks the Fourier transform of a complex function. Finally, the observable critical current $I_c(\beta)$ is calculated by setting the maximum over the complex modulus of the previous expression, yielding:

$$I_c(\beta) = \left| \int_{-\infty}^{\infty} J_c(x) e^{i\beta x} dx \right|, \tag{1.52}$$

From this, we can easily derive that for a rectangular function $J_c(x)$, its Fourier transform and thus its $I_c(B)$ is the sinc function, i.e. Eq. (1.45). If we now set two rectangular functions at the edges of the junction, the resulting $I_c(B)$ is a non-decaying cosine function, i.e. Eq (1.48). These $J_c(x)$ profiles that generate such $I_c(B)$ oscillations are shown for real samples in the insets of Fig. 1.12c-d. From these two primary examples, one can construct other profiles, with the general rule being that a bulk supercurrent will contribute to a decaying interference with field, and an edge supercurrent will result in constant oscillations with field. Finally, a non-symmetric profile $J_s(x)$ generates an interference pattern where the nodes do not reach a vanishing I_c.

Retrieving the critical current density profile $J_c(x)$ from the measured $I_c(B)$

One can now wonder if it's possible to do reverse engineering and extract information about how the supercurrent flows in the junctions, i.e. the critical current density profile $J_c(x)$, from the measured critical current $I_c(B)$ in the experiment. While one could definitely take the inverse Fourier transform of Eq. (1.52), the phase information φ is lost since the expression holds a complex modulus. This problem not having a general solution roots in Quantum Mechanics, where one cannot retrieve the global phase of a wavefunction from a physical measurement; in this case the macroscopic phase of a superconductor or a JJ. The problem has a solution though by making a few assumptions, such as the CPR of the JJ being sinusoidal, i.e. Eq. (1.27) holds. We now demonstrate this method, first introduced by Dynes and Fulton [114], and also show some examples.

From Eq. (1.52), by not taking the complex modulus, we can write

$$\int_{-\infty}^{\infty} J_c(x) e^{i\beta x} dx = \int_{-\infty}^{\infty} J_E(x) \cos(\beta x) dx + i \int_{-\infty}^{\infty} J_O(x) \sin(\beta x) dx = I_E(\beta) + i I_O(\beta).$$

This integral is a complex function that is divided into a real (I_E) and an imaginary (I_O) part, which correspond to the even (J_E) and odd (J_O) components of the density distribution, respectively. Both I_E and I_O can be computed approximately from the measured I_c with an ansatz [115], which we explain in the following and show in Fig. 1.13.

The first consists of obtaining $I_E(\beta)$ by multiplying the experimental $I_c(\beta)$ with a flipping function that switches sign between adjacent lobes (see Fig. 1.13a-b). With this calculation, we are assuming that the phase of the supercurrent changes sign after every Φ_0, (i.e. sinusoidally) just like in Fig. 1.12b. $I_c(B)$ is then mainly described by $I_E(\beta)$,

except at its minima points (nodes) that do not reach $I_c(B) = 0$. Thus, we calculate $I_O(\beta)$ by linearly interpolating between the minima of $I_c(\beta)$ and flipping sign between adjacent lobes (see Fig. 1.13a-b) [115].

Finally, by computing the inverse Fourier transform of $I_E(\beta) + iI_O(\beta)$, the supercurrent density profile $J_s(x)$ is obtained:

$$J_c(x) = \left| \frac{1}{2\pi} \int_{-b/2}^{b/2} [I_E(\beta) + iI_O(\beta)]\, e^{-i\beta x} d\beta \right|. \tag{1.53}$$

where b is the sampling range of β, i.e. how far in magnetic field the oscillations were measured.

In Fig. 1.13 we show an example of applying this method to the measured I_c of a JJ, whose raw data we have also shown in Fig. 1.12c. Importantly, in Fig. 1.13a we can see that the extracted I_c does not reach exactly zero at the nodes, like Eq. (1.45) predicts. This can be due to having an imperfect junction. Indeed, by computing I_E and I_O from I_c, Fig. 1.13b shows that I_E mainly describes the experimental I_c, except at the nodes, where I_O makes some corrections. As a result, the extracted $J_c(x)$ in Fig. 1.13c shows an asymmetry, although very close to a perfect homogeneous profile (black-dashed line).

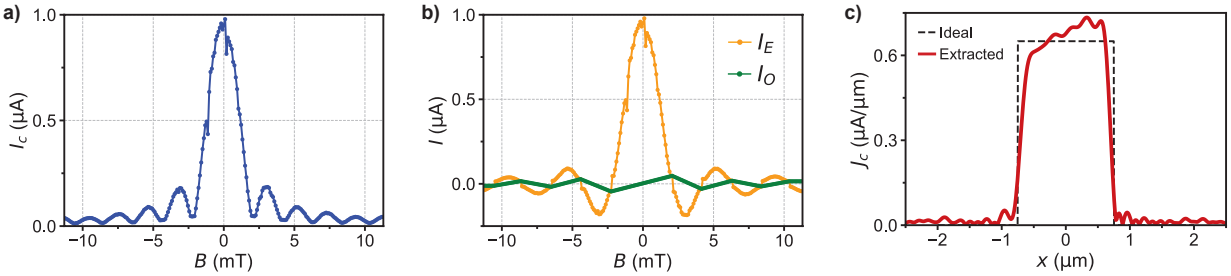

Fig. 1.13: Critical current density profile extraction. a) Extracted critical current I_c of a JJ vs magnetic field B. **b)** Extraction of the even (I_E) and odd functions (I_0) from **a** by flipping sign between nodes. **c)** Calculated critical current density profile J_c from **b** in red vs the lateral dimensions of the junction x. The theoretical fit, taken from the physical width of the JJ, is shown in a black-dashed line.

Chapter 2

Experimental Methods

The work presented in the first section of this chapter led to the following publication:

[P6] J. Díez-Mérida, I. Das, G. Di Battista, **A. Díez-Carlón**, M. Lee, L. Zeng, K. Watanabe, T. Taniguchi, E. Olsson, D.K. Efetov. "High-yield fabrication of bubble-free magic-angle twisted bilayer graphene devices with high twist-angle homogeneity". *Newton* 1, 1 (2025).
Contributions: Sample fabrication, transport measurements and discussion.

As discussed in Chapter 1, graphene-based moiré superlattices give rise to rich physical phenomena not found in monolayer graphene. The formation of these artificial superlattices in mesoscopic devices suffers from several external factors, such as the dielectric environment [116, 117], strain [74, 118] or twist-angle inhomogeneity [17, 119]. This latter is especially important for homobilayer moiré materials, such as TBG. It is thus of great importance to have a controlled and clean fabrication of these twisted vdW heterostructures in order to investigate their numerous quantum phases.

This chapter is divided as follows. Section 2.1 describes an optimized fabrication process that allows us to achieve highly homogeneous graphene-based moiré devices, and in particular TBG [P6]. In Section 2.2, we discuss the challenges of developing a working recipe for superconducting contacts to graphene-based heterostructures and how we overcame them. Lastly, Section 2.3 shows the instrumentation and the basics of low-temperature transport measurements in different cryostats with lock-in techniques.

2.1 vdW heterostructures fabrication

vdW materials were first obtained with the discovery of graphene [4] via the exfoliation method, where a tool as simple as a scotch tape is used to repeatedly peel off layers of graphite. As the out-of-plane vdW forces are weak compared to the in-plane bonding forces between the atoms, the 2D layers of graphite remain intact down to the monolayer limit, allowing for their isolation and study. Since then, a huge number of other 2D materials have been identified [120, 121]. With the innovation of the dry-transfer method [122, 123], these different 2D materials were now possible to assemble, creating heterostructures with combined and emergent physical properties [7]. Possibilities were set to be endless with the discovery of twistronics, where the relative angle between the layers and the resulting moiré superlattice can dramatically change the band structure of the former material [8, 11, 12, 30, 124, 125]. In this section, we describe in detail the fabrication process used to create graphene-based moiré heterostructures, from the exfoliation of the 2D materials, through their assembly, to their nanofabrication and conversion into a measurable electronic device.

2.1.1 Exfoliation

The 2D materials used to create the vdW heterostructures studied in this thesis are obtained through mechanical exfoliation onto a doped Si chip with a 285 nm SiO_2 capping layer. This 285 nm SiO_2 substrate is chosen for its optical contrast, which makes it easier to identify monolayer graphene flakes under monochromatic illumination [126].

The 285 nm Si/SiO_2 substrates come in an standard wafer shape as shown in Fig. 2.1a. Since our vdW samples are in the order of tens of µm, we cut the wafers with a diamond tip into small chips of approximately 1×1 cm^2 (Fig. 2.1b). Subsequently, the chips are flushed with a nitrogen gun at high pressure in order to remove the Si debris accumulated on the surface after cutting. Finally, the chips are further cleaned under a strong O_2 plasma (100 W, 90 mTorr) for 5min in a plasma asher or reactive-ion-etching camera (Fig. 2.1c). This process removes ambient adsorbates from the chip surface, enhancing its adhesiveness to the 2D materials and increasing the number of resulting flakes [127].

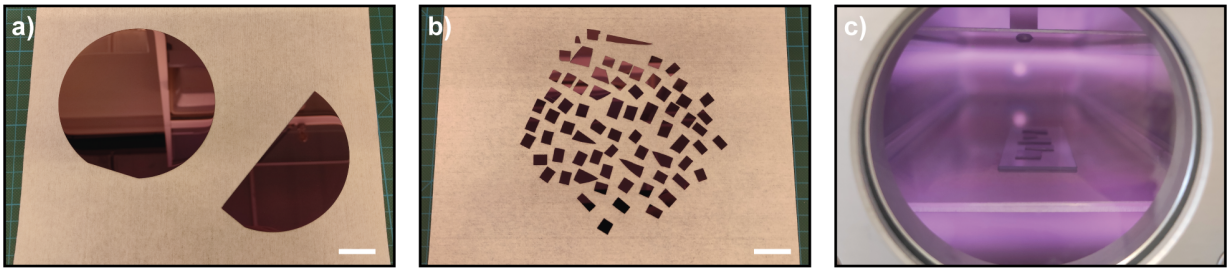

Fig. 2.1: Cleaning of Si/SiO_2 chips. a) Full and half Si/SiO_2 wafers. **b)** The wafer is cut into smaller chips. Scale bars are 2 cm. **c)** The chips are cleaned under an O_2 plasma.

Once we have ready our clean substrates, we proceed to exfoliate on them the 2D materials. First, we describe in detail all the steps of graphene exfoliation process and then explain the differences for hBN and thick graphite:

i) *Tape folding*: a graphite crystal (from NGS®) is placed on a piece of Magic-Scotch™ tape (Fig. 2.2a-b) and then removed, leaving a large piece of graphite on the tape. This is repeated in several areas at one end of the scotch tape (Fig. 2.2c). The tape is then folded as few times as necessary (e.g. 8 times) to completely cover it with graphite (Fig. 2.2d-e), thus minimizing the reduction in the size of the flakes [4].

ii) *Mother and daughter tapes*: to further reduce the thickness of the flakes from this "mother" tape, we create two "daughter" tapes, which we then throw away (Fig. 2.2f).

iii) *Area selection and applied pressure*: the cleaned Si/SiO_2 chips (see Fig. 2.1b) are carefully placed on the "mother" tape covered with graphite (Fig. 2.2g). Choosing a good area where to put the chip is critical in order to obtain graphene flakes. These can be identified by having a grey-matte color, in contrast with shiny regions which would give too thick graphite flakes. The chips are then pressed with our thumb and the use of a wipe. We press as much as we can for 10 s.

iv) *Heating*: the chips glued on the tape and on the wipe are placed on a hot plate at 100°C for 3min. Heating improves the contact area between the flakes and the SiO_2 by removing gas from the interface, thereby increasing the vdW forces [127]. Heating the tape too much time will cause tape residue, i.e. glue, to stick to the SiO_2 surface, which is undesirable. We have found that heating for 3-4 minutes keeps a good balance between high exfoliation yield and low amount of residues.

v) *Peeling off*: after heating, the tape is allowed to cool for 1min before being slowly peeled off the chips (Fig. 2.2h). This slow peeling is crucial to obtain larger flakes, as a fast peeling can break them. The waiting time before peeling allows for a more controlled removal, as the glue becomes less soft.

For hBN, we use crystals provided by our collaborators from Japan [26]. Although its crystallographic structure is very similar to that of graphite, its exfoliation is much harder. Its differences with respect to graphene are the following:

- hBN crystals are much smaller and scarce compared to graphite crystals (Fig. 2.3a). Because of that, we first put a small amount on one end of the tape (Fig. 2.3b).
- After folding to achieve a completely covered tape (Fig. 2.3c), we create a "daughter" tape (Fig. 2.3d) and use it to put our chips in areas with rainbow—not too shiny—colors. This ensures a relatively small flake thickness ($\sim 5-30$ nm).

- The applied pressure with our thumbs should be moderate in this case. Afterwards, the tape is heated only for 1min at 100°C.
- Finally, after waiting 1min for the tape to cool down, we try to peel it off from the chips at an even slower rate than in the case of graphite.

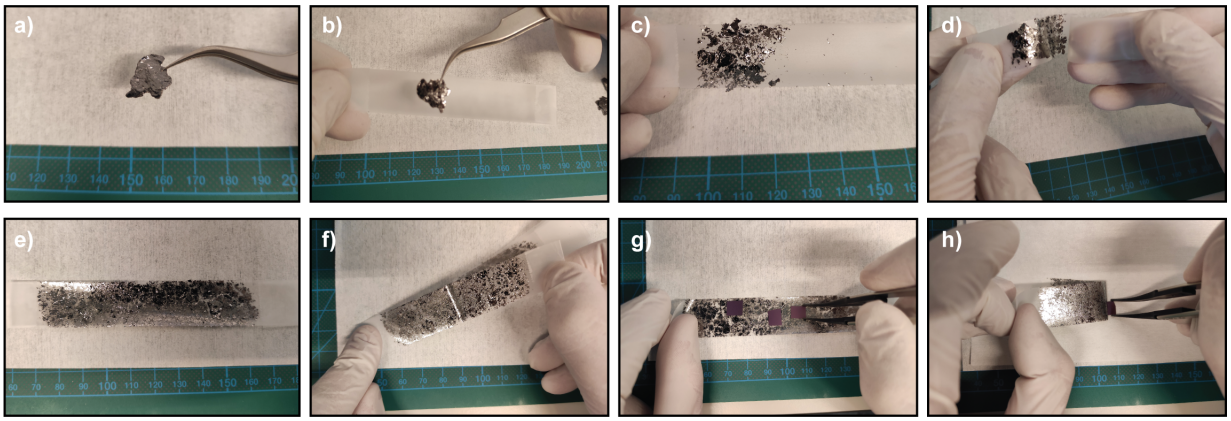

Fig. 2.2: Exfoliation of graphene. a) Graphite crystal used for exfoliation. **b)** The crystal is put into a scotch tape. **c)** Tape after placing the crystal in several spots. **d)** The tape is folded several times. **e)** Tape filled with graphite after folding. **f)** A "daughter" tape is created from the original "mother" tape. **g)** The Si/SiO_2 chips are placed on the resulting "mother" tape. **h)** After heating, the tape is slowly peeled off from the chips.

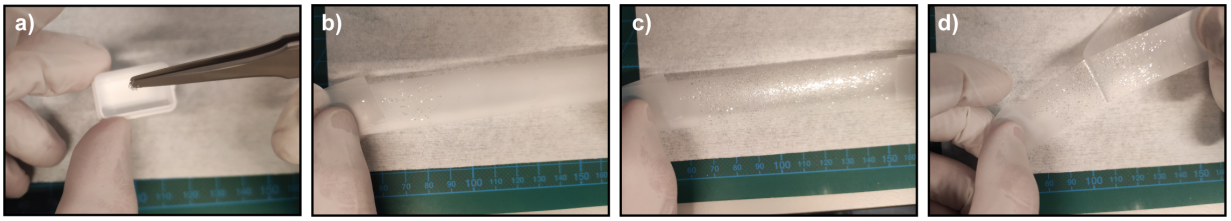

Fig. 2.3: Exfoliation of hBN. a) hBN crystals used for exfoliation. **b)** Tape after placing the crystals in several spots. **c)** Tape filled with hBN after folding. **d)** A "daughter" tape is created from the original "mother" tape.

Lastly, if one wishes to use graphite as a metallic back gate of the vdW heterostructure, the chips where graphene was exfoliated can be used for this purpose. The vdW force between hBN and the graphite back gate is strong enough in order to pick it up from the substrate. However, if one wishes to use graphite as a top gate, the Si/SiO_2 should not be cleaned with O_2 plasma, so that the graphite can be directly picked up with the polycarbonate (PC) stamp. This last point is key for the fabrication of double-gated devices, which is explained in detail in Chapter 5.

2.1.2 Flake identification

During the exfoliation process, flakes of different thicknesses are cleaved on the Si/SiO_2 chips. Given that their absorption of incident light varies approximately linearly for the first few number of layers, the thicknesses of the flakes can be determined under investigation on an optical microscope [128, 129].

In Fig. 2.4a we can see that while monolayer graphene appears similar to the light purple color of the SiO_2, thicker graphite flakes have a darker purple color ($\sim$ 1–5 nm) which can be used for metallic gates. Flakes that are blue ($\sim$ 10 nm) or yellow ($\sim$ 20 nm) are too thick for our needs. The assignment of these thicknesses to the optical color under the microscope can be verified with an Atomic Force Microscopy (AFM), although its use for determining single-layer flakes of 2D materials is very challenging. Alternatively, Raman spectroscopy can be used to unambiguously identify monolayer graphene [130, 131] and the exact number of layers in other 2D materials [132, 133]. In the case of hBN, we generally use flakes of less than 20 nm thickness, i.e. of a light- or dark-blue color under optical investigation (see Fig. 2.4b-c).

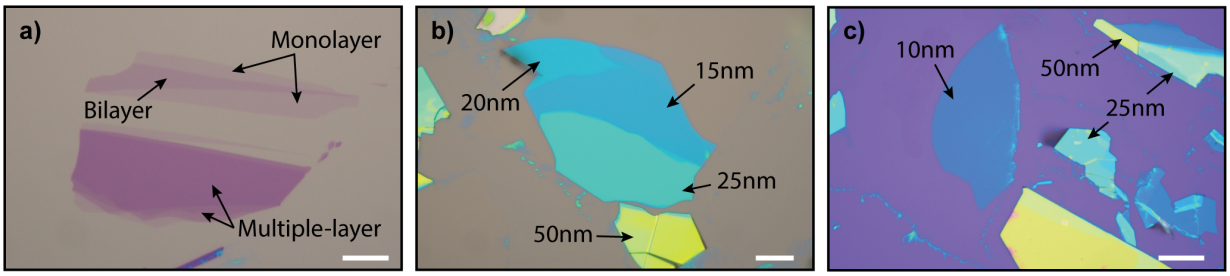

Fig. 2.4: Graphene and hBN flakes identification. a) Monolayer graphene in light pink/purple color, with a visible fold resulting in a bilayer. Multiple layers acquire a darker purple color. **b-c)** hBN flakes of different thicknesses, from thinner in dark blue to thicker in a lighter blue, turning to green and finally yellow. Scale bars are 10 µm.

2.1.3 Stamp preparation

The vertical assembly of vdW heterostructures—the so-called "dry-transfer" method—relies on polymer-based substances to pick up the 2D materials and stack them on top of another [122, 123, 134, 135]. A schematic of the process is shown in Fig. 2.5.

The most widespread used polymers for this technique are polydimethylsiloxane (PDMS), polycarbonate (PC) or polypropylene carbonate (PPC). These are usually assembled on a glass slide, which we term "stamp". Our stamps are made by a commercially available PDMS (Gel-Film 4 from Gel-Pak®) covered with a home-made PC film. The PDMS works as a soft substrate where the adhesive PC layer sits. The choice of PC over PPC stands because of its higher working temperature, which we find helps the transfer process and

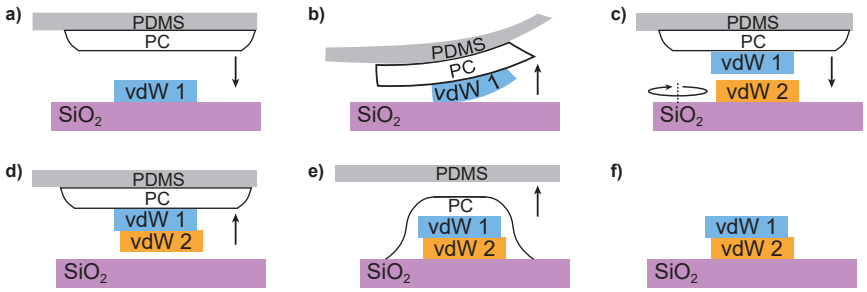

Fig. 2.5: Dry-transfer technique. a-b) Pickup of a vdW material with a PC/PDMS stamp. **c-d)** When picking up a second material, the vdW force between them is strong enough to stack them on top of one another, after rotation if desired. **e-f)** After heating, the stack can be dropped on a chip and the PC is washed away.

will be explained in detail in Subsection 2.1.4. A typical finished stamp can be seen in Fig. 2.7f. We explain in detail the preparation of these in the following.

In order to make the PC films, we dissolve 6% by weight polycarbonate in chloroform. The chemical solution is stirred with magnetic pellets overnight at room temperature. The bottle containing the solution needs to be kept closed carefully, as with time the chloroform will evaporate, changing the concentration of the solution and becoming unusable. With the help of a pipette, the PC solution is placed on top of a previously cleaned glass slide

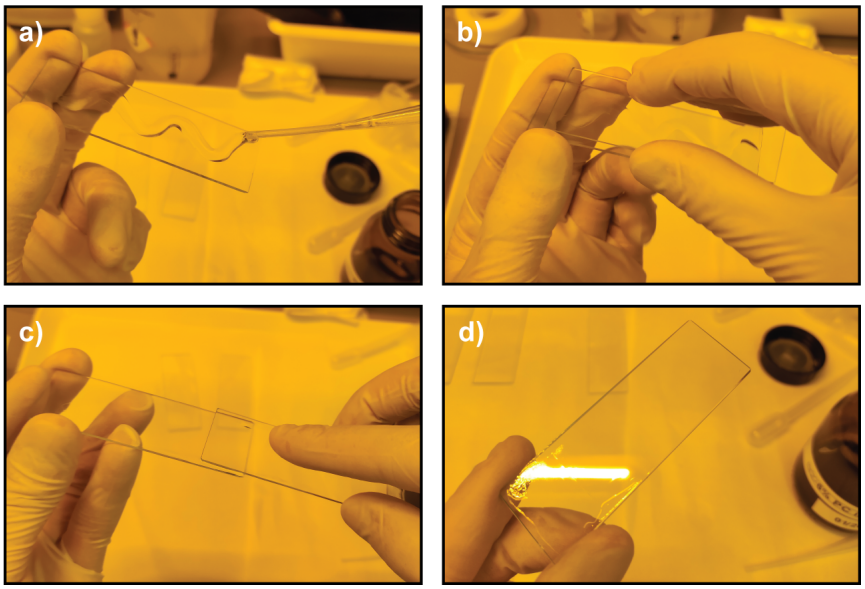

Fig. 2.6: PC film making for stamps. a) The PC solution is dropped onto a clean glass slide with a pipette. **b)** Another clean glass slide is placed on top of the one with the PC solution. **c)** The two glass slides are slowly slid along the long axis, helping to uniformly distribute the PC on both surfaces. **d)** Resulting PC film after heating.

with acetone and IPA (see Fig. 2.6a). The wiggle shape is done in order to maximize the amount of PC on the glass slide. By placing another clean glass slide on top of the one with PC (Fig. 2.6b), and sliding both (Fig. 2.6c), we homogeneously create a PC film on the two surfaces. We heat up both glass slides at 110°C for 5min to evaporate some of the chloroform and achieve a better surface homogeneity. The resulting film can be seen in Fig. 2.6d. In order to use it for making our stamps, we cut it into several areas, as shown in Fig. 2.7c.

Once the PC film is ready, we proceed to make our stamps. First, we cut a small PDMS square of 5×5 mm^2 and place it on a glass slide (Fig. 2.7a). On another side, we prepare a scotch tape with a hollow window in it. This window needs to have slightly larger dimensions than the PDMS square (Fig. 2.7b). The tape with the window is used for picking up the PC film (Fig. 2.7d), which results into a free-standing layer (Fig. 2.7e) after carefully removing the tape. Finally, this tape with the free-standing PC is placed on the glass slide with the PDMS square, resulting in our finished stamp as seen in (Fig. 2.7f). The larger PC film compared to the PDMS ensures that the former sticks out enough to pick up the vdW materials, creating a fine dome-shape. This also helps separating the PC from the PDMS at higher temperatures, for dropping our stack.

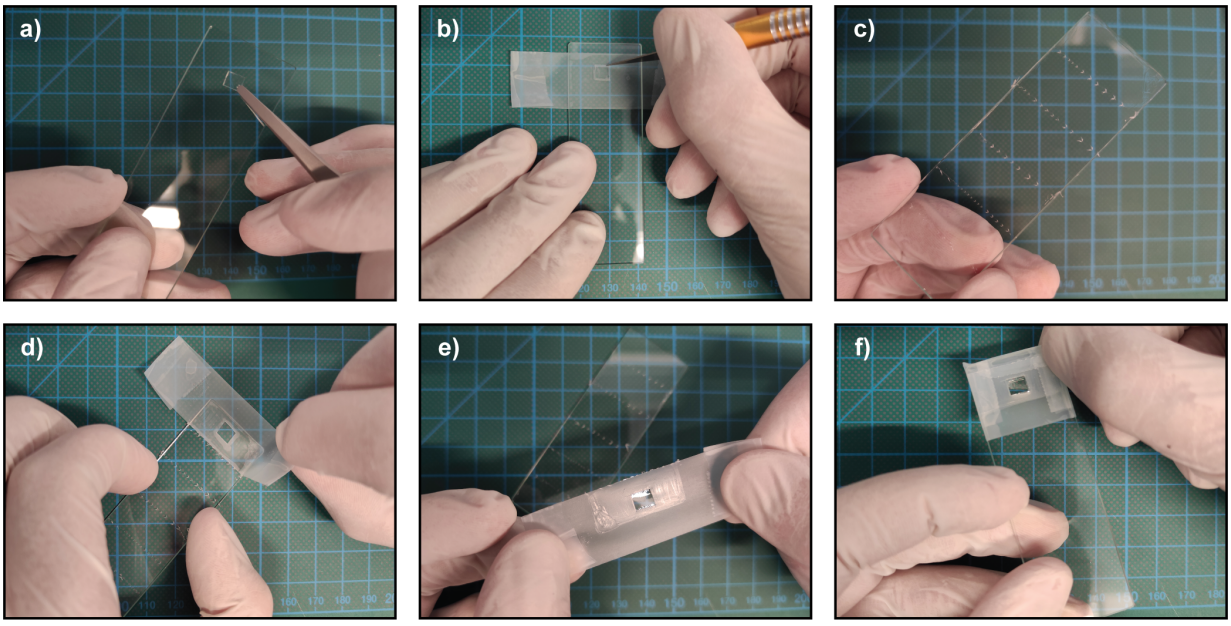

Fig. 2.7: Preparation of PDMS/PC stamps. a) A PDMS square is cut and placed on a glass slide. **b)** In parallel, we prepare a piece of tape with a window slightly larger than the PDMS square. **c)** PC film from Fig. 2.6d after being cut into several areas. **d)** The tape with a window in **b** is placed on one of the PC areas. **e)** Resulting tape with a free-standing PC after a slowly release. **f)** The tape with the PC window in **e** is placed on the glass slide with the PDMS in **a**, finishing our stamp. We use additional tapes on the edges of the glass slide to ensure that the PC film is well attached to the PDMS.

2.1.4 Transfer method: stacking

As just explained, our PDMS/PC stamps are used to stack vdW materials one of top of another. This dry-transfer method [123], commonly known as "stacking", takes place on a transfer stage—a modified microscope where vdW materials are assembled thanks to micro-manipulators for both the sample and the stamp. Fig. 2.8 shows a picture of our transfer stage with the main components annotated. In addition to the typical optical features of a microscope, such as the lenses, camera, objectives and focus adjustment, the transfer stage consists mainly of two parts: the sample stage and the stamp stage.

- The sample stage is visible in Fig. 2.8b. The sample sits on a metallic plate, with a vacuum line in its center, such that the sample does not move during the stacking process. The plate is connected to a heater, which is powered with a current source and controlled with a PID loop. In this way the sample's temperature is controllable up to 200°C with a precision of 0.01°C. Below the heater, separated by an insulating piece, sits a goniometer. This is a critical part of the transfer stage, as it allows to rotate our sample with a precision of 0.016°. All the sample space is movable in the x-y plane with a precision of microns thanks to a micro-manipulator (see Fig. 2.8a).
- A stamp can be put facing downwards thanks to two additional vacuum lines, sitting at the two ends of a trapezoid-shaped arm seen in Fig. 2.8b. In this case, the stamp can be moved in the z direction up and down to approach the sample, as well as in the x-y plane; all thanks to three manual micro-manipulators pointed in Fig. 2.8a. Apart from those, the x-y plane where the stamp stands can also be tilted with two extra micro-manipulators. This allows us to choose the direction in which the PC wavefront from the stamp approaches the sample (see Fig. 2.9a).

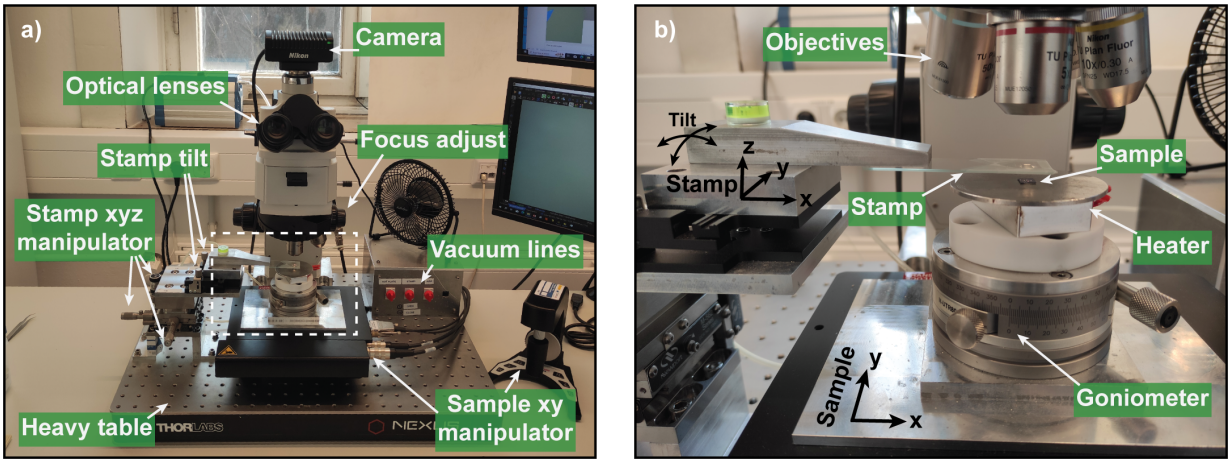

Fig. 2.8: Transfer stage. a) Picture of the transfer stage, with the main components pointed out. **b)** Zoom-in of the dashed rectangle in **a**, where the sample and stamp stages are more visible. Other main components are annotated here.

In Fig. 2.9 we show optical pictures of a stacking process, where we stack a twisted bilayer graphene encapsulated with hBN and a local graphite back gate. In this process, the top hBN is first picked up with the PDMS/PC stamp. After having cut the graphene flake into two parts (see Subsection 2.1.5 for more details), we pick up the first graphene with the top hBN covering all of it. Then, we raise our stamp, we rotate the sample stage 1.116° and we pick up the second graphene part. In this way, the relative angle between the two graphene layers will be the targeted one, safe for a possible relaxation of the angle during the stacking process. Finally, we subsequently pick up a bottom hBN and a graphite narrow flake which acts as a metallic back gate. The whole process is done at a

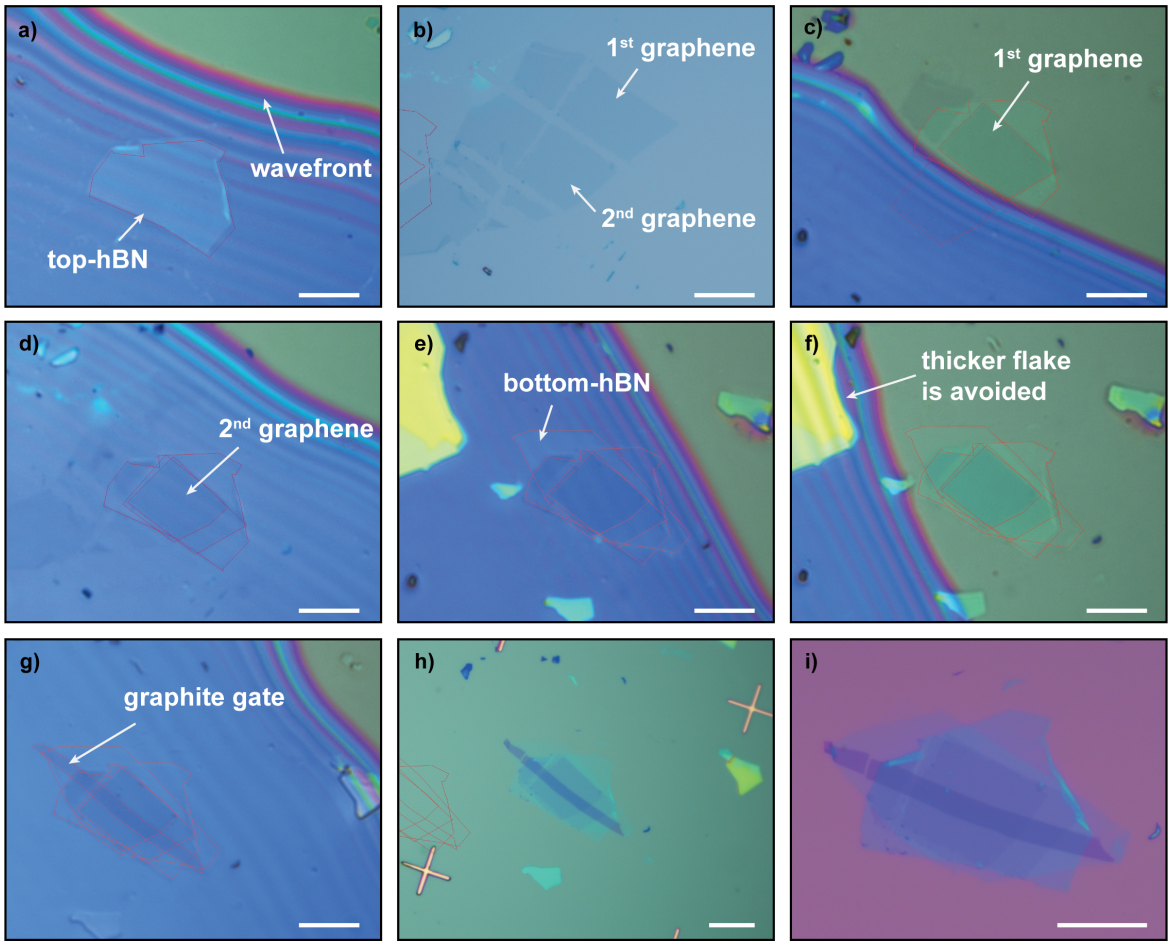

Fig. 2.9: Stacking twisted bilayer graphene. a) Pickup of the top-hBN. **b)** Targeted two halves of a graphene flake after cutting. **c)** Pickup of first half. **d)** Pickup of second half after rotating the stage by 1.116°. **e)** Approaching bottom-hBN. **f)** By controlling the wavefront, a thicker flake on the top left is not picked up. **g)** Bottom graphite gate pickup. **h)** Stack with PC on top of it, after dropping it in a chip with cross markers. **i)** Finalized stack after cleaning the PC. Scale bars are 10 µm. The red drawings are made by us in the camera software to help locate and stack all of the flakes with precision.

temperature of 110°C. We drop our stack on a chip with prepatterned gold cross markers, so that it can be shaped and contacted later in the nanofabrication process. To do so, we go pass the stack with the PC wavefront and heat up to 150°C. Then, by slowly going up with our stamp, this causes the PC to be separated from the PDMS, as it starts to melt. Once we reach 180°C, the PC completely melts on the chip and the stamp with the PDMS can be removed. To clean it, we dip the chip in dichloromethane (DCM) for 5min and rinse it with IPA. The final result can be seen in Fig. 2.9i, showing a very clean stack without appreciable bubbles or inhomogeneities. It is important to note that the resulting vdW heterostructure has clean interfaces between the various 2D materials since their cleavage on the Si/SiO_2 chips during the exfoliation process leaves atomically flat surfaces.

Stacking is a key process in the research of this thesis. Imperfect steps during this procedure can lead to trapped air bubbles, cracks or folds in the vdW crystals, inducing

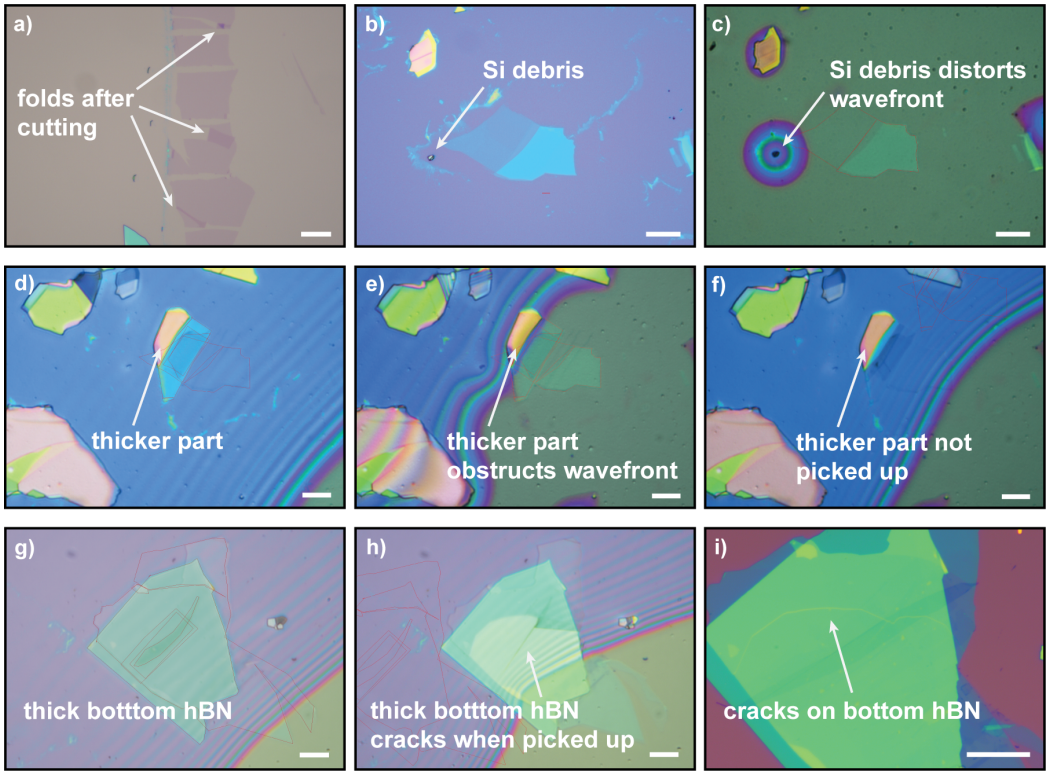

Fig. 2.10: Stacking going wrong. **a)** Graphene flake after AFM cutting, with folds due to strain. **b)** A very thick Si debris next to the top-hBN we want to pick up. **c)** Lack of full contact between PC and hBN. **d)** A bottom-hBN we want to pick up, with a much thicker part. **e)** The wavefront does not go smoothly over that area. **f)** The thicker part cannot be picked up and the bottom-hBN with our stack is destroyed. **g)** A bottom-hBN rather thick ($\sim$ 30 nm with a green color). **h)** When the rest of the stack is put on top of the bottom-hBN to pick it up, the process is abrupt, creating cracks. **i)** Visible cracks after finishing the stack and washing away the PC. Scale bars are 10 µm.

twist-angle inhomogeneity and incontrollable strain profiles. Fig. 2.10 shows the main steps that can go wrong while stacking, mainly due to bad habits. In the following we explain how to fix them. When graphene is cut, especially with the AFM cutting technique, strain can be induced in the flake, resulting in folds, as seen in Fig. 2.10a. These flakes must be avoided, as often these folds do not occur immediately, but over time, making the strain profile in TBG unpredictable. Another main issue when stacking is choosing hBN flakes that have debris around it (Fig. 2.10b-c) or that are attached to thicker parts (Fig. 2.10d-f). This results in a distortion of the wavefront and very likely to violent pickup processes, making the hBNs bend, eventually cracking and folding on the graphene flakes constituting the TBG. The same result can occur if the targeted bottom-hBN is too thick (Fig. 2.10g-i).

These concerns are especially critical when studying TBG at the magic angle 1.1°, which lies close to the natural AB Bernal stacking configuration (0°). Poor stacking can cause relaxation to minimally twisted AB bilayer graphene, forming AB/BA domains. Avoiding such hi-caps during the stacking process is then essential in order to study well-defined quantum phases in ultra-clean samples. With this purpose and during this thesis, my colleagues and I worked out a protocol of fabricating TBG samples close to the magic angle 1.1° with a significant high yield of $\sim 38\%$ [P6]. Such careful stacking process starts with a demanding flake selection. Targeted flakes should be isolated from other unwanted or bulky flakes, as the stacking process will be difficult otherwise (see Fig. 2.10g-i). hBN flakes with terraces of layers on their surfaces should be avoided, as we aim to create a vdW heterostructure with atomically flat interfaces. Some example of proper and not well-fitted flakes for our stacking purposes are shown in Fig. 2.11 and Fig. 2.12.

In the case of hBN, we generally select flakes of less than 20 nm thickness, i.e. of a light

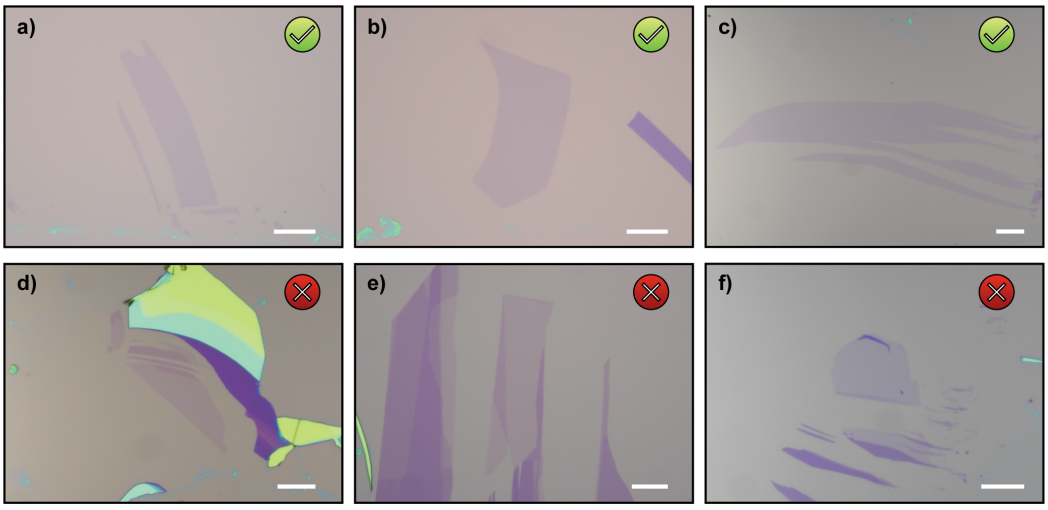

Fig. 2.11: Graphene flakes selection. a-c) Usable, isolated graphene flakes for assembling a clean vdW heterostructure. **d-f)** Unusable flakes, with thicker attached parts or debris around them. Scale bars are 10 µm.

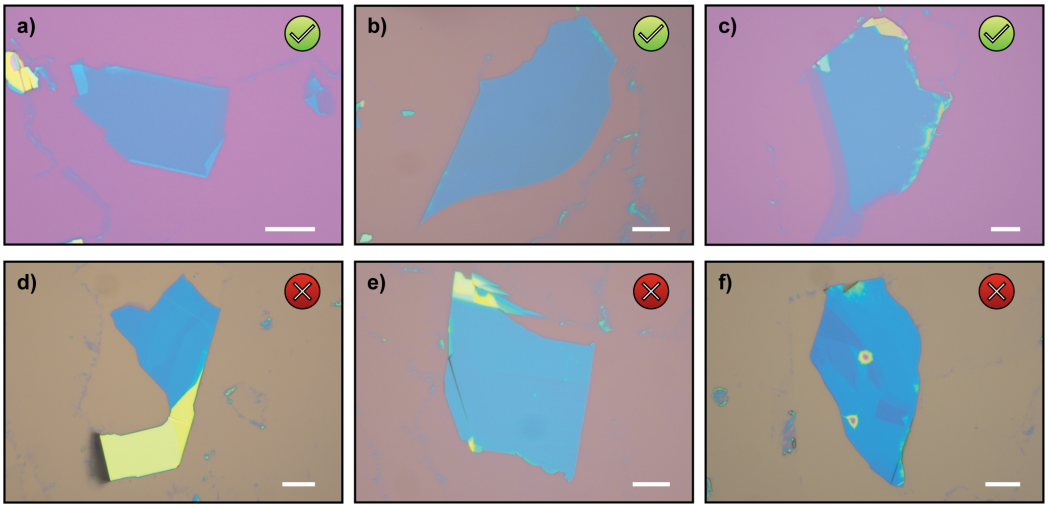

Fig. 2.12: hBN flakes selection. a-c) Usable, isolated hBN flakes for assembling a clean vdW heterostructure. **d-f)** Unusable flakes, with multiple terraces, other thicker flakes around them, cracks or organic residues. Scale bars are 10 µm.

or dark blue color under optical investigation (see Fig. 2.12). Flake size is also critical. We generally use large graphene flakes ($\sim 10 \times 30$ µm^2), so that a clean area after assembling the vdW heterostructure can be easily found (see Fig. 2.11). Also, larger flakes will allow us to cut the graphene into two parts to produce a twisted bilayer graphene heterostructure. This is further illustrated in Subsection 2.1.5. As for hBN, the flakes need to be bigger than that of graphene in order to fully encapsulate it. If graphite flakes for metallic gates are needed, they should be narrower ($\sim 5 \times 20$ µm^2).

Notably, we also found that the yield of magic angle devices would increase if, during the stacking, the graphene layers were pinned by the top-hBN with one of its corners, preventing a potential relaxation of the twist-angle [P6].

2.1.5 Graphene-cutting techniques

When stacking an encapsulated twisted bilayer graphene device, it is imperative to use the same graphene flake and pick up two halves of it, so that the twist-angle between them is set by us when rotating the transfer stage. If two different flakes were used, their relative orientation would not be known, so that an accurate twist-angle cannot be set between them. To cut the graphene there exist various method that have evolved over time, so that less strain and structural movement affects the TBG. These are:

i) *Tear & stack*: this method relies on the vdW force between the top-hBN flake and the graphene [71, 136]. During the stacking process, by covering about half of the graphene, the top-hBN picks it up by tearing it from the rest of the flake (see

Fig. 2.13a-c). Subsequently, the second half can be picked up after rotation. This method greatly introduces strain in the stack, increasing the twist-angle disorder in the TBG. Furthermore, the PC can leave residues on top of the second graphene half, thus trapping dirt in between the graphene layers.

ii) *Cut & stack*: an alternative cleaner method is to use an AFM tip to cut the graphene prior to the stacking process [116, 137]. We do this manually in the transfer stage by setting the tip on a transparent glass slide with a PDMS (Fig. 2.13d). The resulting edges can be rough and typically have a width of 2 µm (Fig. 2.13e-f). Often some cuts can strain the graphene so much that it creates folds (see Fig. 2.10a).

iii) *Laser & stack*: another even less invasive method is to cut the graphene flake with a laser via thermal ablation [138]. The local temperature is rapidly increased under the spot size and the process is helped by oxidative reactions [139]. In our case we use an infrared laser of 1064 nm on a WITec alpha300 Microscope, with a power of 150 mW and a spot size of 1 µm (see Fig. 2.13g-i). By setting a time of 1ms and a single acquisition when the laser courses over the graphene, we obtain clean edges with a separation of 0.5 µm. This method is more versatile as it allows to make cuts into different directions and it does not rely on any mechanical torque on the graphene.

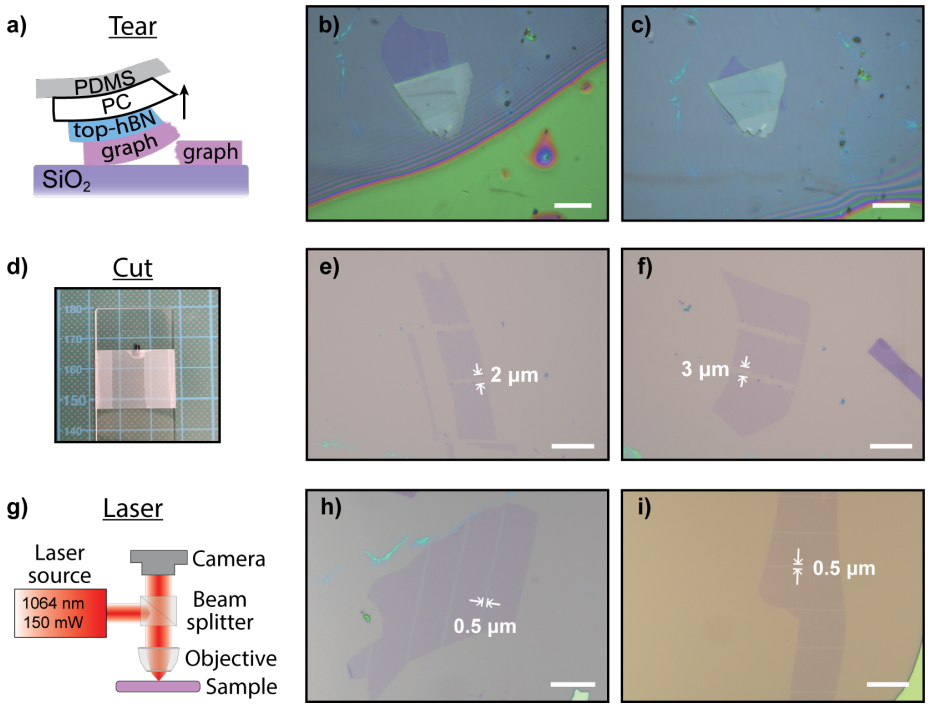

Fig. 2.13: Graphene cutting techniques. a-c) Tear & stack method. The tearing of the graphene occurs by the vdW force between the top-hBN and the graphene. **d-f)** Cut & stack method, manually done with an AFM tip on a glass slide at the transfer stage. **g-i)** Laser & stack method with an infrared laser. Scale bars are 10 µm.

2.1.6 Nanofabrication: lithography, etching and evaporation

In this thesis we study the electronic properties of graphene-based superlattices. Thus, after we have successfully assembled our encapsulated graphene heterostructure, we need to engineer electrical contacts to it. To achieve this, we use one-dimensional (1D) edge contacts, which have been shown to offer less contact resistance and more versatility compared to conventional top contacts [140, 141].

In a 1D contact, the exposed graphene edge is directly contacted with a metal, ensuring that the device remains fully encapsulated with hBN after contact formation, protecting the graphene from polymers used during lithography and from disorder caused by the roughness of the SiO_2 substrate and charge inhomogeneities (electron-hole puddles), which greatly improves device quality and transport properties [142].

Fig. 2.14 sketches the standard nanofabrication steps we follow to achieve this goal. The process begins by spin-coating the chips with an electron beam resist (a), such as polymethyl-methacrylate (PMMA). Next, we use electron beam lithography to define the contact regions with nanometer precision (b). The exposed resist areas are then selectively washed away with a chemical developer, revealing the vdW heterostructure underneath (c). Reactive ion etching is employed to selectively remove the encapsulating hBN, exposing the graphene edge while maintaining the steep profile necessary for an effective contact formation (d) [141]. Finally, metal is deposited via evaporation to form an electrical contact to the graphene layer (e-f). All these nanofabrication steps are carried out in a cleanroom environment. We describe more in detail each of them in the following.

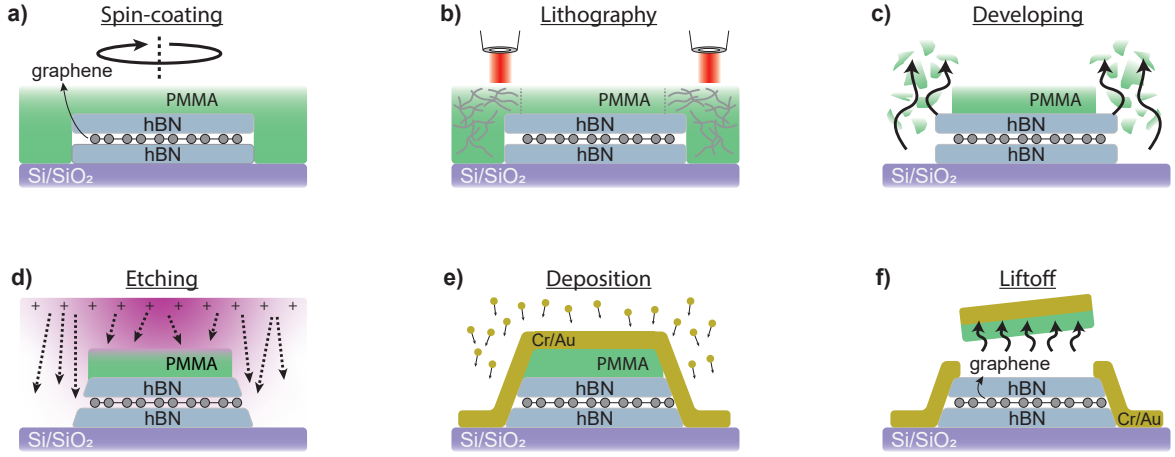

Fig. 2.14: Nanofabrication steps and 1D contact to graphene. **a)** Spin-coating of a PMMA resist. **b)** Exposure of the resist with EBL, breaking the polymer chains. **c)** These parts are removed with a chemical developer. **d)** Etching with RIE. **e)** Metal deposition, e.g. Cr/Au. **f)** Liftoff of the unwanted metallic film by dissolving the PMMA in acetone, leaving graphene with a 1D contact. Scales are exaggerated for explanatory purposes.

Optical and electron beam lithography

Lithography is a fundamental technique in nanofabrication, enabling precise patterning at micro- and nanoscale resolutions. In this work, we employ both maskless optical lithography—or maskless aligner (MLA)—and electron beam lithography (EBL) at different stages of device fabrication. MLA is used for rapid large-area patterning, defining alignment markers and contact pads, while EBL enables high-resolution structuring of nanoscale devices and electrical contacts to encapsulated graphene. The different outputs between these techniques can be seen in Fig. 2.15.

MLA employs a laser to expose photoresist without physical masks, using only the chip's corner references for alignment [143]. The resist undergoes photochemical changes when exposed to UV light (typically 375 nm or 405 nm), making selected regions soluble in a developer. Due to its diffraction-limited resolution of ~ 1 µm, MLA is primarily used for defining features that serve as references for subsequent high-resolution EBL steps. In our case, we use a Heidelberg MLA system with a positive resist, AZ5214, which is developed in MIF726 for 50s and rinsed with deionized water. The optimal parameters found for this process were 80 mJ/cm^2 of dose and -6% focus offset, with the results shown in Fig. 2.15a.

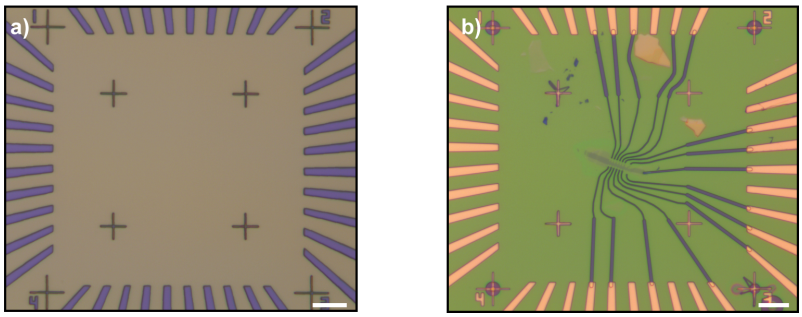

Fig. 2.15: Lithography with MLA and EBL. a) Crosses and wide electrodes exposed (purple color) in an MLA. The resist is AZ5214 (brown). **b)** Finer structures exposed (purple color) in an EBL. The resist is PMMA (green). Scale bars are 10 µm.

For nanoscale patterning of our devices, we use EBL, which writes patterns over an electron-sensitive resist by scanning with a focused electron beam [144]. Here high-energy electrons (10–30 keV) break molecular bonds in the resist, making the exposed regions soluble in a developer solution. The sample is then developed in MIBK:IPA (1:3), selectively dissolving the exposed resist and leaving behind the defined pattern (see Fig. 2.14b-c). One key challenge in EBL is the proximity effect, where scattered electrons lead to unintended exposure in adjacent areas, requiring dose adjustments [145]. The precise alignment of the EBL pattern to the sample is achieved using pre-patterned alignment crosses defined in the MLA step. These crosses, located at the chip edges and near the device area, serve as reference points for aligning the loaded design. The electron gun is briefly opened to visualize the crosses without overexposing them, and alignment is performed using both

3-point and write-field alignment techniques. The result of this alignment can be seen in the exposed crosses in Fig. 2.15b.

In this work we perform EBL using a Raith system with PMMA as the electron-sensitive resist. We prepare the resist to achieve a calibrated thickness of 270 nm after spin-coating for 40s at 4000 rpm. Such thickness is calibrated with an ellipsometer and ensures an optimal liftoff process after metal deposition, preventing unwanted metal residues from remaining on the sample. For Hall-bar devices, which typically feature structures as small as 500 nm, we use a dose of 300 $\mu C/cm^2$ and develop in MIBK:IPA (1:3) for 50s. Examples of exposed and developed samples are shown in Fig. 2.16b and Fig. 2.18a.

Reactive ion etching

Reactive ion etching (RIE) is a dry etching technique widely used for patterning nanostructures with high precision. It operates by combining chemical reactions and physical ion bombardment to remove material from the substrate. In an RIE system, a low-pressure plasma is generated by applying an RF field to a gas mixture, typically containing reactive species like CF_4, O_2, CHF_3 or SF_6. The ions are accelerated toward the sample surface, breaking bonds in the material and facilitating etching through chemical reactions. The difference between the plasma potential and the sample electrode creates a DC bias voltage, which determines the energy of ions bombarding the surface. Higher RF power increases the voltage bias, enhancing ion energy and promoting more physical etching. By adjusting the gas composition, pressure, and RF power, one can control etching rates, selectivity, and profile shape of this anisotropic process.

In our case, we use a mixture of CHF_3 and O_2 to etch both the hBN and the graphene or graphite in our heterostructures. As mentioned before, to create a 1D contact to graphene,

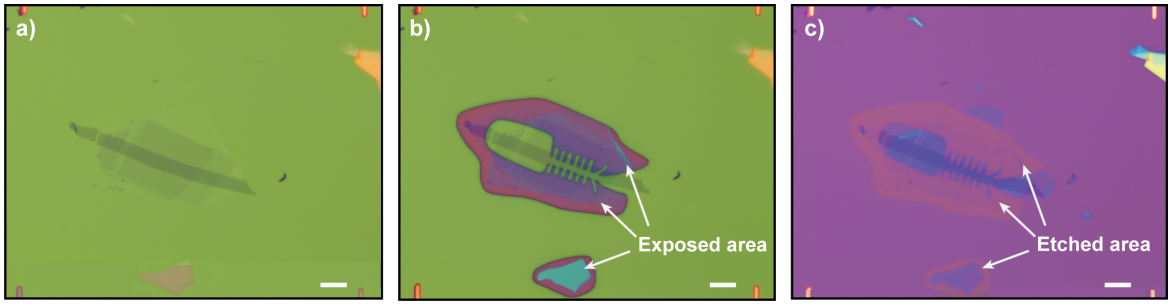

Fig. 2.16: Reactive ion etching to shape a device. a) Sample after spin-coating with PMMA, in green. Same sample as in Fig. 2.9. **b)** After exposing our design in the EBL and developing, the exposed regions do not have any PMMA. **c)** After etching in the RIE with a CHF_3:O_2 mixture and washing out the PMMA, the device has been shaped into a Hall-bar geometry. The etched areas now lack any vdW materials and the SiO_2 turns to a different color as some of its thickness has also been reduced. Scale bars are 10 µm.

the final structure must have a steep—non-vertical—sidewall that exposes the graphene layer (see Fig. 2.14d). This steepness is achieved through a higher etching rate of hBN compared to graphite. This forces the encapsulated graphene to serve a mask layer for the bottom hBN, since it is etched more slowly [141]. In Fig. 2.17 we show the calibration of a CHF_3:O_2 recipe to achieve such a 1D contact in encapsulated graphene heterostructures. The recipe parameters are: CHF_3:O_2 (40:4 sccm), 45 W RF power and 90 mTorr chamber pressure. A sample going through this process can be visualized in Fig. 2.16.

To calibrate the etching rates of the RIE recipe, we exfoliate hBN and graphite onto SiO_2 chips with markers and spin coat them with PMMA. Trenches 1 µm wide are then patterned on the identified flakes with the EBL. To maximize the number of etching tests per exposure, the chips are cut into three parts after development. Each part is etched for a different duration in the RIE with the CHF_3:O_2 recipe, ranging from 10 to 60 seconds. To improve statistical reliability, we use two flakes of each type for each test and measure the etched depth for each time.

After etching and washing away the PMMA in acetone and IPA, we measure the depth of the etched trenches with an AFM. The step heights are analyzed with Gwyddion [146], as shown in Fig. 2.17. By performing this analysis for all etching times and doing a linear fit, we determine the etching rate for hBN and graphite to be 20 ± 1 nm/min and 3.0 ± 0.6 nm/min, respectively. This gives an etching selectivity of approximately 7:1—sufficient to achieve reliable 1D contacts to encapsulated graphene heterostructures [141]. The etched height is calculated as the mean value across all trenches and flakes for each time, with the error bars representing the standard deviation of the measured heights.

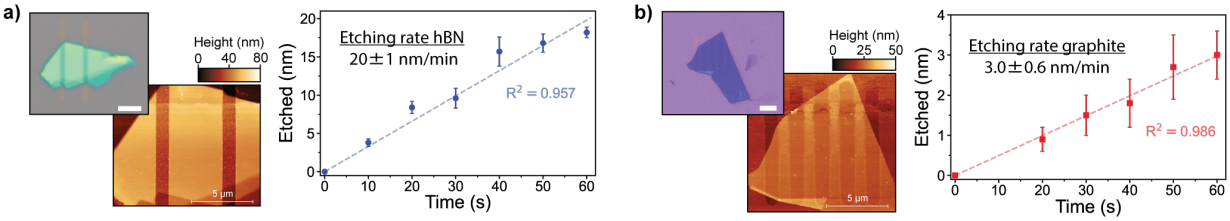

Fig. 2.17: CHF_3:O_2 etching rate of hBN and graphite. a) Left panels show an optical picture of an hBN flake after etching a few trenches for 50s and an AFM picture where the thickness is measured. Right panel shows the extracted depth of the etched trenches for several times, with a linear fit and the concluded etching rate. **b)** Analogous for graphite. Scale bars are 5 µm.

Metallic film evaporation

Once the contact regions are defined through lithography and etching, metal deposition is performed to create reliable electrical connections to the encapsulated graphene. In this work, we use electron beam (e-beam) evaporation, a high-precision physical vapor deposition technique that ensures uniform and high-purity metal films. Here a high-energy

electron beam generated by a thermionic emitter is focused onto a crucible (or pocket) containing the target metal, such as Cr, Ti, Au, Pd or Pt. The intense localized heating causes the metal to sublimate, creating a vapor flux that travels in a line-of-sight trajectory and condenses onto the sample surface, which sits downwards facing the target. The deposition rate is precisely controlled (typically 0.1–1 Å/s) by adjusting the beam power and is monitored in real time using a quartz crystal microbalance. To enhance film uniformity, the sample stage is often rotated during deposition. The process takes place in an ultra-high vacuum (UHV) chamber (10^{-7}–10^{-8} mbar) to minimize contamination and prevent oxidation of deposited materials.

For our devices, we first deposit 5 nm of Cr as an adhesion layer, which also ensures good contact with graphene thanks to their similar work functions [147]. This is followed by 50 nm of Au, which provides high conductivity and electrodes that do not oxidize. They're both evaporated at a rate of 1 Å/s, so that we prevent excessive heating of the resist, which could degrade the pattern quality or lead to unwanted metal diffusion. After deposition, the sample undergoes a lift-off process in hot acetone (3h at 70°C) with the help of a syringe or a pipette, which removes the resist along with the film on top of it (see Fig. 2.14f), leaving behind well-defined electrical contacts. A sample going through this process can be visualized in Fig. 2.18. Ultrasonic techniques—commonly used in the nanofabrication industry for a liftoff process—must be avoided here, as the low frequency vibration can blow our vdW stack or relax the twist-angle of the TBG.

While e-beam evaporation offers superior precision and is particularly effective for high-melting-point materials like Cr, thermal evaporation provides an alternative deposition method. Here the metal is heated resistively in a crucible until it evaporates and condenses on the sample. This technique is more energy-efficient but offers less precise control over deposition rates and is generally better suited for low-melting-point materials like Au or Al. During the first years of this thesis at ICFO, we routinely did thermal evaporation of these two materials.

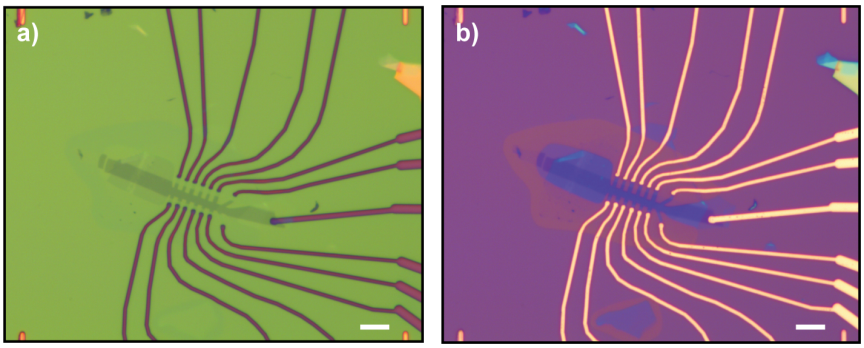

Fig. 2.18: Metallic deposition to contact a device. a) After shaping our sample as shown in Fig. 2.16, we once again expose a new design in the EBL and develop. **b)** Resulting electrodes contacting the encapsulated graphene (1D contact) after etching with CHF_3:O_2, depositing 5/50 nm of Cr/Au, and doing liftoff. Scale bars are 10 µm.

2.2 Josephson junctions fabrication

In the previous section, we have discussed the fundamental nanofabrication techniques and their application to graphene-based vdW heterostructures, particularly for creating Hall-bar structures and investigating quantum transport.

In this section, we shift our focus to the nanofabrication of Josephson junctions with graphene-based heterostructures as the weak link, which represents a major effort in this thesis. One of the key differences from the previous processes is the deposition of superconducting materials, namely Molybdenum-Rhenium (MoRe), which is carried out in a sputtering chamber. This process required significant optimization, from adjusting the sputtering parameters to ensure the film remained superconducting while achieving low strain profiles and good contact with the graphene. An additional challenge was achieving a precise electrode separation of 100–300 nm to ensure ensure a superconducting proximity effect into the graphene weak link. Controlling such fine electrode spacing required optimization of the e-beam lithography dosage, development time, sputtering and liftoff; so that the contacts are not electrically shorted with one another.

2.2.1 Sputtering of superconducting Molybdenum-Rhenium

Magnetron sputtering is a widely utilized physical vapor deposition technique for depositing thin films by ejecting atoms from a target material onto a substrate. This process takes place in a vacuum chamber where energetic ions from a plasma bombard the target, removing atoms that subsequently condense onto the sample substrate to form a uniform film. Sputtering sources often use magnetrons that confine the plasma near the target surface with magnetic fields, increasing ion density and sputtering efficiency. This confinement is achieved by positioning a permanent magnet structure behind the target surface, creating a closed-loop magnetic field that traps electrons and enhances the ionization of the sputtering gas within the confinement zone [148].

There are primarily two sputtering modes: direct current (DC) and radio frequency (RF). DC sputtering employs a constant voltage to generate the plasma, making it particularly effective for depositing conductive materials. It operates in an Ar plasma environment, where positively charged Ar ions are accelerated toward the negatively biased target. The impact ejects the target atoms, which then deposit onto the sample. Fig. 2.19a shows a sketch of this process. This DC mode is nevertheless unsuitable for insulating targets due to charge buildup on the surface, which prevents sustained sputtering. RF sputtering, in contrast, applies an alternating current at radio frequencies (typically MHz), preventing charge accumulation and enabling deposition of both conductive and insulating materials.

A key distinction between sputtering and evaporation techniques (e-beam and thermal evaporation) is that in the latter, the material is heated until it vaporizes and travels in a

line-of-sight trajectory toward the substrate, leading to highly directional deposition. This can result in non-uniform films, particularly on complex surface geometries. In contrast, sputtering occurs at higher pressures, where sputtered atoms undergo multiple collisions, leading to an isotropic deposition in all directions. This results in films with better step coverage, making sputtering especially advantageous for ensuring uniformity over large areas.

For our fabrication of superconducting MoRe contacts on graphene heterostructures, DC sputtering was chosen over evaporation due to its ability to deposit high-melting-point materials. This is because, in sputtering, material removal is achieved through ion bombardment rather than thermal heating. While thermal and e-beam evaporation are well-suited for metals like Au and Al, they become inefficient for refractory materials like MoRe, as the required temperatures for vaporization are extremely high. Despite these advantages, sputtering requires more complex system configurations, as the high-energy plasma environment can induce film stress or cause unwanted damage to sensitive materials. In the case of superconductors, these affect their T_c and H_c, so a careful optimization of the sputtering parameters, such as substrate biasing, temperature and deposition pressure is necessary to achieve high quality superconducting MoRe (50:50 weight).

During this thesis work, we have used a "Von Ardenne LS 320 S" sputtering machine, shown in Fig. 2.19b. Its vacuum chamber reaches pressures as low as $\sim 5 \times 10^{-7}$ mbar. Inside lies one DC generator for two different targets and an RF source for another two targets. The plasma can be generated in an Oxygen or Argon atmosphere, although in our case we only use the latter, as it is an inert gas that does not oxidize our materials. The flow of Ar is measured with a manometer and can be controlled with a PID loop. Between the sample and the targets lies a rotating shutter.

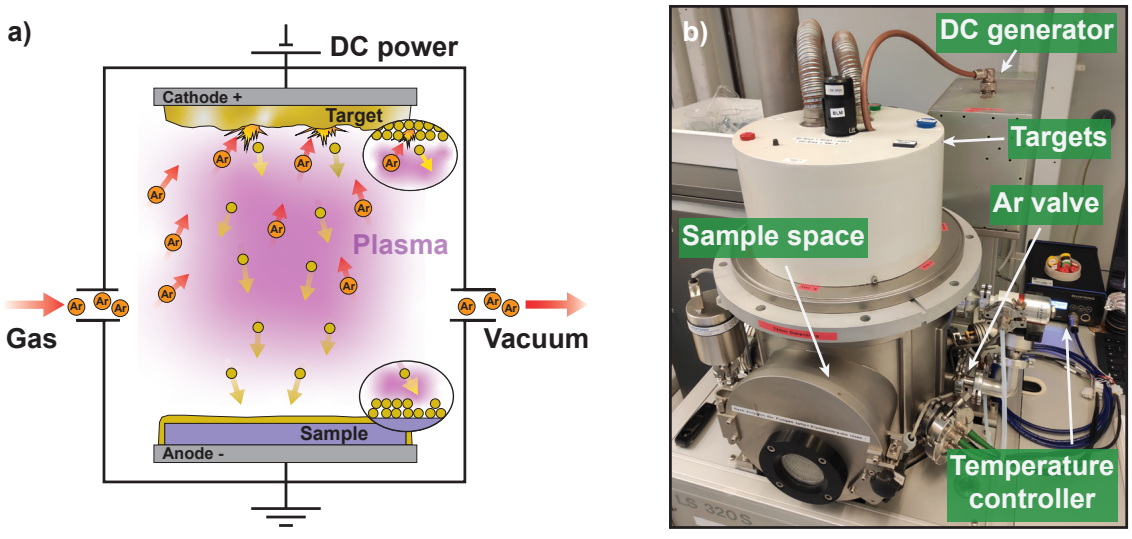

Fig. 2.19: Sputtering process. a) Illustration of how a sputtering process works. **b)** Picture of the "Von Ardenne LS 320 S" sputtering system that we use.

The MoRe sputtering process in this instrument is as follows:

i) *Setup and vacuum overnight*: immediately after etching, the graphene sample is placed in the center of the holder with a small drop of diphenyl oil under it, to ensure the chip does not move during the sputtering process. The chamber is pumped overnight ($\sim$ 14 h), reaching a pressure of $\sim 8 \times 10^{-7}$ mbar.

ii) *Pre-sputter*: the valve that connects the pump to the chamber is closed, and the chamber is then filled with Ar. The flow we select is typically 3×10^{-2} mbar. With our sample protected by a closed shutter, we turn on the DC power source at 30 W and start a pre-sputtering process, where the goal is to clean the MoRe target from impurities that may have been deposited in its surface while kept at air before pumping down the chamber. We do this for 3min.

iii) *Sputtering*: after the pre-sputtering session, the DC power source is increased until the targeted amount where the actual sputtering will take place, i.e. 55 W. The Ar pressure is also reduced to $\sim 3 \times 10^{-3}$ mbar. The shutter is opened and the MoRe is sputtered on the sample. After the desired deposition time is over, i.e. 3min, the shutter is closed again. The DC source is turned off and the Ar valve is closed. The chamber is finally slowly vented and the process is over.

The resulting MoRe film, with a thickness of 100 nm, is superconducting with a critical temperature $T_c \sim 9$ K, as shown in Fig. 2.20a. MoRe is a type-II superconductor and thus, its upper critical magnetic field H_{c2} can be estimated to be $H_{c2} \sim 9$ T by measuring its value at several higher temperatures (see Fig. 2.20b) and extrapolating them with the expression

$$H_{c2}(T) = H_{c2}(0)\left(1 - T^2/T_c^2\right). \tag{2.1}$$

Such values are in agreement with other works in the literature [20, 23, 104]. The method used to extract both T_c and H_{c2} is to find the value of temperature or field at which the resistance R of the film reaches 50% of its normal-state resistance.

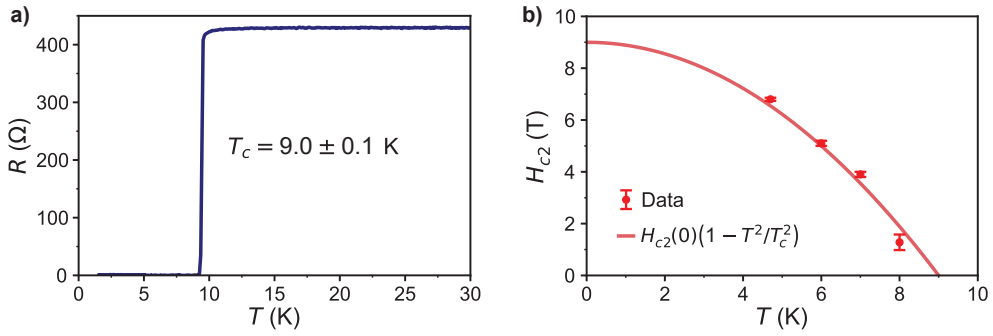

Fig. 2.20: Superconducting sputtered MoRe. a) Resistance vs temperature for a 100 nm thick MoRe film sputtered at 55 W. **b)** Upper critical magnetic field extracted for different temperatures. The fit corresponds to that of Eq. (2.1).

The thickness of the film is known by measuring it with an AFM. From there, the deposition rate of the sputtering process is inferred, which in our case results in 33 nm/min. This is important, as we need to sputter a thickness greater than our vdW stacks in order to contact the graphene layer. With the bottom-hBN being generally lower than 20 nm, we usually aim to sputter between 70 nm and 100 nm of MoRe. It is also crucial to sputter a thick enough film so that its superconducting properties remain intact. In our experience, sputtering 50 nm of MoRe at 55 W already lowers its T_c to 7 K, and 20 nm down to 4 K.

2.2.2 Superconducting contact engineering to graphene

The choice of MoRe as the superconducting material to create Josephson junctions based on graphene weak links is for two reasons. First, its H_{c2} allows for the observation of quantum Hall states and high magnetic field phenomena in the 2DEG weak link while MoRe is still superconducting [23, 149–151]. Second, it has been shown to make a good electrical contact to graphene and carbon-based materials due to its work-function matching [20, 104, 152]. Such is also the case of other materials like Nb [22, 153, 154], NbN [155], NbTiN [156–158] [P2], Ta [159], MoGe [24] or ReW [154].

In order to make Josephson junctions with our superconducting MoRe films and a graphene vdW heterostructure as the weak link, we first need to place the MoRe electrodes very close to one another, so the superconducting proximity effect holds across the whole junction. For that, the junction length L needs to be in the order of the coherence length ξ_N in the weak link. By taking the ballistic regime and $\Delta \sim 1.4$ meV the BCS superconducting gap of MoRe, we estimate $\xi_N = \hbar v_F/\Delta \sim 480$ nm for graphene, with $v_F \sim 10^6$ m/s. Therefore, a junction length of 300 nm or less should be sufficient to achieve a short-ballistic graphene JJ.

Such narrow gaps between the sputtered electrodes need to be first resolved in the e-beam lithography process. For that, we design a dose test where the same structures are exposed for different doses, by keeping the same developing time. The developer we use here is IPA:DIW (7:3), which has been shown to avoid cracks in the PMMA above the hBN due to thermal stress compared to using MIBK:IPA [37, 160, 161]. An example of such dose test is shown in Fig. 2.21a-d. When the dose is too high (Fig. 2.21c), the e-beam proximity effect makes the features wider and it is not possible to resolve the gaps between the electrodes [145]. This would result in shorted electrodes after sputtering. Although these gaps are well defined in the underdosed case (Fig. 2.21a), the inner area of the electrodes shows unexposed areas with some cuts, which will result in an amorphous and discontinuous film after sputtering. When the dose is ideal (Fig. 2.21b), all these problems are avoided, leaving well-defined structures with the desired separation between them.

Fig. 2.21 constitutes a summary of a successful dose test. However, there is much more work behind that we do not show here, such as figuring out the optimal temperature and time of the developer, dose and steps-size values in the e-beam, etc. As an example, one

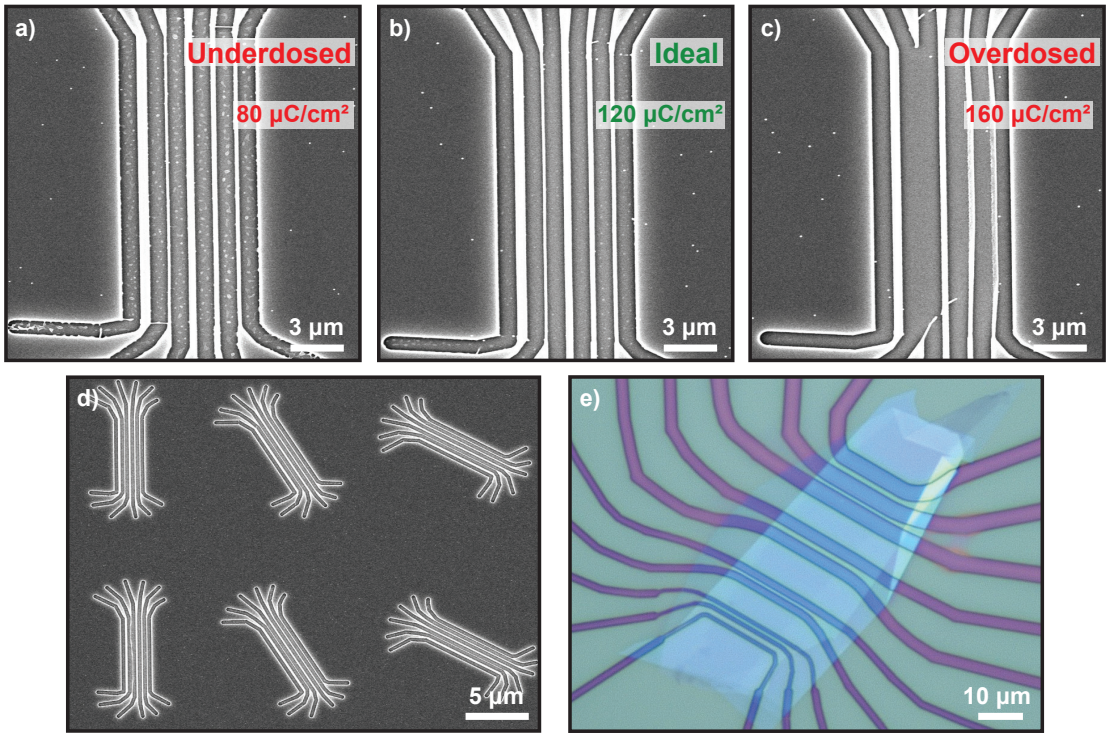

Fig. 2.21: Electron beam optimization of a JJ design. a-c) SEM pictures of the same JJ design for three different doses. **d)** Dose test visualized, where for several orientations the same design is exposed with different doses. **e)** Optical picture of an hBN-encapsulated graphene sample, after developing the JJ design.

important detail that we found is that the optimized electron beam dose and developing time would not concur in the same results if the process was done on an encapsulated graphene sample instead of on a SiO_2 substrate. Fig. 2.21a-d then serves rather as a guide of the process one should follow to find an initial good dose. By doing further optimization on real hBN-encapsulated samples, we have found that the recipe that works consistently for us is: a dose of 100 µC/cm^2 and 80s of developing in IPA:DIW (7:3) at room temperature. The result can be visualized in Fig. 2.21e, where we clearly resolve the gap between the developed features for various lengths (100–600 nm).

With this working lithographic recipe, we proceed to etch our samples after developing to make a 1D contact with the sputtered MoRe. To make JJs with graphene-based moiré heterostructures as the weak link, we first need to make sure that the contact between MoRe and bare monolayer graphene is good, and that the Josephson effect behaves as expected with this well known material.

The results of an hBN-encapsulated graphene device with MoRe contacts in a JJ geometry can be seen in Fig. 2.22. One step prior to this was done to etch away all the vdW stack except a strip with constant width, so that all the JJs have the same width but different length (see Fig. 2.22b). This can give us important information about the regime

of the superconducting proximity effect and allows us to extract the contact resistance between MoRe and graphene, as we will see at the end of the next subsection. The sputtering recipe used here is the same that gave us a superconducting MoRe film (see Fig. 2.20): 55 W of DC power and an Ar pressure of 3×10^{-3} mbar. In Fig. 2.22a-b it can be observed that, although some gaps between the MoRe electrodes are saved, most of them present shorts and in general the leads look rough with not-well-defined edges.

Most importantly, although MoRe is superconducting, the Josephson junctions with graphene as the weak link do not present superconductivity, as its resistance does not drop to zero even at very low temperatures (see Fig. 2.22c). Furthermore, the resistance R vs temperature T curve shows some insulating behavior, as R increases with lowering temperature between 4 K and 9 K. Such behavior is typical of contacts with a Schottky barrier in between the two metals, i.e. a tunneling barrier formed by oxide or too big of a separation between the two metals; in this case MoRe and graphene. This is also confirmed by measuring a decreasing resistance with increasing DC current, which is not shown here.

We found these results repetitively for several devices. One possibility is that the CHF_3:O_2 RIE recipe does not create the appropriate slope at the edges to make a 1D contact, but we rule this out as that recipe works for evaporation of Cr/Au contacts. The issue has to be then with the sputtering recipe. We dwell into what can be changed in order to make a better contact to graphene in the following.

In any DC sputtering process, there are mainly two parameters that can be controlled: the power of the DC source onto the MoRe target and the Ar pressure of the chamber. Increasing the DC power elevates the energy supplied to the plasma, leading to a higher density of Ar ions bombarding the target material, increasing the sputtering yield and thus the deposition rate onto the sample (see Fig. 2.19a). However, excessive power can

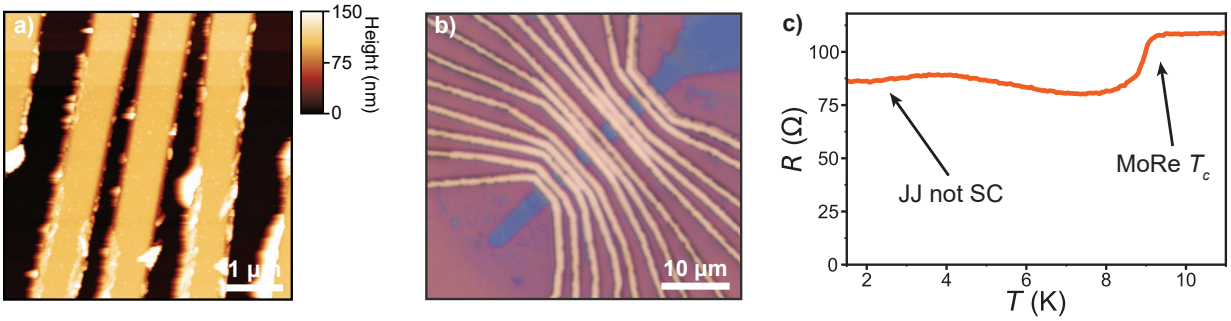

Fig. 2.22: MoRe-graphene JJs sputtered at high power. a) AFM picture of a series of MoRe electrodes after liftoff, sputtered at 55 W and 3×10^{-3} mbar. Several "dog ears" appear, collapsing and shorting some electrodes. In others, the narrow gap between the leads can be resolved. **b)** Optical picture of a series of MoRe leads making a 1D contact to hBN-encapsulated graphene in a JJ architecture, with the same sputtering parameters as in **a**. **c)** Resistance vs temperature in one of the junctions in **b**, where the JJ does not become superconducting, due to an insulating Schottky barrier at the contact.

introduce high-energy particles that may cause defects or stress within the film.

The DC power applied to the target material increases the number of sputtered atoms, as well as increasing their kinetic energy. At low powers, the atoms can reach the substrate with minimal collisions, favoring a more uniform film growth. In contrast, higher powers can cause more frequent collisions, leading to a more porous film structure with higher number of defects. The dependence of the deposition rate with the Ar pressure is not as straightforward as with the DC power. Fewer collisions due to low pressures allow the sputtered atoms to travel more directly to the substrate, potentially increasing the deposition rate. Nevertheless, if the pressure is too low, plasma density may decrease, reducing ionization efficiency and thus lowering the deposition rate. Similarly, if the pressure is too high, too many collisions among the sputtered atoms can cause them to lose their energy and be deposited onto the chamber walls instead of reaching the sample.

The results of varying the power and pressure during the MoRe sputtering process on our JJ design are shown in Fig. 2.23. In these SEM pictures we can see that a lower power (10 W) dramatically improves the sharpness of the electrodes at their edges. This is likely

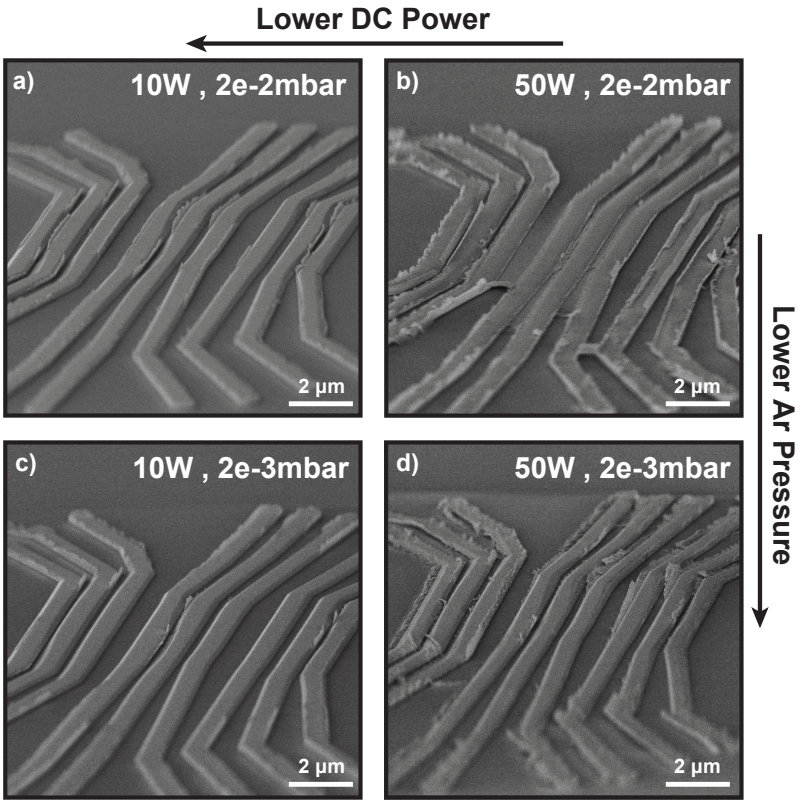

Fig. 2.23: Sputtering with varying DC power and Ar pressure in a JJ design. a-d) SEM pictures of MoRe electrodes in a JJ configuration after liftoff, sputtered on a SiO_2 substrate, for different powers and pressures. The uniformity of the leads and the sharpness of the gaps between them improves as the power and pressure are lowered.

caused by a lower deposition rate resulting in a more uniform deposition process. Reducing the pressure helps getting rid of the "dog ears" that cause shorts between the leads. These are formed because the sputtered atoms are also deposited on the side walls of the PMMA, which are often not lifted off. The "dog ears" term comes from the fact that these thin and tall walls of MoRe are located at the edges, which can easily collapse after flushing during the nanofabrication process, and thus bridge the gap between the electrodes. This is very important for us, since in our JJ configuration, the MoRe electrodes need to be very close one to another, saving a gap of just 100–300 nm.

With these much better-looking structures at 10 W we could indeed create clean junctions with encapsulated-graphene, as shown in Fig. 2.24. However, the resulting MoRe film at such low powers resulted to be not superconducting. Fig. 2.25a shows a systematic study that we performed, where it can be observed that the T_c of MoRe decreases with decreasing DC power, eventually becoming not superconducting; at least down to 1.5 K. The disappearance of cracks in the film with decreasing power can also be seen in Fig. 2.25b-d. When the sputtering process ends, the heated sample due to Ar-ions bombardment needs to cool off, which turns into a thermal-release stress of the film, crumpling and finally causing these cracks. Such thermal stress is the reason why the structures after liftoff are so rough at high powers (see Fig. 2.22 and Fig. 2.23).

The disappearance of the cracks with decreasing power is likely due to a lower deposition rate of sputtered MoRe onto the sample, as verified in Table 2.1. By reducing the applied DC voltage, the amount of MoRe particles pulled out of the target and their kinetic energy are both decreased, leading to a slower sputtering rate. If less amount of sputtered atoms per second arrive to the sample, the film will not get so heated, so that the thermal stress-release in the film when the sputtering process is over will then be less violent. This scenario would potentially lead to less amount of visible cracks, which is consistent with the results of Fig. 2.23 and Fig. 2.25.

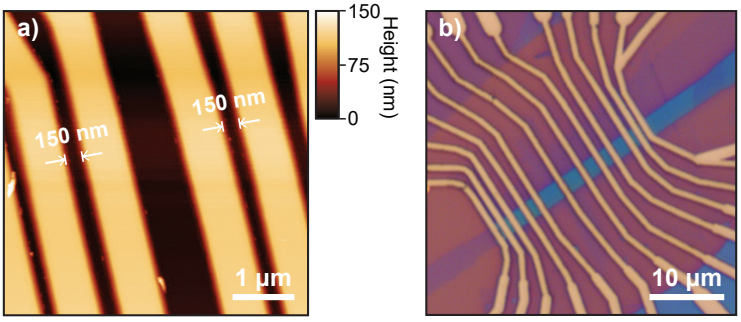

Fig. 2.24: MoRe leads in a JJ design sputtered at low power. a) AFM picture of a series of MoRe electrodes after liftoff, sputtered at 10 W and 2×10^{-3} mbar. No "dog ears" appear and the narrow gap between the leads can be resolved. **b)** Optical picture of a series of MoRe leads making a 1D contact to hBN-encapsulated graphene in a JJ architecture, with the same sputtering parameters as in **a**.

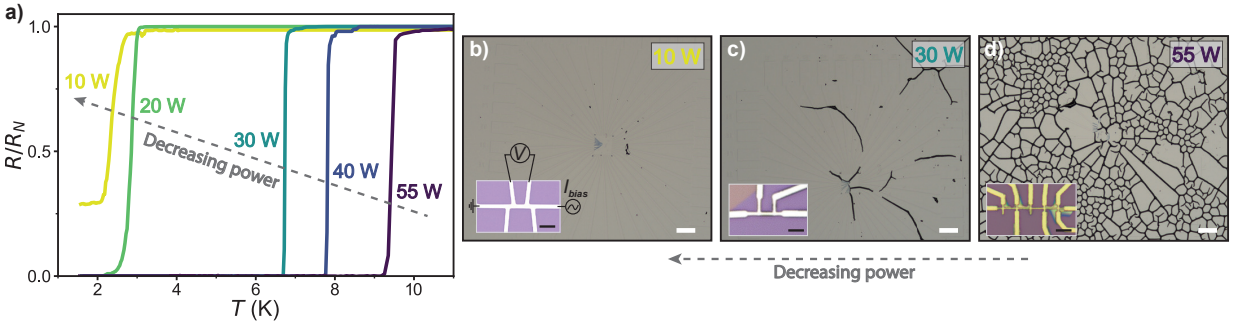

Fig. 2.25: MoRe superconducting transition dependent on sputtering power. **a)** Resistance vs temperature for different DC powers (and thus deposition rate) measured in a MoRe Hall-bar, as indicated in the inset of **b**. **b-d)** Optical picture of a chip after sputtering for different DC powers, along with a Hall-bar after liftoff in the inset. White and black scale bars are 100 µm and 5 µm, respectively.

Surprisingly, the reduced deposition rate led to a deterioration of the MoRe superconducting properties. We conjecture that this is due to a lower purity of the MoRe film, such as the formation of a more porous structure. Yet, given that opposite results were obtained for an study on YBCO films [162], more work should be done to fully grasp how the sputtering parameters affect the superconducting properties of MoRe.

To solve this issue of thermal stress leading to cracks, one possibility would have been to sputter a thinner MoRe film. Taking into account that our hBN-encapsulated graphene heterostructures are about 40 nm thick, the MoRe films needs to be thicker that that in order to guarantee a 1D contact to the graphene. Nevertheless, as mentioned earlier, we found that sputtering less material also resulted in a decreased T_c. Although we could have opted for that route, or to sputter 100 nm of MoRe at an intermediate power, such as 30 W, to have a strain-free film at the cost of reducing the T_c of MoRe, we decided it was a better idea to reproduce the superconducting properties of MoRe reported in other works [20, 23, 104] and avoid other potential unforeseen problems.

DC power (W)	10	20	30	40	55
Rate (nm/min)	5±1	10±2	17±2	22±1	33±2

Table 2.1: MoRe sputtering rate vs DC power. The deposition rate is slower as the power is set smaller. We have estimated the rate by measuring the height of a sputtered MoRe film with AFM. For each case, the sputtering process lasted 3 min.

The goal was then to keep the superconducting properties of MoRe observed when sputtering at 55 W (Fig. 2.20), while reducing the stress in the film and being able to make a reliable 1D superconducting contact to encapsulated-graphene without shorts, unlike in Fig. 2.22.

2.2.3 Minimizing stress with a Peltier device

Here we show how we managed to maintain a high sputtering power and deposition rate while reducing the stress of the film. The solution to this problem was to implement a temperature controller for the sample, so that the thermal stress on the film would not produce cracks, strain and malformations.

For this, we built a sample stage with a heavy thermal load so it could absorb most of the heat, with a heater and a thermometer attached to it. The heater consists of two wires soldered at the two ends of a Peltier device, sitting below and in contact with the sample space while sandwiched between two Teflon spacers. This is shown in Fig. 2.26a-b. By applying a negative (positive) DC voltage to this Peltier device, we create a thermal gradient that cools (heats) the sample. The thermometer consists of a thermocouple connected to the sample plate, whose temperature is readout by a calibrated measurement of its voltage difference. The temperature of the sample can then be controlled actively during the sputtering process with a PID loop programmed in Labview, where the input is the applied DC voltage V and the feedback is the temperature reading T. Fig. 2.26c-d shows how the sample stage inside the vacuum chamber is connected to an outer digital temperature controller via a feedthrough.

With this Peltier device, we first checked that indeed the sample was heating up during the sputtering by ~ 30°C and suddenly cooling down after the process was over, releasing the film stress (see Fig. 2.26e). This was done by reading out the temperature and without applying any voltage.

The idea is then to perform the MoRe sputtering on the sample while it already is at a high enough temperature, so that the temperature gradient between the sputtered MoRe atoms and the sample is not very high. For this, we decided to use a temperature of 70°C. Fig. 2.26f shows the procedure we follow, which we explain in detail here:

i) First, we heat up the sample from room temperature to the targeted 70°C at a rate of 6°C/min. Then, thanks to the PID loop, the voltage is stabilized after a few minutes. We generally use this time to perform the pre-sputtering on the MoRe target at a DC power of 30 W and an Ar pressure of $2-3\times10^{-2}$ mbar.

ii) To start the sputtering process on the sample, we increase the power to 55 W and reduce the Ar pressure to $2-3\times10^{-3}$ mbar. Once the shutter is opened, the sputtered MoRe immediately heats up the sample, but is countered by the Peltier device by decreasing the applied voltage and thus maintaining its temperature at 70°C.

iii) Once the sputtering process is over (3 min), the voltage increases rapidly to avoid a sudden cooling of the sample by keeping it at 70°C. After a few minutes, we controllably bring back the sample to room temperature at a rather slow rate of 2°C/min. The chamber is finally carefully vented and the process is over.

The results of this temperature-controlled MoRe sputtering can be seen in Fig. 2.27. Cracks on the film are not observed on the chip right after sputtering, and the liftoff process

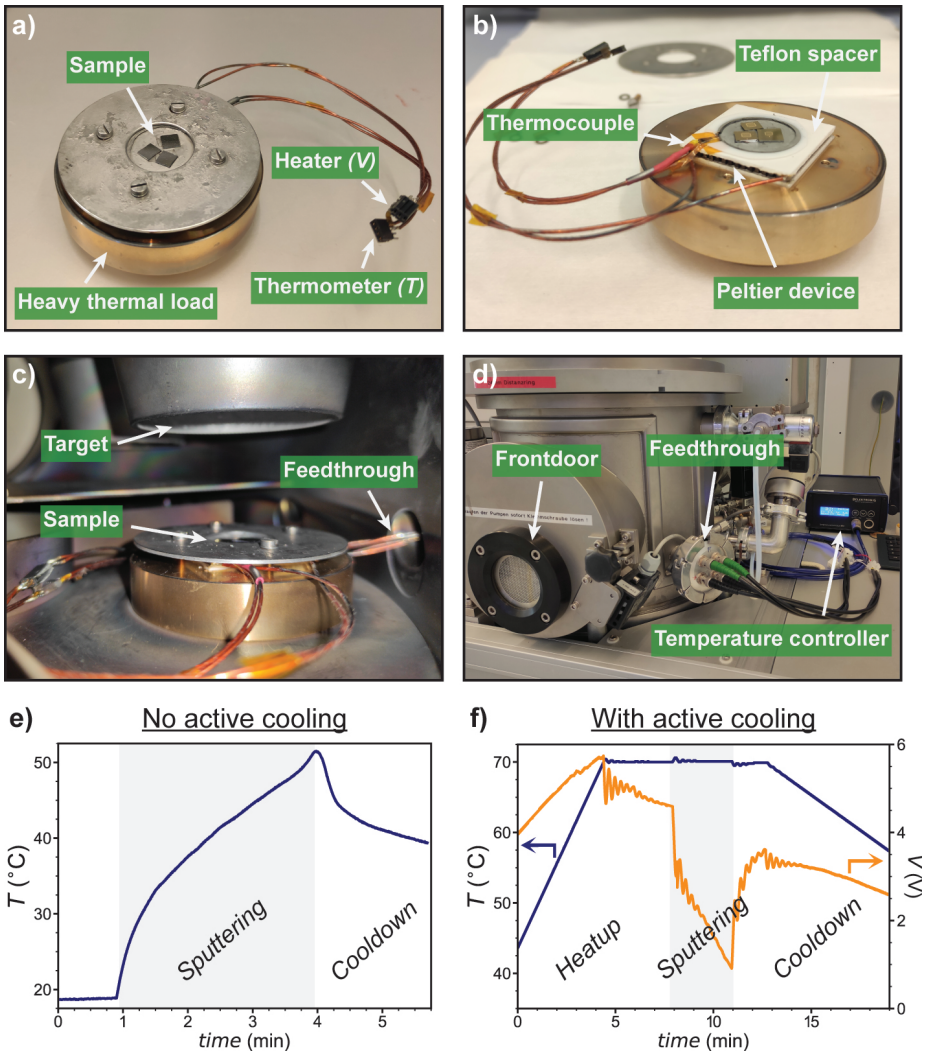

Fig. 2.26: Peltier device for sputtering and active cooling. a-b) Sample stage with heater and thermometer wires attached to a Peltier device in contact with the sample space. **c-d)** Interior of the sputtering chamber, where the stage is placed. The wires are connected to a temperature controller via feedthroughs. **e)** Temperature of the sample, where a sharp increase and drop takes place at the begging and end of the sputtering process, respectively. **f)** The temperature T of the sample (blue in left axis) is controlled thanks to the applied DC voltage V to the thermocouple (orange in right axis), which is controlled with a PID loop. We first heat up the sample from room temperature until 70°C and let it stabilize. When the sputtering starts, V drops to cool down, and when it is over, V rises to heat up; always maintaining T at 70°C. Finally, we controllably cooldown the sample back to room temperature. Gray areas in **e** and **f** indicate the 3 min of sputtering.

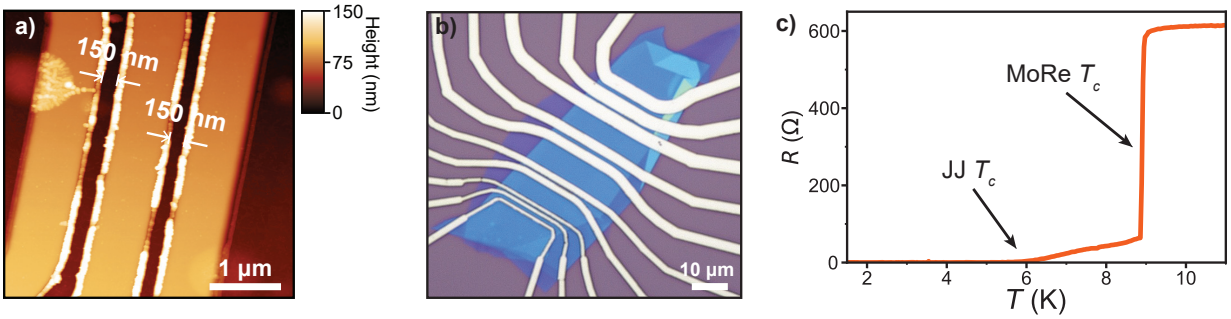

Fig. 2.27: MoRe-graphene JJs sputtered at high power with active cooling. a) AFM picture of a series of MoRe electrodes after liftoff, sputtered at 55 W and 2×10^{-3} mbar. Some "dog ears" appear, but they do not collapse and the narrow gap between the leads can be resolved. **b)** Optical picture of a series of MoRe leads making a 1D contact to hBN-encapsulated graphene in a JJ architecture, with the same sputtering parameters as in **a**. **c)** Resistance vs temperature in one of the junctions in **b**, where the JJ becomes superconducting at 6 K.

leaves well-defined electrodes. We also tried with different temperatures: 40°C, 50°C and 60°C; but we decided the best results were coming out of using a temperature of 70°C. With this recipe, we have consistently made superconducting graphene JJs with high T_c of around 6 K (see Fig. 2.27c), depending on their lengths.

As of now, the recipe had to be changed slightly due to a replacement of the MoRe target. Targets can have different dimensions, and so the applied power to them will not result on the same amount of energy per volume. To achieve the same deposition rate, we changed the recipe accordingly, with the only difference being that the DC power during the sputtering process is now 35 W.

To characterize the quality of our MoRe-graphene contacts, we perform the so-called transfer-length method (TLM). The TLM consists in measuring the resistance of a series of MoRe-graphene junctions with varying length L and constant width W, as shown in the inset of Fig. 2.28a. The resistance R measured across the junctions at 10 K when MoRe is not superconducting (see Fig. 2.28a) is not only that of graphene, but also contains twice the contact resistance R_c. Because we are varying L, we can make a linear fit (see Fig. 2.28b) for a fixed carrier density value according to $R = (\rho L + 2R_c)/W$, where ρ is the resistivity of graphene. From this fit we extract the contact resistance of the junctions for every point in density (Fig. 2.28c), where we achieve a minimum contact resistance of $R_c = 70 \pm 6$ Ω·µm for the electron doped side. These excellent values are comparable or lower to other works with 1D contacts [22, 141]. Furthermore, when graphene becomes superconducting due to the proximity effect, the contact also gets proximitized and its resistance drops down to a few or zero Ohms. An important detail to perform correctly the TLM is that the fabricated electrodes must be designed in the cross-beam configuration shown in the inset of Fig. 2.28a, so that the semi-4probe measurement minimizes the

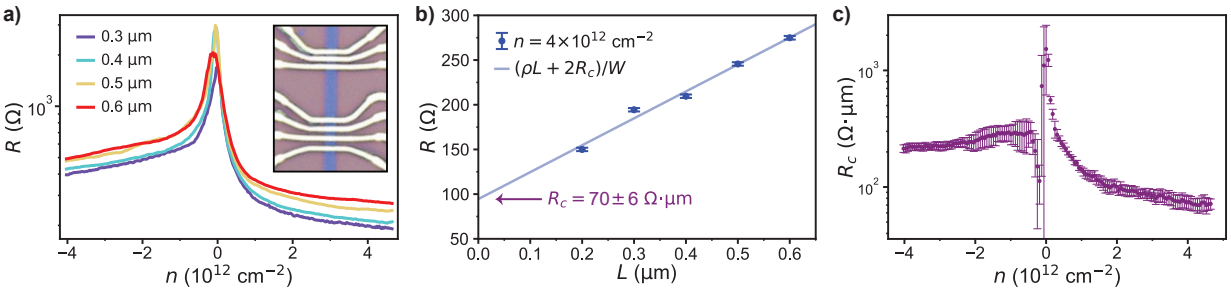

Fig. 2.28: Transfer-length method and contact resistance of MoRe-graphene. **a)** Resistance vs carrier density at 10 K for multiple graphene JJs with varying length. Inset shows a picture of these JJs. **b)** For a fixed n, we can make a linear fit to the data and extract the contact resistance R_c. **c)** Extracted R_c for all carrier densities.

resistance in series of the MoRe wires.

In Fig. 2.29 we show an example of a fabricated MoRe-graphene JJ in the ballistic regime, to highlight the high quality of our devices. First, in Fig. 2.29a we show the differential resistance $\mathrm{d}V/\mathrm{d}I$ map, where the critical current I_c is visibly lower in the hole doped side. This typically observed behavior is due to the MoRe n-doping the graphene, creating an n-p-n profile that increases its normal resistance R_N in the hole side, just as in any graphene transport device [4]. Since I_c and $1/R_N$ scale with each other in the Josephson effect [19, 97], I_c decreases in the hole side.

The formation of these n-p-n profiles can form a cavity if the electrons propagate ballistically in the graphene, giving rise to Fabry-Pérot oscillations in both I_c and R_N (see Fig. 2.29b) [20, 104]. This signature of ballistic transport offers information about the band structure of the weak link, since the Fermi wavelength λ_F of the electron waves causing constructive and destructive interference will be an integer number N of the cavity length L_c, that is:

$$\frac{2L_c}{\lambda_F(n)} = N \tag{2.2}$$

Here N is the number of modes in the cavity, and L_c is in general less than the real junction length L; marked by the size of the p-doped region. For graphene, the Dirac linear dispersion yields $k_F = \sqrt{\pi n}$, from where it follows that $N \sim \sqrt{n}$. Indeed, we find this relation by counting the number of maxima registered in R_N and representing them in Fig. 2.29b. From this example, and as we will see in Chapter 3, it is clear that the investigation of these Fabry-Pérot oscillations in other systems such as the graphene/hBN moiré superlattice can give insights into their underlying band structure.

Finally, Fig. 2.29c shows a measured interference pattern at the electron doped side of the JJ when we apply a perpendicular magnetic field to the graphene layer. There we observe that the I_c follows the typical Fraunhofer relation of a single-slit uniform junction (see Eq. (1.45)). This proves that in our graphene JJs the supercurrent flows uniformly across the junction, as explained previously in Subsection 1.4.3.

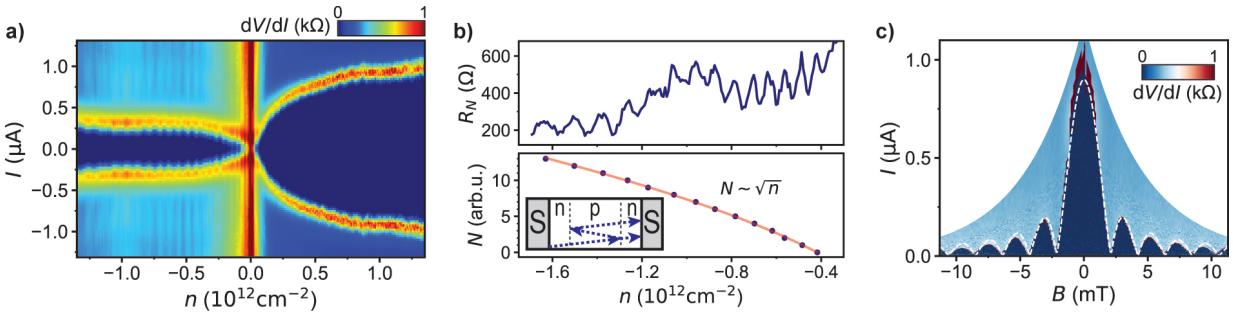

Fig. 2.29: Example of a uniform ballistic graphene Josephson junction. **a)** Differential resistance $\mathrm{d}V/\mathrm{d}I$ vs d.c. current I and carrier density n. **b)** The normal state resistance R_N presents oscillations in n (top panel). By counting their local maxima, we find they follow a square root dependence (red line), proper of a linear Dirac dispersion. **c)** $\mathrm{d}V/\mathrm{d}I$ vs I and magnetic field at $n = 1 \times 10^{12}$ cm^{-2}. The critical current oscillates according to a single-slit Fraunhofer interference pattern, shown in a white-dashed line.

2.2.4 Thermal evaporation of Aluminum

Having a variety of superconducting materials to create graphene JJs is very beneficial to explore different regimes of the superconducting proximity effect. Aluminum has a much smaller critical temperature ($T_c \sim 1.2$ K) and critical field ($H_{c2} \sim 10$ mT) than MoRe. This gives both a larger Ginzburg-Landau coherence length $\xi_{GL} = \sqrt{\Phi_0/2\pi H_{c2}} \sim 180$ nm, and a larger coherence length in the weak link $\xi_N = \hbar v_F/\Delta$, since the superconducting gap $\Delta = 1.764 k_B T_c$ is smaller. Using Al for graphene JJs thus makes the short regime more accessible than with MoRe [19]. This is at the expense however of not being able to explore high-field phenomena with superconducting leads, since H_{c2} is small.

Using a Leybold system in my second year of the PhD, in ICFO, we were able to thermally evaporate superconducting Al. The graphene JJs were successfully created by first evaporating a wetting layer of Ti, which serves to create an ohmic contact to the graphene layer [107, 163]. In this case, the contact was two-dimensional, by just etching the top hBN with an SF_6 recipe [164]. This exposes the graphene and subsequently the Ti/Al (7 nm/70 nm) film is evaporated with a 1 Å rate. In Fig. 2.30 we show an example of such JJs, along with a $\mathrm{d}V/\mathrm{d}I$ map featuring Fabry-Pérot oscillations, highlighting the quality of these devices.

When at LMU, we tried in the HV chamber to create such Ti/Al graphene JJs, but results where unsuccessful. Although Al was superconducting, the contact resistance to graphene was too high (~ 1 MΩ). As opposed to sputtering, the evaporation process is directional. One possible explanation for our bad contacts is then that the lack of a rotating stage for the sample, as we had in the Leybold system, does not allow to create a good contact in the two sides of the junction.

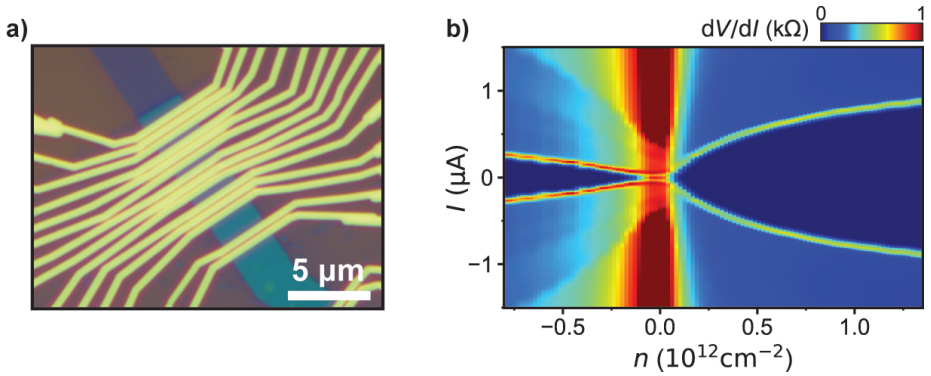

Fig. 2.30: Example of Ti/Al graphene JJs. a) Picture of several junctions fabricated on an encapsulated graphene device and contacted with Ti/Al. **b)** Differential resistance map of a ballistic Al-graphene JJ.

2.3 Low-temperature transport measurements

The experimental probe for measuring the Josephson effect that we use in this thesis is electronic transport at low temperatures. This is achieved by cooling down the samples in cryostats, such as a dilution fridge, as we will explain in the following. To measure the electronic properties of our devices, we use standard low frequency lock-in techniques, which we will cover later.

2.3.1 Cryogenics and electronic filtering

Low-temperature measurements play a crucial role in condensed matter physics, enabling the study of quantum phenomena such as superconductivity, quantum Hall effects, and electron transport in mesoscopic systems [165]. Lowering the temperature limits the thermal excitation energy k_BT (~ 25 meV for 300 K and ~ 8 µeV for 0.1 K), enabling us to study small energy scales down to the µeV range. This is of course also necessary to achieve the superconducting phase in our JJs below their T_c, as we showed in the previous section. Achieving cryogenic temperatures requires specialized refrigeration techniques, all of which rely on helium-based cooling mechanisms. Furthermore, to cool down the electrons it is not in generally sufficient to apply a low temperature bath, but electronic filtering is also required. This prevents any coupling to the environment such as radiation from higher temperatures, cosmic rays, high frequency signals, etc.

In this subsection, we describe the principles behind three cryogenic systems used in our experiments: a Variable Temperature Insert (VTI), an Adiabatic Demagnetization Refrigerator (ADR), and a Dilution Refrigerator (DR). We place particular emphasis on the dilution refrigerator, as it enables measurements at the lowest temperatures and was

the primary system used for the measurements presented in this thesis. We note that all these setups are also equipped with superconducting magnets capable of generating fields up to 8 T. These are oriented perpendicularly to the sample plane and enable us to have an extra tuning knob to explore the quantum phase diagram of our studied 2D materials.

All cryostats discussed here are dry cryostats, meaning they do not use liquid helium baths but instead rely on closed-cycle helium-4 (^{4}He) capable of cooling down to 4.2 K, which is the boiling temperature of this gas at atmospheric pressure. These setups consist of a so-called pulse tube compressor, which follows a thermodynamic cycle similar to a standard refrigerator, as shown in Fig. 2.31a.

First, a compressor moves its piston to compress the ^{4}He to pressures of ~ 10 mbar in a smaller space, thus increasing its temperature. This is connected to a regenerator, consisting of a porous material with low thermal conductivity, such as metal foam or cotton fiber. This component slowly cools down the gas across it, reaching ambient temperature when it reaches the pulse tube, but still at high pressure. This first side of the pulse tube is called the cold end. As the ambient temperature, high pressure gas travels to the other side of the pulse tube, it will compress the gas that is already there, causing it to heat up. Hence this side is called the hot end. Since the tube gas is under pressure, it will be forced to move into the restriction valve and the inertance tube. At some point, before the gas gets to the end of the tube and completely fills it, the piston from the compressor will be reversed. This causes an expansion of the gas inside the pulse tube, thus dropping its temperature in the cold end. The cold heat exchanger from where we can have cooling power is called the cold head, which is in thermal contact with the parts of the cryostat that we want to cool down. This process is a modification of the Stirling cycle, where thanks to the out-of-phase movement of the piston and the gas through the intertance tube, the cycle is not closed, so that by repeating the process we can then successively decrease the temperature in the cold end at the completion of every cycle [166].

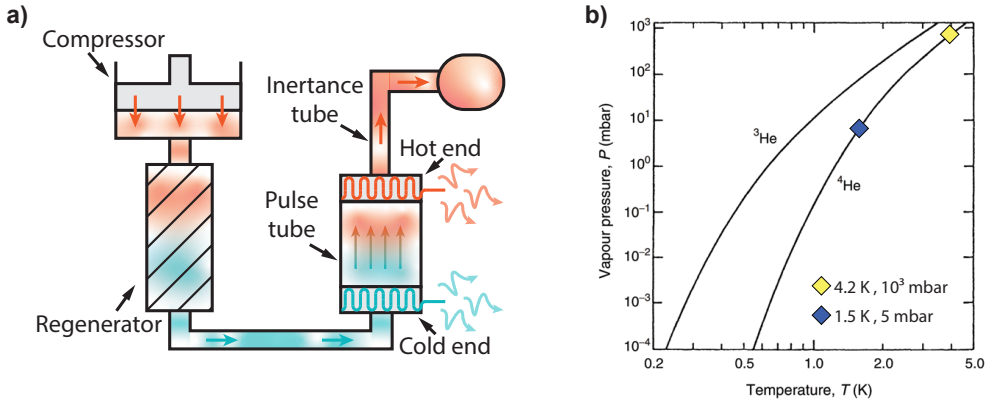

Fig. 2.31: Pulse tube cooling and superfluid ^{4}He. a) Working principles of a pulse tube cooling thermodynamic cycle. **b)** Vapor pressures of ^{4}He and ^{3}He. We indicate the typically achieved temperatures by pumping on the helium gas. Adapted from [166].

With this method we can achieve a base temperature of 4.2 K, where ^{4}He enters the superfluid phase and it can flow without dissipation. This phase is crucial for low-temperature physics, as it enables highly efficient thermal transport and can be further used in heat-exchange mechanisms within dilution refrigerators. To get down to lower temperatures, we can use different techniques, as explained next.

Variable Temperature Insert

The VTI allows to further cool down to 1.5 K by continuously pumping on the ^{4}He gas. The technique it uses is evaporative cooling, which is achieved by a controlled pumping of helium vapor to lower its pressure above the liquid helium bath. The VTI operation is based on the thermodynamic relationship between the vapor pressure and the temperature of liquid helium, as shown in Fig. 2.31b. At 4.2 K, ^{4}He is at its boiling point under atmospheric pressure; however, by pumping on the helium vapor down to ~ 5 mbar, the boiling temperature is reduced to ~ 1.5 K [166]. This phenomena is explained by the Clausius-Clapeyron relation:

$$\frac{dP}{dT} = \frac{L}{T \cdot \Delta V}, \tag{2.3}$$

where dP/dT describes the change in pressure with temperature, L is the latent heat of vaporization, and ΔV is the volume change [166].

In the case of this thesis, we have used an ICE Oxford VTI system. In order to isolate the coldest part (1.5 K) from the outside room temperature ambient, the VTI has two stages at different temperature (50 K and 4 K), which are further separated from each other by radiation shields. An advantage of this setup is that the sample is quickly introduced with a loading stick inside a chamber filled with He gas. This chamber is enclosed by a second one, through which helium is continuously circulated by pumping it with a needle valve. When the cold chamber reaches 4.2 K thanks to the cold head, we use the needle valve to regulate the pressure with which we further pump the ^{4}He, allowing us to reach 1.5 K (see Fig. 2.31b). Another advantage of this setup is that the temperature control can be rapidly changed by adjusting the helium flow rate and using heaters in the sample space.

Adiabatic Demagnetization Refrigerator

Another cryogenic principle is adiabatic demagnetization, based on the property that ordinary magnetic materials, such as paramagnetic salts, experience an entropy decrease when a magnetic field is applied due to the alignment of their atomic dipoles. This cooling is a powerful technique used to achieve sub-Kelvin temperatures by exploiting the magnetocaloric effect in paramagnetic materials [167].

In this process, a paramagnetic salt is first cooled to an initial temperature T_i using conventional cryogenic methods, such as a pulse tube ^{4}He crycooler, which allows to reach

4.2 K as explained before. Then the salt is placed in a strong external magnetic field H_i on the order of several tesla, which forces the magnetic atomic dipoles of the material to align. This alignment reduces the magnetic entropy of the salt as the degrees of freedom associated with the random orientation of the dipoles are diminished. Once the material is fully magnetized and the system has equilibrated at T_i, the external magnetic field is gradually reduced adiabatically to a lower value H_f. This causes the magnetic dipoles to randomize, increasing their entropy. Since the process is adiabatic, the total entropy of the system is conserved; therefore, the increase in magnetic entropy is counterbalanced by a reduction in the lattice entropy, which results in a lowering of the overall temperature to a final value T_f [168].

The thermodynamic behavior of this process can be expressed through the relation:

$$\left(\frac{\partial T}{\partial H}\right)_S = -\frac{T}{C}\left(\frac{\partial M}{\partial T}\right)_H, \tag{2.4}$$

where C is the heat capacity of the system, M is the magnetization and the subscript S indicates that the derivative is taken at constant entropy. This equation indeed shows how a reduction in the magnetic field H under adiabatic conditions leads to a decrease in temperature T. From there we can also understand that materials which exhibit a large change in magnetization with temperature (i.e., a large $\partial M/\partial T$) are especially effective for adiabatic demagnetization because they provide a more pronounced cooling effect [168].

An ADR system is particularly interesting as it avoids the use of the expensive ^{3}He/^{4}He mixture. In our lab, we have worked with a Kiutra system, which achieves continuous cooling at 150–300 mK. The setup consists of a series of heat switches and two interconnected ADR units that work together to extract heat from the sample stage and pump it into the 4.2 K thermal bath.

Dilution fridge

The DR or dilution fridge is a powerful cryogenic system, capable of continuous cooling to mK temperatures. Its exceptionally high cooling power is achieved by using a mixture of ^{3}He and ^{4}He and exploiting its phase separation at sub-Kelvin temperatures. ^{3}He is a very expensive isotope of helium given that it is generally found as a byproduct of nuclear reactions [166, 168].

Fig. 2.32a shows the phase diagram of the ^{3}He/^{4}He mixture, where it can become a normal fluid, a superfluid, or a liquid with the two phases (isotopes) separated. The latter happens below the tricritical point at 0.87 K, where the phase rich in ^{3}He is called the concentrated phase ($\sim$100%) and the one dissolved in ^{4}He is called diluted phase (up to $\sim 6\%$). This separation happens in space too, with the rich phase sitting on top of the dilute phase due to its lower density.

Because the specific heat of the two phases are different, the dilution process occurs

when ^{3}He atoms are transferred from the concentrated phase into the dilute phase, absorbing heat. The enthalpy difference ΔH between the two phases then results into a cooling process according to:

$$Q = \Delta H \cdot \dot{n}_3 \approx 84T^2 \cdot \dot{n}_3, \tag{2.5}$$

where Q is the heat extracted and $\dot{n}$ is the ^{3}He flow rate [166]. This provides continuous refrigeration as long as ^{3}He is circulated (see Fig. 2.32b). The dilution fridge in our lab is a Bluefors SD system with a circulation rate of $\dot{n}_3 \sim 0.5$ mmol/s and a base temperature of $T \sim$35 mK, with a resulting cooling power of $Q \sim 50$ µW. Fig. 2.32c shows a picture of our setup where we point out its main parts.

We now explain how a dilution fridge is able to make the phase separation and take

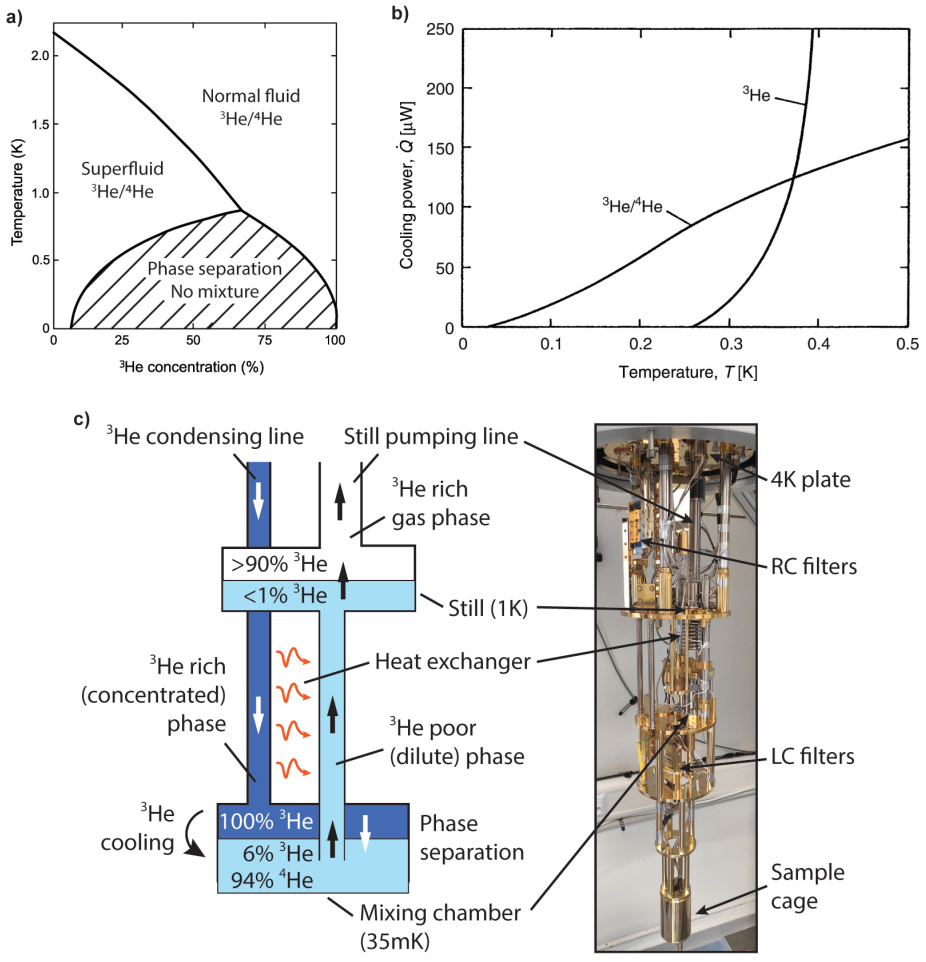

Fig. 2.32: ^{3}He/^{4}He mixture cooling and dilution refrigerator. a) Phase diagram of the ^{3}He/^{4}He mixture depending on the ^{3}He concentration and temperature. **b)** Cooling power of the mixture and ^{3}He alone, with a ^{3}He flow rate of 5 L/s. Adapted from [166]. **c)** Working principles of the mixture cooling in a dilution refrigerator, along with a picture of our Bluefors SD system.

advantage of its cooling power to achieve mK temperatures. As a guide, we use the sketch shown in Fig. 2.32c.

Once a temperature of 4.2 K is reached with a ^{4}He pulse tube cryocooler, the ^{3}He/^{4}He mixture is introduced into the system through what is called the condensing line. Before reaching there, with a small compressor, the pressure of the mixture is raised to $\sim$2 bar. Then, the heat exchangers in the incoming condensing line pre-cool the pressurized mixture to low enough temperature for it to partially condense.

After all the mixture is condensed, it will be enough to fill the mixing chamber, the heat exchangers and part of the still. By now pumping on the still, evaporative cooling occurs, eventually dropping the temperature of the mixture below 0.87 K and incurring in a phase separation (Fig. 2.32a). Because of gravity, the heavier dilute phase will get to the bottom of the mixing chamber, eventually settling as shown in Fig. 2.32c.

Finally, the ^{3}He pumped away from the still is returned into the system through the condensing line. This happens thanks to ^{3}He having a lower vapor pressure than ^{4}He (see Fig. 2.31b). As the ^{3}He travels through the condensing line, it gets precool thanks to the heat exchanger with the still (see Fig. 2.32c). Once it reaches the mixing chamber, it is forced to pass through the phase boundary, resulting in the cooling process explained before. The cooling power will then depend on the amount of ^{3}He traversing the phase boundary, i.e. the flow rate, as captured by Eq. (2.5).

Electron temperature and electronic filtering

One final important aspect in measuring electronic transport properties at ultra-low temperatures is ensuring that the electrons in the sample are also cooled to the base temperature of the refrigerator. Since unwanted high-frequency noise in electrical circuits heats up electrons, without proper care, the temperature recorded during measurements would reflect the elevated temperature of the hot electrons rather than the actual fridge temperature.

To achieve proper electron cooling, first, the signal lines are thermally anchored at various stages of the cryostat (e.g. at 50 K, 4 K and 1 K) to progressively reduce their temperature and second, high-frequency filtering. Since the measurement signals we typically use are at very low frequencies (tens of Hz), applying filters that attenuate signals at higher frequencies effectively cools down the electrons without compromising the desired low-frequency information. In these systems, the electronic temperature is related to frequency ν via the relation $h\nu = k_B T$.

The required attenuation $A(\nu)$ to shield the cold electron temperature T_e from a hotter reservoir T_h can be estimated by the expression:

$$A(\nu) = \frac{e^{h\nu/k_B T_h} - 1}{e^{h\nu/k_B T_e} - 1}. \tag{2.6}$$

Thus, if we want to achieve an electron temperature of 35 mK (mixing chamber) and shield it from a radiation at $T_h = 1$ K (still plate), we need an attenuation of $A(\nu) \sim -30$ dB at above a cutoff frequency $\nu \sim 5$ GHz [169].

In our dilution fridge, instead of setting up one single filter, we include a combination of low-pass RC (65 MHz) and LC (225 MHz) filters, commercially available from QDevil, at the 1 K still plate and at the 35 mK mixing chamber, respectively. On top of that, the sample is electromagnetically shielded by conductive enclosures, preventing environmental noise from coupling into the measurement circuit (see Fig. 2.32c). Nevertheless, achieving an electron temperature equal to the bath temperature is very challenging, as other sources of electronic noise such as instruments, ground loop currents and mechanical vibrations can heat up the electrons. Care has to be taken into the setup buildup and regular checks on the instruments for achieving good experimental conditions.

2.3.2 Low-frequency transport measurements

Lock-in technique

Lock-in amplifiers are electronic instruments widely used in experimental physics due to their ability to extract weak AC signals buried in noise. This is particularly essential when measuring electrical transport properties of low-dimensional materials at low temperatures, where signals are often on the nanovolt or picoampere scale. The key idea is to modulate the signal of interest at a known reference frequency and then selectively detect only that frequency component, greatly enhancing the signal-to-noise ratio.

The process, called demodulation or phase-sensitive detection, works as follows. First, an AC signal at a specific frequency f (generally low, e.g. 10 Hz) is applied to our device (this modulation can be generated by the lock-in amplifier itself). The response signal measured by the lock-in contains both the desired response and a background of broadband noise, including thermal, environmental, and electronic noise. The instrument simultaneously generates a reference signal at the same frequency f as the excitation, and then it multiplies it by the measured signal. As a result, only the components of the measured signal that share the same frequency and phase as the reference will yield a nonzero average when integrated over time [170].

The lock-in provides mainly two outputs: the in-phase (X) and quadrature (Y) components, corresponding to the cosine and sine projections of the measured signal relative to the reference. It also provides the signal's amplitude R and phase θ, given by:

$$R = \sqrt{X^2 + Y^2} \quad , \quad \theta = \arctan(Y/X). \tag{2.7}$$

The ability to measure phase shifts θ with respect to the reference signal also enables lock-in amplifiers to distinguish between different conduction mechanisms, such as purely resistive ohmic transport versus capacitive displacement currents.

Since most forms of noise are random and spread over a broad frequency range, a key advantage of lock-in detection is its ability to reject broadband noise and isolate the signal of interest, thereby achieving a very high signal-to-noise ratio. The electrical noise in a system can come from thermal Johnson-Nyquist noise, $1/f$ noise, from power lines (50/60 Hz), RF sources, mechanical vibrations, etc. Since broadband noise extends over a wide frequency range, lock-in amplifiers improve signal detection by filtering out all frequency components except for the reference frequency. Given a noise power spectral density $S_V(f)$, the noise detected within a narrow bandwidth Δf is:

$$V_{\text{noise}} = \sqrt{S_V(f)\Delta f}. \tag{2.8}$$

Thus, by setting a small detection bandwidth, the lock-in amplifier significantly reduces the contribution of random noise, enhancing the signal-to-noise ratio [170].

Circuit schemes for transport in Josephson junctions

As explained above, to measure the electronic transport of our samples under AC excitations, we use a lock-in to both generate a current bias I at a certain frequency and measure the resulting voltage drop V. Another lock-in is generally used for measuring the draining AC current I after it passes through the device, so that the resistance can be estimated by Ohm's law $R = V/I$. This scheme can be used then to measure the resistance across the sample as a function of temperature, magnetic field and gate voltage; in a Hall-bar device or a JJ.

To focus more on the measurements of Josephson junctions, in Fig. 2.33 we show two circuits used for measuring current-voltage characteristics and differential resistance curves. In order to do these measurements in a JJ, we use four contacts, where two ends of the superconducting leads are used for biasing (source) and collecting (drain) the current. The other two ends are used for measuring the voltage drop across the junction. This is called a semi-4-probe scheme, because the contact resistance is still included in the measured voltage. In both circuits, several DC sourcemeters (Keysight Keithley) are needed, to bias a DC current and to apply gate voltage V_g to the Si substrate or to a local graphite gate.

For the IV circuit (Fig. 2.33a), we do a pure DC measurement. For this, we use a DC source (Keithley) to generate a DC voltage V_{DC}, which is transformed into the source current $I_{\text{DC}} = V_{\text{DC}}/R_1$ by simply connecting a known resistance R_1 in series. The draining current is set to ground and the voltage drop across the sample is collected with a voltage amplifier. Apart from multiplying the signal, this instrument allows us to filter different ranges of frequencies. Since this is a DC measurement, we filter all frequencies above 1 Hz at 12 dB. The output is finally connected to a multimeter where we read the DC voltage V. An example of the obtained data with this scheme is also shown in the figure, where the superconducting transition of the JJ is clearly visible.

For measuring the $\mathrm{d}V/\mathrm{d}I$ of a device, we need to make a derivative of the previous

measurement. This is naturally achieved in electronic circuits by adding a small AC excitation I_{AC} to the DC bias I_{DC} and measuring the AC voltage. Indeed, if we take $I_{\mathrm{DC}} = I_0$ and $I_{\mathrm{AC}} = \mathrm{d}I\sin(\omega t)$, with $\mathrm{d}I \ll I_0$, the total resulting voltage will be:

$$V\Big(I(t)\Big) = V\Big(I_0 + \delta I\sin(\omega t)\Big) \approx V(I_0) + \left.\frac{\mathrm{d}V}{\mathrm{d}I}\right|_{I_0} \mathrm{d}I\sin(\omega t) + \mathcal{O}\left((\mathrm{d}I)^2\right). \tag{2.9}$$

Here $V(I_0)$ is the DC voltage across the device, while the term

$$\mathrm{d}V = \left.\frac{\mathrm{d}V}{\mathrm{d}I}\right|_{I_0} \mathrm{d}I\sin(\omega t) \tag{2.10}$$

represents the small AC voltage component that results from the applied AC current. Consequently, by measuring this AC voltage amplitude using a lock-in amplifier, which selectively detects signals at the modulation frequency ω, we can determine the differential resistance at the bias point I_0 as:

$$\left.\frac{\mathrm{d}V}{\mathrm{d}I}\right|_{I_0} = \frac{\mathrm{d}V}{\mathrm{d}I}. \tag{2.11}$$

In Fig. 2.33b we show how this combination of DC ($I_{\mathrm{DC}} = V_{\mathrm{DC}}/R_1$) and AC ($I_{\mathrm{AC}} = V_{\mathrm{AC}}/R_2$) source signals is done. The collected draining current $\mathrm{d}I$ is first converted to voltage and then measured in a lock-in. The voltage drop $\mathrm{d}V$ is first passed through an amplifier and finally measured in a lock-in. Both this amplifier and the current-voltage converter allow us to multiply our signal and filter it. We typically send an AC signal of 17.777 Hz, so that by choosing to use a band-pass filter below 10 Hz and above 30 Hz at 12 dB, we can take out the DC signal from the collected draining current. The settings

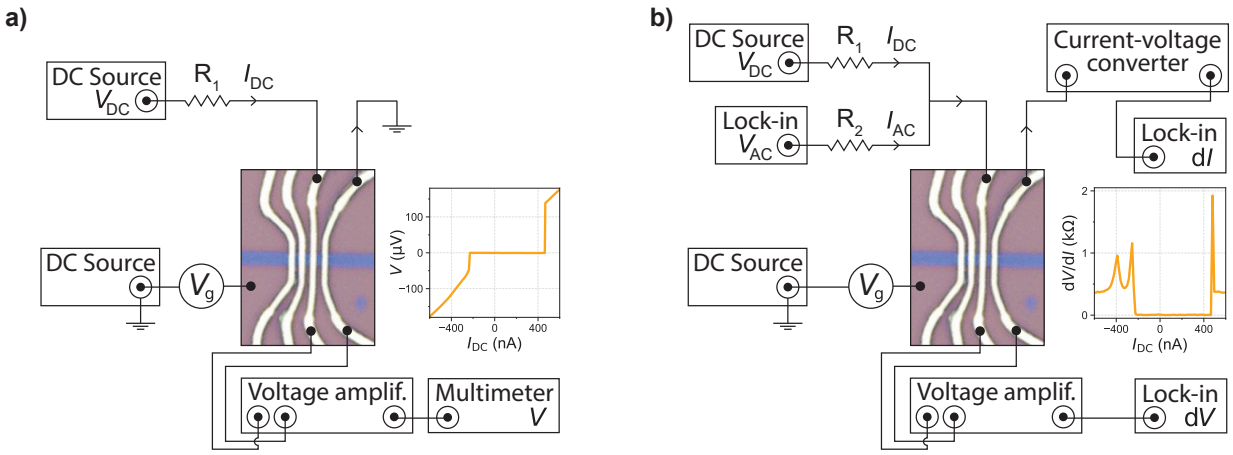

Fig. 2.33: Current-voltage and differential resistance characteristics measurements. a) Circuit of an IV characteristic measurement. **b)** Circuit of a differential resistance measurement. In both sketches, the shield of the BNC ports are all connected to the ground, although we only show it in the DC Source for the gate for illustrative purposes.

we generally use in the lock-in (Standford SR830) are a time constant of 300 ms with a 12 dB filter over a time window of 0.9 s. With this, the differential resistance is obtained by simply dividing both quantities dV and dI. An example of the obtained data with this scheme is also shown in the figure, where the superconducting transition of the JJ is clearly visible

We note that in between the sample at cryogenic temperatures and the sketched lines that go to the instruments, a series of RC and LC filters are placed inside the DC lines of the dilution fridge.

The advantage of measuring the IV curve is that, because it is a DC measurement, we do not need to put any filters over a time window as in AC, so that the acquirement of data is very fast (typically 0.1 s per point). The advantage of the dV/dI measurement on the other hand is that we avoid the $1/f$ noise that is inherently picked up in DC measurements. Furthermore, when compared to the IV curve measured in the JJ, its precise derivative can give us more information about extra resonances due to Andreev reflections, as shown at negative current values in Fig. 2.33b. If we take the numerical derivative from Fig. 2.33a, we barely see this extra peak and the data overall comes out more noisy. The asymmetry of the data in current is due to a hysteresis in the JJ, because of overheating or underdamped dynamics. The sweeping goes from negative to positive values, so that the first transition corresponds to the retrapping current I_r and the second transition to the switching or critical current I_c.

Chapter 3

High-field superconductivity in a ballistic moiré superlattice Josephson junction

The work presented in this chapter led to the following publication:

[P1] **A. Díez-Carlón**, et al. "High-field superconductivity in a ballistic moiré superlattice Josephson junction". *In preparation* (2025).
Contributions: Sample fabrication, measurements, data analysis, discussion and paper writing.

In this chapter, we show for the first time a ballistic Josephson effect in a graphene-based moiré superlattice Josephson junction, namely the heteromoiré formed by aligning graphene and hBN, coupled with MoRe superconducting leads. The so-far unexplored ballistic regime in this system allows us to study the Fabry-Pérot oscillations at hole doping in Section 3.1, which depend on the Fermi surface of the moiré bands. For electron doping and once the superlattice density is reached, in Section 3.2 we find that the superconducting proximity effect holds up to fields of as much as 7 T; much greater than those previously reported in graphene. We attribute this result to a cyclotron orbit breakdown and open orbits at the van Hove singularities found at these fillings of the moiré bands.

The work of this chapter, still in progress, represents the conclusion of a year-long collaboration with my colleague Daniil Ivanov [171], who helped with the device fabrication.

3.1 Ballistic moiré-graphene Josephson junctions

The study of the Josephson effect in the ballistic regime offers a sensitive probe of many physical phenomena in a 2DEG weak link, from the interference of Fabry-Pérot oscillations [20, 22, 104], the switching dynamics of the critical current I_c and its dependence on temperature [104], as well as the study of the proximity effect at high magnetic fields [22, 172] and in the Quantum Hall regime [23, 24]. Despite an extensive study of these effects, all prior work has focused on monolayer graphene.

A natural question is how the ballistic Josephson effect evolves when the weak-link band structure is modified by a moiré potential. Experimental studies of the superconducting proximity effect in a moiré weak link remain scarce to this date [173, 174] [P2], and none have yet accessed the ballistic regime. Here we address this challenge by engineering, for the first time, a ballistic Josephson junction whose weak link is a graphene/hBN moiré superlattice coupled to MoRe superconducting leads. While the main Dirac cone of graphene/hBN and its Fermi velocity remain barely unchanged [30, 36–38], thus giving potential access to ballistic transport in a Josephson junction architecture [20, 22, 104], the formation of moiré minibands at higher densities reachable by electrostatic gating make of this moiré material a very suitable platform where to test the ballistic Josephson effect in other band structures than that of monolayer graphene.

Our samples consist of a van der Waals heterostructure in which a monolayer graphene is encapsulated between two hBN dielectrics; with one of them closely aligned to the crystallographic edges of the graphene (see Fig. 3.1a). The stacks are patterned into a rectangular mesa of width $W \sim 1.5$ µm and then coupled with sputtered MoRe superconducting leads, forming one-dimensional edge contacts. The resulting device is a Josephson junction of length L, where the carrier density n of the graphene/hBN superlattice is tuned by applying a gate voltage to the doped Si substrate. Our transport measurements follow a two-probe scheme, where the voltage V across the junction is recorded as a current bias I is applied through the superconducting electrodes.

We focus on device GH1 with length $L \sim 200$ nm (see Table 3.1). The alignment of graphene with hBN is evidenced in Fig. 3.1c by the observation in the normal state resistance R_N of two satellite Dirac points (sDP) at carrier densities corresponding to a fully filled electron/hole moiré band $\pm n_s$ (see black arrows in the corresponding band structure of Fig. 3.1b). This measurement is done at 10 K to avoid any superconducting proximity effects from the MoRe, which has a critical temperature $T_c \sim 9$ K. The effect of the moiré superlattice is further confirmed by the observation of the Hofstadter butterfly in the Quantum Hall regime (see inset of Fig. 3.1c) [36, 37], from where we extract a twist-angle $\theta = 0.21° \pm 0.01°$.

By now measuring the differential resistance $\mathrm{d}V/\mathrm{d}I$ as a function of a d.c. current bias I below the MoRe critical temperature, we confirm the formation of a JJ. Fig. 3.1d shows this, where the nonlinear $\mathrm{d}V/\mathrm{d}I$ curves evidence superconducting states (dark-blue

regions in the colormap) below a critical current I_c that changes with density. Importantly, Fig. 3.1d demonstrates the presence of the Josephson effect in the graphene/hBN junction throughout its whole band structure, with the exception of vanishing critical currents at the CNP ($n/n_s = 0$) and in the hole satellite Dirac point (hDP, $n/n_s = -1$). This is due to the presence of small gaps in the bands of graphene/hBN at those fillings, as shown in Fig. 3.1b. The electron satellite Dirac point (eDP) at $n/n_s = 1$ has a finite I_c instead, since two sets of bands cross at that point. Overall, the smaller I_c for hole doping compared to the electron side is due to the formation of a n-p-n junction, as the MoRe contacts n-dope the graphene in their vicinity and thus raise the R_N at $n/n_s < 0$ (see Fig. 3.1c). The $\mathrm{d}V/\mathrm{d}I$ map measurements are done at 2 K to prevent premature switching of the I_c at base temperature, which is proper of underdamped junctions or due to overheating effects [93, 109], and can complicate the analysis of the I_c with density [104].

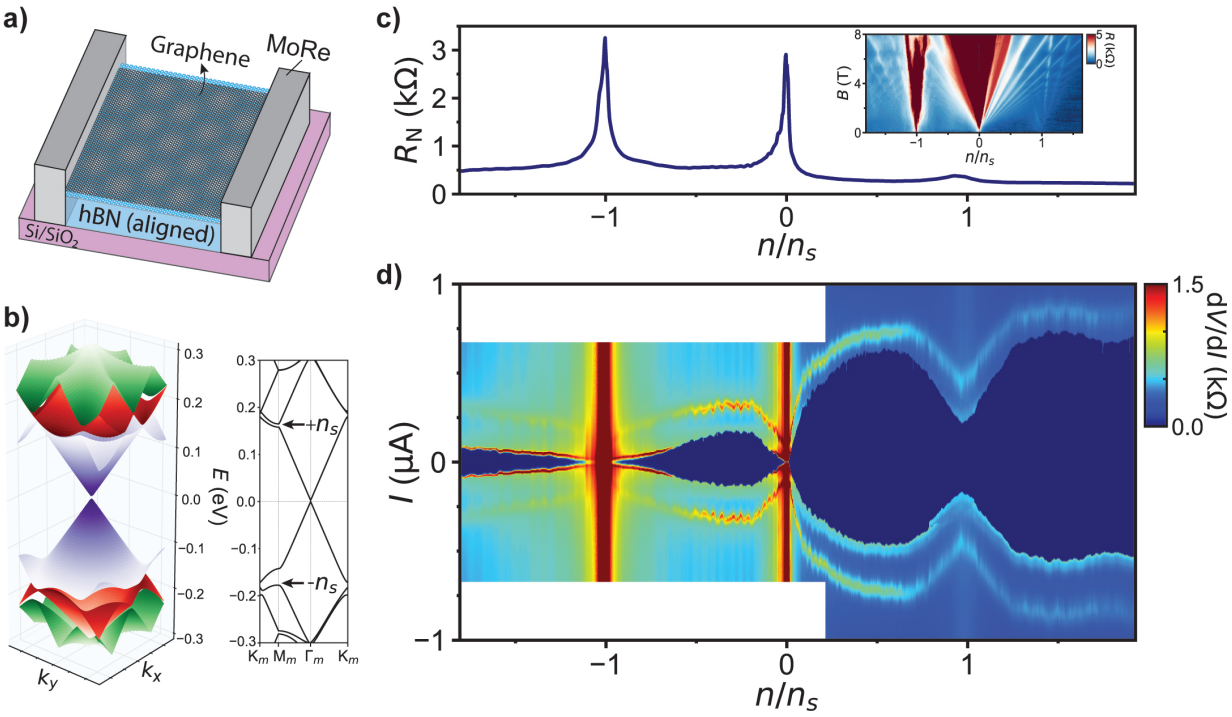

Fig. 3.1: Josephson junction with a graphene/hBN moiré superlattice weak link. **a)** Device schematic, where an encapsulated hBN-aligned-graphene is coupled to MoRe superconducting leads by one-dimensional edge contacts. **b)** Calculated band structure of graphene/hBN for $\theta = 0.2°$. **c)** Normal state resistance R_N measured at 10 K, as a function of the carrier density n normalized by the superlattice density n_s. Inset shows a Landau Fan measurement at 35 mK, where another set of Landau levels emerge at $n/n_s = \pm 1$ and their crossings form a Hofstadter butterfly fractal behavior. **d)** Map of differential resistance $\mathrm{d}V/\mathrm{d}I$ vs d.c. current bias I and n/n_s, measured at 2 K and within the same range as **c**. The dark blue regions indicate superconducting proximitized states, where the transition at positive I corresponds to the critical current I_c.

3.1.1 Fabry-Pérot oscillations

In high-quality graphene devices, ballistic transport is essential for observing quantum interference effects such as Fabry-Pérot (FP) oscillations. Analogous to the interference of light in optical Fabry-Pérot interferometers, these oscillations arise when electrons reflect between two partially reflecting barriers, such as n-p–n junctions, forming an electronic cavity [175, 176]. Within this cavity of length L_c, standing wave patterns develop due to the constructive and destructive interference of all outgoing electron wavefunctions, leading to oscillations in the device's resistance as a function of carrier density or gate voltage [176, 177]. The resonant condition for these standing waves is thus:

$$N = \frac{2L_c}{\lambda_F}, \tag{3.1}$$

where $N \in \mathbb{Z}$ is the number of modes in the cavity and $\lambda_F = 2\pi/k_F$ the Fermi wavelength. These resonances have also been measured in graphene Josephson junctions, where the cavity occurs because a n-p-n junction is formed due to the n-doping of graphene from the superconducting contact such as MoRe [20].

In the case of graphene/hBN moiré superlattices, FP oscillations have been studied previously in gate-defined p-n-p junctions [178] and in a Hall-bar geometry with the transverse electron focusing effect caused by the skipping orbits at low magnetic fields [179]. Here though, we provide evidence for phase-coherent Fabry-Pérot interference in the supercurrent, which has not been observed before in this system. Fig. 3.2a-b shows two zoom-in scans of Fig. 3.1d, close to the hole superlattice density $n/n_s = -1$ and to the CNP, respectively. The oscillations in the I_c can be clearly seen in the contour of the dark-blue regions with zero resistance, and also in the R_N with the change of colors at $I > I_c$.

We are interested into evaluating the dependence of the FP oscillations with carrier density n, which we can tune in our experiment. Since $n = \int_0^{E_F} dE\ \mathrm{DOS}(E)$ by definition, with $\mathrm{DOS}(E_F)$ the density of states per unit area and energy at the Fermi level, we need to first relate λ_F or k_F with E_F and the DOS. For a 2DEG, $\mathrm{DOS}(E) = \frac{gk}{2\pi}\frac{dk}{dE}$, where g is the total degeneracy of the 2DEG states. In the case of graphene, considering its valley and spin degeneracies $g = g_v g_s = 4$, as well as its linear dispersion $E = \hbar v_F k_F$, yields $\mathrm{DOS}(E) = \frac{2E}{\pi\hbar^2 v_F^2}$ and a carrier density $n = k_F^2/\pi$, from where we find:

$$k_F = \sqrt{\pi n}. \tag{3.2}$$

We note that in the derivation of Eq. (3.2), the size of the Fermi velocity v_F is unimportant. Thus, any linear dispersion will yield the same result as in Eq. (3.2). Combining this with Eq. (3.1) finally yields:

$$N = L_c\sqrt{n/\pi} \tag{3.3}$$

By now extracting consecutive minima or maxima on the I_c or R_N, N_i and N_{i+1}, as shown in Fig. 3.2a-b, we can test the prediction of Eq. (3.3) for a linear Dirac dispersion.

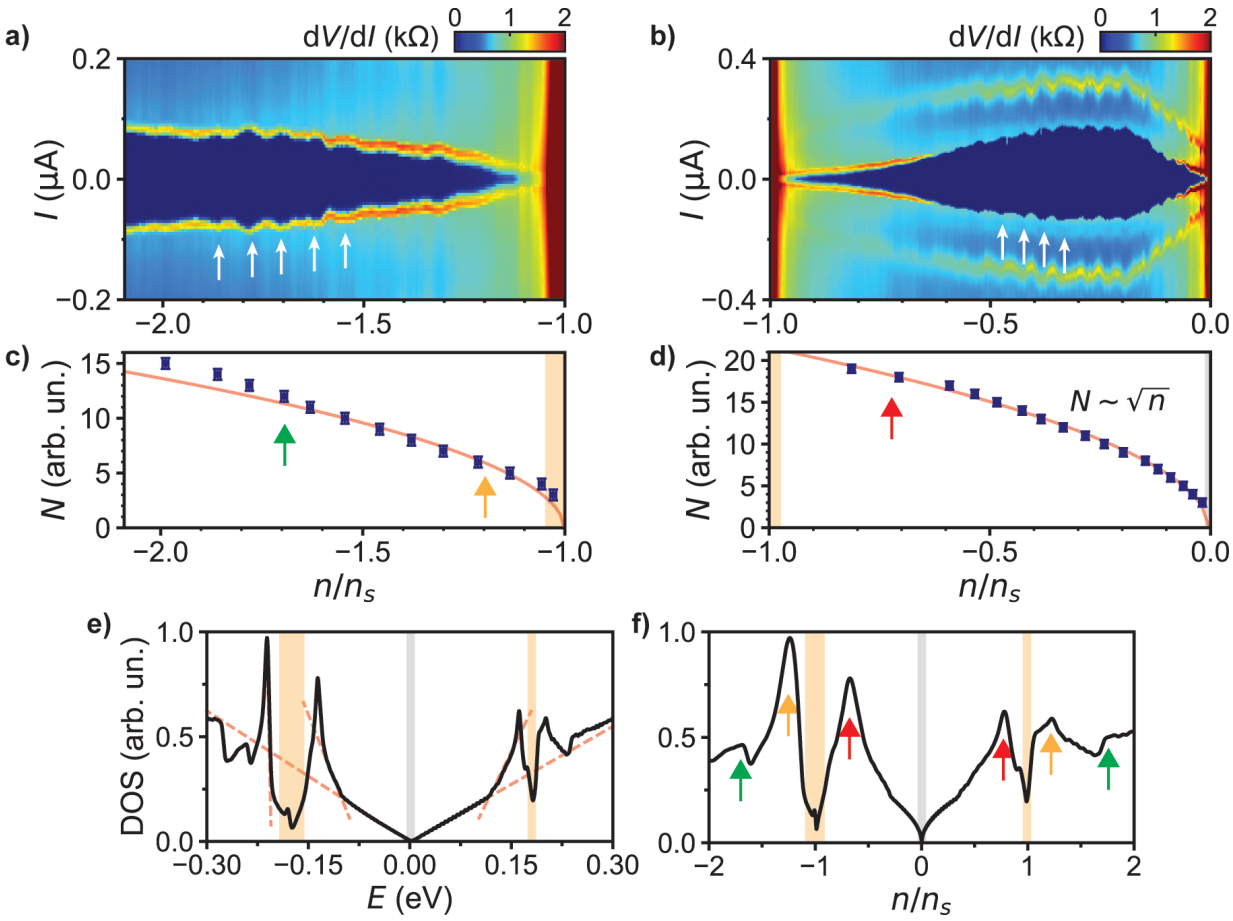

Fig. 3.2: Fabry-Pérot oscillations over several moiré bands. a-b) Map of differential resistance $\mathrm{d}V/\mathrm{d}I$ vs d.c. current bias I for two different ranges of the normalized carrier density n/n_s, measured at 2 K. Some local maxima in the I_c are indicated with white arrows. **c-d)** Extracted consecutive maxima in the I_c or minima in the R_N from **a-b**. While for the Dirac cone band at $-1 < n/n_s < 0$ in **d** we find $N \sim \sqrt{n}$ (red solid line), that is not the case for the bands at $n/n_s < -1$ in **c**. The errorbars in the y-axis account for a potential missable extrema in the oscillating I_c or R_N. **e-f)** Density of states vs energy E and n/n_s, respectively. The linear dependence of the DOS with E (equivalent to a square root dependence with n) is marked by red-dashed lines. In the case of the Dirac cone band, this is well followed, while the vHs, indicated by colored arrows near $n/n_s \approx \pm 1$ and ± 2, leave nonlinear terms that could explain the deviation of the data in **c** from $\sqrt{n}$.

For the Dirac cone band at $-1 < n/n_s < 0$, as we can see in Fig. 3.2d, the expression with the square root dependence fits extremely well, which in the least-squares method gives a coefficient $R^2 = 0.997$. However, for densities $n/n_s < -1$ in Fig. 3.2c, we observe that the square root dependence of Eq. (3.3) no longer predicts the positions of all the oscillations in n/n_s, with $R^2 = 0.975$. The fit rather overestimates them at $n/n_s \lesssim -1.5$ and underestimates them very close to $n/n_s \sim -1$. This result indicates that the energy

dispersion at these fillings of the moiré minibands cannot be fully linear, which is consistent with certain band structure models [32, 33, 179].

An example is the band structure shown in Fig. 3.1b, from where we calculate the density of states and show it in Fig. 3.2e-f. This is done for a graphene/hBN moiré superlattice with $\theta = 0.2°$ by following the phenomenological model of Ref. [32], which was explained in detail in Subsection 1.2.1. The ranges where the DOS is linear in Fig. 3.2e are marked by red dashed lines, which are mainly in the Dirac cone band. At fillings below the hDP, the band structure consists of two nonisotropic bands, with the presence of three vHs marked by three vertical arrows. All this makes the DOS rather non-linear in energy. Since these features are very model-dependent [32, 33], here we have chosen the parameters that best match to our experimental data, in terms of the gaps at $\pm n_s$, and the presence of the vHs giving a potential explanation of why the FPs on Fig. 3.2c do not fit the square root dependence for a linear band structure, as it was reported in Ref. [178]. We also note that such model has been used to reproduce other transport experiments [38, 173, 179–183]. We will come back to these vHs later in our inspection of high-field superconductivity.

From the slope of the fits in Fig. 3.2c-d, one could in principle also estimate L_c. However, finding the exact number of modes N is a difficult task, and requires to study the extra phase that these resonances acquire when applying low-magnetic fields [20]. To estimate L_c, we can nevertheless measure the distance between each FP oscillations, which in the case of Eq. (3.3) gives:

$$L_c = \frac{\pi}{\sqrt{n_{i+1}} - \sqrt{n_i}}. \tag{3.4}$$

For the Dirac cone band at $-1 < n/n_s < 0$, in Fig. 3.2d we find values of $L_c = 250 \pm 45\,\text{nm}$, consistent with the length of our device $L \sim 200 \pm 10\,\text{nm}$. We also observe that the length of the cavity decreases down to $L_c \sim 150\,\text{nm}$ as the density decreases towards the CNP. This has been observed previously in these n-p-n junctions [22], and has been attributed to the reflectiveness and sharpness of the p-n interface, which decreases as the density gets closer to the n-type doping of the MoRe contacts, thereby decreasing L_c. In the case of the other moiré minibands at $n/n_s < -1$ in Fig. 3.2c, the use of Eq. (3.3) is less justified, since the band structure is not linear as we discussed before. Doing so gives $L_c = 180 \pm 54\,\text{nm}$, decreasing down to $L_c \sim 100\,\text{nm}$ at the hDP. When $n/n_s < -1.7$, that is, when the vHs is reached, $L_c \sim 300\,\text{nm}$, which indeed gives unphysical results [178].

The oscillations in Fig. 3.2 having their origin in a Fabry-Pérot interference can be unequivocally proven when measuring the differential resistance in the normal state as a function of a d.c. voltage bias V_b. As the FP resonances modify the transmission of carriers, the mesoscopic conductance G_0 is altered according to $G(E_F) = G_0 + \delta G \sin(2\pi E/E_0)$. This modulation of the electronic transport is a periodic function of E_F/E_0, where $E_0 = hv_F/2L_c$ is the energy scale of the resonant standing waves, since $E_F = hv_F/\lambda_F$ for graphene [22, 176, 177]. The total current flowing through the cavity is then $I = \int_{E_F - eV_b/2}^{E_F + eV_b/2} dE\ G(E) = G_0 V_b + \delta G \frac{E_0}{\pi e} \sin(\frac{2\pi E_F}{E_0}) \sin(\frac{\pi e V_b}{E_0})$. By calculating the differential conductance dI/dV_b, we

finally arrive at a general expression for the differential resistance $R = \mathrm{d}V/\mathrm{d}I$:

$$R(E_F, V_b) = R_0 + \delta R \sin\left(\frac{2\pi E_F}{E_0}\right)\cos\left(\frac{\pi e V_b}{E_0}\right). \tag{3.5}$$

In Fig. 3.3a-b we show the measurements of the numerical derivative dR/dn of the differential resistance R in Eq. (3.5) with density n, and as a function of V_b, since E_F is related to n. These are the same two different ranges of density indicated by the white arrows in Fig. 3.2a-b. In the colormaps, as well as in the linecuts in Fig. 3.3c-d, the periodicity both in n and V_b is very clear, demonstrating that the oscillations observed in Fig. 3.2 are indeed FP resonances.

To analyze these results, we rewrite the expression Eq. (3.5) in terms of n for graphene, where $E_F = \hbar v_F k_F = \hbar v_F \sqrt{\pi n}$, giving:

$$R(n, V_b) = R_0 + \delta R \sin\left(2L_c\sqrt{\pi n}\right)\cos\left(\frac{2\pi e L_c}{h v_F} V_b\right), \tag{3.6}$$

which is a function of two independent periodic n and V_b terms. The condition in the first periodic function is the same as (3.4). For the second, another condition is given for the

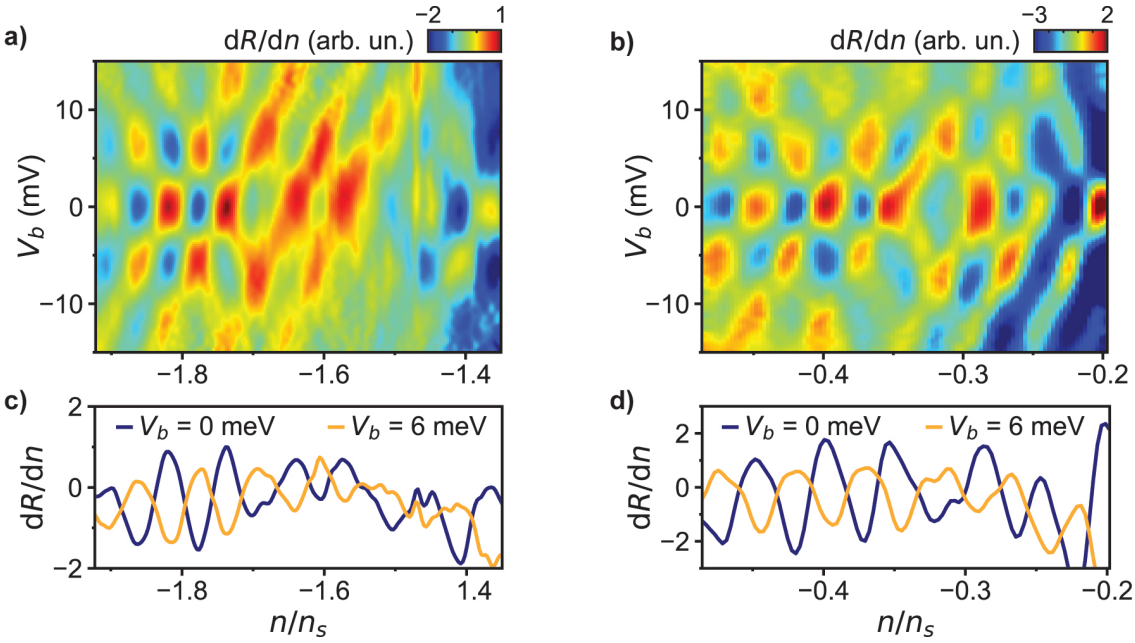

Fig. 3.3: Fabry-Pérot oscillations in the normal state. a-b) Map of change in the differential resistance with carrier density, dR/dn, vs d.c. voltage bias V_b and normalized carrier density n/n_s. Panel **a** shows the measured FP oscillations at the moiré minibands for $n/n_s < -1$, while their behavior at the Dirac cone band around the CNP can be seen in **b**. The measurements are performed at 10 K. **c-d)** Linecut of dR/dn at two different values of V_b, where the oscillations have opposite phases.

length of the cavity:

$$L_c = \frac{hv_F}{2e(V_{b_{i+1}} - V_{b_i})} \tag{3.7}$$

This expression allows us to estimate the Fermi velocity of the bands, provided the dispersion is linear and if we know the length of the cavity, which we have estimated previously from Eq. (3.4). We note that the decreasing value of L_c as we approach the CNP and hDP can be visualized by the elongtaion of the checkerboard pattern in Fig. 3.3c-d along the V_b axis. For the Dirac cone band at $-1 < n/n_s$, the corresponding Fermi velocity gives $v_F = 0.7 \pm 0.1\,\mathrm{m/s}$, whereas for the moiré bands at $n/n_s < -1$, $v_F = 0.5 \pm 0.1\,\mathrm{m/s}$. These values are consistent with the renormalized Fermi velocity of the satellite Dirac points along one direction of the mBZ, although we note that the nonlinearities in the moiré bands can become important, as we have shown in Fig. 3.2e-f, so that the use of Eq. (3.7) is less justified in this analysis. Nevertheless, by measuring the dependence of the critical current with temperature, we show an alternative method to estimate the v_F of the bands, as we explain next.

3.1.2 Length dependence of the long-ballistic regime

The temperature dependence of I_c is also consistent with a ballistic, long regime, as we show next. For long Josephson junctions, I_c is governed by an exponential scaling $I_c \propto e^{-k_B T/\delta E}$, where $\delta E \approx \hbar v_F / 2\pi L$ [22, 98, 104]. This decaying rate δE is directly related to the Thouless energy $E_{Th} = \hbar v_F / L$, which is the characteristic energy of a JJ in the long-ballistic regime (see Table 1.1 and Table 1.2). We then measure the $I_c(T)$ dependence for four different graphene/hBN aligned JJs with increasing length L (see GH1-4 in Table 3.1). Fig. 3.4a-b shows these measurements for the two shortest devices, where we can see that the I_c follows an exponential decay with temperature T. Most importantly, it does so for multiples values of density n/n_s, spanning over different bands; from the Dirac cone at the CNP to the moiré minibands.

Device	L (µm)	W (µm)	θ (°)
GH1	0.20	1.50	0.21
GH2	0.30	1.50	0.38
GH3	0.50	1.50	0.27
GH4	0.60	1.50	0.22

Table 3.1: Summary of all graphene/hBN moiré Josephson junction devices. Shown parameters include length L (± 0.01 µm), width W (± 0.01 µm) and twist-angle θ ($\pm 0.01°$).

By extracting the rate of the exponential decay δE, we find that it scales linearly with $1/L$, as shown in Fig. 3.4c. Along with the observation of FP oscillations, this result provides another evidence that our graphene/hBN JJs are ballistic in their entire

accessible band structure, and moreover in the long regime. From this fit we can also extract the Fermi velocity at the density $n/n_s \sim 1.3$ where the δE values where extracted, giving $v_F \approx (0.34 \pm 0.05) \times 10^6$ m/s. This value is in good agreement with values $v_F \approx (0.5 \pm 0.1) \times 10^6$ m/s reported in previous experiments [30, 38, 184], and with the model of the band structure shown previously in Fig. 3.1b and Fig. 3.2e-f.

Another evidence of our devices belonging to the long-ballistic regime follows from the $1/L$ dependence of the $I_c R_N$ product, as shown in Fig. 3.4d. At zero temperature, $I_c \approx E_{Th}/R_N$ in the long junction regime [22, 98, 106]. At the same time, for a ballistic sample, the normal state resistance R_N does not depend on its length (as it is determined only by its cross-sectional width and the Fermi wavelength). Therefore, $I_c R_N \approx E_{Th} \propto 1/L$ is expected for long-ballistic junctions, in agreement with our measurements in Fig. 3.4d.

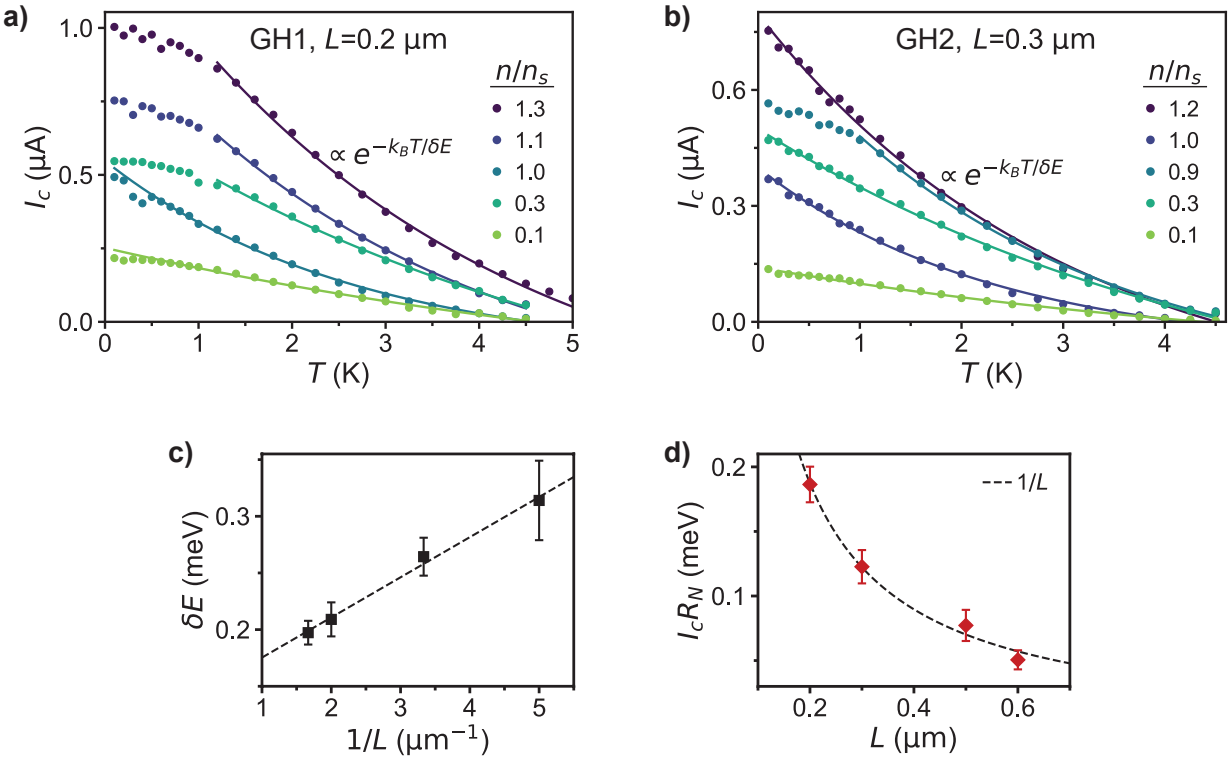

Fig. 3.4: Long-ballistic regime evidence in the length dependence of $I_c(T)$ and $I_c R_N$. a-b) Critical current I_c vs temperature T for different points in carrier density, and for devices GH1 and GH2, respectively. At high temperatures, I_c follows an exponential trend. The solid lines represent a fit to the function $\propto e^{-k_B T/\delta E}$. **c)** Extracted δE from the exponential fits in **a-b** at a fixed $n/n_s \sim 1.3$ and for several devices with varying length L (see devices GH1-4 in Table 3.1). The dashed line represents a linear $1/L$ fit to the data. **d)** $I_c R_N$ product at a fixed $n/n_s \sim 1.2$, for devices GH1-4 with varying length L, where a $1/L$ dependence is evident. The errorbars come from the average value of I_c, which is measured at base temperature 35 mK and is random due to premature switching.

3.2 High-field superconductivity and cyclotron breakdown

In this section we show that the evidence of a finite supercurrent at high magnetic fields, and its dependence with the carrier density, can also give us information about the moiré miniband structure of graphene/hBN.

3.2.1 The superconducting proximity effect for increasing magnetic fields

In a Josephson junction, the supercurrent is carried by Andreev bound states (ABS), which consist of electron-hole pairs that are created by two coherent Andreev reflections at the interfaces of the two superconducting leads with the normal metal weak link. These electron-hole pairs have exact opposite momenta and thus retrace the trajectories of each other, as shown in Fig. 3.5c. In the presence of a perpendicular magnetic field however, the ABS acquire an extra phase shift that depends on their trajectories along the cross section of the junction, leading to an interference of the mesoscopic supercurrent (see Fig. 3.5d). In a JJ with an homogeneous supercurrent density profile, the critical current $I_c(B)$ follows the typical Fraunhofer pattern of Eq. (1.45). This is the case in our device, as shown in Fig. 3.5a.

However, at relatively small magnetic fields > 10 mT, in Fig. 3.5b we observe a deviation from the expected exponential decay. Although some lobes merge with each other and some others are missing, the periodicity of the oscillations $\Delta B \sim 2.5$ mT in general still matches one unit of flux quanta Φ_0 threading through the junction (flux-focusing effects considered), which is a signature of edge transport. Most importantly, their amplitude does not follow a clear trend but rather chaotic. This same phenomena has been studied previously in graphene JJs in Refs. [22, 23]. In a semiclassical picture, as the magnetic field is increased, the electron and holes forming the ABS acquire a finite cyclotron motion with opposite directions. If the field is strong enough, the electrons and holes cannot retrace each other, so that no ABS is formed, as shown in Fig. 3.5e. Following a geometrical analysis on the cyclotron trajectories, one finds that the ABS will much more likely be formed at the edges of the junction, where the Andreev reflections do not occur as there is no superconducting region [22]. The value of field where the ABS disappear from the bulk was found to be $B^* \approx \Delta/eLv_F$. In our case, for $L \sim 200$ nm and $v_F \sim 0.5 \times 10^6$ m/s, we find $B^* \sim 13$ mT, which indeed coincides with the values at which the deviation from the Fraunhofer interference occurs in Fig. 3.5b.

This combination of scattering at the edges of the weak link, along with the cyclotron orbits of the electron-hole pairs, provides a chaotic billboard motion of the ABS, which leads to the observed random superconducting pockets with dominating edge transport

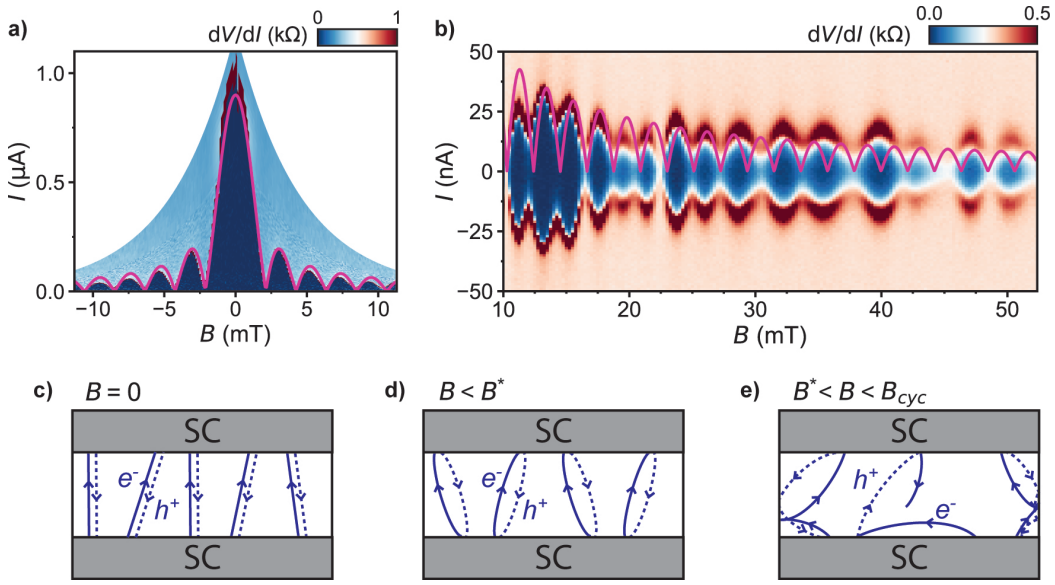

Fig. 3.5: Interference patterns at increasing magnetic fields. a) Interference pattern measured at $n/n_s = 1.7$, where the differential resistance $\mathrm{d}V/\mathrm{d}I$ is measured as a function of the d.c. current bias I and perpendicular magnetic field B. The exponential decay of the critical current $I_c(B)$ agrees well with a uniform single-slit junction (magenta solid line) with the same area as our the device, considering flux focusing effects. **b)** Continuation of the measurement in **a** for higher fields, where the Fraunhofer exponential decay no longer fits the observed oscillations at $\gtrsim 12$ mT, but show a rather random behavior. All data is taken at 35 mK. **c-e)** Sketch of the electron-hole trajectories forming the ABS, for different regimes of magnetic field. Once $B > B^*$, the pairs cannot easily retrace each other, unless they scatter with the edges of the sample.

[22]. These pockets can have a maximum critical current $I_Q \approx e\Delta/h \sim 50$ nA, which is the maximum supercurrent that can be carried by a single ABS [22, 93]. This random trajectories of ABS that can still carry a finite supercurrent from one superconducting lead to another can survive up to the magnetic field that is necessary for a cyclotron orbit to have a diameter greater than the length of the junction [22, 23]. This translates to the condition $2r_c = L$, where

$$r_c = \frac{\hbar k_F}{eB} \tag{3.8}$$

is the cyclotron radius. We name this specific field $B_{cyc} = \hbar k_F/2eL$. The condition $2r_c = L$ is also the semiclassical condition for Landau levels to form in a 2DEG. As the cyclotron orbits shrink in size and the electrons or holes cannot travel directly from one lead to another through the middle of the junction, the bulk becomes insulating, and the conduction electron or holes can only travel through skipping orbits through the edge of the sample.

Crucially, this high-field superconductivity can only be observed in ballistic JJs, where the critical currents can achieve the ballistic limit I_Q, and the decoherence of the ABS is

minimal so that they can retrace each other even in the presence of high magnetic fields that shape the trajectories of the electron-hole pairs [22]. Thus, our observation of this phenomena in Fig. 3.5b is well justified, as our JJs lie in the long-ballistic regime.

While it was originally thought that the LLs in graphene could not carry ABS, this was proved otherwise in other experimental works [23, 24], where they observed a superconducting proximity effect in the Quantum Hall regime. Unlike at low fields or at the semiclassical regime, where the Andreev reflection process consists of an incident electron retro-reflecting as a hole, the mechanism at the superconductor-Quantum Hall interface is different. Since in the QHE both electrons and holes have the same chirality, the electron-hole pairs forming the ABS also need to be chiral [23, 24]. These chiral Andreev edge states thus co-propagate forward along the interface by continuously converting from electrons to holes and viceversa, upon successive reflections. Importantly, in a JJ, the chiral ABS will form a chiral loop that connects both electrodes, yielding an Aharonov-Bohm quantum interference with a double $2\Phi_0 = h/e$ flux periodicity. This double periodicity of the I_c is the hallmark of the chiral nature of these ABS, although this was not experimentally observed until recently [24].

The critical currents of these fragile superconducting states are nevertheless too small, in the order of $I_c \lesssim 1$ nA. This requires an electronic temperature not much bigger than $T = E_J/k_B = \hbar I_c/2ek_B \sim 30$ mK, so that thermal fluctuations do not wash out the superconducting phase. Unfortunately, and although it would be extremely interesting to expand this proximitized Quantum Hall regime into the Hofstadter fractal spectra of our graphene/hBN JJs, we have not been able to detect such small critical currents in our experimental setup. Instead, in the following we focus in the semiclassical regime $B^* < B < B_{cyc}$ (or $2r_c > L$), where the critical currents can approach the single-mode ballistic limit I_Q, which we can well resolve.

3.2.2 Proximity effect at high magnetic fields in the moiré bands

In Fig. 3.6a we present our measurements of the superconducting proximity effect at high fields for electron doping in our graphene/hBN JJ. The zero resistance pockets marked by dark-blue regions, and indicative of superconducting states, lie exactly below the $2r_c = L$ yellow curve at $n/n_s < 1$, where $r_c = \hbar\sqrt{\pi n}/eB$ is the expression for a linear Dirac dispersion as is the case for the C1 band (see Fig. 3.6d) [22, 23]. However, for densities slightly lower than $n/n_s = 1$, marked by a red arrow in Fig. 3.6a, we start to observe small random pockets of superconductivity above the $2r_c = L$ curve. This point in density at $n/n_s \approx 0.9$ coincides with the position of the saddle point between the C1 and C2 bands in the graphene/hBN moiré minibands, as shown in Fig. 3.6d.

As we continue to increase the density, the LLs stemming from the CNP cross with another set of LLs from the eDP at $n = n_s$, as expected for the Hofstadter butterfly [35–37]. At the crossing of these LLs we also observe small random pockets of superconductivity

between 2 T and 4 T. Most surprisingly, the LLs from the CNP get interrupted at densities $n/n_s > 1.3$ (see orange arrow in Fig. 3.6a), where the superconducting proximity effect takes a huge phase space, spanning to as much as ~ 7 T, and clearly surpassing the $2r_c = L$ condition from the linear dispersion of C1, which we now mark with a dashed curve.

We note that the superconducting nature of these zero-resistance states is further

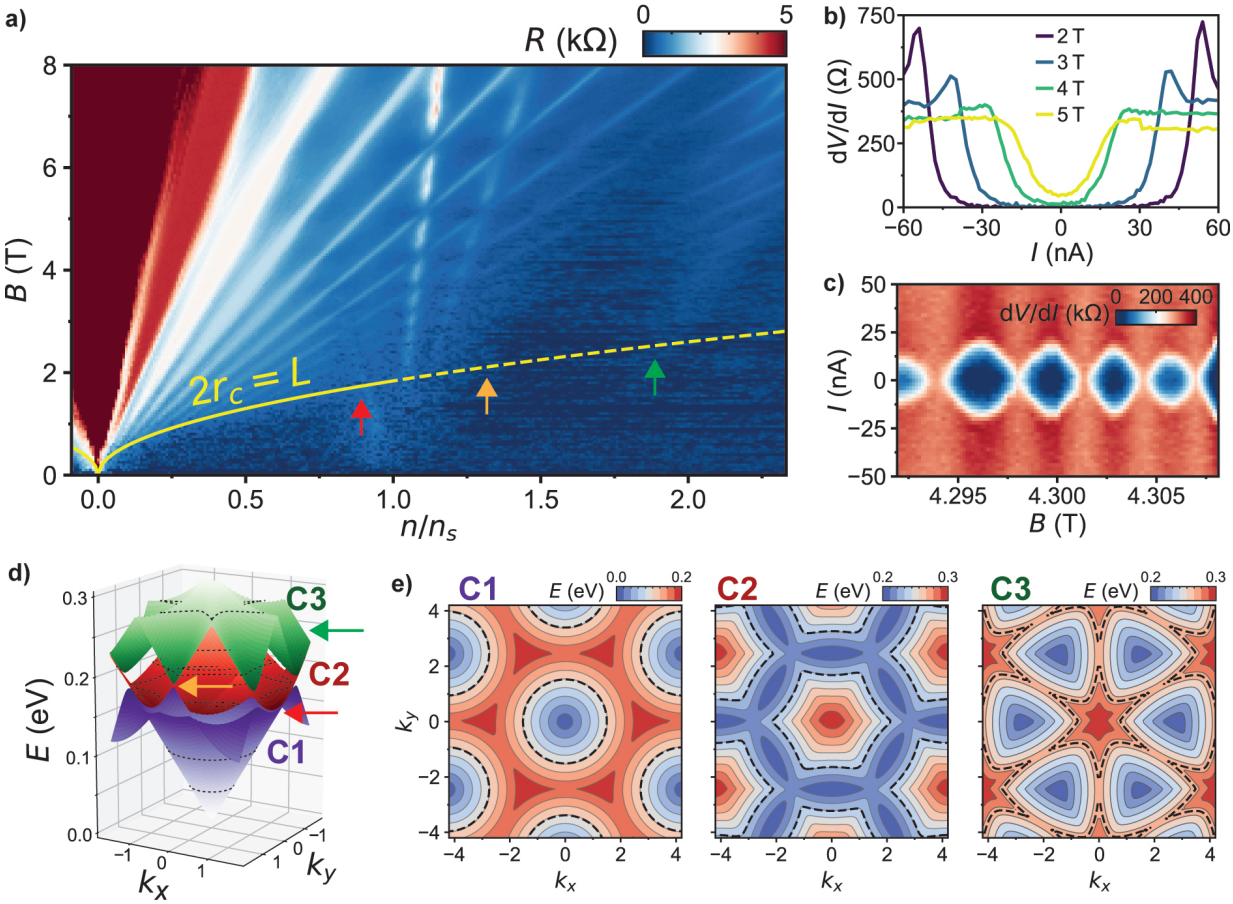

Fig. 3.6: High-field superconductivity in the moiré bands. a) Map of resistance R vs magnetic field B and normalized carrier density n/n_s, measured at 35 mK. The dark-blue regions indicate zero-resistance states that span up to ~ 7 T. The coloured arrows follow the same color-code as in **d**. **b)** Differential resistance $\mathrm{d}V/\mathrm{d}I$ curves vs current bias I measured at several magnetic fields at a fixed $n/n_s = 1.7$. **c)** Interference pattern measured around 4.3 T at $n/n_s = 1.7$. **d)** Miniband structure of the graphene/hBN superlattice, with the first three conduction bands C1, C2 and C3 indicated. Equipotential contours are shown with the dashed contours and the energy levels of the saddle-point vHs are indicated with a red, orange and green arrows. These are also shown in the density of sates in Fig. 3.2e-f for the same band structure. **e)** From left to right, the Fermi surface colorplots of the three conduction bands C1, C2 and C3 shown in **d**, respectively. The surfaces enclosed by dashed lines correspond to energies of 0.10 eV, 0.25 eV and 0.29 eV, respectively.

demonstrated by the observation of nonlinear $\mathrm{d}V/\mathrm{d}I$ curves (Fig. 3.6b) and interference patterns (Fig. 3.6c). Our statement that these superconducting states at high fields belong to the semiclassical regime,and not to the Quantum Hall regime, lies in that the amplitude of the oscillations in I_c appear to be random (see Fig. 3.6c), and we often observe very high supercurrents up to the $I_Q \sim 50$ nA limit. The observed telegraphic signal of the superconducting states in Fig. 3.6a is due to the fact that in the measurement, the magnetic field is the slow variable and has relatively big steps of ~ 20 mT. It can then be considered that there is a random probability of measuring either a finite or zero resistance, depending on whether the field hits a node or a superconducting lobe, as one can see in the interference patterns of Fig. 3.5b and Fig. 3.6c.

We emphasize here that the observation of superconductivity up to such high fields has not been done in bare graphene, where the semiclassical regime is well delimited by the $2r_c = L$ condition (see Fig. 3.7e for a comparison). Since the shape of the cyclotron orbit in a 2DEG is a full rotation around the Fermi surface (see dashed lines in Fig. 3.6e for example), to understand why this is observed in graphene/hBN at the second and third moiré minibands only, we turn to the band structure in Fig. 3.6d. There we find the presence of saddle-point van Hove singularities close to the three crossings between the C1, C2, C3 bands; indicated by colored arrows (see also Fig. 3.2e-f following the same color-code). As it turns out, the position of these vHs in filling correspond to the points in Fig. 3.6a where we observe deviations from the $2r_c = L$ condition.

These vHs mark the transition from electron to hole character, where the cyclotron orbit vanishes because its trajectory changes signs and becomes ill defined. In the vicinity of these points, neighboring electron-like and hole-like pockets approach each other in k-space; so that quantum tunneling between those trajectories occurs, producing the so-called magnetic breakdown which generates open orbits that skip across the vHs region instead of forming closed cyclotron loops [179, 182, 185]. This could then explain the observation of superconductivity at higher fields than expected for these fillings: as the electron-hole pairs no longer have closed cyclotron orbits, they can travel more freely in open orbit motions from one superconducting lead to the other, retracing each other and creating an ABS. This retracing is still more probable to happen at the edges, as discussed previously, so that the superconducting pockets are still random and fluctuations in the I_c are still observed, with a SQUID-like behavior such as in Fig. 3.6c due to edge-dominated transport. We note that the three vHs do not appear for all band structure models of graphene/hBN, which have been explained in detail in Subsection 1.2.1. Thus, our study can serve as an experimental test for these models.

The range in between the two vHs in $n/n_s \sim 1.3$ and ~ 1.9, where the superconducting pockets with the highest fields are observed, corresponds to small and anisotropic Fermi surface pockets (see the C2 and C3 panels in Fig. 3.6e), which could cause smeared cyclotron orbits as well [179]. If one were to approximate k_F as the average radius of the irregular Fermi surfaces of C2 and C3 (see Fig. 3.6e) [179], we find that it would not be significantly greater than the one from C1. The resulting $2r_c = L$ curve emanating from $n/n_s = 1$ would

not be greater than the yellow one either, unable thus to capture the superconducting phase boundary that we observe at high fields.

The open orbits also delocalize Landau levels, such that they cannot form near the vHs [182], which is what ultimately enables the presence of superconductivity at these high fields. This phenomena could have been overlooked in the past due to the use of a Hall-bar geometry, where the motion of electrons and their cyclotron orbits are not so constrained as in our junction architecture [35, 36, 179]. While in Ref. [179] this cyclotron breakdown was studied at zero or low magnetic fields ($\lesssim 0.3$ T) by measuring the transverse-electron-focusing effect in skipping orbits, here we provide evidence of a similar effect at high fields where the Hofstadter energy spectra could also play a role. It would then be important to study how the Hofstadter solution can change the cyclotron orbits and thus the proximity effect and the formation of LLs at these moiré bands. This analysis is beyond this Thesis work, and will be implemented in the final manuscript [P1] for its future publication.

Another important point we want to stress is the reproducibility of our results. Although it is not shown here, we have found the same dependence of the superconducting phase in the n-B phase diagram of Fig. 3.6a for sample GH2, which is a slightly longer junction than GH1 and has a different twist-angle $\theta \sim 0.38° \pm 0.01°$ (see Table 3.1).

We also would like to note that in Fig. 3.6a we do observe some superconducting pockets where LLs are formed at around $n/n_s \sim 1$, between 2 T and 4 T, as well as some others at $n/n_s \sim 1.5$ between 4 T and 5 T. These superconducting states should belong to the Quantum Hall regime, where the interplay between the ABS and the LLs create the Andreev chiral edge states [24], as discussed before. Since the I_c that we register at those points are very small, we are not able to resolve the $\mathrm{d}V/\mathrm{d}I$ curves and make any conclusions about how the I_c oscillates with field in this special regime. It would nevertheless be very interesting to extend this study in the future to the investigation of Andreev chiral edge states when the proximitized LL is rather a crossing of LLs due to the Hofstadter fractal spectra; a feature unique to moiré superlattices.

3.2.3 Comparison with a ballistic monolayer graphene JJ

Here we briefly show the study of a monolayer graphene JJ not aligned with hBN, which also falls in the long-ballistic regime, so that we can compare the results of our graphene/hBN moiré JJs. This device has a length $L \sim 300$ nm and width $W \sim 1.5$ µm.

Fig. 3.7a shows a differential resistance map, where close to the CNP both the I_c and R_N clearly oscillates with a FP interference. Not only for hole doping(n-p-n junction), but as well in the electron side (n-n'-n junction), although for a lower density range. This is expected since the lower normal state resistance for electron doping reduces the number of reflections and the FP interferometry becomes weaker. As we derived in Eq. (3.3), the linear band structure of graphene (Fig. 3.7c) gives $N \propto \sqrt{n}$, just as its DOS (Fig. 3.7d). This is corroborated in Fig. 3.7b, where the square root dependence fits perfectly the

observed oscillations.

As for the proximity effect at high magnetic fields, the superconducting region in Fig. 3.7e falls well below the $2r_c = L$ yellow curve delimiting the semiclassical regime, where $r_c = \hbar\sqrt{\pi n}/eB$. We note that the densities that we reach here ($\lesssim 5 \times 10^{12}$ cm^{-2}) are the same that we reach in our graphene/hBN aligned JJs, so that a one-to-one comparison can be made with Fig. 3.6a.

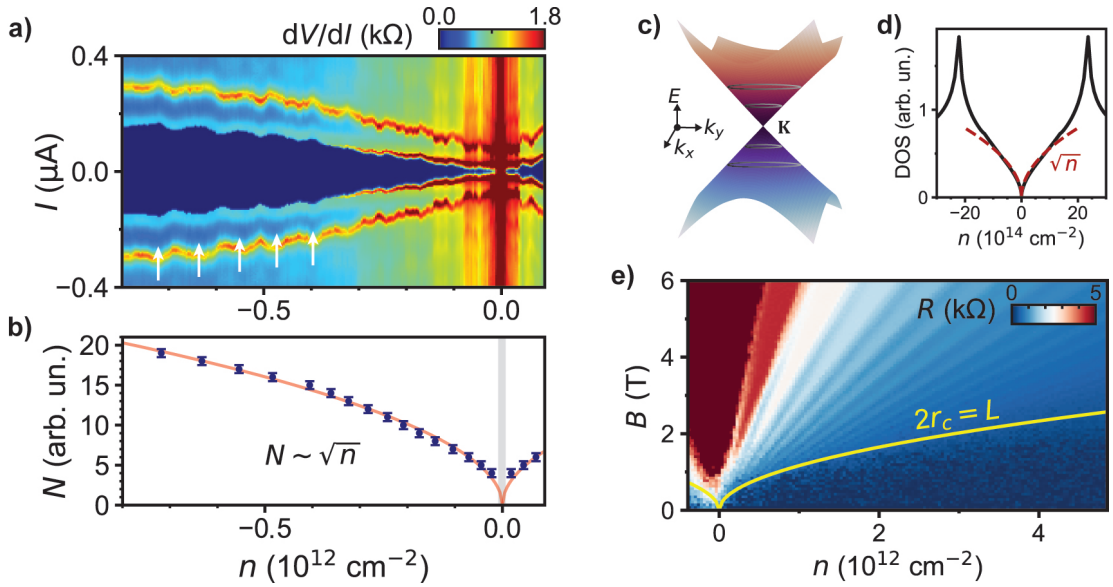

Fig. 3.7: Fabry-Pérots and high-field superconductivity in a ballistic graphene JJ. a) Map of differential resistance dV/dI vs d.c. current bias I and carrier density n, for a non-aligned monolayer graphene JJ, measured at 2 K. The dark blue regions indicate superconducting proximitized states, where the transition at positive I corresponds to the critical current I_c. **b)** By extracting the consecutive maxima in the I_c or the minima in the R_N from **a**, we find that $N \sim \sqrt{n}$. Some of them at high carrier density are pointed in **a** with white arrows. The errorbars account for a potential missable extrema in the oscillating I_c or R_N. **c)** Low energy band structure of graphene at the **K** point, where the circular Fermi surfaces are shown in the gray contours. **d)** Density of states vs n, showing a $\sqrt{n}$ dependence when the band structure at low energies and densities is linear, as in **c**. **e)** Landau Fan diagram of the JJ measured at 35 mK, where the superconducting states are visible below the $2r_c = L$ curve (yellow). Here $r_c \propto \sqrt{n}$, due to the linear Dirac dispersion proper of graphene.

Chapter 4

Probing the flat band limit of the superconducting proximity effect in TBG Josephson junctions

The work presented in this chapter led to the following publication:

[P2] **A. Díez-Carlón**, J. Díez-Mérida, P. Rout, D. Sedov, P. Virtanen, S. Banerjee, R. Penttilä, P. Altpeter, K. Watanabe, T. Taniguchi, S.Y. Yang, T.T. Heikkilä, P. Törmä, M.S. Scheurer, D.K. Efetov. "Probing the flat-band limit of the superconducting proximity effect in twisted bilayer graphene Josephson junctions". *arXiv:2502.04785* (2025). Under review in *Physical Review X*. `http://arxiv.org/abs/2502.04785`
Contributions: Sample fabrication, measurements, data analysis, discussion and paper writing.

In this chapter, we study the superconducting proximity effect in a Josephson junction formed by a twisted bilayer graphene weak link and s-wave superconducting leads. According to the theory of SNS junctions, this proximity effect should be suppressed in the flat bands of TBG due to their small Fermi velocity and bandwidth (Section 4.1), and yet we observe it to be as strong as in its dispersive bands (Section 4.2). Furthermore, only in this flat band limit we detect an unconventional scaling between the critical current and the normal state conductance (Section 4.3), potentially indicative of attractive interactions between electrons boosting the supercurrents in this regime. In Section 4.4, by studying multiple devices with different twist-angles—thus tuning the bandwidth of the

flat bands—and examining the dependence of the critical current on filling, calculations find good agreement with the experiment but only if contributions from quantum geometry and multiband pairing to the proximity effect are considered, revealing the importance of these mechanisms into the formation of superconducting phases in flat band systems. Lastly in Section 4.5, we observe unconventional interference patterns with broken inversion at half-filling of the bands, enabling us to engineer a reversible Josephson diode, and providing insights on the symmetries of the ground states at these fillings.

4.1 Quantum Geometry and superconductivity in the flat band limit

When a superconductor is placed in proximity to an adjacent normal conductor, superconducting correlations extend into the latter over a characteristic coherence length ξ_N. In a Josephson junction, where the normal metal forms a weak link between two superconductors, the induced correlations are manifested by the generation of a dissipationless supercurrent mediated by phase-coherent Andreev pairs [97, 102, 186, 187]. The maximum value of this supercurrent; the critical current I_c, is in general correlated with ξ_N, which in turn directly depends on the Fermi velocity v_F of the weak link [93, 97, 102, 188].

An interesting regime appears then when a perfectly flat band system serves as the weak link in a JJ [189–191] [P4], where the zero v_F prohibits the existence of a ξ_N and thus of a supercurrent. Additionally, a normal state conductance G_N, which in conventional JJs scales with I_c [93, 97, 102, 188], cannot be well defined in such system due to the absence of a Fermi surface. Nevertheless, recent theoretical works [P4] [191] have proposed that, thanks to the quantum geometric contributions to superfluidity in flat bands [192–197]—which scale with attractive interactions—a supercurrent can still flow in this case. In this section we will explain the concept of this quantum geometry and how it plays a role in driving superconducting phases in flat band systems.

4.1.1 The quantum metric

In a given band, the distance between nearby Bloch states $u_{\mathbf{k}+d\mathbf{k}}$ and $u_{\mathbf{k}}$ in the Brillouin zone is given by:

$$d\ell^2 = \langle u_{\mathbf{k}+d\mathbf{k}} - u_{\mathbf{k}} | u_{\mathbf{k}+d\mathbf{k}} - u_{\mathbf{k}} \rangle \approx \sum_{i,j} \langle \partial_{\mathbf{k}_i} u_{\mathbf{k}} | \partial_{\mathbf{k}_j} u_{\mathbf{k}} \rangle d\mathbf{k}_i d\mathbf{k}_j \tag{4.1}$$

Therefore, from here we can define the quantum metric $g_{ij}(\mathbf{k}) = \langle \partial_{\mathbf{k}_i} u_{\mathbf{k}} | \partial_{\mathbf{k}_j} u_{\mathbf{k}} \rangle$ as the real two-rank tensor that measures these distances. In a more general way, we can define the quantum geometric tensor $\mathcal{B}_{ij}(\mathbf{k})$ as the projector of the overlap of Bloch states derivatives:

$$\mathcal{B}_{ij}(\mathbf{k}) = \langle \partial_{\mathbf{k}_i} u_{\mathbf{k}} | \left(1 - |u_{\mathbf{k}}\rangle\langle u_{\mathbf{k}}|\right) | \partial_{\mathbf{k}_j} u_{\mathbf{k}} \rangle = \langle \partial_{\mathbf{k}_i} u_{\mathbf{k}} | \partial_{\mathbf{k}_j} u_{\mathbf{k}} \rangle - \langle \partial_{\mathbf{k}_i} u_{\mathbf{k}} | u_{\mathbf{k}} \rangle \langle u_{\mathbf{k}} | \partial_{\mathbf{k}_j} u_{\mathbf{k}} \rangle. \tag{4.2}$$

This two-rank tensor can be decomposed in its real symmetric and imaginary antisymmetric part, which have direct physical implications [198]. From Eq. (4.1), we can deduce that the quantum metric is the real part:

$$g_{ij}(\mathbf{k}) = \mathrm{Re}(\mathcal{B}_{ij}(\mathbf{k})), \tag{4.3}$$

and the imaginary part turns out to be related to the Berry curvature:

$$\Omega_{ij}(\mathbf{k}) = \frac{1}{2}\mathrm{Im}(\mathcal{B}_{ij}(\mathbf{k})). \tag{4.4}$$

This last property is very important, as the integral of the Berry curvature over the Brillouin zone gives the band's Chern number C:

$$C = \frac{1}{2\pi}\int_{\mathrm{B.Z.}} d\mathbf{k}^2\ \Omega(\mathbf{k}). \tag{4.5}$$

We will see how the quantum metric naturally emerges when calculating the superfluid weight D_s of a superconductor, and how this contribution becomes dominant in flat bands compared to the conventional term from the BCS theory. To this end, let us first introduce this quantity in the framework of a BCS superconductor.

4.1.2 Superfluidity in the BCS theory

The simplest phenomenological description of the electromagnetic response of superconductive materials is based on the London equations [84, 93], which follow from the relation

$$\boldsymbol{J_s} = -D_s\boldsymbol{A}, \tag{4.6}$$

with $\boldsymbol{J_s}$ the supercurrent density and $\boldsymbol{A}$ the vector potential. Eq. (4.6) describes a purely non-dissipative response, fundamentally different from the usual normal-state behavior of a material to the application of an external electromagnetic field, which is dissipative and characterized by Ohm's law $\boldsymbol{j} = \sigma\boldsymbol{E}$, with $\boldsymbol{E} = -\partial\boldsymbol{A}/\partial t$ the electric field. The counterpart of the conductivity σ for a superconductor is the so-called superfluid weight D_s [199], which is an intrinsic property of the material.

Hence a nonzero superfluid weight $D_s \neq 0$ is the very criterion of superconductivity. In tandem with Maxwell's equations, Eq. (4.6) provides a quantitative description of the two essential phenomena that define the superconductive state: perfect conductivity and perfect diamagnetism. As an example, the London penetration depth λ_L is essentially the same observable as the superfluid weight since the two are related by $\lambda_L = 1/\sqrt{\mu_0 D_\mathrm{s}}$, a simple consequence of Eq. (4.6) together with Ampère's law.

Under the framework of the BCS theory [86, 87], the superfluid weight essentially tells about the kinetic energy of the Cooper pairs when driven by a supercurrent. More

formally, in a superconductor with order parameter $\Delta(\boldsymbol{r}) = |\Delta(\boldsymbol{r})|e^{i\varphi(\boldsymbol{r})}$, the superfluid weight measures the energy required to create a modulation of the order parameter phase $\varphi(\boldsymbol{r})$, which is expressed by a term in the free energy of the form [192]:

$$\Delta F = \frac{\hbar^2}{2e^2}\int d^3\boldsymbol{r}\sum_{ij}[D_s]_{ij}\partial_i\varphi(\boldsymbol{r})\partial_j\varphi(\boldsymbol{r}). \tag{4.7}$$

In general the superfluid weight is a two-rank tensor $[D_s]_{ij}$ in anisotropic systems, and is also known as the superfluid stiffness. The BCS theory [86, 87] gives the following result for the superfluid weight of a single spinful electron band at zero temperature:

$$[D_s]_{ij} = \frac{e^2}{\hbar^2}\int_{\text{B.Z.}}\frac{d^N\mathbf{k}}{(2\pi)^N}\,f\left(\epsilon(\mathbf{k})\right)\frac{\partial^2\epsilon(\mathbf{k})}{\partial\mathbf{k}_i\partial\mathbf{k}_j} \tag{4.8}$$

where N is the spatial dimension, $\epsilon(\mathbf{k})$ the single-particle dispersion of the partially filled band and $f(\epsilon)$ is the electron occupation probability in the superconducting BCS ground state. Crucially, the curvature of the single-particle band dispersion $\partial_{\mathbf{k}_i}\partial_{\mathbf{k}_j}\epsilon(\mathbf{k})$ is the most important microscopic property affecting the superfluid weight according to Eq. (4.8).

For a band where the dispersion can be approximated by $\epsilon(\mathbf{k}) = \hbar^2\mathbf{k}^2/2m_{\text{eff}}$, Eq. (4.8) simply gives:

$$D_s = \frac{e^2 n_s}{m_{\text{eff}}}, \tag{4.9}$$

where n_s is the density of Cooper pairs. Instead, for a perfect flat band with zero curvature, we would expect $D_s = 0$ according to Eq. (4.8).

4.1.3 Quantum geometric contribution to the superfluidity

It has been shown in recent years that the superfluid weight in a multiband system consists of two terms, referred as conventional and geometric contributions [192, 194, 200]:

$$D_s = D_s^{\text{conv}} + D_s^{\text{geom}}. \tag{4.10}$$

D_s^{conv} is essentially similar to the superfluid weight of Eq. (4.8) as discussed above, and is zero in a flat band. As we will see now, in contrast, D_s^{geom} can be non-zero in a flat band. If the band is quasi-flat, both of these contributions are present.

The general formula for D_s in a multiband system is quite complex, but is simplified in the limit when the (quasi-)flat band of interest is separated from other bands by a gap E_{gap} that is larger than the superconducting gap: $E_{\text{gap}} \gg \Delta$. In a system with the above conditions and within the flat band limit, where $D_s^{\text{conv}} \propto \partial_{\mathbf{k}_i}\partial_{\mathbf{k}_j}\epsilon(\mathbf{k}) \to 0$ and $D_s = D_s^{\text{geom}}$, the superfluid weight can be analytically solved [192]:

$$[D_s^{\text{geom}}]_{ij} = \frac{4e^2}{(2\pi)^N\hbar^2 N_{\text{orb}}}U\nu(1-\nu)\int_{\text{B.Z.}}d^N\mathbf{k}\;g_{ij}(\mathbf{k}), \tag{4.11}$$

where ν is the filling fraction of the isolated flat band, N_{orb} is the number of orbitals where the flat band states have a nonzero amplitude, $g_{ij}(\mathbf{k})$ is the quantum metric, and U is the energy scale of the effective attractive interaction between the electrons (either caused by phonons, spin fluctuations, etc.).

Eq. (4.11) essentially indicates that a nonzero superfluid weight (and thus a supercurrent) arises from a finite quantum metric and attractive interactions. Note that no dispersive term appears, in contrast to Eq. (4.8). Thus, this quantum geometric contribution becomes crucial in flat band systems where the usual kinetic energy-based mechanism fails to predict a superconducting phase. To test these predictions, by rewriting each expression Eq. (4.8) and Eq. (4.11) in terms of the superconducting gap Δ and expanding to $T \ll T_c$, one can find that the two results give two different dependencies on Δ [192], which could be directly probed in experiments [59, 197, 201–203].

Finally, we note that recent works [194–196] have shown that the geometric term can dominate in moiré systems and multiband lattice models, which is of especial interest for us. In the rest of this chapter, we present our experimental results on a twisted bilayer graphene Josephson junction, where we analyze how the quantum geometry and other contributions can affect the supercurrent when flowing through the TBG flat bands.

4.2 A Josephson junction with a TBG weak link

The above results on how the quantum geometry can dominate the supercurrent in a flat band superconductor can give an idea that, if a conventional superconductor proximitizes a flat band system, forming a JJ, the I_c would not necessarily be zero even though v_F vanishes. The theoretical models describing this are very recent and more complicated than the one presented above, as the supercurrent now flows according to the Josephson effect. However, experimental studies of the proximity effect at this regime are still lacking.

The interacting flat bands of magic angle TBG [8–10] make one very suitable candidate where to test these predictions, shown to host a rich phase diagram with strongly correlated electron physics. While its bands may not be perfectly flat [11], they are separated by a band gap from a set of highly dispersive bands, to which the Fermi level can be shifted by simply applying a gate voltage. Moreover, the bandwidth of the flat bands can be tuned by varying the twist-angle across different devices. Together, these features make TBG Josephson junctions a uniquely tunable system for studying the flat band limit of the superconducting proximity effect, enabling direct comparisons between flat and dispersive regimes and systematic exploration of the role of bandwidth and interactions.

Here we show how we were able to create such JJ with a TBG weak link and proximitize both its flat and dispersion bands. Our samples consist of a van der Waals heterostructure of twisted bilayer graphene encapsulated with hBN and patterned into a rectangular mesa of width $W \sim 1.5$ µm. The devices are capacitively coupled to a SiO_2/Si back gate that

allows to control the carrier concentration in the TBG, and are contacted with sputtered s-wave superconducting NbTiN leads that form one-dimensional edge contacts, resulting in junctions of length $L \sim 200$ nm. Depicted in Fig. 4.1a is a schematic of a typical device along with our measurement setup. All data were obtained at a temperature of 35 mK.

It is worth noting that previous experiments on gate-defined JJs, which exploited the electric tunability of TBG, were able to use its intrinsic superconducting state and induce a proximity effect in other fillings of the bands [204, 205] [P3]. While these devices benefit from perfectly transparent interfaces, they face limitations such as carrier density variation across the junction, which creates multiple phases in series rather than a single state, and the inability to isolate and study the weak link from the adjacent superconducting regions [205, 206] [P3]. Additionally, the unknown pairing mechanism of superconductivity in TBG adds further complexity to the interpretation of the proximity effect [207]. Compared to these previous efforts, our approach facilitates the exploration of the Josephson effect across different twist-angles and to study both the flat and dispersive bands of TBG.

First, we focus on device D2 with a twist-angle $\theta \sim 1.00° \pm 0.01°$. When the gate voltage V_g is tuned across the band structure of TBG (Fig. 4.1c), the measured two-terminal resistance (red line in Fig. 4.1b) shows peaks at integer fillings of the moiré unit cell $\nu = 0$, ± 2, ± 4, characteristic of samples near the first magic angle $\theta_m \sim 1.1°$ [11, 13, 14, 17] [P9]. Additionally, low-resistance states are recorded near the charge-neutrality point (CNP, $\nu = 0$), as well as in the dispersive bands at $|\nu| > 4$. These superconducting pockets are found at fillings where TBG has not been previously shown to exhibit intrinsic superconductivity, indicating they arise from an induced superconducting proximity effect from the NbTiN.

The formation of a JJ is confirmed by the observation of non-linear current-voltage characteristics in the above-mentioned low resistive regions, indicative of the d.c. Josephson effect (Fig. 4.1d). The switching from the zero-resistance to the normal state is detected as a sharp transition in voltage and presents a hysteretic behavior between the retrapping (I_r) and critical (I_c) currents, as is common for underdamped junctions or due to self-heating effects [93, 109]. The phase coherence of the JJ is further demonstrated by the observation of oscillations in I_c when a perpendicular magnetic field B is applied to the junction. Fig. 4.1e shows such an interference pattern at the dispersive bands, where the critical current decays following a typical Fraunhofer diffraction pattern, evidencing the uniformity of the supercurrent across the junction at these high carrier densities. Furthermore, the period of the measured oscillations $\Delta B \sim 2.5 \pm 0.2$ mT matches well the expected periodicity from the physical area of our junction $\Delta B_o \sim 2.3 \pm 0.1$ mT, where flux-focusing effects have already been accounted for (see Table 4.1).

The presence of the Josephson effect in the TBG junction throughout its whole phase diagram is illustrated in Fig. 4.1f, where the differential resistance dV/dI is recorded as a function of d.c. current I while tuning V_g. The registered I_c across all fillings is shown in blue in Fig. 4.1b. We note that we also observe superconducting states at the hole (electron) side of filling $\nu = -2$ ($\nu = 2$), as regularly reported in intrinsic superconducting

TBG transport devices [12, 17]. However, the observed I_c in the superconducting dome at $\nu < -2$ reaches its maximum at $\nu \sim -2.9$ and spans down to $\nu \sim -3.5$, exceeding the range of filling where TBG typically shows an intrinsic SC state [12, 14, 17]. Additionally, we do not observe any transition in the I_c or in the measured interference patterns at these fillings (as we will discuss later in Section 4.5). We then conclude that the observed I_c in our JJs is mainly caused by the proximity effect.

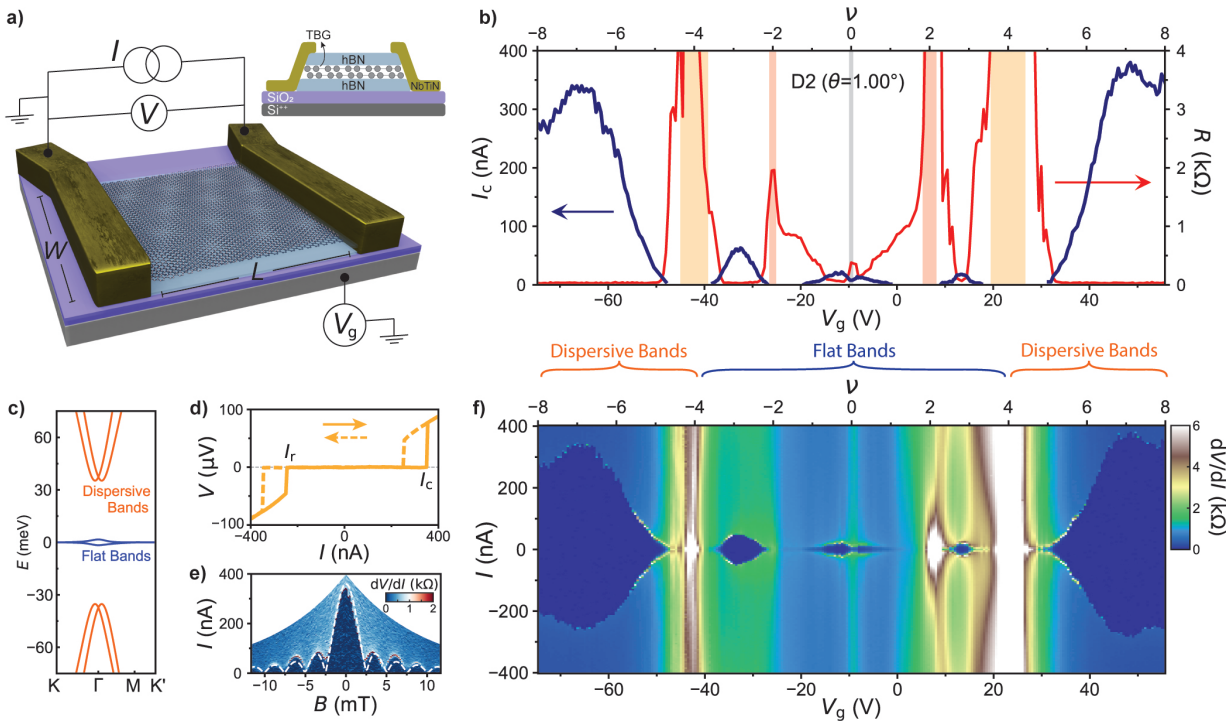

Fig. 4.1: Superconducting proximity effect in a TBG Josephson junction. a) Device schematic of a TBG sheet acting as the weak link of a JJ. The voltage V across the junction is recorded as a current bias I is applied through the superconducting electrodes in a two-probe measurement. The carrier density is tuned by a gate voltage V_g to the doped Si. **b)** Resistance R in red (right axis) at zero current bias, as a function of V_g (bottom) and of the corresponding moiré filling factor ν (top). Shaded vertical lines indicate the presence of the charge-neutrality point (gray), the correlated insulators at half-filling of the flat bands (red), and the band insulators between the flat and dispersive bands (yellow). Regions with low resistance have a finite critical current I_c (blue, left axis), extracted from the non-linear characteristics measured in **f**. **c)** IV curve measured at $V_g = 50$ V. The solid and dashed lines have opposite sweep directions as indicated by the arrows. **d)** Interference pattern recorded at the dispersive bands, for $V_g = 60$ V, which agrees well with a uniform single-slit junction (white dashed line). **e)** Band structure of TBG for $\theta = 1.00°$. **f)** Differential resistance dV/dI map, where dark blue regions indicate superconducting states. Their contour along positive values of I was used for extracting I_c in **b**. All data was obtained in device D2. Adapted from [P2].

4.3 Unconventional scaling between I_c and G_N

In Fig. 4.1b, the maximal critical currents that we observe in the flat bands are of $I_c \sim 65$ nA, only a factor of five lower compared to the dispersive bands with $I_c \sim 350$ nA. This is surprising, as we would have expected a much stronger suppression of the SC proximity effect in the flat bands as compared to the dispersive bands, given the large reduction in the bandwidth and Fermi velocity [191, 197] [P4]. Since I_c values itself do not allow for a direct estimate of the strength of the SC proximity effect, it is instead typically approximated with the I_cR_N product [93, 97, 102]. Here R_N is the normal state resistance of the JJ, which we extract through resistance measurements at a current $I > I_c$.

Fig. 4.2f shows I_cR_N vs ν, where we find especially large values in the dome shaped proximity-induced regions between fillings $\nu = \pm 2$ and $\nu = \pm 4$, which are comparable to the ones in the dispersive bands. This further confirms that unlike the initial expectations, the SC proximity effect is surprisingly large in the flat bands of TBG [97, 102, 106]. In Fig. 4.2 we also show other devices that do not have flat bands in their band structure, so that we

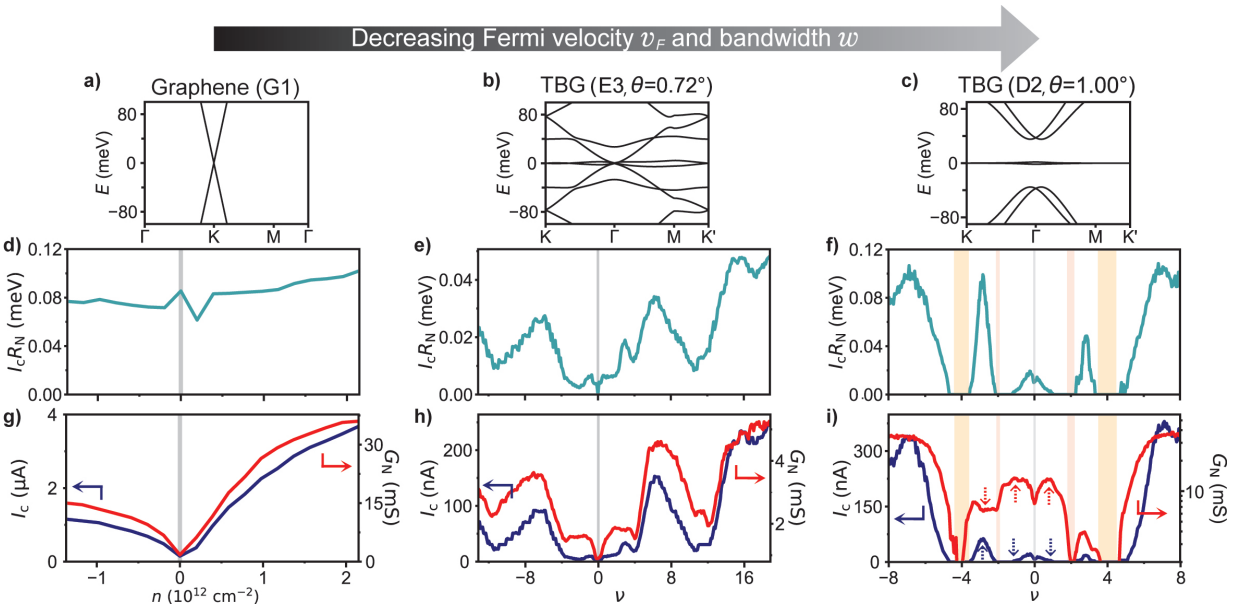

Fig. 4.2: Strength of the proximity effect and I_c vs G_N scaling. a-c) Band structure for the indicated devices, from bigger to lower Fermi velocity v_F and bandwidth w. **d-f)** I_cR_N product which estimates the strength of the proximity effect. **g-i)** Critical current I_c in blue (left axis) and normal state conductance G_N in red (right axis), both as a function of moiré filling factor ν and carrier density n in the case of the monolayer graphene device. For G1, E3 and the dispersive bands of D2, these two quantities scale with each other, whereas in the flat bands of D2 clear violations of this scaling occur. In **i**, following the same color code, the dashed vertical arrows indicate whether the corresponding quantity has reached a maximum or a minimum.

can compare our results with the proximity effect in the flat band limit, as explained next. These are a monolayer graphene JJ (G1) and a TBG JJ with a twist-angle away from θ_m (E3, $\theta \sim 0.72° \pm 0.01°$), whose main physical parameters are shown in Table 4.1 along with other samples. Their I_cR_N product dependence with filling (Fig. 4.2d-e), as well as a more quantitative justification of why the flat bands of TBG in D2 would be expected to have lower I_cR_N compared to the dispersive bands, will be explained later in Subsection 4.3.1.

In typical JJs, Andreev pairs undergo dephasing processes, the strength of which scales with the normal state resistance R_N. It is therefore often found that that I_c correlates with $G_N = R_N^{-1}$, the normal state conductance [93, 97, 102]. In Fig. 4.2g-h we demonstrate this is the case in JJs with single layer graphene or small twist-angle TBG as the weak links. There, we plot the critical current I_c and overlay it with the filling dependence of the normal state conductance G_N, and find that these two quantities follow each other closely. Many previous experiments had already shown this conventional scaling [19, 20, 98, 159, 208].

The same trend is also found when looking at the dispersive bands of our device D2, as seen in Fig. 4.2i. However and in strong contrast to this, the flat bands show the exact opposite trend, as pointed out by vertical dashed arrows. Here both I_c and G_N increase when doping away from the CNP, but while I_c peaks at $|\nu| \sim 0.3$ and decreases beyond these points, finally vanishing at $|\nu| \sim 1$, G_N continues to increase until $|\nu| \sim 1$. At higher doping, where the I_c domes at $|\nu| > 2$ are, the same conduct appears: because G_N shows smaller values than near the CNP, we expect a vanishing I_c and yet we observe similar ($\nu > 2$) or even bigger values ($\nu < -2$). This can be seen in more detail in Fig. 4.3c too.

Device	L **(µm)**	W **(µm)**	θ **(°)**	ΔB **(mT)**	ΔB_o **(mT)**	I_cR_N **(meV)**	l_{mfp} **(nm)**	ξ_N **(nm)**
D1	0.20	1.00	0.94	3.6	3.4	0.16	36	51
D2	0.15	1.50	1.00	2.8	2.5	0.11	35	45
D3	0.15	1.50	1.24	2.8	2.5	0.12	23	33
E1	0.15	1.50	0.45	2.5	2.5	0.10	20	98
E2	0.25	1.50	0.51	2.1	2.1	0.05	36	101
E3	0.25	1.50	0.72	2.1	2.1	0.05	31	89
G1	0.45	4.50	-	0.5	0.5	0.10	196	155
G2	0.35	4.50	-	0.6	0.6	0.14	190	148
G3	0.45	3.30	-	0.7	0.7	0.11	253	178

Table 4.1: Summary of all TBG and graphene Josephson junctions devices. D1-3 are the TBG JJs close to the magic-angle, E1-3 are the ones further from it, and G1-3 are monolayer graphene JJs. Shown parameters include length L (±0.01 µm), width W (±0.01 µm), twist-angle θ (±0.01°), measured field-periodicity of the critical current oscillations ΔB (±0.2 mT) and the expected periodicity from the physical device area by including flux focusing effects ΔB_o. Transport properties include the maximum values found of the product of the critical current with the normal resistance I_cR_N, the mean-free-path l_{mfp}, and the superconducting coherence length in the weak link ξ_N.

To verify that this unconventional scaling appears only in the flat bands of TBG, we have studied two more devices close to the magic angle: D1 ($\theta \sim 0.94 \pm 0.01°$) and D3

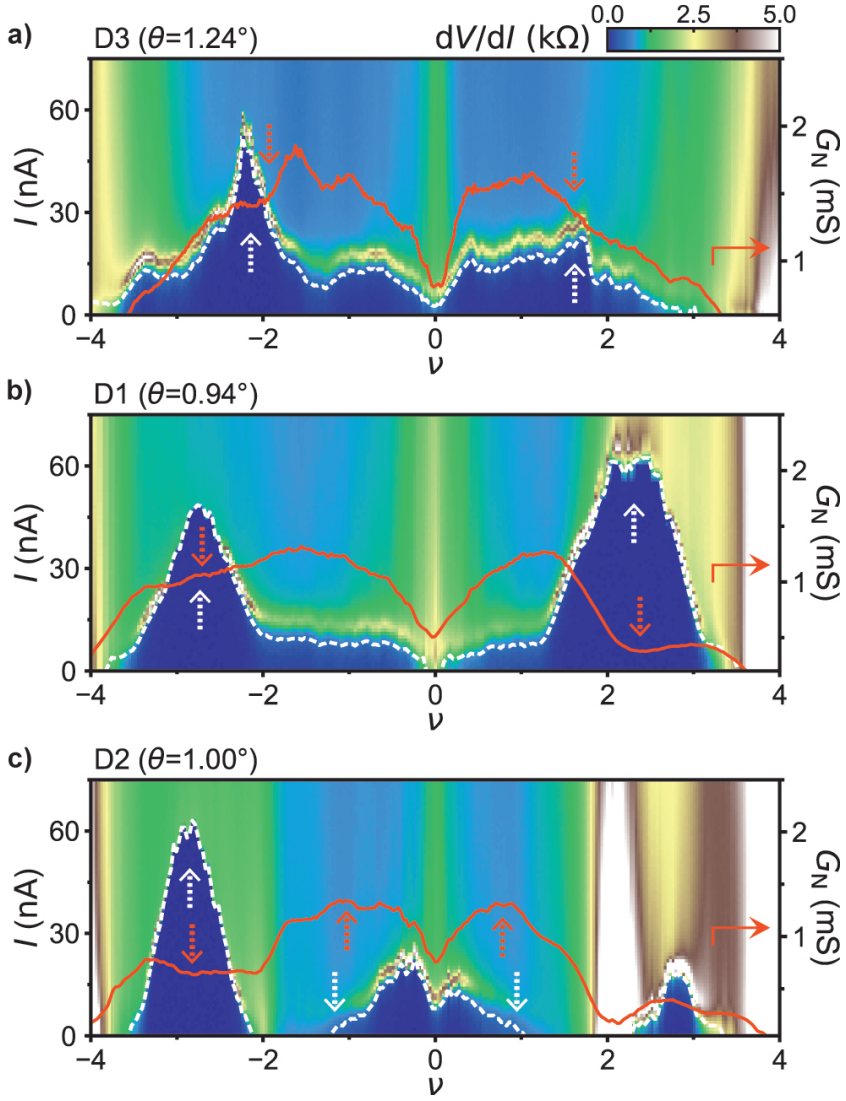

Fig. 4.3: Proximitized flat bands with varying twist-angle. a-c) Colormaps of measured differential resistance dV/dI as a function of d.c. current I (left axis) and filling ν of the flat band, for devices D3, D1 and D2, respectively. The solid red line corresponds to the normal state conductance G_N (right axis). The critical current I_c of each device is extracted by following the contour of the dark-blue regions in the colormaps, marked by white-dashed lines. The dashed vertical arrows indicate the regions where I_c and G_N do not scale with each other. In D1 and D3, the observed Josephson effect holds throughout the entirety of the flat bands, given the absence of correlated states at integer fillings. In the case of D2 (the closest to θ_m), the superconducting phases get interrupted by insulating states at half-filling. Adapted from [P2].

($\theta \sim 1.24 \pm 0.01°$). Their geometrical and transport parameters are gathered in Table 4.1. Their differential resistance colormaps are shown in Fig. 4.3 alongside the I_c in dashed white lines (left axis) and G_N in red solid lines (right axis). We have also placed vertical arrows (following the same color code) pointing at ranges in filling where the I_c does not scale with G_N.

For instance, in sample D1 (Fig. 4.3b), $G_N \sim 0.5$ mS and I_c is nearly zero at the CNP, both following the same increasing trend up to $\nu \sim 1.3$ and down to $\nu \sim -1.5$. However, with further doping, G_N decreases and I_c increases in turn, forming dome-shaped peaks. Compared to the CNP, at $\nu \sim \pm 2$ a higher I_c of ~ 50 nA is observed despite having the same G_N value. A similar trend is observed in sample D3 (Fig. 4.3a). For device D2, the same violation of the I_c vs G_N scaling discussed before in Fig. 4.2i can be further seen in Fig. 4.3c.

4.3.1 Estimation of the expected decrease of I_cR_N in the flat bands

In this subsection, we justify of our comments above about the flat bands being expected to lead to a weak induced superconductivity by the conventional theory of Josephson junctions, given the large reduction in their Fermi velocity. We do this by performing an analysis based on the theory of long-diffusive junctions, where we can give an initial estimation of how much the induced-superconductivity should be quenched in the flat bands, as compared to the dispersive bands and other devices far from the flat band limit.

By extracting the electron mean-free-path, $l_{\mathrm{mfp}} = \hbar L\sqrt{\pi}/e^2 W R_N \sqrt{n}$, where n is the electron carrier density, and comparing it ($l_{\mathrm{mfp}} < 35$ nm) to the length of our junctions $L \sim 200$ nm (see Table 4.1), we can conclude that all of them are in the diffusive regime since $l_{\mathrm{mfp}} < L$ [98]. This includes both TBG and monolayer graphene JJs, and is also consistent with their I_cR_N values being much smaller than the superconducting gap of NbTiN, $\Delta \sim 2.1$ meV (see Fig. 4.2d-f and Table 4.1) [209, 210].

The superconducting coherence length inside the weak link in this diffusive regime is expressed as $\xi_N = \sqrt{\hbar D/\Delta} = \sqrt{\hbar v_F l_{\mathrm{mfp}}/2\Delta}$, where $D = v_F l_{\mathrm{mfp}}/2$ is the diffusion coefficient in two dimensions. Since in general, a band structure does not have a constant v_F, alternative we can use the Einstein relation of diffusive transport

$$\sigma_N = D e^2 \mathrm{DOS}, \tag{4.12}$$

where $\sigma_N = L/WR_N$ is the conductivity and DOS the density of states at the Fermi level. Thus, from there we get $\xi_N = \sqrt{\hbar L/We^2 \Delta R_N \mathrm{DOS}}$, and by using the DOS of the band structures in Fig. 4.2a-c, we find the values of ξ_N shown in Table 4.1, where for all samples $\xi_N < L$, implying that they are in the long regime [97, 98, 106].

According to the theory of long-diffusive SNS junctions [106], the maximum I_cR_N

product is limited by the Thouless energy $E_{Th} = \hbar D/L^2 \ll \Delta$. To evaluate the extent to which E_{Th} limits the $I_c R_N$ in our devices, we can estimate it by using again the Einstein relation in Eq. (4.12). The results are shown in Fig. 4.4a-c in green. There we can see that for G1, E3 and the dispersive bands of D2, E_{Th} reaches values of ~ 0.1 meV, each following a very similar trend to the measured $I_c R_N$ products in Fig. 4.2d-f. For the flat bands of D2 however, this value drops to extremely low values $\sim 10^{-8}$ meV, due to the very small v_F (or diverging DOS).

In the theoretical limit of long junctions, where $E_{Th}/\Delta \to 0$, the ratio $I_c R_N/E_{Th}$ reaches a maximum value of ~ 10.8 at zero temperature [106]. In Fig. 4.4d-f we show these $I_c R_N/E_{Th}$ ratios alongside this theoretical limit, represented with a black-dashed line. In the case of G1 it stays quite constant at ~ 1 and for E3 it ranges from ~ 0.1 to ~ 1. In Fig. 4.4f, the dispersive bands of D2 also give $I_c R_N/E_{Th} \sim 0.1-1$ when taking the DOS of the continuum model (brown datapoints at $|\nu| > 4$). These values are consistent with previous studies of graphene JJs in this regime [211, 212], where the low $I_c R_N/E_{Th}$ ratio compared to the theoretical limit was attributed to an increment of the electron dwell time in the junction due to imperfect interfaces. The conclusion here is that, for devices far from the flat band limit, there is no excess of supercurrent than what is expected from their DOS and the conventional theory of SNS junctions. This is also consistent with the observed conventional scaling between I_c and G_N in Fig. 4.2g-i.

In contrast, for the flat bands, the diverging DOS results in $I_c R_N/E_{Th} \sim 10^5$ (brown datapoints in Fig. 4.4f at $|\nu| < 4$), far too big compared to the theoretical limit. This already hints at our observed proximity-induced superconductivity to be higher in the flat bands of TBG than what is expected from the conventional Josephson effect, especially comparing

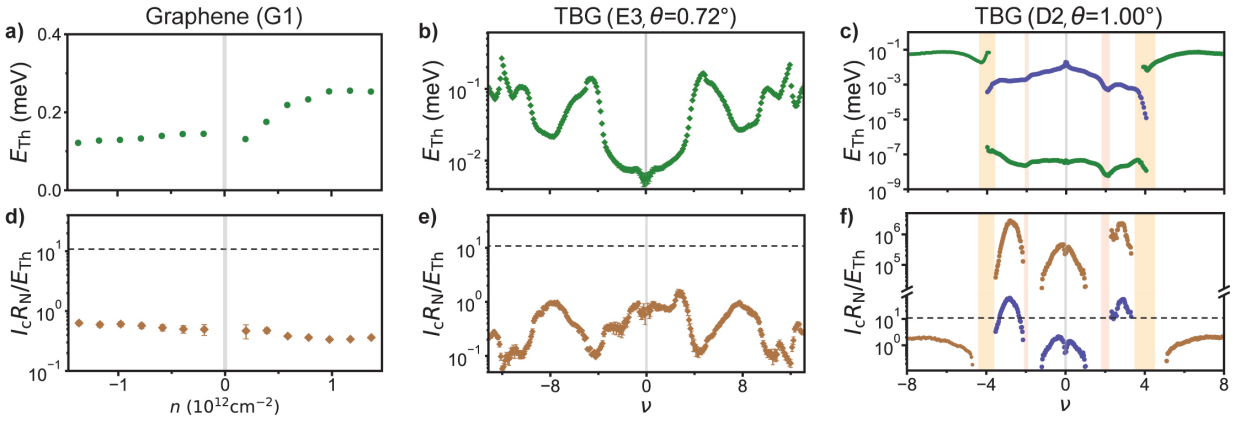

Fig. 4.4: Scaling of the proximity effect according to the theory of long-diffusive JJs. a-c) Thouless energy E_{Th} estimated from the density of states of the band structures shown in Fig. 4.2. **d-f)** Ratio $I_c R_N/E_{Th}$ vs moiré filling factor ν and carrier density in the case of G1. The horizontal black-dashed line represents the theoretical limit ~ 10.8 of long-diffusive SNS junctions. In **c** and **f**, the violet datapoints in the flat bands correspond to E_{Th} estimated by taking $D = v_F l_{\mathrm{mfp}}/2$ and a constant $v_F \sim 4 \times 10^4$ m/s.

this result with the previous discussion about the dispersive bands and other devices away from the magic-angle with higher dispersion, where the limit ~ 10.8 is not surpassed. Even by taking much greater values of v_F than those predicted by the continuum model (and $D = v_F l_{\mathrm{mfp}}/2$), for example $v_F \sim 4 \times 10^4$ m/s [11], we find that the proximity effect still surpasses the theoretical limit by almost one order of magnitude in $I_c R_N / E_{Th}$ (purple datapoints at $|\nu| < 4$ in Fig. 4.4c,f). This suggests the presence of additional mechanisms responsible for such strong values in the flat band limit, as we will address in the following. We note that this estimation represents a lower bound, since v_F in TBG was generally found to be even lower at these fillings of the bands [197, 213]—which would result in larger $I_c R_N / E_{Th}$—and non-ideal interfaces with the superconducting contacts can cause a further reduction of the limit ~ 10.8 [106, 211, 212].

We note that this analysis relies on several simplifying assumptions, such as the carriers in the weak link being ruled by diffusive transport and modeled by the Usadel equations, perfect transparency in the SN boundaries by neglecting any suppression of the superconducting gap Δ, and a sinusoidal current-phase relation [106]. Therefore, it mainly serves only as a justification that the proximity-induced superconductivity in the flat bands is expected to be much weaker than what we observe, from the theory of conventional SNS junctions.

4.3.2 Interaction-driven critical current

In the flat bands of TBG we have observed an exceeding I_c compared to the values that one would expect from the measured G_N (Fig. 4.3), as well as an unexpected large $I_c R_N$ that is comparable to the dispersive bands (Fig. 4.2f), although their Fermi velocities differ by orders of magnitude. These experimental observations hint at a new mechanism to drive the supercurrent in flat bands.

One reasonable possibility is that the exceeding I_c values could come from an extra contribution that is independent of G_N and thus of band dispersion. Such often-neglected term, I_c^{int}, indeed exists and scales with attractive interactions U, contributing to the total critical current because it boosts the Cooper pair transport through SNS junctions [P4]. It is then an important contribution in (quasi-)flat bands, where the range of pair correlations without interactions can become short due to localization in non-interacting transport. Similarly, as in the superfluid weight, part of this increase is related to the quantum geometry and is independent of band dispersion. In the following, we summarize the main ingredients and assumptions behind this model worked out by our collaborators, and refer to [P4] and the Supplementary of [P2] for a more detailed derivation.

To illustrate how the interaction-induced part of the critical current emerges, we consider a simple Ginzburg-Landau theory description of a perfect flat band in a normal state with effective attractive interactions of strength $U > 0$ between the electrons. Here the free energy of the system can be written as an expansion of the mean field Δ describing the

attractive interactions:

$$F = \sum_i \frac{\Delta_i^2}{U} - T\sum_{\omega_n} \log\det\left[i\omega_n + \mu - \mathcal{H}(\Delta)\right] \tag{4.13}$$

Here i is an index of the unit cell, $\omega_n = 2\pi T(n+1/2)$ are the Matsubara frequencies. The Hamiltonian $\mathcal{H}$ is a Bloch Hamiltonian that incorporates the attractive coupling to the flat band. To this free energy, a Ginzburg-Landau expansion can be done to emulate the physics of TBG by inputting some of its microscopic parameters, such as the moiré unit cell area A_m and the averaged Brillouin zone minimal quantum metric ξ_g [P4][214, 215]. This expansion gives

$$F = \frac{\xi_g^2}{4TA_m}|\nabla\Delta|^2 + \frac{T-T_c}{4TT_cA_m}|\Delta|^2 + \frac{1}{96T^3A_m}|\Delta|^4, \tag{4.14}$$

where $T_c = U/4k_B$. This means that for $T < T_c$, the attractive interactions U are strong enough to create an intrinsic superconducting state in TBG. However, we do not work in this regime, but rather choose to work out the solution for $T > T_c$, where the interactions are still there but TBG remains in the normal state.

This SNS problem consists on minimizing F at $T > T_c$ while keeping the order parameters in the superconducting banks to be $\Delta_S \sim 2.1$ meV, i.e. the gap of NbTiN in our case. This condition $\Delta(x<0,y) = \Delta_S e^{-i\varphi/2}$, $\Delta(x>L,y) = \Delta_S e^{i\varphi/2}$ makes the problem analytically solvable if the quartic $|\Delta|^4$ term is neglected. For a junction length L large compared to $L_g = \xi_g\sqrt{U/(4k_BT-U)}$, the result is the typical free energy of a JJ, $F = \hbar I_c^{\text{int}}\cos(\varphi)/2e$, where in this case the critical current stems only from the attractive interactions. Its expression is then [P4]:

$$I_c^{\text{int}} = \frac{8e}{\hbar}\frac{WL_g}{A_m}\frac{\Delta_S^2}{U}\left(1 - \frac{U}{4k_BT}\right)e^{-L/L_g}. \tag{4.15}$$

Note that I_c^{int} does not dependent on the normal state conductance G_N and is only the contribution to the total I_c that originates from the attractive interactions. Indeed, from Eq. (4.15) one can see that I_c^{int} becomes zero when U vanishes. The total I_c would also contain a component due to transport of electron pairs traversing the SNS junction without interactions; this is the component dependent on G_N that is typically considered and is proportional to the Fermi velocity. However, in a quasi-flat band it becomes small and therefore it is of interest to consider also I_c^{int}. In the simplest approximation, the two components simply sum together.

Quantitatively, I_c^{int} approaches the experimental $I_c \sim 50$ nA by inputting the twist-angles and geometrical factors of our JJs, and by setting $U \sim 10$ μeV, $T \sim 100$ mK, and $\xi_g \sim 40$ nm; as consistent with [214, 215]. As we show in Fig. 4.5, by setting a dome shape dependence with filling in U, we can reproduce the domes seen at $|\nu| > 2$ in devices D1 and D2, where the I_c vs G_N scaling violation is the strongest. These results serve as an

order of magnitude check that the typical energy, temperature and length scales of the experimental system can provide critical currents of the order of magnitude observed in the experiments, within the simple Ginzburg-Landau theory. A thorough analysis of the possibility of interaction-induced critical current would require a more complete microscopic theory of TBG interactions. The most important message of our Ginzburg-Landau theory approach is to show a possible scenario where the I_c that does not depend on G_N.

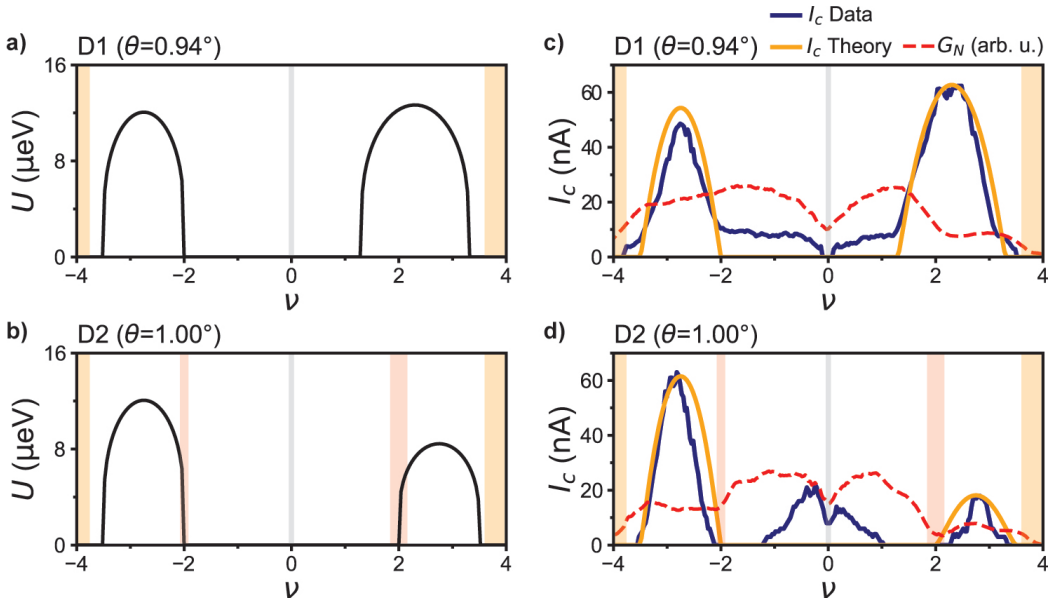

Fig. 4.5: Interaction-induced critical current in the TBG flat bands. a-b) Effective strength of the attractive interaction U, with a filling dependence taken to have a dome shaped behavior; for devices D1 and D2, respectively. The temperature is taken to be 100 mK. **c-d)** Experimentally measured I_c (blue) and G_N (red), along with the predicted critical current from interactions I_c^{int} vs filling ν; for devices D1 and D2, respectively. The dome dependence of I_c^{int} comes from **a-b**. Notably, since in Eq. (4.15), I_c^{int} does not depend on G_N, it could explain our observed violation of the I_c vs G_N scaling at certain fillings of the flat bands. Especially at $|\nu| > 2$, where I_c is higher or similar to near the CNP, despite G_N being smaller.

4.4 Quantum geometric and multiband contributions to the proximity effect

We now turn our attention to how I_c evolves with the filling of the flat bands (Fig. 4.3). This trend is highlighted by the appearance of superconducting pockets in the shape of domes close to the band insulators between fillings $\nu = \pm 2$ and $\nu = \pm 4$. In order to get a better understanding of the driving forces behind these domes, we use the powerful tuning

knob of TBG, the bandwidth w, which can be controlled directly by the twist-angle θ. As we will see next, by tuning w, we can effectively tune the band dispersion and interactions.

In Fig. 4.6e-g we also show the I_c vs ν for the three devices, along with their band structure according to the continuum model in Fig. 4.6b-d. It appears that as the w of the flat bands is lowered, the dome-shaped SC regions move closer to the band-edges at $\nu = \pm 4$. Also, while I_c is suppressed in D1 and D3 close to the CNP, in D2, which has the lowest bandwidth, the region around the CNP shows enhanced I_c values.

Seeking the qualitative understanding of this observed critical current variation with filling and twist-angle, we use the continuum model of TBG [9, 44] and perturbation theory to compute the linear response function of its electronic bands to an external superconducting field induced by tunneling from an s-wave superconductor. Here we summarize the main ideas and results behind the model worked out by our collaborators Denis Sedov and Mathias Scheurer, and refer to the Supplementary of [P2] for a more detailed derivation.

Considering a general electron system without interactions and, thus, without intrinsic superconductivity, its pairing term is induced by the Cooper pair tunneling from an s-wave superconductor placed in its proximity. The Hamiltonian of such system can be written as

$$\mathcal{H} = \int d\mathbf{r}\; c^\dagger_{\sigma,\eta}(\mathbf{r})\,[h_{\sigma,\eta} - \mu]\,c_{\sigma,\eta}(\mathbf{r}) + \int d\mathbf{r}\left[\Delta(\mathbf{r}) c^\dagger_{\uparrow,+}(\mathbf{r}) \cdot c^\dagger_{\downarrow,-}(\mathbf{r}) + \text{h.c.}\right], \tag{4.16}$$

where $c_{\sigma,\eta}(\mathbf{r})$ ($c^\dagger_{\sigma,\eta}(\mathbf{r})$) is the fermionic operator which annihilates (creates) an electron with spin $\sigma = \uparrow, \downarrow$ and valley $\eta = +, -$ at a point $\mathbf{r}$; $h_{\sigma,\eta}$ is the single-particle Hamiltonian of the material that is being proximitized (TBG in our case); $\mu = E_F$ is the chemical potential or Fermi level; and $\Delta(\mathbf{r})$ is the contact-induced pairing amplitude.

For this system, we want to compute the superconducting pairing correlation function $\langle c_{\downarrow,-}(\mathbf{r}) \cdot c_{\uparrow,+}(\mathbf{r})\rangle$ which we treat as a response function of the TBG bands to the external superconducting field $\Delta(\mathbf{r})$ using perturbation theory. First, we assume that the induced pairing amplitude varies continuously within the unit cell (u.c.) of TBG, i.e. $\Delta(\mathbf{R}+\mathbf{a}) \approx \Delta(\mathbf{R})$, where $\mathbf{R}$ is the lattice vector of a certain u.c. and $\mathbf{a}$ a vector within it. Thus, we study the SC correlator averaged over the u.c., such that at a distance $\mathbf{R}$ from the extrinsic superconductor into the TBG it takes the form

$$\phi_{\mathrm{R}} = \int_{\text{u.c.}} d\mathbf{a}\; \langle c_{\downarrow,-}(\mathbf{R}+\mathbf{a}) \cdot c_{\uparrow,+}(\mathbf{R}+\mathbf{a})\rangle. \tag{4.17}$$

Here, besides the dominant induced Cooper pair components with opposite spin $(\uparrow,\downarrow)$ and valleys $(+,-)$ [19, 216], a possible small admixed intravalley component in TBG is expected to be quickly suppressed with $\mathbf{R}$.

By treating the pairing term $\Delta(\mathbf{R})$ as a perturbation and taking the linear approximation, the main form of the studied SC correlator is derived:

$$\phi_{\mathrm{R}} = \sum_{\mathbf{q},\mathbf{k}} \sum_{\mathbf{R}'} e^{i\mathbf{q}(\mathbf{R}-\mathbf{R}')} \Delta(\mathbf{R}') \sum_{n,n'} \phi^{\text{disp}}_{\mathbf{k},\mathbf{q},n,n'}\; \phi^{\text{geom}}_{\mathbf{k},\mathbf{q},n,n'}. \tag{4.18}$$

This quantity can thus be expressed as the Fourier transform of the product of two contributions. The first term

$$\phi^{\text{disp}}_{\mathbf{k},\mathbf{q},n,n'} = \frac{\tanh\left(\xi_{-\mathbf{q}/2,n'}/2\right) + \tanh\left(\xi_{+\mathbf{q}/2,n}/2\right)}{\xi_{\mathbf{k}-\mathbf{q}/2,n'} + \xi_{\mathbf{k}+\mathbf{q}/2,n}} \tag{4.19}$$

represents the kinetic contribution to the induced superconductivity, which is determined by the dispersion $\xi_{\mathbf{k},n} = E_{\mathbf{k},n} - \mu$ of the n-th electronic band with respect to the Fermi level, and resembles the structure of the finite-momentum Cooper susceptibility. Importantly, the induced Andreev pairs do not need to reside only in one single band at the Fermi level E_F, but can also have weight across multiple bands, as the sum over n in Eq. (4.18) indicates. The contribution from this multiband pairing to ϕ_{R}, however, diminishes the further these bands are from E_F and the larger their dispersion is (see Eq. (4.19)), and thus is expected to be significant only in the flattest bands. Andreev pairs formed by two electrons belonging to two different bands can also contribute to Eq. (4.19) if $n \neq n'$, known as an interband process.

The second term in Eq. (4.18),

$$\phi^{\text{geom}}_{\mathbf{k},\mathbf{q},n,n'} = \left| \int_{\text{u.c.}} d\mathbf{a}\ e^{i\mathbf{q}\mathbf{a}}\ u^{\dagger}_{\mathbf{k}-\mathbf{q}/2,n'}(\mathbf{a})\ u_{\mathbf{k}+\mathbf{q}/2,n}(\mathbf{a}) \right|^2, \tag{4.20}$$

involves the overlap between Bloch states at different momenta and is, thus, determined by the quantum geometry of the bands. To prove this, we can take the flat band limit by approximating the bands to a flat dispersion $\xi_{\mathbf{k},n} \xrightarrow[\text{F.B.}]{} 0$. Further expanding over small values of $\mathbf{q}$, we end up with

$$\phi_{\text{R}} \xrightarrow[\text{F.B.}]{} \sum_{\mathbf{q},\mathbf{R}'} e^{i\mathbf{q}(\mathbf{R}-\mathbf{R}')} \Delta(\mathbf{R}') \sum_{n,n',\mathbf{k}} \left[\delta_{n,n'} - g_{\mu\nu,nn'}(\mathbf{k}) q^{\mu} q^{\nu} - A_{\mu\nu}(\mathbf{k}) q^{\mu} q^{\nu} + \mathcal{O}(|\mathbf{q}|^4) \right], \tag{4.21}$$

where $g_{\mu\nu,nn'}(\mathbf{k})$ is the quantum metric of a multiband system:

$$g_{\mu\nu,nn'}(\mathbf{k}) = \text{Re}\left(\delta_{n,n'} \langle \partial_{\mu} u_{\mathbf{k},n} | \partial_{\nu} u_{\mathbf{k},n} \rangle - \langle \partial_{\mu} u_{\mathbf{k},n'} | u_{\mathbf{k},n} \rangle \langle u_{\mathbf{k},n'} | \partial_{\nu} u_{\mathbf{k},n} \rangle \right). \tag{4.22}$$

Thus proving the connection between the quantum metric (compare Eq. (4.22) and Eq. (4.3)) and the formation of the contact-induced superconductivity. It is worth noting that, in the flat band limit, the filling factor of the now completely flat bands loses its meaning. Therefore, to study the contribution from the quantum geometry in Eq. (4.20) to the induced-superconductivity in TBG, we do not do it under this flat band limit but rather analyze how it changes ϕ_{R} in Eq. (4.18), comparing to the dispersion term in Eq. (4.19) alone, as we will see below.

We note that ϕ_{R} is a quantity that decays the further it travels into the TBG from the s-wave superconductor. Therefore, it can be thought as the coherence length, which is a proxy of the critical current. If one is bigger, so is the other, and vice-versa. To compare ϕ_{R} with our experimental I_c, we take its value at a distance in unit cells coinciding with

the center of our junctions. With this monotonic relation between the two quantities, the main features in the twist-angle and filling dependence of I_c are expected to be captured by ϕ_{R}. The strength of this formalism lies in that we can explicitly account for the different

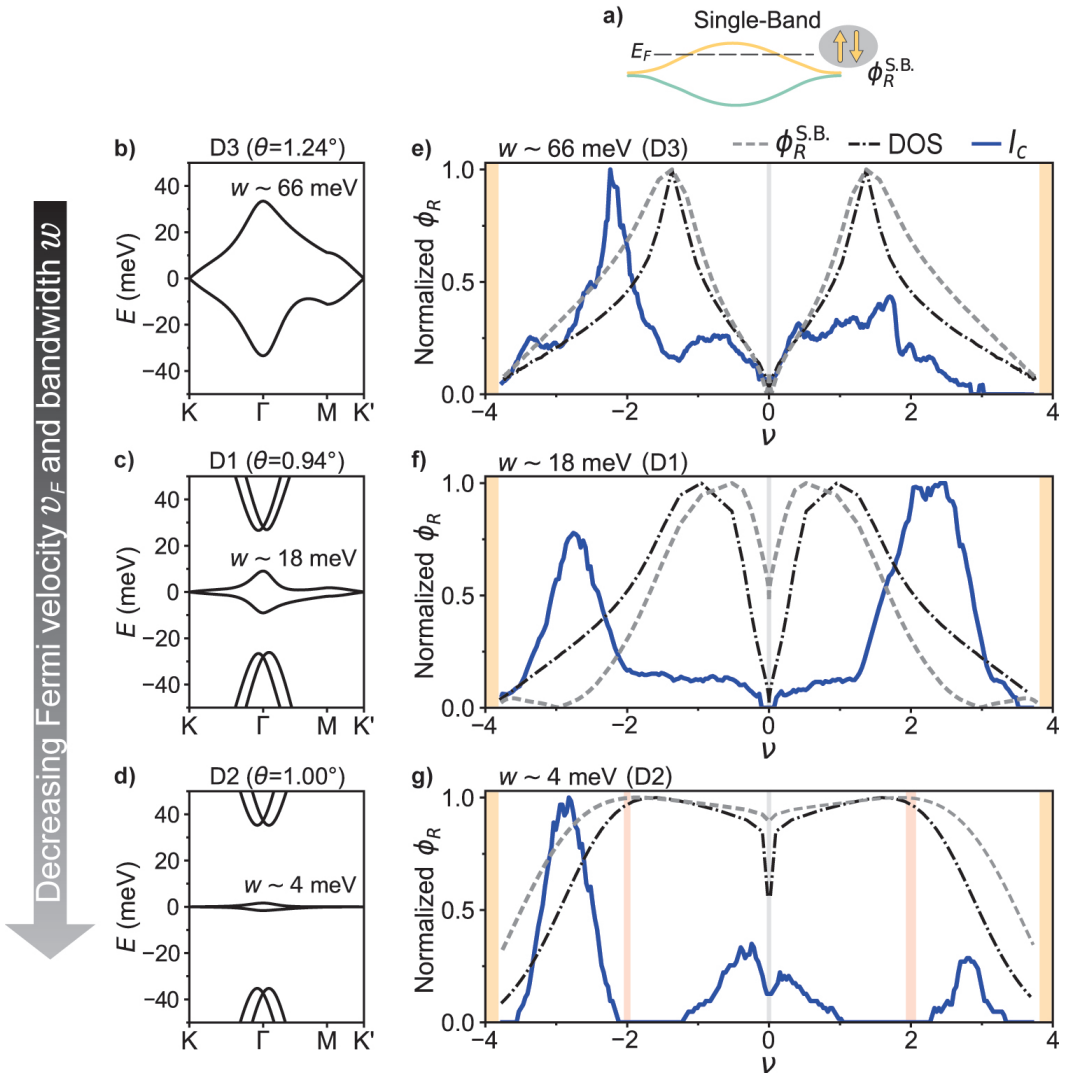

Fig. 4.6: Proximity effect with decreasing bandwidth in the flat bands. a) Sketch illustrating the contribution to the induced superconductivity accounted for. Here, we take the atomic limit and thus only consider the contribution from the dispersion of the same single band where the Fermi level E_F lies, $\phi_{\mathrm{R}}^{\mathrm{S.B.}}$. **b-d)** Band structure of the TBG continuum model along high-symmetry points for the three different θ corresponding to samples D3, D1 and D2, respectively. The bandwidth w of the flat bands is also shown. **e-g)** Computed superconducting correlator ϕ_{R} vs filling factor ν for the single-band process illustrated in **a** (gray-dashed line), along with the density of states from the band structures in **b-d** (black-dotted line). The experimental I_c is shown in dark blue.

contributions to the proximity effect, which include the band dispersion (single band and multiband) and the quantum geometric terms.

We thus begin by studying only dispersion-driven effects by taking the atomic limit, where the Bloch states are completely momentum independent, exactly like an atomic insulator. In this limit, we get $\phi^{\text{geom}}_{\mathbf{k},\mathbf{q},n,n'} \xrightarrow[\text{A.L.}]{} \delta_{n,n'}$, so that not only the quantum geometric contribution of the states is suppressed, but also removes the interband contributions to the SC correlator completely, leaving $\phi_{\text{R}} \sim \sum_{\mathbf{k},\mathbf{q}} \sum_n \phi^{\text{disp}}_{\mathbf{k},\mathbf{q},n,n}$.

At first, we constrict the Cooper pairs contributing to the proximity effect to only be formed from the same band where the Fermi level lies, e.g. the electron flat band (Fig. 4.6a). We can do this in Eq. (4.18) by not taking into account the sum over other bands n. This single-band contribution is thus

$$\phi^{\text{S.B.}}_{\text{R}} \sim \sum_{\mathbf{k},\mathbf{q}} \phi^{\text{disp}}_{\mathbf{k},\mathbf{q},n,n}. \tag{4.23}$$

In this case, as ν is varied, we find that the calculated $\phi^{\text{S.B.}}_{\text{R}}$ approximately follows the density of states for all w (Fig. 4.6e-g). It shows peaks close to half-filling $\nu = \pm 2$, which rapidly decrease close to the band edges $\nu = \pm 4$ and the CNP. Although this scenario very well matches the broadest bandwidth $w \sim 66$ meV (Fig. 4.6e) with our I_c measurements, it dramatically fails to describe the observed features of devices D1 and D2 with lower w (see Fig. 4.6f-g). For the flattest bands, $w \sim 4$ meV, the peaks in $\phi^{\text{S.B.}}_{\text{R}}$ strongly broaden and show an almost constant value across the entire range of ν, failing to produce dome shaped regions.

By now departing from the atomic limit, we incorporate the overlap between Bloch states at different momenta, which is determined by the quantum metric of the bands; known to play a dominant role in the superfluidity of flat band systems [192–197]. The result,

$$\phi^{\text{Q.G.}}_{\text{R}} \sim \sum_{\mathbf{k},\mathbf{q}} \phi^{\text{disp}}_{\mathbf{k},\mathbf{q},n,n} \phi^{\text{geom}}_{\mathbf{k},\mathbf{q},n,n}, \tag{4.24}$$

is shown in the orange traces of Fig. 4.7f-h. In the case of the highest w, with considerable dispersion, $\phi^{\text{Q.G.}}_{\text{R}}$ (Fig. 4.7f) does not change much from $\phi^{\text{S.B.}}_{\text{R}}$ (Fig. 4.6e). However, consistently with the importance of this contribution in flat bands, $\phi^{\text{Q.G.}}_{\text{R}}$ is strongly altered from $\phi^{\text{S.B.}}_{\text{R}}$ and the DOS as the bandwidth is lowered in Fig. 4.7g-h, giving rise to dome shaped features that move closer to the band-edges, as experimentally observed in the I_c of devices D1 with $w \sim 18$ meV and D2 with $w \sim 4$ meV. We find that overall, the $\phi^{\text{Q.G.}}_{\text{R}}$ term better matches the findings of the $w \sim 4$ meV case, as it predicts a finite induced-superconducting phase in the center of the band and close to the CNP, which is observed in device D2.

Similar trends are found when multiband processes are considered, shown in the bright blue traces of Fig. 4.7f-h. Here, in the atomic limit, so that only dispersion-driven effects weigh in, we sum over other bands where E_F lies:

$$\phi^{\text{M.B.}}_{\text{R}} \sim \sum_{\mathbf{k},\mathbf{q}} \sum_n \phi^{\text{disp}}_{\mathbf{k},\mathbf{q},n,n}. \tag{4.25}$$

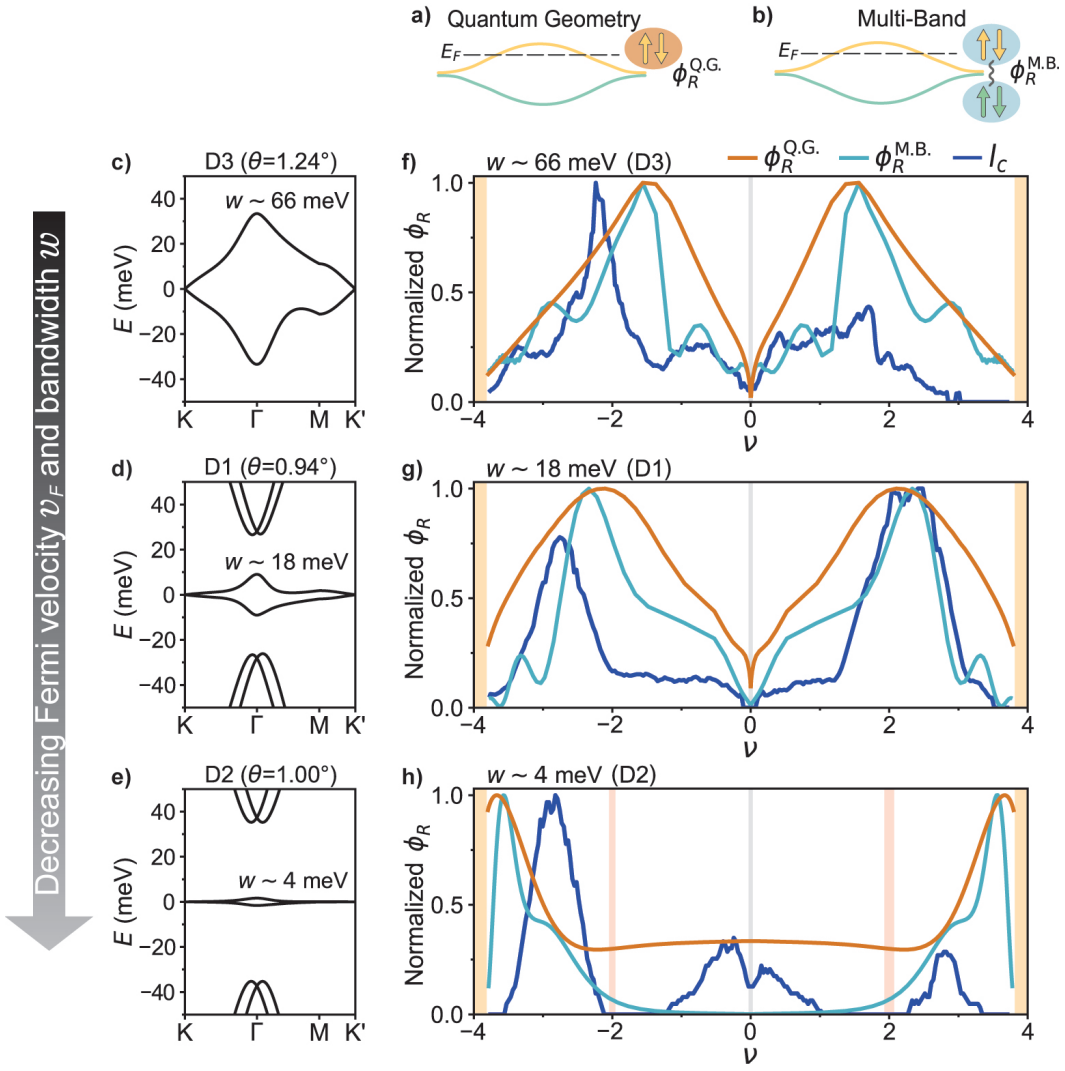

Fig. 4.7: Quantum geometric and multiband contributions to the induced superconductivity in the flat bands. a-b) Sketches illustrating the different contributions to the induced superconductivity. The color of the spin of the electrons forming the Andreev pair indicates which band they are coming from. In **a**, we depart from the atomic limit and consider the quantum geometry contribution, alongside the dispersion from the same band where the Fermi level E_F is. In **b**, we take the atomic limit and consider not only the dispersion from the same band where the E_F lies, but also the interference with more bands, i.e. multiband pairing. **c-e)** Band structure of the TBG continuum model along high-symmetry points for the three different θ corresponding to samples D3, D1 and D2, respectively. The bandwidth w of the flat bands is also shown. **f-h)** Computed superconducting correlator ϕ_{R} vs filling factor ν for the two processes illustrated in **a-b**, following the same color-code as the sketches of the Andreev pairs. The experimental I_c is shown in dark blue.

As in the case of the quantum geometry, $\phi_{\mathrm{R}}^{\mathrm{M.B.}}$ departs from the single-band case and the DOS as w decreases. The quantitative match with the experimental data, especially with D1, confirms the importance of this mechanism in driving superconducting phases in the flat band limit, as previously pointed out. The moderate mismatch in D2 compared to D1 and D3 could come from the fact that only the former shows correlated states due to interactions, which are not considered in our model.

We also note that if both quantum geometry and multiband effects are considered, an interband effect also weighs in, where $n \neq n'$ and the Andreev pairs are formed by two electrons coming from two different bands. This results in $\phi_{\mathrm{R}} \sim \sum_{\mathbf{k},\mathbf{q}} \sum_{n,n'} \phi^{\mathrm{disp}}_{\mathbf{k},\mathbf{q},n,n'} \phi^{\mathrm{geom}}_{\mathbf{k},\mathbf{q},n,n'}$, giving broader single domes around $|\nu| \gtrsim 2$, similar to $\phi_{\mathrm{R}}^{\mathrm{Q.G.}}$ and $\phi_{\mathrm{R}}^{\mathrm{M.B.}}$ (this can be found in the Supplementary material of [P2]).

Finally, we have shown the importance of the unconventional quantum geometric and multiband effects when describing the SC proximity effect in the flat bands. In the case of the dispersive bands, the primary contributions do not include unconventional terms. Since the dispersive bands have large characteristic group velocities, the contact-induced superconductivity is mainly determined by the electrons in the small (relative to the bandwidth) vicinity of the Fermi surface. We should clarify here that the multiband effect is also present in the dispersive bands when and only when the Fermi surface crosses multiple bands. However, in stark contrast to the flat bands, here, the proximity effect is expected to be well described by the energetically local quantity at the Fermi surface. Motivated by the fact that the overlap between the Bloch functions from different bands is generally small ($\phi^{\mathrm{geom}}_{\mathbf{k},\mathbf{q}=0,n,n'} \sim \delta_{n,n'}$) we can also neglect the interband pairing. To demonstrate the conventional nature of the dispersive bands' proximity effect, we show in Fig. 4.8 that the DOS of the continuum model captures well the qualitative behavior of the measured I_c.

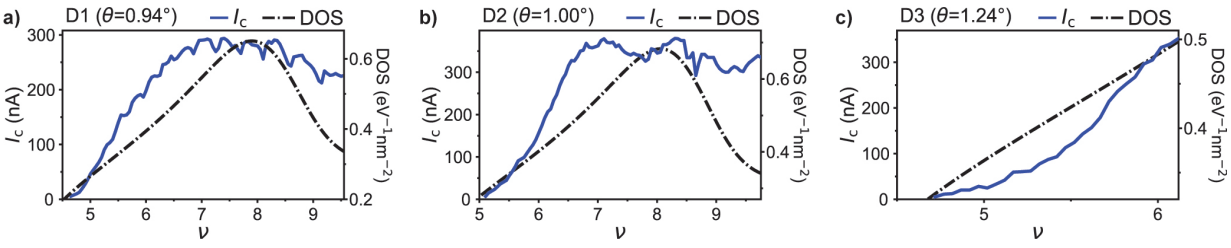

Fig. 4.8: Proximity effect in the dispersive bands. a-c) Measured critical current in the dispersive bands (solid blue lines, left axis), along with the calculated density of states from the continuum model (black dashed lines, right axis), as a function of filling ν; respectively for devices D1, D2, D3.

Overall and despite the simplicity of the continuum model in describing the flat bands of TBG, the qualitative agreement with the data highlights that when the bandwidth reaches the flat band limit, quantum geometric and multiband processes could become important in the understanding of the susceptibility of TBG to develop superconducting

phases [217]. It may explain the formation of dome shaped SC regions between half-filling and the band edges, which roughly coincide with the regions that typically also show intrinsic superconductivity in TBG devices at the magic angle. It is therefore interesting to consider whether similar effects, as the ones that were worked out here, can also explain the position of the SC domes in TBG.

Nevertheless, we want to stress that to fully capture and explain the proximity effect in this correlated system, future theoretical models should further account for interactions, as our current approach does not explain the vanishing I_c due to the correlated states at integer fillings. The presence of interactions at half-fillings of the bands in our TBG JJs is further suggested by a consistent observation of a symmetry-broken Josephson effect, which will be the focus of the remainder of this chapter.

4.5 The Josephson diode effect

In a conventional JJ, the current–phase relation is approximately $I_s(\varphi) = I_c \sin(\varphi)$. Since changing the direction of the supercurrent across the junction must cause a change of sign in the phase difference φ between the two superconductors, this yields

$$I_s(\varphi) = -I_s(-\varphi). \tag{4.26}$$

From here, we can conclude that the critical current I_c is the same in magnitude for a forward (I_c^+) and reverse (I_c^-) current bias. This relation stems from the assumed inversion symmetry in the junction, and the inherent time-reversal symmetry of conventional superconductors, where the Cooper pairs are formed by time-reversal pairs of electrons [102]. Thus, achieving a Josephson junction with a preferred direction, that is, where $I_c^+ \neq I_c^-$, would require to deliberate break one of those symmetries. From a practical standpoint, this device would create a dissipationless supercurrent in one direction while resistive in the opposite; i.e. a superconducting analog of a semiconducting diode. As such, this effect has been coined as the Josephson diode effect (JDE) if engineered in a JJ [218], or superconducting diode effect if found in a bare superconducting material [219].

Since the 1990s, researchers have explored methods to obtain a non-reciprocal supercurrent in a more trivial way, by means of creating asymmetric or nonuniform JJs thanks to self-induced field effects from the supercurrent [220–222]. Such early approaches included asymmetric SQUIDs [223] or a rectifying motion of Josephson [224, 225] or Abrikosov vortices [226, 227]. These devices relied on engineering the inversion symmetry-breaking, while the time-reversal symmetry (TRS) was broken by applying an external magnetic field B. Thus, the JDE was observable at a finite field only.

More recent works in the late 2010s showed that this non-reciprocity could be induced by Rashba spin-orbit coupling (SOC) in a non-centrosymmetric superconductor [228–230]. In these Rashba-type superconductors, where the spatial inversion is uniaxially broken

along, let's say the z axis, the spin-orbit interaction causes spin-dependent band splitting, so that the Cooper pairs are formed by electrons with opposite spin and momenta (both in the x-y plane), i.e. $\sigma(\boldsymbol{k}) = -\sigma(-\boldsymbol{k})$. By then applying and in-plane time-reversal symmetry breaking magnetic field, say B_y, this creates an imbalance in the energy of the electrons in the orthogonal direction of the plane depending on whether their spin is parallel or antiparallel, thus creating a nonlinear response current I_x, which can be detected in a transport experiment if the strength of the Rashba spin-orbit coupling is strong enough. In a more general framework, it was shown that broken symmetries can lead to non-linear electrical and optical responses, known as Magneto-Chiral Anisotropy [231, 232]. The expression for the resistance within this theory is

$$R = R_0(1 + \gamma \boldsymbol{B} \cdot \boldsymbol{I}). \tag{4.27}$$

For the case we are discussing here, γ is related to the strength of the Rashba SOC, and the field $\boldsymbol{B}$ and current $\boldsymbol{I}$ vectors need to be coplanar and perpendicular to the broken spatial symmetry. In these experiments, the non-linear term in the resistance was observed within the second-order:

$$R^{2w} = \frac{1}{2}\gamma R_0 \mu_0 B I, \tag{4.28}$$

which can be measured with typical lock-in techniques by detecting the second harmonic of the reference frequency signal.

In 2020, another superconducting diode was intrinsically found in a stacked Nb/V/Ta superlattice, which is superconducting and non-centrosymmetric [233]. The difference with other works being that they directly observed the relation $I_c^+ \neq I_c^-$ at finite magnetic field. These discoveries sprouted more active research over the past five years on finding quantum materials with these broken symmetries.

One straightforward approach is to proximitize a non-centrosymmetric weak link. Depending on whether the SOC mechanism is driven by Rashba-type interactions or valley-Zeeman splitting, the Josephson diode is enabled by an in-plane [234, 235] or out-of-plane [236–238] magnetic field, respectively. Either of these produce a non-sinusoidal current-phase relation, so that Eq. (4.26) does not hold anymore and $I_c^+ \neq I_c^-$. Indeed, the most basic model of a Josephson diode includes an anomalous phase shift φ_0 in the CPR, and/or second harmonic terms $\sin(2\varphi)$ [219, 239–242]. This is straightforward to see, as this modified CPR simply is

$$I_s(\varphi) = \alpha_1 \sin(\varphi) + \alpha_2 \sin(2\varphi + \varphi_0) \tag{4.29}$$

where $\alpha_2 \ll \alpha_1$ are real prefactors. The maxima of Eq. (4.29) is then achieved at $\varphi \approx \pi/2$, so that the critical current in the two directions is:

$$I_c^{\pm} = I_s(\pm\pi/2) = \alpha_1 \mp \alpha_2 \sin(\varphi_0), \tag{4.30}$$

evidencing a JDE only if $\alpha_2, \varphi_0 \neq 0$.

Another way of engineering a Josephson diode is to leverage the inversion symmetry breaking of the unconventional FFLO superconductors [243], where the Cooper pairs acquire a finite momentum shift q that spatially modulates their pairing by Δe^{2iqx}. The modulation occurs in a certain direction x along which a perpendicular in-plane field B_y is applied, such that $q \approx \pi W L B_y / 2\Phi_0$ [244, 245]. While the Cooper pairs in a BCS superconductor would normally have a bound energy of Δ at $\pm k_F$, here they gain an energy shift $\Delta \pm \hbar q v_F$ now that they acquire momentum [246]. In a JJ, this acquired momentum yields extra terms in the CPR, such as a phase-shift $\varphi_0 = 2\arccos(\hbar q v_F/\Delta)$, thus producing a JDE [246–248].

One final very interesting case is to achieve a JDE when no magnetic field is applied, which can only be done if there exists a spontaneous breaking of TRS in the material as a result of finite magnetization. Some experiments have proven this by proximitizing a magnetic tunnel barrier [249, 250] or weak link [P3] with the overall structure lacking inversion symmetry, or by having a bare superconductor that couples and magnetizes under an external magnetic field [251, 252]. Nevertheless, it is also worth noting that this zero-field JDE can also be engineered by trapping flux in the junctions [253].

In this section, we report the observation of the JDE in our TBG JJs, which is found to change upon gate voltage, twist-angle and magnetic field, making these devices a highly tunable platform where to study this effect. Later in Section 5.2 we will also show the observation of the JDE in gate-defined TBG JJs.

4.5.1 Interference patterns with broken inversion symmetry

We start by studying an interference pattern of the $\nu < -2$ superconducting dome in device D2 by setting $\nu = -2.5$. When recording the critical current as a function of magnetic field in opposite directions of the d.c. current, $I_c^+(B)$ and $I_c^-(B)$, we find that $I_c^+(B) \neq |I_c^-(B)|$, as clearly seen in the mid panel of Fig. 4.9a. Such observation indicates inversion symmetry is broken in our JJs and is unlike the conventional symmetric patterns observed near the CNP or in the dispersive bands (see Fig. 4.1e and Supplementary of [P2]).

As explained before, this non-reciprocity is a hallmark of the Josephson diode effect, which requires both inversion, C_{2z}, and time-reversal symmetry breaking. Importantly, in our devices TRS is broken by applying an external magnetic field perpendicular to the graphene layers. This rules out Rashba spin-orbit coupling as a possible mechanism, where an in-plane magnetic field perpendicular to the direction of the current is needed to produce the non-reciprocity [219, 234, 235]. Furthermore, the TBG weak link itself does not intrinsically break TRS, as no asymmetry is recorded at zero field, i.e. we find $I_c^+(0) = |I_c^-(0)|$. This is further confirmed by reversing both current and field directions, yielding $I_c^+(B) = |I_c^-(-B)|$ (see bottom panel of Fig. 4.9a); an expression that conserves this said symmetry.

While the inversion symmetry breaking enables the realization of a Josephson diode

at finite magnetic fields, the time-reversal invariance ensures that the direction of the supercurrent can be reversed, making the diode programmable by applying exact opposite fields. Such programmability is illustrated in Fig. 4.9b, where the asymmetry of the $\mathrm{d}V/\mathrm{d}I$ curves with respect to I reveal the non-reciprocal transport that breaks inversion symmetry and enables a JDE at finite field. Here the shaded regions mark the I values at which the Josephson diode is operational. Both curves are also antisymmetric between each other, confirming the underlying TRS of the system.

The rectification measurements in Fig. 4.9c demonstrate the operation of the diode, where exact opposite values of current bias are applied over time, showing that the dissipationless flow of the electric current happens in one direction only. The reversibility of the direction of the diode is achieved when an exact opposite magnetic field is applied, following the same color code as in Fig. 4.9b. More recitification measurements at other fields and fillings can be found in the Supplementary material of [P2].

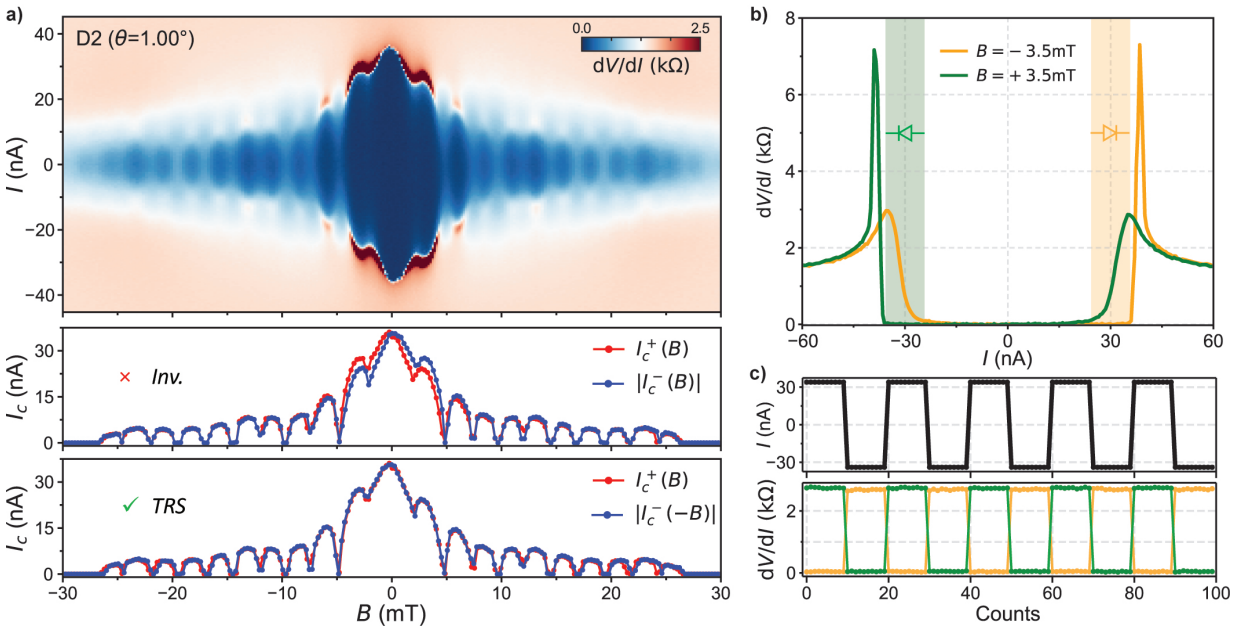

Fig. 4.9: Asymmetric critical current oscillations and reversible Josephson diode effect. a) Top panel shows measured differential resistance $\mathrm{d}V/\mathrm{d}I$ as a function of d.c. bias current I and magnetic field B, at $\nu = -2.5$. The critical current of the dark-colored oscillations is extracted for positive (I_c^+) and negative (I_c^-) directions of I. These are represented for the same and opposite values of magnetic field in the middle and bottom panels, respectively. **b)** $\mathrm{d}V/\mathrm{d}I$ traces measured at opposite magnetic fields. Shaded regions mark the current bias values at which the Josephson diode is operational. The measurements are performed at $\nu = -2.9$. **c)** Demonstration of the reversible JDE in **b**, performed by switching between the superconducting and normal states when opposite currents are applied, in this case +34 nA and −34 nA. All data belongs to sample D2. Adapted from [P2].

Previous works on gate-defined TBG JJs [P3] and twisted trilayer superconducting devices [251] had demonstrated zero-field superconducting diodes, although only after a magnetization field was applied to them. That is, upon cooling down of the samples and without previously applying any moderate magnetic field (> 50 mT), the asymmetry at zero field was not observed. This suggests that the ground states of these systems do preserve TRS in principle, but can couple to a sufficient strong coercive field. Alternatively, in this work we avoid magnetizing our junctions to prevent trapped flux in the superconducting leads [253–255], opting instead to record the interference patterns while sweeping carefully the field from top to bottom. This also eliminates remanent fields in the coil of our magnet, so that the zero field point coincides with a zero magnetic flux in the devices.

4.5.2 Symmetry-breaking across a large range of filling

Another difference with the previous observation of the Josephson diode in TBG [P3] is that, in this work, we find that the key features reported in Fig. 4.9 extend across the entire filling of the SC dome, spanning from $\nu \sim -2$ to $\nu \sim -3.5$. This is depicted in Fig. 4.10a, where I_c^+ and I_c^- are shown for identical (left panel) and opposite (right panel) magnetic field values. The asymmetry

$$\Delta I_c = I_c^+(B) - |I_c^-(B)| \tag{4.31}$$

is found most pronounced at the center of the dome at $\nu = -2.9$, but is no longer detectable at the edges of it at $\nu = -2.3$ and $\nu = -3.4$. This is also the case for the diode efficiency parameter

$$\eta(B) = \Delta I_c / (I_c^+(B) + |I_c^-(B)|), \tag{4.32}$$

which measures the percentage of rectification in the diode. We represent it at a magnetic flux $\Phi = \Phi_0/2$ in Fig. 4.10b, where it is found to correlate with the I_c of the dome. Here Φ_0 is the superconducting magnetic flux quantum. Furthermore, our observation of inversion symmetry breaking consistently appears in the domes at the hole side of $\nu \sim -2$ for all our TBG JJs close to θ_m (D1-3) and, in some cases (D1-2), on the electron side of $\nu \sim 2$; confirming the reproducibility of our findings. This is shown in Fig. 4.10c, where for all three devices η correlates with the I_c values of their respective domes. In this case, to compare the JDE between different devices we have calculated the maximum value of η between $-2\Phi_0$ and $2\Phi_0$ (see Supplementary in [P2] for more extraction examples). Such extent of the asymmetry with filling suggests a distinct phase to be responsible for the JDE.

According to the Bistritzer MacDonald continuum model, the flat bands of TBG have C_{2z} and spinless time-reversal $\mathcal{T}$ symmetries [9]. Yet, our observations at fillings $|\nu| > 2$ of the flat band do not align with this single-particle framework, suggesting the need to account for interactions capable of spontaneously breaking C_{2z}. Several interacting ground states that spontaneously break either of these symmetries in TBG have been proposed. Valley polarization was suggested to explain the abundance of orbital magnetism and

broken inversion found at these bands [P3] [251, 256, 257], although original nematicity measurements [57, 258] showed C_{3z} symmetry-breaking instead. In addition, recent experiments in scanning tunneling microscopy have pointed towards the most likely candidates at such fillings having intervalley coherent or incommensurate Kekulé spiral orders [74], which do not break C_{2z}. Therefore, none of the above candidates are consistent with our findings, suggesting a different origin. Indeed, a sublattice-polarized phase emerges as the only candidate that fulfills our observed symmetry relations [252, 259, 260], where each valley carries opposite Chern numbers $C = 1$ and $C = -1$.

The inversion symmetry breaking resulting from a geometrical asymmetry in the sample, such as a non-uniform junction with different width of contacts, can be ruled out in

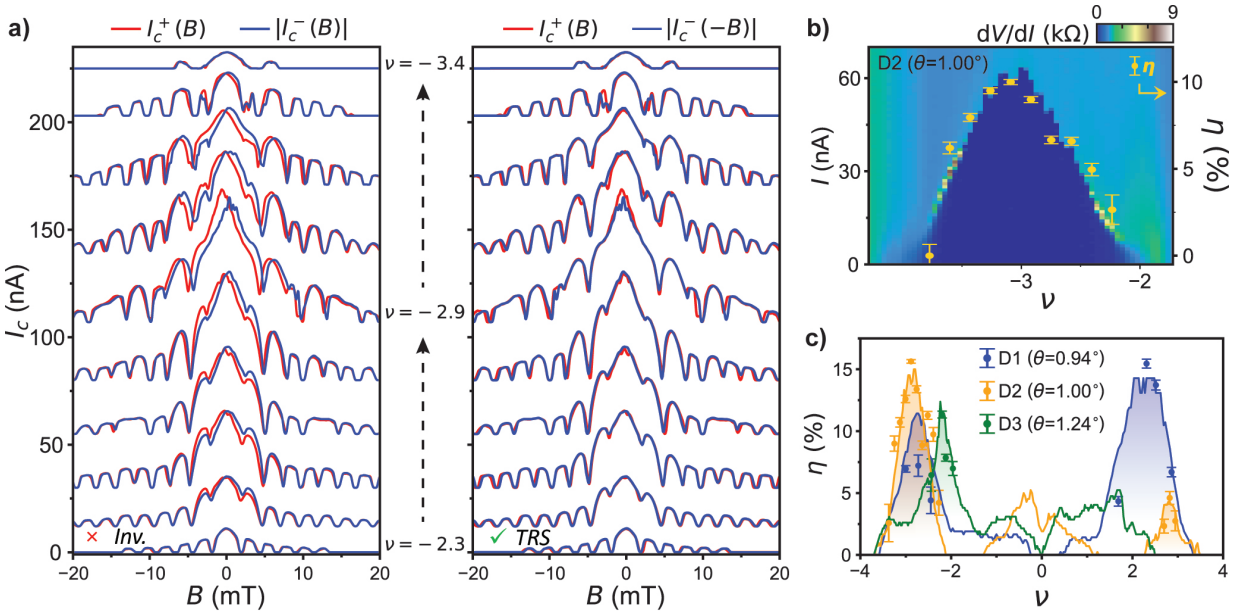

Fig. 4.10: Inversion symmetry breaking and TRS conservation across the whole dome. a) Critical current I_c as a function of magnetic field B for increasing filling factor ν, from bottom to top. The curves are each vertically shifted for clarity. Left panel shows the mismatch between both directions of the current I_c^+ and I_c^-, while the right panel demonstrates the critical currents are equal upon reversing both current and field directions. All traces correspond to D2. **b)** Differential resistance $\mathrm{d}V/\mathrm{d}I$ colormap as a function of d.c. current I (left axis) and ν. Represented along with error bars is the extracted diode efficiency η (right axis) from a as a function of ν and computed at a magnetic flux $\Phi = \Phi_0/2$. All data corresponds to D2. **c)** Maximum value of $\eta(B)$ between $-2\Phi_0$ and $2\Phi_0$, represented with error bars and as a function of ν for all junctions near the magic angle D1-3. The line plots correspond to the critical current at zero field (in arbitrary units) as a function of ν. The shaded regions correspond to fillings of the flat band where a finite asymmetry was recorded. In every case, these domes correlate to the diode efficiency. Adapted from [P2].

our case, given that this effect would be independent of the electron density and yet, the JDE is only observed for specific densities; only in the flat bands and in devices close to the θ_m (see Supplementary in [P2] for all data). Nevertheless, since we cannot quantify the amount of strain in our samples, unlike in STM [74, 261], we cannot rule out that this tuning parameter is favoring a sublattice polarized ground state with broken C_{2z} symmetry at these fillings. We note that this is different from a strain-induced structural breaking of C_{2z}, which would lead to a JDE at all carrier densities.

Self-field effects caused by inhomogeneous current bias and screening currents [97, 253] cannot be the cause of the JDE either, since our small I_c results in a bigger Josephson penetration length $\lambda_J = \Phi_0 tW/4\pi\mu_0 I_c \lambda_L^2 \sim 7$ µm compared to the dimensions of the junction $W \sim 1.5$ µm, $L \sim 0.2$ µm [97, 188, 262]. Here $t \sim 0.6$ nm is the thickness of TBG, μ_0 is the magnetic vacuum permeability and $\lambda_L \sim 400$ nm is the London penetration length of NbTiN [263].

In the next section we discuss the possibility of the JDE being formed by a symmetry broken state or topological edge states leading to a non-sinusoidal current-phase relation, evidenced by the dominant edge supercurrents at these fillings.

4.5.3 Supercurrent dominated by edge states

Analogous observations to ours have been previously reported in JJs with topological insulators as the weak link, where the TRS conservation was forced by the topological protection of these materials when tuned into their quantum spin Hall insulating phase [264–267]. These works showed that these topological edge states, along with higher-order terms that bring the current-phase relation into a non-sinusoidal form, could give a JDE [219, 222]. Testing these possible mechanisms would require phase sensitive measurements, which we leave for future works. Nevertheless, we can perform the analysis described in Subsection 1.4.3 by taking the inverse Fourier transform of the measured $I_c(B)$ in the interference patterns, and calculate their critical current density profile $J_c(x)$, which could at the very least reveal some importance of edge transport in our devices.

Starting with the interference patterns of our samples where the JDE takes places (Fig. 4.11a-b), we observe that the $I_c(B)$ oscillations of the interference pattern do not follow an exponential decay proper of a homogeneous supercurrent profile, but rather stay constant at fields > 10 mT. Furthermore, the absence of the first pair of nodes in $I_c(B)$, and the node-lifting in general, is a signature of an asymmetry in the supercurrent density profile [114, 115]. Indeed, by calculating $J_c(x)$ we find a supercurrent density profile skewed and concentrated on the edges of the sample, in line with previous works on gate-defined TBG JJs [P3].

In contrast, the I_c of the interference patterns from the dispersive bands decay exponentially following the typical Fraunhofer pattern (Fig. 4.11c-d), although occasionally they can feature some node-lifting (Fig. 4.11e-f). This results into a slight asymmetry in

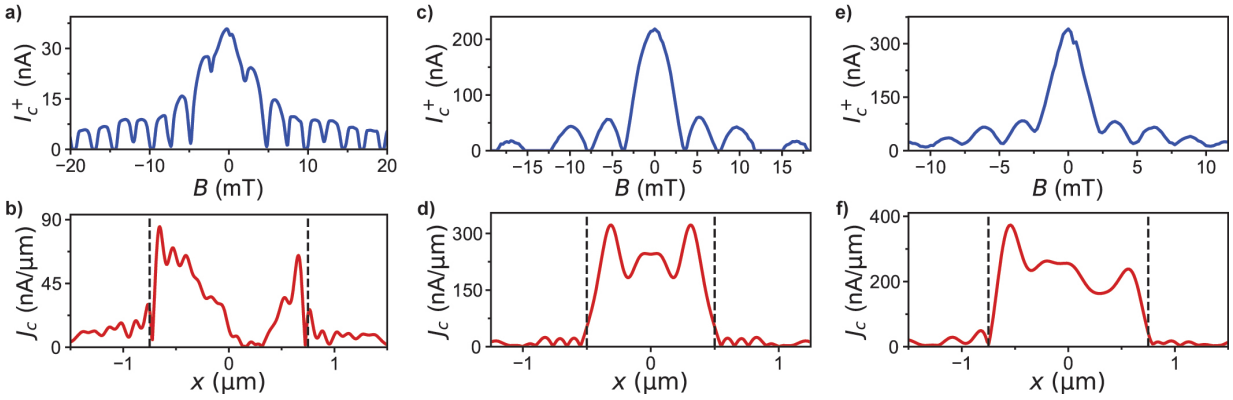

Fig. 4.11: Supercurrent density profile and node-lifting. a) Critical current in one direction of the current, I_c^+ vs magnetic field B, extracted from the interference pattern at $V_g = -30$ V ($\nu = -2.5$) in D2 from Fig. 4.9. **b)** Corresponding critical current density profile J_c as a function of the lateral dimensions x of the JJ. Dashed black lines indicate the physical limit of the device. The same profile is found for I_c^-. **c-d)** Analogous for $V_g = 50$ V ($\nu = 8.8$) in D1. **e-f)** Analogous for $V_g = 50$ V ($\nu = 7.1$) in D2. Adapted from [P2].

the critical current density profile, where the bulk of the junction, $J_c(x = 0)$, nevertheless carries much more supercurrent than in the case of the interference patterns where the JDE is observed (Fig. 4.11b). The fact that no JDE is observed in the dispersive bands proves that the asymmetry in the supercurrent profile resulting in node-lifting is not enough no produce a diode effect, and an anomalous or extra term in the current-phase relation is needed. Testing these possible mechanisms would require phase sensitive measurements [202, 267], which we leave for future works. Such higher harmonics or anomalous phases could be a result of a symmetry-broken state as discussed in the previous section [268, 269], or by topological edge states [264, 266, 267]. We expand on the latter case, since the abundance of edge transport at these fillings compared to others is already hinted in Fig. 4.11 and was also observed in the gate-defined TBG JJs [P3].

By performing a more quantitative analysis, in Fig. 4.12a we show the extracted critical current density profile $J_c(x)$ for all the fillings of the $\nu < -2$ dome in device D2, following the same order as in Fig. 4.10a. To quantify the amount of supercurrent that is carried through the edges and the bulk, we integrate the obtained $J_c(x)$ over the regions shown in Fig. 4.12b. The results are plotted in Fig. 4.12c, following the same colour code as in Fig. 4.12b. The error bars are set by integrating over a 5% bigger/smaller width x. Compared to the I_c of the dome measured at zero field (black datapoints), the supercurrents carried by the bulk and the edges follow the same trend, peaking at $\nu = -2.9$. Furthermore, the left edge of the sample carries significantly more supercurrent than the bulk, while the right edge supports about the same amount. To better visualize this, we plot in Fig. 4.12d the ratio of the edge and bulk critical currents. Indeed, the right edge I_c (orange) is about one time the bulk, except from the right side of the dome, between $\nu = -2.3$ and -2.5, where it

doubles the bulk supercurrent. The left edge I_c (violet) is twice the bulk, reaching three times on the right side of the dome. In conclusion, while it is true that edge transport dominates over the bulk, its magnitude does not scale with the I_c of the SC dome as the diode efficiency η does (see Fig. 4.10c-d), but rather stays constant across the dome.

Finally, given the range of twist-angles and fillings of the flat bands where the JDE is found, a natural question is whether the presence of the intrinsic superconducting phase of TBG (S' in the following) could play a significant role. However, and as noted before, the observed I_c in the superconducting dome of D2 at $\nu < -2$ reaches its maximum at $\nu \sim -2.9$ and spans down to $\nu \sim -3.5$, exceeding the range of filling where TBG typically shows an intrinsic SC state [12, 14, 17]. Furthermore, we do not observe any discontinuity in the I_c vs ν, T or B, nor an additional resonance in the $\mathrm{d}V/\mathrm{d}I$, nor a change in the interference patterns as the filling is tuned from $\nu = -2$ to $\nu = -3.5$ (see Fig. 4.10a). Such features would be expected if the TBG was intrinsically superconducting in the typical filling range

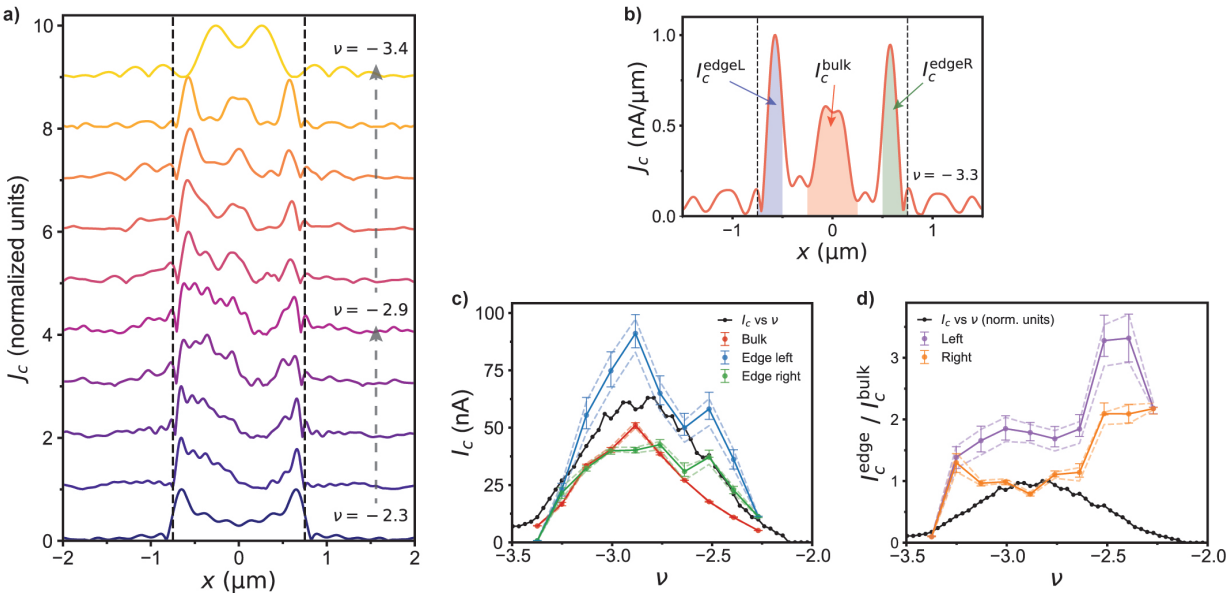

Fig. 4.12: Supercurrent density profile in the Josephson diode: Bulk vs Edge. **a)** Waterfall plot of the critical current density profile J_c as a function of the lateral dimensions of the junction x, for different values of filling of the band ν. Each trace of J_c has been normalized and spaced by one unit. Dashed black lines indicate the physical limit of the junction. **b)** Normalized J_c vs x at $\nu = -3.3$ from **a**. The red, blue and green areas correspond to the critical current in the bulk, left edge and right edge of the sample, respectively. **c)** Critical current I_c vs ν. Black data is the extracted I_c at zero field (same as in Fig. 4.10b). The I_c of the bulk and the edges are extracted from the supercurrent density profiles in **a**, following the example in **b**. **d)** Ratio of the I_c of the edges and the bulk as a function of ν. Black data is the extracted I_c at zero field, in normalized units. All data corresponds to device D2. Adapted from [P2].

$-2.8 < \nu < -2$ [202, 205, 270]. Additionally, we observe oscillations in I_c whose period matches the total area of the junction, as expected for an SNS junction. If the TBG was superconducting, there would be no oscillations and the I_c would monotonously decay with field [202, 205]. The independence in temperature of the inductance associated with the junction is also consistent with this, as we explain next.

The temperature dependence of the interference patterns, measured at fixed $\nu = -2.9$ for device D2, are presented in Fig. 4.13a-c. There it can be seen that the asymmetric oscillations persist up to $T \sim 0.8$ K, beyond which the supercurrent gets washed out as thermal fluctuations $k_B T$ become comparable to the Josephson energy $E_J = \hbar I_c / 2e$ [93]. We have demonstrated that the supercurrent where the JDE is observed is dominated by a skewed edge transport. Such SQUID-like inhomogeneous supercurrent density profile, along with the high kinetic inductance of the superconducting TBG [59, 202, 206] has been proved to give rise to an asymmetry in the interference patterns of TBG gate-defined structures [201, 206]. If this was the case in our experiment, the inductance associated with the tilt of the interference pattern should increase with temperature and diverge once it reaches the critical temperature [201]. Instead, we find it independent of the temperature, as seen in Fig. 4.13e.

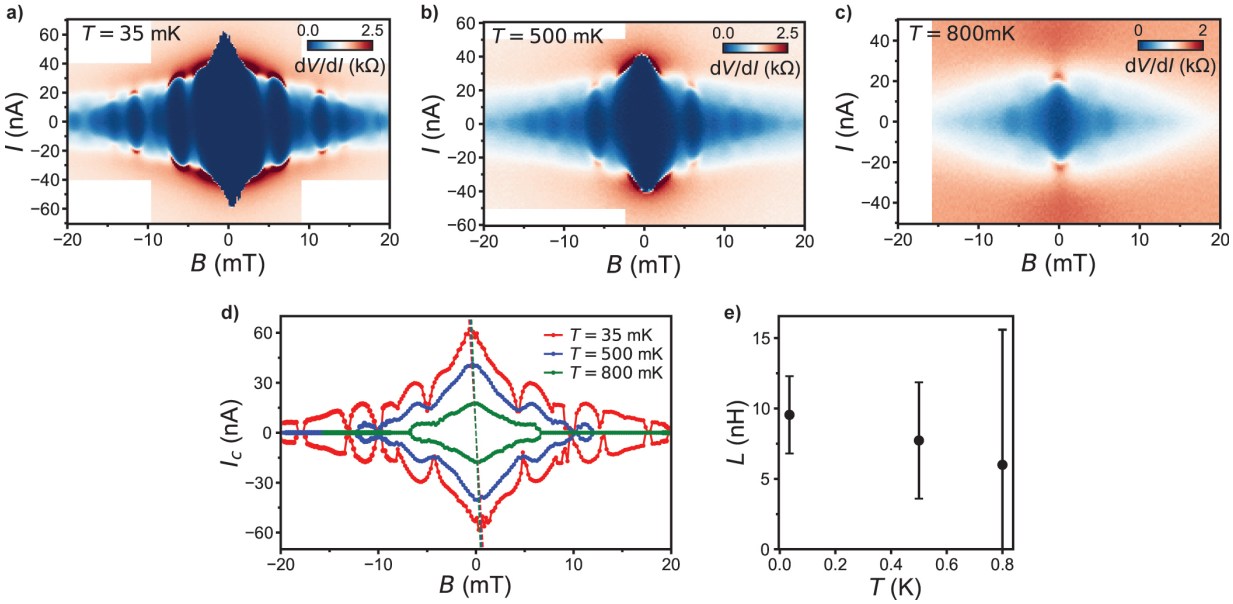

Fig. 4.13: Temperature dependence of the asymmetric oscillations. a-c) Interference patterns measured at fixed $\nu = -2.9$ for device D2, at different temperatures. **d)** Corresponding extracted critical current. **e)** Extracted inductance $L = \Phi / I$ from the slope of the maxima of the center lobes in the I_c vs B curves in **d**, showing independence with temperature. Adapted from [P2].

Chapter 5

Gate-defined junctions of monolithic twisted bilayer graphene

The work presented in this chapter led to the following publications:

[P3] J. Díez-Mérida, **A. Díez-Carlón**, S.Y. Yang, Y.-M. Xie, X.-J. Gao, J. Senior, K. Watanabe, T. Taniguchi, X. Lu, A.P. Higginbotham, K.T. Law, D.K. Efetov. "Symmetry-broken Josephson junctions and superconducting diodes in magic-angle twisted bilayer graphene". *Nature Communications* 14, 2396 (2023). https://doi.org/10.1038/s41467-023-38005-7.
Contributions: Sample fabrication, measurements, data analysis, discussion and paper writing.

[P5] R. Luque-Merino, D. Călugăru, H. Hu, J. Díez-Mérida, **A. Díez-Carlón**, T. Taniguchi, K. Watanabe, P. Seifert, B.A. Bernevig and D.K. Efetov. "Interplay between light and heavy electron bands in magic-angle twisted bilayer graphene", *Nature Physics* (2025). https://doi.org/10.1038/s41567-025-02912-x
Contributions: Sample fabrication, transport measurements and discussion.

[P8] J.D. Mehew, R. Luque-Merino, H. Ishizuka, A. Block, J. Díez-Mérida, **A. Díez-Carlón**, K. Watanabe, T. Taniguchi, L.S. Levitov, D.K. Efetov, K.-J. Tielrooij. "Ultrafast Umklapp-assisted electron-phonon cooling in magic-angle twisted bilayer graphene", *Science Advances* 10, adj136 (2024). https://doi.org/10.1126/sciadv.adj1361
Contributions: Sample fabrication and transport measurements.

During the first and a half years of this thesis work, the main goal was to develop gate-defined junctions in TBG in close collaboration with my colleague Jaime Díez Mérida [271]. Thanks to TBG's gate-tunability and by creating double-gated structures with graphite, we were able to create Josephson junctions as well as p-n junctions withing a single TBG sheet. In this chapter we show the optimization we worked out for the nanofabrication of these devices and their characterization, as well as the JJ experiments that we carried out [P3]. Lastly we will also show the optoelectronic experiments [P5] [P8] that were carried out with these devices in collaboration with my colleague Rafael Luque Merino [272].

The idea of this project consisted in trying to exploit the gate-tunability of the phase diagram of TBG in order to make a Josephson junction entirely of the same material. That is, by engineering multiple gates above and below the TBG, one could have its superconducting state on two sides while at the middle any other state of its phase diagram: a metal, correlated insulator, etc. When this project started, this was an important milestone for the research field, as a last definitive proof of superconductivity in TBG was still lacking: controlled phase-coherence. At that point, interference patterns were already observed in standard transport devices when measuring the I_c of the SC state as a function of perpendicular magnetic field [11, 13, 14]. These oscillations were thus accidental; the interpretation being that twist-angle inhomogeneity across the device could cause one or several Josephson junctions in series. Controlled phase-coherence of the SC state of TBG was then first achieved in Refs. [204, 205] by creating gate-defined JJs, confirming that the zero-resistance state with phase transitions in temperature, current and magnetic field was indeed a superconducting condensate with a global wavefunction.

The interest of creating these devices also lies in that, since the phase diagram of TBG has exotic quantum states such as correlated insulators, strange metals, topological and magnetic states, a tunable gate-defined JJ would allow to create all kinds of hybrid junctions within a single device. To this date, many other nanostructures with local electrostatic gates have been exploited in TBG, such as SQUIDs [201], interferometers [206], and superconducting constrictions [273].

5.1 Fabrication and characterization of gate-defined devices

To realize such multiple gating structures, we stack encapsulated TBG with two local graphite gates: one at the bottom and another at the top of the stack. The goal is to first fabricate the device into a Hall-bar, measure all contact pairs, and then selectively cut the top graphite between the pair of contacts that exhibits a superconducting state or has the closest twist-angle to the magic angle 1.1°. Fig. 5.1a shows a schematic of the targeted device geometry.

When stacking these samples, it is important to avoid etching the SiO_2 substrates where

we exfoliate the top graphite flakes, as otherwise the adhesiveness of the PDMS/PC stamp will not be strong enough to pick up the flakes. Another important point is that the top hBN in the stack must be larger than the two graphene flakes forming the TBG, extending beyond them on at least one edge. This is because the top graphite has to be contacted with Cr/Au electrodes (without any prior etching), as shown in Fig. 5.1b. If the TBG extends beyond all edges of the top hBN, the electrodes will inevitably create an electrical short between the top graphite and the TBG, making the top gate ineffective.

The idea of contacting the top graphite in several places, as shown in Fig. 5.1b, is that multiple cuts can be made so that each of those electrodes acts as an independent top gate. In this way, one device could have more than one gate-defined junction. However, rather than predefining the junctions, our approach is to first pattern the device into a Hall-bar geometry and contact the TBG (see Subsection 2.1.6). Then, after measuring at low temperatures and identifying the suitable pair of contacts, we cut the top graphite between such pair to form a gate-defined junction. This is visualized in Fig. 5.1d.

For precise etching of the top graphite without damaging the top hBN, we use an oxygen RIE process with 50 W of RF power, 100 sccm of O_2 and 90 mTorr of chamber pressure, resulting in a high etching rate of ~ 1 nm/s. These high powers gave us the

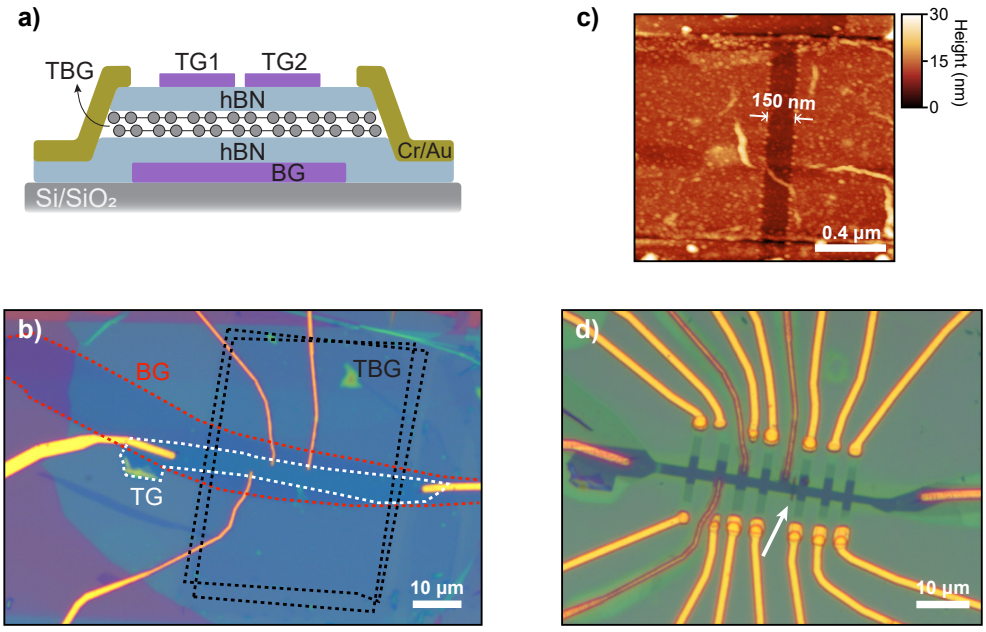

Fig. 5.1: Fabrication of gate-defined TBG devices. a) Sketch of the device geometry from the side, with a graphite bottom gate (BG) and a split graphite top gate (TG1-2) in purple. **b)** Real example of a double-gated stack after contacting the top graphite (white) in several places with Cr/Au electrodes. **c)** AFM of a cut on the top graphite to split it into two top gates. **d)** The same device as in **b**, after etching the top graphite with a cut, indicated with an arrow. The sample is shown under PMMA for better visualization.

best results, with a well defined profile along the perpendicular direction of the Hall-bar channel. The etched regions were aimed to be as short as possible, such as the one shown in Fig. 5.1c with a gap of ~ 150 nm, so that a Josephson junction could be made. Here some residues after nanofabrication from PMMA appear to be bridging the gap of the two sides, but these polymers are highly insulating, so that no electrical short can happen once the graphite is completely etched. We found that the top hBN was mildly etched with this process; about 1 nm. This will be taken into account when optimizing the recipe, as we will explain later in this section.

After the cut is done, the device is ready to be measured with multiple gates, as shown in Fig. 5.2a. We do so with a 4-probe scheme, where the voltage drop V_{xx} is measured across the junction in the longitudinal direction of the a.c. current I. With this three-gates structure (one back gate BG and two top gates TG1 and TG2), there are two types of configurations one can create: a p-n or a p-n-p junction. To first characterize the device globally, we tune the back gate while keeping $V_{\mathrm{TG1}} = V_{\mathrm{TG2}} = 0$, thus changing the carrier density across the entire space between the two V_{xx} probes. The resulting $R_{xx} = V_{xx}/I$ trace, shown in Fig. 5.2b (bottom axis), is typical of a TBG device near the magic angle. This specific device has a twist-angle of $\theta = 1.14° \pm 0.02°$. The two top gates can also be used together (V_{TGs}) to globally tune the carrier density while keeping $V_{\mathrm{BG}} = 0$, as shown in the top axis of Fig. 5.2b.

After the global characterization, we independently tune the gates to demonstrate control of the gate-defined junction. We start with the p-n junction configuration, where V_{TG1} and V_{TG2} are tuned separately while keeping $V_{\mathrm{BG}} = 0$, creating a carrier density profile such as the one in Fig. 5.2c. The dashed vertical lines indicate the ~ 150 nm physical cut of the split gate. The corresponding resistance map, shown in Fig. 5.2e, displays perpendicular features corresponding to the resistance peaks in Fig. 5.2b at integer fillings of the flat bands ν. Their perpendicular orientation between each other demonstrates that we have completely independent control of the carrier density on either side of the junction. The features being more resistive in one direction than the other are due to a difference in the length of the two channels: the one under TG1 being 3 µm long while the other under TG2 being 0.6 µm (see Fig. 5.2a).

By now independently tuning V_{BG} and both top gates together, V_{TGs}, we can engineer a p-n-p junction as shown in Fig. 5.2d. When measuring the resistance map in Fig. 5.2f, this results in the vertical features corresponding to a measured resistance that depends only on V_{BG}, meaning they are coming from the middle area where we have split the top gates (pink shade in Fig. 5.2d). The diagonal features instead correspond to the two sides areas, which are gated by both the top gates and the back gate (blue shade in Fig. 5.2d). The slope of these diagonals depends on the relative capacitance of the BG (C_{BG}) and the TGs (C_{TGs}), so that the carrier density is changed according to $n = C_{\mathrm{BG}} V_{\mathrm{BG}} + C_{\mathrm{TGs}} V_{\mathrm{TGs}}$. From the map in Fig. 5.2f, one can see that taking an horizontal (vertical) cut while maintaining $V_{\mathrm{TGs}} = 0$ ($V_{\mathrm{BG}} = 0$) corresponds to the traces in Fig. 5.2b as a function of V_{BG} (V_{TGs}).

Compared to the diagonal features, the measured R_{xx} of the cut area (vertical features)

is much weaker since it corresponds to a much shorter length 0.15 µm compared to the total length of the 4-probe measurement 4 µm. Another detail is that the vertical lines in the resistance map are not perfectly vertical like the ones in Fig. 5.2e. This is because the

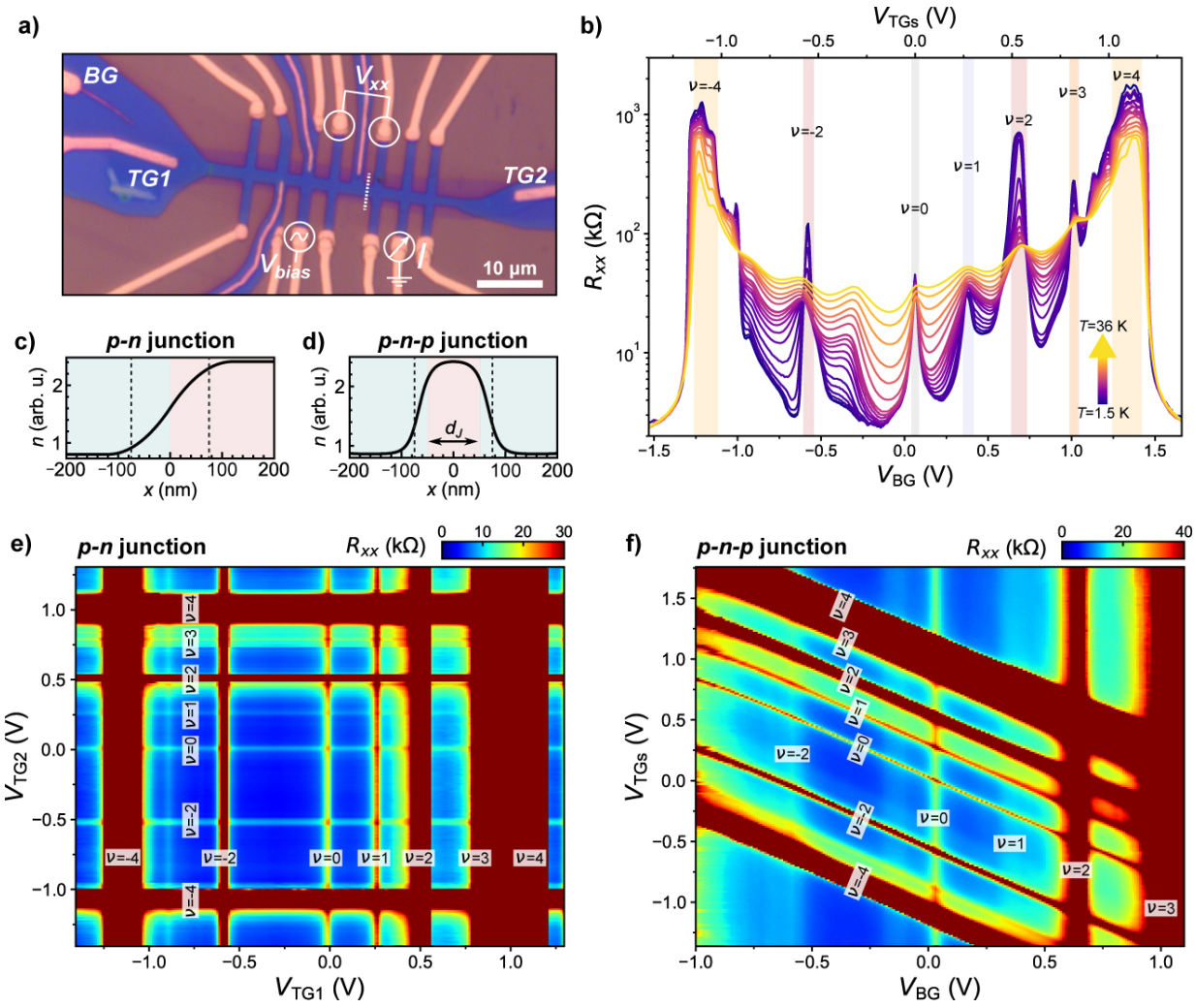

Fig. 5.2: Gate-defined TBG junctions. **a)** Optical picture of a gate-defined TBG device, along with a 4-probe transport measurement scheme across the junction. The cut that splits the top graphite gate is indicated by a dashed line. **b)** 4-probe longitudinal resistance R_{xx} of the device in **a** for different temperatures and as a function of back gate voltage (bottom) and both top gates together (top). **c)** Carrier density in a p-n junction from the electrostatic potential of the two top gates. **d)** Carrier density in a p-n-p junction from the electrostatic potential of the back gate and the two top gates. The dashed vertical lines indicate the physical cut of the split gate. **e)** Dual gate map of R_{xx} vs TG1 and vs TG2 at 1.5 K. This configuration corresponds to a p-n junction. **f)** Dual gate map of R_{xx} vs back gate and vs both top gates together at 1.5 K. This p-n-p configuration can be used for a JJ.

middle area can also be affected by the electrostatic potential of the top gates, as demonstrated in Fig. 5.2d. There, we can see that the carrier density continuously changes and is only flat in the center of the junction along a smaller length d_J than the one corresponding to the physical cut of the top graphite (vertical dashed lines). This observation is very important since our goal is to create a gate-defined JJ with this p-n-p configuration, where the sides would be tuned into the superconducting state of TBG.

In order to understand the optimal length of the cut in the graphite and the respective thicknesses of the hBN dielectrics, we did simulations of the electrostatic profiles by solving the Poisson differential equation in two dimensions with a finite element method:

$$\nabla\left[\epsilon(x,y)\nabla V(x,y)\right] = \rho(x,y)/\epsilon_0. \tag{5.1}$$

Here V is the electrostatic potential, ρ the charge density, ϵ the dielectric constant ($\epsilon = 4$ for hBN) and ϵ_0 the vacuum electrical permittivity. The problem can be simplified as we are mainly interested in the solution along the TBG sheet, which can be considered one-dimensional.

By varying the thicknesses of the bottom and top hBN, we found that the device could have a sharper electrostatic profile with a more homogeneous carrier density in the junction area, the thicker the top hBN was than the bottom hBN (see SI in [P3] and [271] for more details). This is also rather intuitive: if the back gate is closer to the TBG than the top gate, its electrostatic field will be stronger in the junction. This observation proved to be key for us in order to increase the success yield of engineering gate-defined JJs.

Finally, it is important to note that our multi-gated geometry allows for further configurations. One could also independently tune the top gates TG1 and TG2, as in Fig. 5.2e, while also changing the BG, giving rise to a p-n-p' junction, where three parts of the device would have different carrier densities. As an example, this was exploited in Ref. [205] to do tunneling spectroscopy experiments.

Overall, details such as the size and thicknesses of the hBN dielectrics when stacking and a good control over the graphite etching proved to be essential in order to successfully optimize the nanofabrication of these gate-defined junctions. We nevertheless sometimes found that after splitting the top gate, the device would not show the exact same features as prior to the etching process. This could be caused by a small etching of the TBG at its edges, as the heterostructure has a steep profile when shaped with the CHF_3:O_2 recipe. Other gate-defined junction experiments instead used gates of Au [204, 205], so that no post-process etching had to be done. The main reason to choose graphite over Au lies in that the device is entirely composed of vdW materials, which has been shown to give an atomic flat surface with better electrostatic profiles and screening from long-range potential fluctuations than evaporating a metallic film [37, 274].

Future improvements of these devices could bring the best of both approaches by using the nanopatterning anodic oxidation technique to etch away the top graphite prior to stacking without the need of a mask [275].

5.2 Gate-defined Josephson junctions in TBG

In this section we present the results of our work on gate-defined TBG Josephson junctions [P3], where we use the p-n-p configuration shown in Fig. 5.2d,f and the SC state of TBG itself to probe the d.c. Josephson effect. We mainly explore the proximity effect when the junction is tuned close to $\nu = -2$, where we observe a broken inversion symmetry interference pattern, along with magnetic hysteresis. By studying the effect of magnetization on the asymmetry of the I_c oscillations, we conclude that our findings are consistent with the ground state of the weak link being a valley polarized phase with orbital magnetization. Finally, we demonstrate how the combination of magnetization and its current-induced switching enables the realization of a programmable zero-field Josephson diode.

Along with other recent works on WTe_2 [276], these junctions are unique in that all components are made of the same 2D material, ensuring an ultra-clean interface between the superconductors and the weak link—an aspect that has posed a major challenge when engineering heterojunctions [277–280]. This approach has nevertheless certain limitations. Because the measurement contacts are always placed on the adjacent regions that are tuned to the superconducting state (see Fig. 5.3a-b), the weak link cannot be studied in isolation when using the global back gate. As a result, determining the phase diagram of the weak link relies on the assumption of twist-angle homogeneity throughout the whole area between the contacts, whereas the geometry discussed in Chapter 4 solves this issue. Additionally, since the carrier density across the junction must vary continuously (see Fig. 5.2d), the effective junction length d_J changes as the carrier density n_J is varied. This prevents the weak link from exhibiting one single state, resulting instead in several phases in series that traverse the complex phase diagram of TBG [205, 206] [P3].

In our case, a 150 nm gap between the split top gates results in an effective junction length of $d_J \sim 100$ nm, which is short enough to enable the proximity effect. This is consistent with our estimate of the Ginzburg-Landau coherence length of superconducting TBG, $\xi_{GL} \sim 100$ nm. We obtain this value by measuring its critical temperature T_c and its critical field B_c at different temperatures: $B_c = \Phi_0/2\pi\xi_{GL}^2(1 - T/T_c)$.

5.2.1 Symmetry-breaking and edge states

The device we use for this study is a TBG with a twist-angle of $\theta = 1.11° \pm 0.02°$, featuring all correlated states at integer fillings and a superconducting state at $\nu < -2$, as shown in the 4-terminal R_{xx} measurement of Fig. 5.3c.

The dual gate structure and the cut in the top graphite allows us to independently tune the doping level in three different regions, as depicted in Fig. 5.3b. The carrier density in the junction or weak link, n_J, is controlled by changing V_{BG}. In order to create a JJ in the device, the carrier density on the side regions is set to the optimal

doping of the superconducting state, $n_{SC} = -1.72 \times 10^{12}$ cm^{-2} (see Fig. 5.3c and top panel of Fig. 5.3d). The carrier density in the junction n_J can be continuously changed according to $n_J = C_{\mathrm{BG}} V_{\mathrm{BG}}$, while the sides can be kept at n_{SC} if the top gates are changed accordingly with the relation $V_{\mathrm{TGs}} = (n_{SC} - C_{\mathrm{BG}} V_{\mathrm{BG}})/C_{\mathrm{TGs}}$. This essentially means that we must follow the direction of the diagonal features of the dual-gate map such as the one in Fig. 5.2f.

Such configuration results in a gate-tunable JJ, where the proximity effect varies as n_J is changed. This is visualized in the dV/dI map of Fig. 5.3d and is evidenced by a varying I_c (contour of the dark-blue region in the I axis) when n_J varies. Here we show that we can tune the junction from the SC state (SC/SC/SC) into the normal metal region (SC/N/SC) and close to the correlated insulator (SC/CI/SC). The range of n_J is only limited around $-3 < \nu < -2$ because, as explained before and visualized in Fig. 5.2d, the effective length of the junction d_J decreases as $|n_J - n_{SC}|$ is increased.

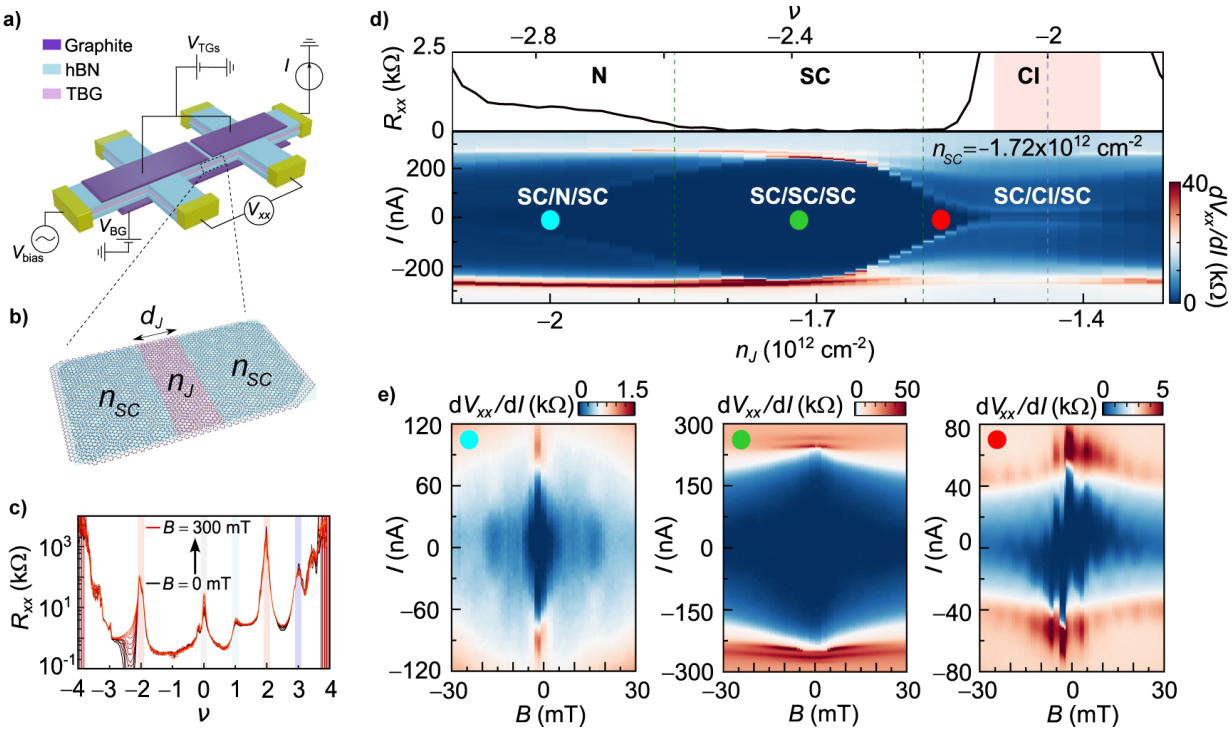

Fig. 5.3: Gate-defined TBG Josephson junction. a) Sketch of the device and measurement configuration. **b)** Zoom-in of the junction area, where the two sides are gated into TBG's superconducting state, while the junction is tuned to a different state. **c)** 4-probe resistance R_{xx} vs filling ν for different values of applied magnetic field. This shows that there is a superconducting state at the hole side of $\nu = -2$. **d)** Top panel shows R_{xx} vs ν (top). Bottom panel shows the differential resistance map of the JJ in the same range vs carrier density of the junction n_J (bottom). **e)** Interference patterns measured at three different densities, indicated with colored circles in **d**. Adapted from [P3].

By now measuring the interference patterns as a perpendicular field B is applied to the device (Fig. 5.3e), we see that the SC/SC/SC configuration for $n_J \sim -1.7\times10^{12}$ cm^{-2} gives a decreasing I_c without any oscillations and disappearing at $B_c \sim 100$ mT, evidencing that the device is uniformly doped into the superconducting state. In the SC/N/SC we do see oscillations in I_c, following what seems the typical decay of a Fraunhofer interference pattern. This proves that a JJ is formed. It is important to note that although this interference pattern follows the typical exponential decay of the Fraunhofer pattern, the observed periodicity $\Delta B \sim 4.5$ mT is much smaller that the expected value $\Delta B \approx \Phi_0/WL \sim 20 \pm 1$ mT from the geometrical factors of our junction $L \sim 100$ nm and $W \sim 1.0$ µm. The explanation for this is that, in this JJ, the superconductors are two-dimensional. The TBG therefore does not screen the external magnetic field as other thick superconductors would, i.e. the London penetration length λ_L is too large compared to its thickness $t \sim 0.7$ nm. In this 2D limit, another characteristic length, the Perl length $\Lambda = 2\lambda_L^2/t$, is the one responsible for screening currents that flow in the device in order to create a varying phase difference with B that gives rise to the observed interference patterns [205]. Different works have derived the periodicity of the magnetic field in this limit [262, 281, 282], which gives

$$\Delta B_{2\mathrm{D}} \approx 1.8\frac{\Phi_0}{W^2} \tag{5.2}$$

for a junction of width W. This is very different from the 3D case, $\Delta B_{3\mathrm{D}} \approx \Phi_0/WL$, and strikingly, $B_{2\mathrm{D}}$ does not depend on the length L of the junction. With this consideration, we get a value that reasonably approximates to our observations $B_{2\mathrm{D}} \sim 3.7 \pm 0.5$ mT.

While the SC/N/SC configuration in Fig. 5.3e has all the expected symmetries along the I and B directions, we observe that when n_J is tuned towards the SC/CI/SC configuration, at $n_J \sim -1.56\times10^{12}$ cm^{-2}, the interference pattern shows an asymmetry with respect to the current $I_c^+(B) \neq I_c^-(B)$, which is a signature of inversion symmetry breaking. On top of that, due to a magnetic hysteresis and previous magnetization of the sample, there is an asymmetry with respect to the B-field $I_c^+(B) \neq I_c^-(-B)$, indicating time-reversal symmetry breaking. These two inequalities are a signature of a Josephson diode, which was extensively discussed in Section 4.5. As we will see later, this JDE is a bit different than from Chapter 4 in that here it happens also at zero field after the sample is magnetized.

For now, we go on to analyze in detail the I_c oscillations with field (see Fig. 5.4a). At low field, we see that the I_c does not vanish to zero, which is a signature of an asymmetry in the supercurrent density profile J_S. As we learned in Subsection 1.4.3 and Section 4.5, this asymmetry is not enough to produce a diode effect though. In addition, the I_c does not exponentially decay like in the SC/N/SC JJ, suggesting that edge transport dominates in this SC/CI/SC configuration. Finally, the I_c oscillations disappear at $\sim \pm 20$ mT just to revive at ± 40 mT. This double beating suggests that there is a fast and a slow periodicity, which could correspond to transport from the bulk and the edges. Indeed, by using the reversed Dynes-Fulton method, we find that the supercurrent density profile $J_S(x)$ in Fig. 5.4c gives rise to an interference pattern in Fig. 5.4b that resembles very well our data in Fig. 5.4a. Here the bulk supercurrent helps to reproduce the big envelope oscillations

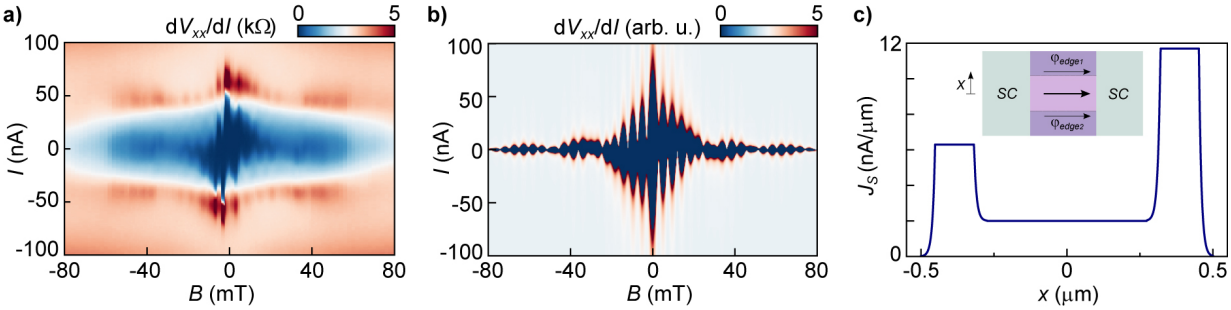

Fig. 5.4: Supercurrent carried by edge states in the symmetry-broken phase. a) Same interference pattern as in the right panel of Fig. 5.3e, measured at $n_J \sim -1.56 \times 10^{12}$ cm^{-2}, but up to higher fields. **b)** Calculated interference pattern from the supercurrent density in **c**. **c)** Supercurrent density J_S vs real-space coordinates x along the width of the junction, where the physical limit of the device is at ± 0.5 µm. The inset shows the model we have used with the two edge supercurrents carrying a different phase $\varphi_{edge1,2}$. Adapted from [P3].

of periodicity ~ 20 mT, while the two edge channels give the fast oscillations of ~ 4.5 mT periodicity. The difference in absolute value between the supercurrent in the two edges gives the non-zero I_c nodes. Now, in order to reproduce the asymmetry between I_c^+ and I_c^-, we have also added different phases to the two edge currents, so that the CPR is no longer sinusoidal and a JDE can be reproduced.

This extra phase φ effectively adds up to the external magnetic field $B = B_{ext} + \varphi$. Adding a global phase will not change the I_c (see Eq. (1.52)), but if one assigns different phases to the two edges, φ_{edge1} and φ_{edge2} while keeping $\varphi_{bulk} = 0$, an imbalance will be made in the $I_c(B)$ function, creating an asymmetry with respect to the current: $I_c^+(B) \neq I_c^-(B)$. These different phases and amplitudes can be regarded as the two edge channels having different Fermi velocities [266]. Finally, to recreate the tilt of the Fraunhofer, where an approximated time-reversal symmetry $I_c^+(B) = I_c^-(B)$ holds, we assign opposite signs to the phase of the two edges: $\varphi_{edge1} = +\pi/4$ and $\varphi_{edge2} = -\pi/4$. As we will see in the following, this time-reversal symmetry is broken if we pre-magnetize the sample.

Overall we conclude that the edge supercurrent in the SC/CI/SC configuration plays an important role in the symmetry breaking. This also hints at a non-sinusoidal current-phase relation, which would need further experiments to be explored.

5.2.2 Orbital magnetism and valley polarization

By measuring the interference pattern shown in Fig. 5.4a now at 800 mK in Fig. 5.5b, we observe that the abrupt jumps in the I_c at low fields disappear, but the asymmetry remains. This is shown in Fig. 5.5c, where we can see that $I_c^+(B) \neq |I_c^-(B)|$. There is an offset in magnetic field in the central peak too, which enables to have an asymmetry at

zero field, i.e. i.e. $I_c^+(0) \neq |I_c^-(0)|$, which we will exploit later to prove the existence of the Josephson diode with the rectification measurements. Fig. 5.5a shows that this offset and the asymmetry at zero field only appears if the sample is pre-magnetized by large external magnetic fields, such as the purple ($B_M = 500$ mT) and orange ($B_M = -300$ mT) traces.

Since none of these features are observed in the SC/SC/SC nor the SC/N/SC configurations (see Fig. 5.3e), we suggest that the CI state at $\nu = -2$ in the weak link of the JJ is an unconventional insulating state. Specifically, such state should account for the inversion symmetry breaking and be prone to magnetization, breaking time-reversal symmetry too and generating a spontaneous net magnetic flux that moves the position of the central peak away from zero-field. Below, we propose that our observations are consistent with an interaction-induced valley polarized (VP) state with net orbital magnetization.

As explained before in Subsection 1.3.2, the flat bands of TBG at the Fermi level ($\nu = 0$) are 4-fold degenerate because of the spin and valley conservation. In the one-valley Hamiltonian, these degeneracies are protected by the $C_{2z}\mathcal{T}$ symmetry, while in the full-valley Hamiltonian both C_{2z} and $\mathcal{T}$ are individually preserved. Several quantum transport and STM studies have reported signatures of these symmetries being broken at integer fillings of the flat bands. These involve Chern insulators at high magnetic fields [15, 16] and quantum anomalous Hall effect (AHE) at zero-field [80, 81]; the latter thought to be the same Chern insulators nucleating at zero-field and competing with insulating phases [283]. In these cases, the $\mathcal{T}$ symmetry is broken with an external magnetic field or spontaneously broken by the system, showing an spontaneous magnetization in the AHE. As for the C_{2z} symmetry, it can be broken by aligning the TBG with hBN, as reported by Refs. [80, 81], or by electron-electron interactions [14, 283]. One interpretation is that these broken symmetries and the degeneracy lifting both lead to the appearance of two sets of four bands, one for the electron flat band and another for the hole flat band. These four bands, each carrying a different flavor, carry a Chern number of $C = 1$ or $C = -1$ [16]. Depending on how the bands get filled, the different integer fillings can have a finite or zero total Chern number. One possible candidate that can arise in the case of the $\nu = -2$ CI is a valley polarized state with Chern number $C = -2$ [256, 257, 259, 284], which could explain our findings since in our case these symmetries are both broken in our JJ when we tune the weak link close to $\nu = -2$ (slightly on its hole side).

To further support this hypothesis, we construct a model of a JJ made with two s-wave superconductors and a TBG weak link in such ground state at half-filling. The result is shown in Fig. 5.5d and the full derivation of this model can be examined in the SI of [P3] and in Ref. [284]. By comparing with the experiment in Fig. 5.5c, we can see that the theory reproduces very well the shift of I_c from zero field. Importantly, in order to explain the asymmetry of the I_c curves, this model needs an extra assumption: that the small currents $I \sim 10$ nA can switch the polarization of the orbital magnet, as it has been observed at other fillings in TBG [82, 83, 285]. With this assumption, the theory can reproduce both I_c^+ and I_c^- values and their respective asymmetry. Finally, we find that if the $C_{2z}\mathcal{T}$ breaking terms are removed from the model, the TBG bands become

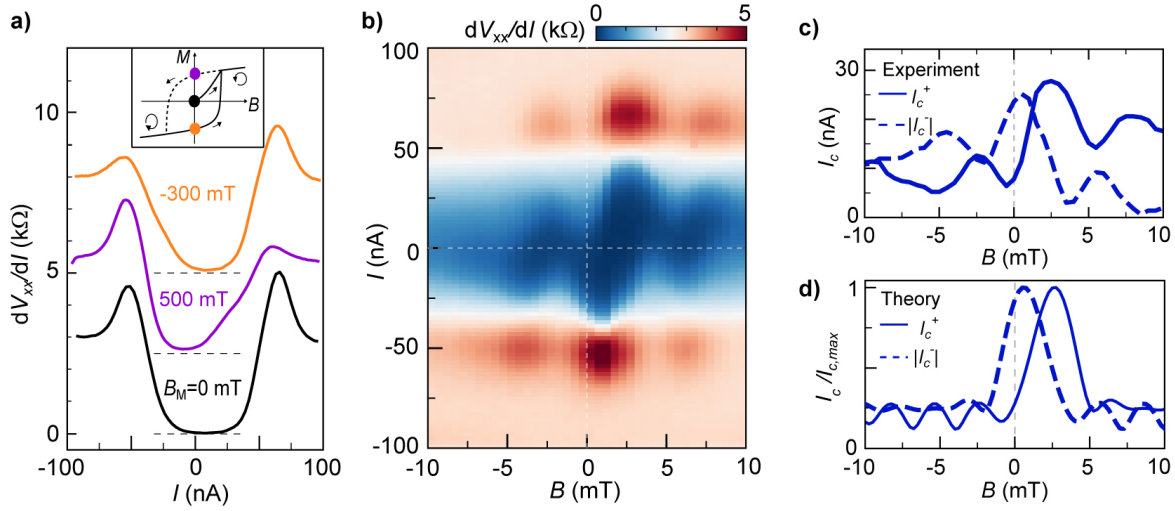

Fig. 5.5: JJ with orbital magnetism. a) Differential resistance vs current measured at zero field and base temperature for different pre-magnetization B_M field values. If no field is applied after cooldown of the sample (black trace), there is no recorded asymmetry at zero field. If however, the sample is pre-magnetized to large fields, such as the purple ($B_M = 500$ mT) and orange ($B_M = -300$ mT) traces, the $\mathrm{d}V/\mathrm{d}I$ is no longer symmetric. The inset indicates that this is consistent with a hysteresis cycle of magnetization vs applied external field. **b)** Interference pattern measured at 800 mK. **c)** Extracted critical current in both directions of the d.c. current, I_c^+ and $|I_c^-|$, from **b**. **d)** Theoretical calculation of the critical current with a VP state in $\nu = -2$, showing a good agreement with the experimental observation in **c**. Adapted from [P3].

topologically trivial with a zero orbital magnetic moment, and the resulting interference pattern is totally symmetric in both current and field [P3]. This suggests that the observed features are a direct consequence of the electronic ground state near $\nu = -2$ carrying orbital magnetization.

Since our observation of the symmetry-broken interference pattern occurs at $\nu \sim -2.2$ and not exactly at $\nu = -2$, one possibility is that the state in the junction is a Chern insulator with a coercive field matching the pre-magnetization fields that we are applying. Such a state has been previously identified at slightly elevated magnetic fields $B > 300$ mT [117], which is in good agreement with the observed coercive field of the JJ. In such scenario, this valley polarized state with orbital magnetization and $C = -2$ would be characterized by the presence of edge states, consistent with our findings in Fig. 5.4. One important point though is that we do not see any magnetic state when we measure the 4-probe resistance across the entire device with only the back gate, that is, across the total area where both the weak link and the superconducting regions lie. An explanation for this could be twist-angle inhomogeneity, i.e. the magnetic state only lies in the trench area, or that this state showcases domains of different magnetic behavior, as observed in SQUID-on-tip experiments [286]. In this case, there could be domains of different Chern

number, so that the small area of the weak link could have domains that sum up to a non-zero total Chern number, and thus show magnetization, while the whole device area could sum to a zero total Chern number.

To pinpoint the exact ground state of TBG at half-filling is of great importance, as it could shed light into the mechanisms driving the interactions in this material, and because it could act as the parent state of the TBG superconducting state. After this work, others have pointed at the valley polarization of the half-filled bands [256]. Nevertheless, the general theoretical understanding [260, 287, 288], backed up by more recent STM experiments [74, 289, 290] are consistent with inter-valley coherent or incommensurate Kelulé spiral ground states. These are many-body ground states with more complicated mechanisms than fully polarizing the spin or valley quantum numbers, and rather have an admixture or imbalance between them.

The concept of the Josephson diode effect has been already introduced and discussed extensively in Section 4.5. In the case of this study, we find non-reciprocal transport at finite fields, such as the one we observe in [P2], and also at zero-field when the sample was pre-magnetized. This latter makes the diode even more programmable, as we show in Fig. 5.6. There, the direction of the diode can be reversed at zero field by previously applying opposite magnetization fields.

Such effect was also reported later without any junction in superconducting twisted trilayer graphene [251], where the proposed explanation also involved an imbalance in the valley polarization of the bands [252]. Furthermore, in this case the intrinsic superconducting state seems to gain this imbalance from its parent state in the valley polarized phase of the normal metal. Future works on these systems should involve a deeper study of the mechanism behind this pre-magnetization, both experimentally and theoretically.

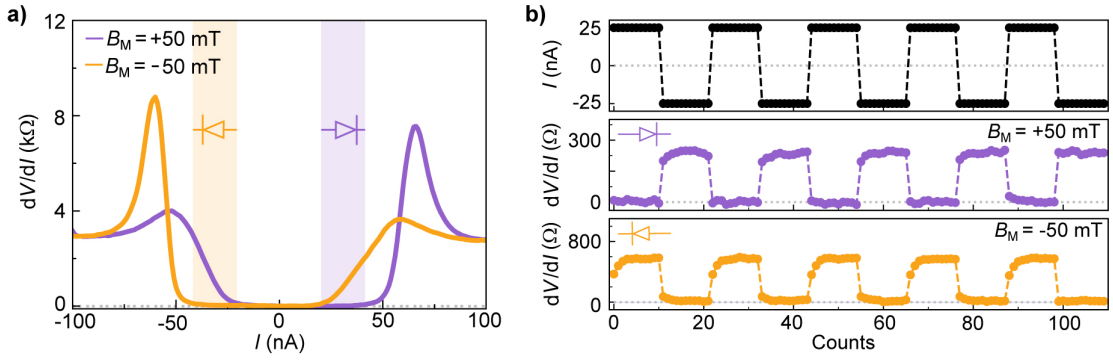

Fig. 5.6: Zero-field programmable Josephson diode. **a)** Differential resistance $\mathrm{d}V/\mathrm{d}I$ vs d.c. current I measured at zero field and base temperature, for two different pre-magnetization fields B_M. The shaded vertical lines indicate the direction and values of I where the Josephson diode is operational. **b)** Rectification measurements from **a**, where $\mathrm{d}V/\mathrm{d}I$ is measured in the middle and bottom panels for two opposite values of I shown in the top panel, i.e. ± 25 nA. Adapted from [P3].

For the former, a big improvement would be to have a SQUID on-chip so that the real magnetic flux traversing the sample could be double-checked to be zero after applying the pre-magnetization fields.

5.3 Gate-defined p-n junctions in TBG

In this section we further exploit the capabilities of our multiple-gated TBG devices to form p-n junctions, as we showed in Fig. 5.2c,e. These structures enable to study both thermal [58, 291–294] and light-matter coupling [295–299] properties, which can offer valuable information into deciphering the ground states of TBG at different fillings of the flat bands [300–302].

The p-n junction architecture, apart from allowing us to probe these properties locally by controlling the chemical potential, it enhances the photo-response upon light illumination. This allows us to first study the light-matter interaction of TBG by measuring the cooling dynamics of the electrons [P8], and finally dwell into its thermoelectric response [P5].

5.3.1 Cooling dynamics and Umklapp scattering

This study investigates the cooling dynamics of electrons in TBG upon light illumination, providing insight into its electron-phonon interactions. The time-resolved photocurrent measurements were performed in the group of Prof. Klaas Jan Tielrooij, using the gate-defined TBG p-n junction samples [P8]. A schematic of the experimental setup is shown in Fig. 5.7a, where the photovoltage generated at the junction serves as a probe of the electronic temperature T_e.

By comparing the cooling behavior of TBG ($\theta = 1.24°$) with another non-twisted Bernal bilayer graphene (BLG) sample, we find that the cooling rate in TBG remains significantly faster than in BLG, even at cryogenic temperatures. As shown in Fig. 5.7b, the decay of the photovoltage in TBG (blue data points) occurs on a much shorter timescale than in BLG (red data points). In BLG, cooling times extend into the nanosecond range at low temperatures due to reduced acoustic phonon interactions, while in TBG, cooling times remain in the picosecond range down to 5 K (Fig. 5.7c). This suggests that an additional cooling mechanism is at play in TBG, which we identify as Umklapp electron-phonon scattering. This process is enabled by the mini-Brillouin zone of the moiré superlattice, allowing efficient momentum transfer that would otherwise be forbidden in untwisted graphene systems (Fig. 5.7e).

The cooling dynamics of electrons can be studied using excited-state relaxation measurements, where a laser is used to thermally excite the electron system. Upon excitation, electrons are initially promoted to high-energy states, after which they rapidly

undergo electron-electron scattering, leading to thermalization into a hot carrier distribution—characterized by a Fermi-Dirac distribution at an elevated electronic temperature T_e. This hot-carrier population then cools down via electron-phonon interactions, involving acoustic, optical, or substrate phonons. Cooling occurs on the order of picoseconds at room temperature, but as the lattice temperature is reduced, phonon occupation decreases, leading to less efficient cooling and longer relaxation times [303].

These processes are directly accessible through time-resolved photovoltage (TrPV) microscopy and continuous-wave photomixing (CW-PM), which allow precise measurement of the electron cooling time by tracking the evolution of T_e after optical excitation. Both techniques rely on optical excitation of the TBG p-n junction, generating a photovoltage via the photothermoelectric effect, which is proportional to the electronic temperature T_e. In TrPV measurements, the delay time between two ultrashort laser pulses is varied, and the photovoltage signal is recorded. Due to the sublinear dependence of photovoltage on carrier temperature, a dip in the signal is observed when the pulses overlap ($dt = 0$), and the subsequent recovery is used to extract the cooling time. In CW-PM, a beat frequency is created by two continuous-wave lasers, and the resulting photovoltage oscillations allow cooling times to be determined from the frequency-dependent damping [304, 305]. The combination of these methods provides a precise measurement of the cooling dynamics across different time regimes.

As shown in Fig. 5.7b-c, in BLG, cooling slows from 300 K to 5 K, consistent with the expected suppression of phonon occupation at low temperatures [306, 307]. However, in TBG, cooling times remain nearly constant at approximately 3 ps across a wide temperature range, indicating that an additional, highly efficient cooling mechanism is present. This mechanism is not due to diffusive cooling, as we find a lack of dependence on laser spot size, which contrasts with BLG, where cooling becomes slower for larger spot sizes due to spatial heat diffusion.

By now changing the laser power and spot size, we can check whether the cooling rate depends on the initial electron temperature. In BLG, increasing laser power leads to longer cooling times due to phonon bottlenecks, as acoustic and optical phonons become limiting factors in the cooling process [308]. However, in TBG, the cooling time remains largely independent of laser power, further suggesting that a different mechanism dominates cooling in this system. Additionally, by measuring the cooling time as a function of band filling, we observe a nearly constant response across the entire flat band, with a significant increase at full band filling ($\nu = \pm 4$), as shown in Fig. 5.7d. This behavior suggests that moiré phonons play a key role in the cooling process.

To understand the microscopic origin of this ultrafast cooling, we consider the two flat bands and the two higher dispersive bands. Theoretical calculations reveal that electron-phonon Umklapp scattering dominates the cooling process at low temperatures ($T < 10$ K). In contrast to normal electron-phonon interactions, which are limited by momentum conservation constraints, Umklapp processes allow efficient energy transfer by leveraging the small superlattice Brillouin zone of TBG (see Fig. 5.7e). The spatially compressed

Wannier orbitals and low-energy moiré phonons facilitate these interactions, leading to a cooling mechanism that remains highly effective even at cryogenic temperatures.

The dominance of Umklapp scattering in electron cooling has important implications for understanding transport properties in TBG. Since electron-phonon interactions play a crucial role in resistivity, superconductivity, and the strange metal phase observed in TBG, these results suggest that Umklapp scattering could be a key factor in these emergent properties. Understanding how electrons lose energy in TBG may thus provide insight into broader questions regarding the role of phonons in correlated electronic phases.

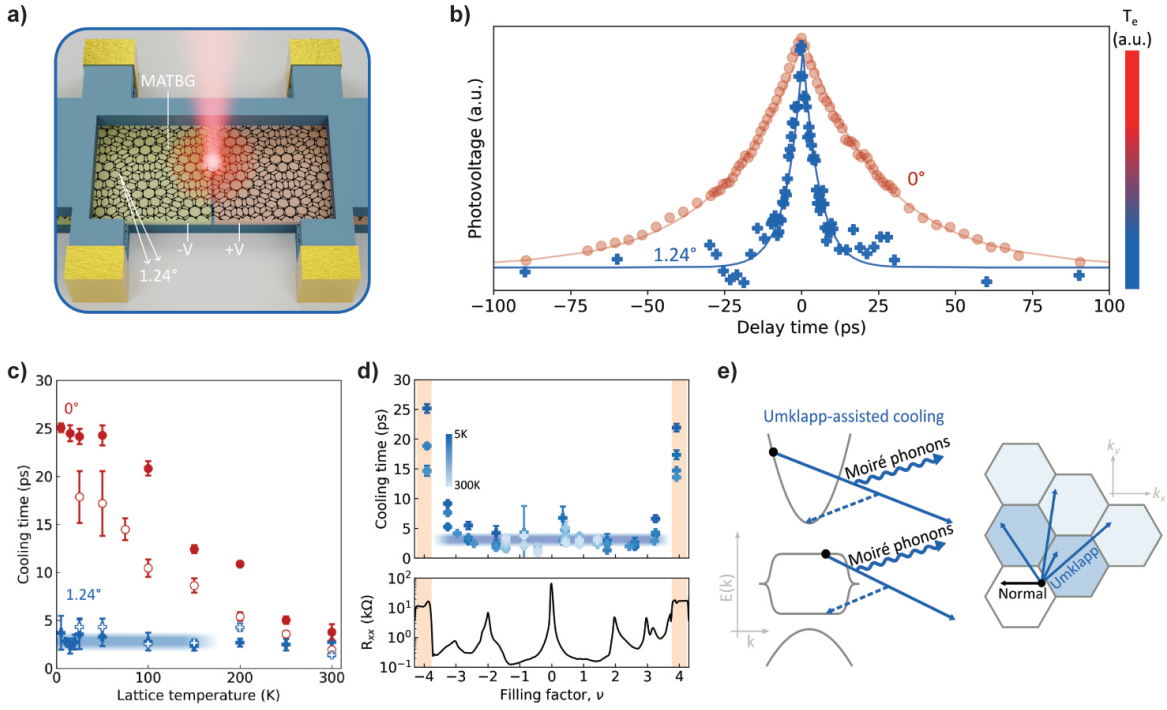

Fig. 5.7: Ultrafast Umklapp-assisted cooling in TBG p-n junctions. a) Schematic of the experiment, where the two top gates of the TBG p-n junction are set to opposite voltages. The illumination then generates a photovoltage that is proportional to the electronic temperature T_e. **b)** Photovoltage vs delay time at a lattice temperature of 25 K, where the cooling dynamics of TBG (blue), represented by the decay, are much faster than for BLG (red). **c)** Cooling time vs lattice temperature shows a constant TBG cooling (blue) from 5 K to 300 K, while the cooling of BLG (red) becomes slower at lower temperatures. The filled (open) symbols correspond to TrPV (CW-PM) measurements. Error bars represent the statistical spread across different gate voltages. **d)** Filling dependence of the cooling time (top) and resistance (bottom). **e)** Schematic of the Umklapp scattering processes (solid blue arrows) in the TBG bandstructure (left) and in the higher Brillouin zones (right), allowing for electron relaxation via coupling to moiré phonons (wiggly lines). The dashed arrows represent the equivalent final state in the first BZ. Adapted from [P8].

5.3.2 Thermoelectric transport and heavy-fermion physics

Both transport and STM experiments have put into evidence that, surprisingly, the flat bands of TBG exhibit an interplay between itinerant and localized carrier behavior. While superconductivity [12–14], metallicity [53–55] and topologically non-trivial states [15, 16] account for the existence of itinerant carriers, the presence of correlated insulators at integer fillings [11] on the other hand suggest the presence of localized electrons. Thermoelectricity can be another powerful probe to reveal more aspects about the nature of the carriers in the flat bands of TBG and shed more light into this dichotomy [291–293]. In this work [P5], we further exploit the p-n junction architecture to study the photo-thermoelectric effect in TBG by measuring the Seebeck coefficient, which reveals an anomalous response at integer fillings that can be understood withing the theoretical framework of the topological heavy-fermion model, as we will explain in the following.

The thermoelectric effect describes the generation of an electric field in a material subjected to a temperature gradient. This is caused by the diffusion of charge carriers at the Fermi level from the hot side to the cold side, thus creating a voltage difference V between the two ends [309]. The strength of this thermoelectric effect is quantified by the Seebeck coefficient S, which depends on the charge of the carriers and their band dispersion:

$$V = S\Delta T, \tag{5.3}$$

where ΔT represents the temperature difference between the two ends. This expression only holds under the linear regime, where $\Delta T \ll T$.

The Seebeck coefficient S is linked to the electronic properties of the material via its general conductivity $\sigma(\mu, E)$, as described by the Mott relations [310]. Often, these expressions are taken in the simpler semiclassical limit, where electron correlations are neglected and the DOS varies slowly. The Seebeck coefficient for a degenerate Fermi gas in this limit is given by the so-called semiclassical Mott formula [310]:

$$S = \frac{\pi^2 k_B^2 T}{3e} \frac{1}{R} \frac{\mathrm{d}R}{\mathrm{d}V_g} \frac{\mathrm{d}V_g}{\mathrm{d}E}\bigg|_{E=E_F} \tag{5.4}$$

where R is the sample's resistance and V_g is the applied gate voltage. This simplified formula, which relies on experimentally measurable resistance R and the DOS, successfully describes the Seebeck coefficient of many materials, such as monolayer graphene [311–314], where S changes sign at charge neutrality due to the bipolar transport of electrons and holes in the Dirac cone (see Fig. 5.8c). Extrema in resistance (i.e. in the CNP) corresponds to a zero Seebeck coefficient since $S \propto \mathrm{d}R/\mathrm{d}V_g$ [311, 312].

In our experiment, we use the p-n junction configuration (see Fig. 5.2e) to establish a chemical potential difference $\Delta\mu$ across the junction, resulting in a difference in Seebeck coefficients too, $S_1 - S_2$, according to Eq. (5.4). Now by shining a continuous-wave excitation of $\lambda = 1550$ nm on the sample, we induce an increase in the electronic temperature ΔT_e at

the center of the junction and a temperature gradient pointing away from the center (see Fig. 5.8a-b). The sample temperature here is $T = 10\,\mathrm{K}$, with an estimated temperature difference $\Delta T_e \leq 1\,\mathrm{K}$, which ensures we are in the linear heating regime. In such configuration, we then measure a photo-thermoelectric (PTE) voltage $V_{\mathrm{PTE}} = (S_1 - S_2)\Delta T_e$. Fig. 5.8d) shows the measured V_{PTE} around the CNP of a TBG sample ($\theta = 1.14°$), where it exhibits sign changes in a six-fold pattern as the polarity of the carriers is reversed. This has been previously observed in monolayer graphene devices around the Dirac point [313, 314], confirming our measured response to have a photo-thermoelectric origin.

By now setting $\nu_2 = 0$ and continuously tuning ν_1 with the split gates, the response $V_{\mathrm{PTE}} = S_1 \Delta T$ is simply proportional to the Seebeck coefficient of TBG throughout its flat bands. Fig. 5.8g shows this for two samples ($\theta = 1.14°$, $\theta = 1.06°$), where we mainly focus on the electron side. The transport data R_{xx} of the $\theta = 1.14°$ sample can be seen in Fig. 5.2b. Unlike the response around the CNP, V_{PTE} does not change sign at every integer filling where correlated states appear in transport, but rather shows a negative value in the whole electron flat band. The bottom panel of Fig. 5.8g contrasts our data with the expected response from the semiclassical Mott formula, which we estimate by $\mathrm{d}R_{xx}/\mathrm{d}\nu_1$ from the transport data and according to Eq. (5.4). While capturing well the behavior around the CNP, it fails to reproduce the response at integer ν, as it predicts a vanishing S due to a peak in resistance. Thus, the strong correlated physics of the TBG flat bands cannot be described by this non-interacting limit.

As previously discussed in Subsection 1.3.2, the Dirac-revival picture [73] has been often used to visualize the Fermi surface reconstructions appearing at integer fillings of the TBG flat bands. Fig. 5.8e sketches this, where the flat band is split into four sets by flavors, each modeled as a Dirac cone. When TBG is doped away from $\nu = 0$, all these are continuously filled. At every other integer ν though, one of the Dirac cones (of a certain flavor) becomes fully filled, falling below the Fermi level, while all the other Dirac cones are reset to their CNP. This picture explains the sawtooth and square root dependence of the chemical potential observed in local single-electron-transistor [52, 73] and thermodynamic measurements [69, 138], as well as other experiments showing a positive thermoelectricity response [292]. However, this scenario can not account for our full negative PTE measurements, as it would predict a sign-changing Seebeck at a slight higher ν than the integer value, given the bigger DOS for filled holes than electrons (see Fig. 5.8e).

In order to explain our findings, we first use a simple parabolic two-band model, mimicking the low-energy band structure of a correlated insulator at integer $\nu = \mathbb{Z}$. If the electron (red) and hole (blue) bands are symmetric in k-space, with equal effective masses m_e^*, m_h^* and lifetimes τ_e, τ_h; S will be antisymmetric like in Fig. 5.8c. If however, the bands have different masses, the resulting S becomes skewed, since the DOS now is not symmetric. We find that only when $m_h^* \ll m_e^*$ and $\tau_h \ll \tau_e$, S becomes fully negative, as depicted in Fig. 5.8f. Such mass and lifetime asymmetry potentially responsible for the observed anomalous, fully negative PTE, hints at an interplay between light and heavy band structures, which can be naturally accounted by the Topological Heavy Fermion model;

an interacting theory of the TBG flat bands. In this formalism, developed in the group of Prof. Andrei Bernevig [75], the flat bands arise from the hybridization between correlated localized 'heavy' f-electrons and dispersive 'light' c-electrons. Importantly, in this framework, due to interactions and the lack of the so-called 'rigid' approximation, the flat bands strongly reconstruct upon doping nearly integer ν, resembling a two-band model at these fillings. Furthermore, exact calculations of the Seebeck coefficient within this theory demonstrate the good agreement with the experiment [P5]. This model can also account for the low-power and temperature dependence of the V_{PTE}. For a more detailed discussion on these measurements and the theoretical modeling we refer to Refs. [P5] [272, 301].

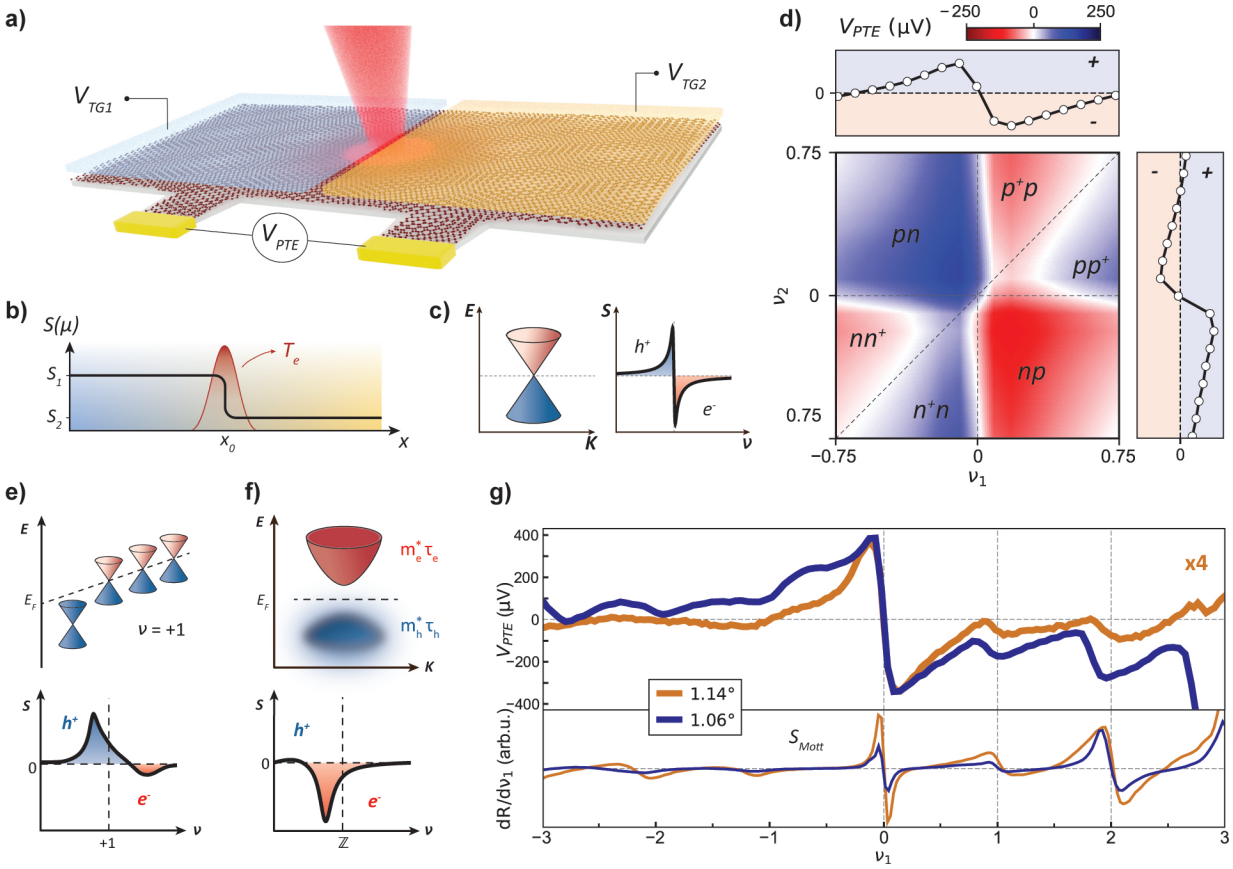

Fig. 5.8: Photo-thermoelectric effect in TBG with gate-defined p-n junctions. **a)** Measurement scheme, where a continuous wave laser generates a thermal gradient at the center of the gate-defined p-n junction, generating a finite PTE voltage thanks to the step in the chemical potential set by the two top gates. **b)** This results in different Seebecks S_1 and S_2 for the two sides. **c)** A symmetric band structure such as graphene (left) leads to a S that changes sign (right). **d)** V_{PTE} vs ν of the two top gates around CNP, showing a graphene-like response. **e)** Expected S from the Dirac-revival picture. **f)** Negative S from different masses and lifetimes. **g)** V_{PTE} vs ν_1 in the flat bands (top), along with the expected result from the semiclassical Mott formula (bottom). Adapted from [P5].

Conclusions and Outlook

Conclusions

This dissertation set out to uncover how the Josephson effect manifests in graphene-based moiré superlattices, especially in twisted bilayer graphene, and how it can reveal the roles of flat band physics, quantum geometry, and symmetry-broken correlated electronic phases.

In Chapter 2 we have detailed a stacking protocol for producing homogeneous twisted vdW heterostructures, particularly relevant for obtaining TBG samples near the magic angle with a high yield [P6]. Additionally, we have presented our efforts to develop a reliable nanofabrication recipe for high-quality superconducting contacts to graphene heterostructures with low contact resistance. These experimental challenges have been central to this thesis, as overcoming them has enabled us to study the Josephson effect in several types of graphene-based moiré superlattices.

In Chapter 3 we have demonstrated ballistic Josephson transport in a graphene/hBN superlattice, characterized by Fabry-Pérot oscillations and supercurrents that persist up to high magnetic fields. By studying their dependence on the filling of the moiré minibands, we can extract information about the underlying band structure, including a renormalized Fermi velocity and the presence of van Hove singularities [P1].

Chapter 4 focuses on magic-angle twisted bilayer graphene Josephson junctions, where, despite expectations of a suppressed proximity-induced superconductivity in the flat bands due to their much smaller Fermi velocity, we observe equally robust I_cR_N products in both the flat and dispersive bands. This surprising result is accompanied by a clear violation of the I_c–G_N scaling, which is otherwise ubiquitous in conventional Josephson junctions. To test recent theoretical predictions regarding the role of quantum geometry in the proximity effect, we have studied several TBG JJs with varying twist-angles, thereby tuning the bandwidth of the flat bands. For relatively broad bandwidths, conventional mechanisms based on band dispersion qualitatively reproduce the experimental dependence of I_c on filling. However, as the bandwidth narrows, such models fail to capture the dome-like features observed in our experiment. These can only be explained instead by incorporating

the unconventional contributions from the quantum geometry of the bands or multiband pairing mechanisms. Our results demonstrate that the proximity effect in the flat bands of TBG is a sizable phenomenon larger than expected from conventional theory, and point toward unconventional mechanisms driving the Josephson effect in flat band systems [P2].

Finally, in Chapter 5 we have leveraged the intrinsic superconducting state of TBG to engineer gate-defined Josephson junctions. There, we have reported a symmetry-broken Josephson effect at half-filling of the moiré flat bands and achieved a programmable zero-field Josephson diode, enabled by a ground state exhibiting finite orbital magnetization [P3]. We have further investigated this effect in Chapter 4, where although no magnetization was present, the inversion symmetry breaking could be observed over a broader range of fillings in both the electron and hole flat bands, as well as at other twist-angles, thanks to the extrinsic JJ architecture [P2]. Altogether, we have demonstrated the first realization of a Josephson diode in TBG, both in extrinsic and intrinsic Josephson junctions, establishing a platform for exploring symmetry-breaking phenomena in the ground states of TBG.

Perspectives

While this thesis has explored the Josephson effect in selected graphene-based moiré superlattices, much remains to be understood about the broader landscape of the superconducting proximity effect in these systems. Further investigations using alternative device architectures, new experiments, and diverse twisted heterostructures are essential. In particular, extending the study of the Josephson effect to other correlated quantum phases, beyond those addressed here, may offer deeper insights into the fundamental mechanisms at play and pave the way toward new quantum functionalities.

Further investigations of the interplay between superconductivity and flat bands

Quantum geometry predicts that the superfluidity in a perfectly flat band system is not necessarily zero [192], which has led to similar predictions when these perfect flat bands are proximitized in a JJ [191] [P4]. An important question is then whether the Josephson effect can be realized in a truly flat band system. Materials with such idealized band structures, like the Lieb lattice, have yet to be discovered or synthesized. The imperfectly flat bands of TBG remain the best candidate to date, although their phase diagram suffers from device-to-device variation arising from twist-angle disorder [119], strain [261] and the dielectric environment [116, 117]. Alternatively, simulations of the Bogoliubov–de Gennes Hamiltonian in artificial lattices, such as those realizable in ultracold atom platforms, may offer new interesting insights and a powerful platform where to test the most basic predictions of quantum geometry [196].

Nonetheless, much remains to be explored regarding the interplay between superconductivity and flat bands in TBG JJs and other twisted multilayer systems. For instance, the AC Josephson effect has been predicted to exhibit sizable quantum geometric effects [315]. Specular interband Andreev reflections could also be studied in TBG JJs, where the typical FWHM of the CNP lies below the meV range, which has posed a significant challenge in monolayer and bilayer graphene for their observation [316]. By adding a tunneling probe in the middle of a TBG JJ, one could also probe the energy levels of the Andreev Bound states when proximitizing the flat bands [21].

Finally, mirror-symmetric twisted trilayer graphene provides another particularly interesting system, as its flat bands are crossed by a Dirac cone belonging to one of the graphene layers. This Dirac cone remains decoupled at zero electrical displacement field, but hybridizes with the flat bands under finite values [60, 61]. As a result, the flat band bandwidth can be tuned continuously within a single device by varying the displacement field, offering an excellent platform to probe the role of flat bands in the superconducting proximity effect.

Phase-sensitive measurements in TBG and the order parameter symmetry

Our investigations of the Josephson effect have focused on recording the critical current as a function of filling, magnetic field and temperature. Future studies with TBG JJs should aim to implement phase-sensitive experiments, where the current-phase relation can be directly accessed, providing deeper insights into the superconducting proximity effect in the flat band limit.

Regarding the intrinsic superconducting state of TBG, although it has been extensively studied and there have been some evidences pointing towards a nodal gap [12, 50, 57–59], no experiment to date has revealed any information about the symmetry of its order parameter. This would require tunneling experiments capable of resolving in-plane momenta, rather than the out-of-plane component as in STM measurements [50] or tunneling spectroscopy in transport devices [21]. While ARPES can resolve the band structure of materials in momentum space, it cannot go to such low temperatures (< 1 K) and its energy resolution of ~ 20 meV is bigger than the bandwidth of the flat bands. As such, it is not a suitable technique to probe the superconducting state of TBG.

One potential platform for such investigations are Josephson junctions, which historically played a key role in identifying the d-wave symmetry of the superconducting order parameter in cuprates [317]. These experiments are incredibly challenging though, as the contact between the superconducting TBG (S') and the s-wave superconducting lead (S) must include a tunneling barrier, such that two SIS' JJs are placed within a SQUID architecture. This also requires precise knowledge of the crystallographic orientation of the moiré superlattice, since the two JJs need to be formed in the two directions of momentum space that one wants to probe the order parameter in. In order to gain a complete

knowledge of the symmetry, multiple junction directions must thus be engineered. Given that mesoscopic devices are prone to twist-angle disorder, which can convolute the tunneling currents by picking up contributions from different directions in k-space, a local-probe technique may be more suitable for this task. The recently developed Quantum Twisting Microscope, which enables in-situ twisting and momentum-resolved spectroscopy of the band structure of a 2D material, has the potential to open up this avenue [318].

Superconductivity in the Quantum Hall regime and the Hofstadter butterfly

Magnetism and superconductivity have long been considered to be two incompatible phases of matter. The observation of the superconducting proximity effect at high magnetic fields in the Quantum Hall regime [23, 24] has challenged this notion, opening a promising avenue for the study of topological superconductivity. These experiments have remained limited to monolayer graphene, which currently stands as the only 2DEG for which engineering transparent superconducting contacts is possible, and have so far focused exclusively on the $\nu_{\mathrm{LL}} = 2$ LL [24]. A natural extension would be to study the spin-polarized $\nu_{\mathrm{LL}} = 1$ state, as well as the fractional LLs. The latter are especially interesting, as the quasiparticles at play, the so-called parafermions, can host Majorana zero modes when proximitized by a superconductor [319].

Extending these studies to other material systems could also offer important new insights. In the context of this thesis, our observation of high field superconductivity in graphene/hBN moiré superlattice JJs in Chapter 3 opens an avenue for exploring the Josephson effect when proximitizing the Landau levels' crossings within the Hofstadter fractal spectrum. Studying the magnetic phase diagram of TBG with the proximity effect would also be very intriguing, as it features not only LLs, but symmetry-broken Chern insulators as well [15, 16]. Investigating the Josephson effect across these different topological phases could reveal the microscopic mechanisms underlying the formation of crossed Andreev bound states. Realizing such experiments, however, would require engineering short-ballistic TBG JJs, a significant experimental challenge given the low Fermi velocity of the flat bands.

On a broader scope, engineering transparent superconducting contacts to other high-mobility semiconducting 2DEGs, such as GaAs or InAs, could also significantly advance our understanding of the superconducting proximity effect in both the integer and fractional Quantum Hall regimes [320].

Exploring the Josephson effect in other moiré materials

The field of moiré quantum materials is rapidly evolving. Since the beginning of this thesis, several strongly correlated phenomena have been observed in moiré materials based on transition metal dichalcogenides (TMDs), such as WSe_2, WS_2, $MoTe_2$, WTe_2, or TaS_2.

These include superconductivity [67, 68], antiferromagnetism [321], Chern insulators [322], Quantum Spin Hall phases [323], and charge density wave order [324]. Exploring these quantum phases with the Josephson effect makes a compelling avenue of research, although it has proven to be extremely challenging to engineer superconducting contacts to TMDs [325]. Nevertheless, very recent advancements to overcome this limitation hold a lot of promise [326–328].

Only very recently as well, a Fractional Anomalous Quantum Hall Effect (FAQHE) was discovered in both twisted bilayer $MoTe_2$ [329–331] and five-layer rhombohedral graphene aligned with hBN [332]. This novel phase of matter, thus far observed exclusively in moiré superlattices, consists of a fractional Chern insulator at zero magnetic field and holds great promise for advancing our understanding of topological phases as well as enabling future applications. If such a state could be coupled to superconducting leads in a Josephson junction architecture, theoretical predictions suggest that such a device would host topological superconductivity and Majorana zero modes at zero magnetic field [319, 333]. This prospect directly relates to the achievements of this thesis, where we have studied the superconducting proximity effect in other graphene-based moiré superlattices in Chapter 3 and Chapter 4. Furthermore, integer and fractional AQHE phases have now been reported in four-, five- and six-layer rhombohedral graphene aligned with hBN, along with superconducting phases [65, 66, 334, 335]. Thus, these findings also open the door to explore the Josephson effect in such exotic phases by engineering gate-defined JJs in these systems, an approach that we have studied ourselves in the case of twisted bilayer graphene in Chapter 5.

All in all, the exploration of the Josephson effect in 2D materials and especially in moiré superlattices holds great promise, from uncovering the fundamental mechanisms that govern the proximity effect in exotic quantum phases, to enabling new quantum technologies inspired by these discoveries.

Bibliography

[1] Geim, A. K. & Novoselov, K. S. The rise of graphene. *Nature Materials* **6,** 183–191 (2007).

[2] Mermin, N. D. Crystalline Order in Two Dimensions. *Physical Review* **176,** 250–254 (1968).

[3] Abrahams, E., Anderson, P. W., Licciardello, D. C. & Ramakrishnan, T. V. Scaling Theory of Localization: Absence of Quantum Diffusion in Two Dimensions. *Physical Review Letters* **42,** 673–676 (1979).

[4] Novoselov, K. S. *et al.* Electric field in atomically thin carbon films. *Science* **306,** 666–669 (2004).

[5] Novoselov, K. S. *et al.* Two-dimensional gas of massless Dirac fermions in graphene. *Nature* **438,** 197–200 (2005).

[6] Morozov, S. V. *et al.* Strong Suppression of Weak Localization in Graphene. *Physical Review Letters* **97,** 016801 (2006).

[7] Novoselov, K. S., Mishchenko, A., Carvalho, A. & Castro Neto, A. H. 2D materials and van der Waals heterostructures. *Science* **353,** aac9439 (2016).

[8] Li, G. *et al.* Observation of Van Hove singularities in twisted graphene layers. *Nature Physics* **6,** 109–113 (2010).

[9] Bistritzer, R. & MacDonald, A. H. Moiré bands in twisted double-layer graphene. *Proceedings of the National Academy of Sciences of the United States of America* **108,** 12233–12237 (2011).

[10] Lopes dos Santos, J. M. B., Peres, N. M. R. & Castro Neto, A. H. Continuum model of the twisted graphene bilayer. *Physical Review B* **86,** 155449 (2012).

[11] Cao, Y. *et al.* Correlated insulator behaviour at half-filling in magic-angle graphene superlattices. *Nature* **556,** 80–84 (2018).

[12] Cao, Y. *et al.* Unconventional superconductivity in magic-angle graphene superlattices. *Nature* **556,** 43–50 (2018).

[13] Yankowitz, M. *et al.* Tuning superconductivity in twisted bilayer graphene. *Science* **363,** 1059–1064 (2019).

[14] Lu, X. *et al.* Superconductors, orbital magnets and correlated states in magic-angle bilayer graphene. *Nature* **574,** 653–657 (2019).

[15] Nuckolls, K. P. *et al.* Strongly correlated Chern insulators in magic-angle twisted bilayer graphene. *Nature* **588,** 610–615 (2020).

[16] Das, I. *et al.* Symmetry-broken Chern insulators and Rashba-like Landau-level crossings in magic-angle bilayer graphene. *Nature Physics* **17,** 710–714 (2021).

[17] Balents, L., Dean, C. R., Efetov, D. K. & Young, A. F. Superconductivity and strong correlations in moiré flat bands. *Nature Physics* **16,** 725–733 (2020).

[18] Mak, K. F. & Shan, J. Semiconductor moiré materials. *Nature Nanotechnology* **17,** 686–695 (2022).

[19] Heersche, H. B. *et al.* Bipolar supercurrent in graphene. *Nature* **446,** 56–59 (2007).

[20] Calado, V. E. *et al.* Ballistic Josephson junctions in edge-contacted graphene. *Nature Nanotechnology* **10,** 761–764 (2015).

[21] Bretheau, L. *et al.* Tunnelling spectroscopy of Andreev states in graphene. *Nature Physics* **13,** 756–760 (2017).

[22] Ben Shalom, M. *et al.* Quantum oscillations of the critical current and high-field superconducting proximity in ballistic graphene. *Nature Physics* **12,** 318–322 (2016).

[23] Amet, F. *et al.* Supercurrent in the quantum Hall regime. *Science* **352,** 966–969 (2016).

[24] Vignaud, H. *et al.* Evidence for chiral supercurrent in quantum Hall Josephson junctions. *Nature* **624,** 545–550 (2023).

[25] Castro Neto, A. H. *et al.* The electronic properties of graphene. *Reviews of Modern Physics* **81,** 109–162 (2009).

[26] Watanabe, K., Taniguchi, T. & Kanda, H. Direct-bandgap properties and evidence for ultraviolet lasing of hexagonal boron nitride single crystal. *Nature Materials* **3,** 404–409 (2004).

[27] Elias, C. *et al.* Direct band-gap crossover in epitaxial monolayer boron nitride. *Nature Communications* **10,** 2639 (2019).

[28] Zhang, Y., Tan, Y. W., Stormer, H. L. & Kim, P. Experimental observation of the quantum Hall effect and Berry's phase in graphene. *Nature* **438,** 201–204 (2005).

[29] Goerbig, M. O. Electronic properties of graphene in a strong magnetic field. *Reviews of Modern Physics* **83,** 1193–1243 (2011).

[30] Yankowitz, M. *et al.* Emergence of superlattice Dirac points in graphene on hexagonal boron nitride. *Nature Physics* **8,** 382–386 (2012).

[31] McGilly, L. J. *et al.* Visualization of moiré superlattices. *Nature Nanotechnology* **15,** 580–584 (2020).

[32] Wallbank, J. R. *et al.* Generic miniband structure of graphene on a hexagonal substrate. *Physical Review B* **87,** 245408 (2013).

[33] Moon, P. & Koshino, M. Electronic properties of graphene/hexagonal-boron-nitride moiré superlattice. *Physical Review B* **90,** 155406 (2014).

[34] Wallbank, J. R., Mucha-Kruczyński, M., Chen, X. & Fal'ko, V. I. Moiré superlattice effects in graphene/boron-nitride van der Waals heterostructures. *Annalen der Physik* **527,** 359–376 (2015).

[35] Ponomarenko, L. A. *et al.* Cloning of Dirac fermions in graphene superlattices. *Nature* **497,** 594–597 (2013).

[36] Dean, C. R. *et al.* Hofstadter's butterfly and the fractal quantum Hall effect in moiré superlattices. *Nature* **497,** 598–602 (2013).

[37] Hunt, B. *et al.* Massive dirac fermions and hofstadter butterfly in a van der Waals heterostructure. *Science* **340,** 1427–1430 (2013).

[38] Yu, G. L. *et al.* Hierarchy of Hofstadter states and replica quantum Hall ferromagnetism in graphene superlattices. *Nature Physics* **10,** 525–529 (2014).

[39] Harper, P. G. Single Band Motion of Conduction Electrons in a Uniform Magnetic Field. *Proceedings of the Physical Society. Section A* **68,** 874 (1955).

[40] Hofstadter, D. R. Energy levels and wave functions of Bloch electrons in rational and irrational magnetic fields. *Physical Review B* **14,** 2239–2249 (1976).

[41] Wannier, G. H. A Result Not Dependent on Rationality for Bloch Electrons in a Magnetic Field. *physica status solidi (b)* **88,** 757–765 (1978).

[42] Thouless, D. J., Kohmoto, M., Nightingale, M. P. & Den Nijs, M. Quantized Hall Conductance in a Two-Dimensional Periodic Potential. *Physical Review Letters* **49,** 405–408 (1982).

[43] Albrecht, C. *et al.* Evidence of Hofstadter's Fractal Energy Spectrum in the Quantized Hall Conductance. *Physical Review Letters* **86,** 147–150 (2001).

[44] Lopes dos Santos, J. M. B., Peres, N. M. R. & Castro Neto, A. H. Graphene Bilayer with a Twist: Electronic Structure. *Physical Review Letters* **99,** 256802 (2007).

[45] Nam, N. N. T. & Koshino, M. Lattice relaxation and energy band modulation in twisted bilayer graphene. *Physical Review B* **96,** 075311 (2017).

[46] Tarnopolsky, G., Kruchkov, A. J. & Vishwanath, A. Origin of Magic Angles in Twisted Bilayer Graphene. *Physical Review Letters* **122,** 106405 (2019).

[47] Leconte, N. *et al.* Relaxation effects in twisted bilayer graphene: A multiscale approach. *Physical Review B* **106,** 115410 (2022).

[48] Andrei, E. Y. & MacDonald, A. H. Graphene bilayers with a twist. *Nature Materials* **19,** 1265–1275 (2020).

[49] Choi, Y. *et al.* Electronic correlations in twisted bilayer graphene near the magic angle. *Nature Physics* **15,** 1174–1180 (2019).

[50] Oh, M. *et al.* Evidence for unconventional superconductivity in twisted bilayer graphene. *Nature* **600,** 240–245 (2021).

[51] Saito, Y. *et al.* Isospin Pomeranchuk effect in twisted bilayer graphene. *Nature* **592,** 220–224 (2021).

[52] Rozen, A. *et al.* Entropic evidence for a Pomeranchuk effect in magic-angle graphene. *Nature* **592,** 214–219 (2021).

[53] Cao, Y. *et al.* Strange metal in magic-angle graphene with near Planckian dissipation. *Physical Review Letters* **124** (2019).

[54] Polshyn, H. *et al.* Large linear-in-temperature resistivity in twisted bilayer graphene. *Nature Physics* **15,** 1011–1016 (2019).

[55] Jaoui, A. *et al.* Quantum critical behaviour in magic-angle twisted bilayer graphene. *Nature Physics* **18,** 633–638 (2022).

[56] Proust, C. & Taillefer, L. The Remarkable Underlying Ground States of Cuprate Superconductors. *Annual Review of Condensed Matter Physics* **10,** 409–429 (2019).

[57] Cao, Y. *et al.* Nematicity and competing orders in superconducting magic-angle graphene. *Science* **372,** 264–271 (2021).

[58] Di Battista, G. *et al.* Revealing the Thermal Properties of Superconducting Magic-Angle Twisted Bilayer Graphene. *Nano Letters* **22,** 6465–6470 (2022).

[59] Tanaka, M. *et al.* Superfluid stiffness of magic-angle twisted bilayer graphene. *Nature* **638,** 99–105 (2025).

[60] Park, J. M. *et al.* Tunable strongly coupled superconductivity in magic-angle twisted trilayer graphene. *Nature* (2021).

[61] Hao, Z. *et al.* Electric field–tunable superconductivity in alternating-twist magic-angle trilayer graphene. *Science* **371,** 1133–1138 (2021).

[62] Park, J. M. *et al.* Robust superconductivity in magic-angle multilayer graphene family. *Nature Materials* **21,** 877–883 (2022).

[63] Zhang, Y. *et al.* Promotion of superconductivity in magic-angle graphene multilayers. *Science* **377,** 1538–1543 (2022).

[64] Su, R. *et al.* Superconductivity in twisted double bilayer graphene stabilized by WSe2. *Nature Materials* **22,** 1332–1337 (2023).

[65] Choi, Y. *et al.* Superconductivity and quantized anomalous Hall effect in rhombohedral graphene. *Nature* **639,** 342–347 (2025).

[66] Han, T. *et al.* Signatures of chiral superconductivity in rhombohedral graphene. *Nature,* 1–3 (2025).

[67] Xia, Y. *et al.* Superconductivity in twisted bilayer WSe2. *Nature* **637,** 833–838 (2025).

[68] Guo, Y. *et al.* Superconductivity in 5.0° twisted bilayer WSe2. *Nature* **637,** 839–845 (2025).

[69] Zhou, H. *et al.* Isospin magnetism and spin-polarized superconductivity in Bernal bilayer graphene. *Science* **375,** 774–778 (2022).

[70] Zhou, H. *et al.* Superconductivity in rhombohedral trilayer graphene. *Nature* **598,** 434–438 (2021).

[71] Cao, Y. *et al.* Superlattice-Induced Insulating States and Valley-Protected Orbits in Twisted Bilayer Graphene. *Physical Review Letters* **117** (2016).

[72] Young, A. F. *et al.* Spin and valley quantum Hall ferromagnetism in graphene. *Nature Physics* **8,** 550–556 (2012).

[73] Zondiner, U. *et al.* Cascade of phase transitions and Dirac revivals in magic-angle graphene. *Nature* **582,** 203–208 (2020).

[74] Nuckolls, K. P. *et al.* Quantum textures of the many-body wavefunctions in magic-angle graphene. *Nature* **620,** 525–532 (2023).

[75] Song, Z.-D. & Bernevig, B. A. Magic-Angle Twisted Bilayer Graphene as a Topological Heavy Fermion Problem. *Physical Review Letters* **129,** 047601 (2022).

[76] Choi, Y. *et al.* Correlation-driven topological phases in magic-angle twisted bilayer graphene. *Nature* **589,** 536–541 (2021).

[77] Wu, S. *et al.* Chern insulators, van Hove singularities and topological flat bands in magic-angle twisted bilayer graphene. *Nature Materials* **20,** 488–494 (2021).

[78] Saito, Y. *et al.* Hofstadter subband ferromagnetism and symmetry-broken Chern insulators in twisted bilayer graphene. *Nature Physics* **17,** 478–481 (2021).

[79] Pierce, A. T. *et al.* Unconventional sequence of correlated Chern insulators in magic-angle twisted bilayer graphene. *Nature Physics* **17,** 1210–1215 (2021).

[80] Sharpe, A. L. *et al.* Emergent ferromagnetism near three-quarters filling in twisted bilayer graphene. *Science* **365,** 605–608 (2019).

[81] Serlin, M. *et al.* Intrinsic quantized anomalous Hall effect in a moiré heterostructure. *Science* **367,** 900–903 (2020).

[82] Polshyn, H. *et al.* Electrical switching of magnetic order in an orbital Chern insulator. *Nature* **588,** 66–70 (2020).

[83] He, W. Y., Goldhaber-Gordon, D. & Law, K. T. Giant orbital magnetoelectric effect and current-induced magnetization switching in twisted bilayer graphene. *Nature Communications* **11,** 1–8 (2020).

[84] London, F., London, H. & Lindemann, F. A. The electromagnetic equations of the supraconductor. *Proceedings of the Royal Society of London. Series A - Mathematical and Physical Sciences* **149,** 71–88 (1935).

[85] Meissner, W. & Ochsenfeld, R. Ein neuer Effekt bei Eintritt der Supraleitfähigkeit. *Naturwissenschaften* **21,** 787–788 (1933).

[86] Bardeen, J., Cooper, L. N. & Schrieffer, J. R. Microscopic Theory of Superconductivity. *Physical Review* **106,** 162–164 (1957).

[87] Bardeen, J., Cooper, L. N. & Schrieffer, J. R. Theory of Superconductivity. *Physical Review* **108,** 1175–1204 (1957).

[88] Giaever, I. Energy Gap in Superconductors Measured by Electron Tunneling. *Physical Review Letters* **5,** 147–148 (1960).

[89] Müller, K. A. & Bednorz, J. G. The Discovery of a Class of High-Temperature Superconductors. *Science* **237,** 1133–1139 (1987).

[90] Stewart, G. R. Unconventional superconductivity. *Advances in Physics* **66,** 75–196 (2017).

[91] Josephson, B. D. Possible new effects in superconductive tunnelling. *Physics Letters* **1,** 251–253 (1962).

[92] Anderson, P. W. & Rowell, J. M. Probable Observation of the Josephson Superconducting Tunneling Effect. *Physical Review Letters* **10,** 230–232 (1963).

[93] Tinkham, M. *Introduction to Superconductivity* (Dover, Mineola, 1996).

[94] Anderson, P. W. & Dayem, A. H. Radio-Frequency Effects in Superconducting Thin Film Bridges. *Physical Review Letters* **13,** 195–197 (1964).

[95] Zimmerman, J. E. & Silver, A. H. Macroscopic Quantum Interference Effects through Superconducting Point Contacts. *Physical Review* **141,** 367–375 (1966).

[96] Clarke, J. & Pippard, A. B. Supercurrents in lead—copper—-lead sandwiches. *Proceedings of the Royal Society of London. Series A. Mathematical and Physical Sciences* **308,** 447–471 (1969).

[97] Likharev, K. K. Superconducting weak links. *Reviews of Modern Physics* **51,** 101–159 (1979).

[98] Lee, G.-H. & Lee, H.-J. Proximity coupling in superconductor-graphene heterostructures. *Reports on Progress in Physics* **81,** 056502 (2018).

[99] Andreev, A. F. Thermal Conductivity of the Intermediate State of Superconductors. *Sov. Phys. JETP* **19** (1964).

[100] Blonder, G. E., Tinkham, M. & Klapwijk, T. M. Transition from metallic to tunneling regimes in superconducting microconstrictions: Excess current, charge imbalance, and supercurrent conversion. *Physical Review B* **25,** 4515–4532 (1982).

[101] Ambegaokar, V. & Baratoff, A. Tunneling Between Superconductors. *Physical Review Letters* **10,** 486–489 (1963).

[102] Golubov, A. A., Kupriyanov, M. Y. & Il'ichev, E. The current-phase relation in Josephson junctions. *Reviews of Modern Physics* **76,** 411–469 (2004).

[103] Beenakker, C. W. J. & van Houten, H. *Quantum Transport in Semiconductor Nanostructures* (Academic Press, 1991).

[104] Borzenets, I. V. *et al.* Ballistic Graphene Josephson Junctions from the Short to the Long Junction Regimes. *Physical Review Letters* **117** (2016).

[105] Usadel, K. D. Generalized Diffusion Equation for Superconducting Alloys. *Physical Review Letters* **25,** 507–509 (1970).

[106] Dubos, P. *et al.* Josephson critical current in a long mesoscopic S-N-S junction. *Physical Review B* **63,** 064502 (2001).

[107] Lee, G. H., Kim, S., Jhi, S. H. & Lee, H. J. Ultimately short ballistic vertical graphene Josephson junctions. *Nature Communications* **6,** 1–9 (2015).

[108] Della Rocca, M. L. *et al.* Measurement of the Current-Phase Relation of Superconducting Atomic Contacts. *Physical Review Letters* **99,** 127005 (2007).

[109] Courtois, H., Meschke, M., Peltonen, J. T. & Pekola, J. P. Origin of Hysteresis in a Proximity Josephson Junction. *Physical Review Letters* **101,** 067002 (2008).

[110] Little, W. A. & Parks, R. D. Observation of Quantum Periodicity in the Transition Temperature of a Superconducting Cylinder. *Physical Review Letters* **9,** 9–12 (1962).

[111] Rowell, J. M. Magnetic Field Dependence of the Josephson Tunnel Current. *Physical Review Letters* **11,** 200–202 (1963).

[112] Jaklevic, R. C., Lambe, J., Silver, A. H. & Mercereau, J. E. Quantum Interference Effects in Josephson Tunneling. *Physical Review Letters* **12,** 159–160 (1964).

[113] Storm, J.-H., Hömmen, P., Drung, D. & Körber, R. An ultra-sensitive and wideband magnetometer based on a superconducting quantum interference device. *Applied Physics Letters* **110,** 072603 (2017).

[114] Dynes, R. C. & Fulton, T. A. Supercurrent Density Distribution in Josephson Junctions. *Physical Review B* **3,** 3015–3023 (1971).

[115] Hart, S. *et al.* Induced superconductivity in the quantum spin Hall edge. *Nature Physics* **10,** 638–643 (2014).

[116] Saito, Y. *et al.* Independent superconductors and correlated insulators in twisted bilayer graphene. *Nature Physics* **16,** 926–930 (2020).

[117] Stepanov, P. *et al.* Untying the insulating and superconducting orders in magic-angle graphene. *Nature* **583,** 375–378 (2020).

[118] Kazmierczak, N. P. *et al.* Strain fields in twisted bilayer graphene. *Nature Materials* **20,** 956–963 (2021).

[119] Uri, A. *et al.* Mapping the twist-angle disorder and Landau levels in magic-angle graphene. *Nature* **581,** 47–52 (2020).

[120] Mas-Ballesté, R., Gómez-Navarro, C., Gómez-Herrero, J. & Zamora, F. 2D materials: to graphene and beyond. *Nanoscale* **3,** 20–30 (2011).

[121] Gupta, A., Sakthivel, T. & Seal, S. Recent development in 2D materials beyond graphene. *Progress in Materials Science* **73,** 44–126 (2015).

[122] Caldwell, J. D. *et al.* Technique for the Dry Transfer of Epitaxial Graphene onto Arbitrary Substrates. *ACS Nano* **4,** 1108–1114 (2010).

[123] Castellanos-Gomez, A. *et al.* Deterministic transfer of two-dimensional materials by all-dry viscoelastic stamping. *2D Materials* **1** (2014).

[124] Luican, A. *et al.* Single-Layer Behavior and Its Breakdown in Twisted Graphene Layers. *Physical Review Letters* **106,** 126802 (2011).

[125] Sanchez-Yamagishi, J. D. *et al.* Quantum hall effect, screening, and layer-polarized insulating states in twisted bilayer graphene. *Physical Review Letters* **108,** 21 (2012).

[126] Blake, P. *et al.* Making graphene visible. *Applied Physics Letters* **91,** 063124 (2007).

[127] Huang, Y. *et al.* Reliable Exfoliation of Large-Area High-Quality Flakes of Graphene and Other Two-Dimensional Materials. *ACS Nano* **9,** 10612–10620 (2015).

[128] Ni, Z. H. *et al.* Graphene thickness determination using reflection and contrast spectroscopy. *Nano Letters* **7,** 2758–2763 (2007).

[129] Gorbachev, R. V. *et al.* Hunting for monolayer boron nitride: Optical and raman signatures. *Small* **7,** 465–468 (2011).

[130] Ferrari, A. C. *et al.* Raman Spectrum of Graphene and Graphene Layers. *Physical Review Letters* **97,** 187401 (2006).

[131] Ferrari, A. C. & Basko, D. M. Raman spectroscopy as a versatile tool for studying the properties of graphene. *Nature Nanotechnology* **8,** 235–246 (2013).

[132] Zhang, X. *et al.* Review on the Raman spectroscopy of different types of layered materials. *Nanoscale* **8,** 6435–6450 (2016).

[133] Li, X.-L. *et al.* Layer-Number Dependent Optical Properties of 2D Materials and Their Application for Thickness Determination. *Advanced Functional Materials* **27,** 1604468 (2017).

[134] Zomer, P. J. *et al.* Fast pick up technique for high quality heterostructures of bilayer graphene and hexagonal boron nitride. *Appl. Phys. Lett* **105,** 13101 (2014).

[135] Frisenda, R. *et al.* Recent progress in the assembly of nanodevices and van der Waals heterostructures by deterministic placement of 2D materials. *Chemical Society Reviews* **47,** 53–68 (2018).

[136] Kim, K. *et al.* Van der Waals Heterostructures with High Accuracy Rotational Alignment. *Nano Letters* **16,** 1989–1995 (2016).

[137] Chen, G. *et al.* Evidence of a gate-tunable Mott insulator in a trilayer graphene moiré superlattice. *Nature Physics* **15,** 237–241 (2019).

[138] Park, J. M. *et al.* Flavour Hund's coupling, Chern gaps and charge diffusivity in moiré graphene. *Nature* **592,** 43–48 (2021).

[139] Pérez-Mas, A. M. *et al.* Graphene patterning by nanosecond laser ablation: the effect of the substrate interaction with graphene. *Journal of Physics D: Applied Physics* **49,** 305301 (2016).

[140] Léonard, F. & Talin, A. A. Electrical contacts to one- and two-dimensional nanomaterials. *Nature Nanotechnology* **6,** 773–783 (2011).

[141] Wang, L. *et al.* One-dimensional electrical contact to a two-dimensional material. *Science* **342,** 614–617 (2013).

[142] Robinson, J. A. *et al.* Contacting graphene. *Applied Physics Letters* **98,** 053103 (2011).

[143] Menon, R., Patel, A., Gil, D. & Smith, H. I. Maskless lithography. *Materials Today* **8,** 26–33 (2005).

[144] Vieu, C. *et al.* Electron beam lithography: resolution limits and applications. *Applied Surface Science. Surface Science in Micro & Nanotechnology* **164,** 111–117 (2000).

[145] Owen, G. & Rissman, P. Proximity effect correction for electron beam lithography by equalization of background dose. *Journal of Applied Physics* **54,** 3573–3581 (1983).

[146] Nečas, D. & Klapetek, P. Gwyddion: an open-source software for SPM data analysis. *Open Physics* **10,** 181–188 (2012).

[147] Cusati, T. *et al.* Electrical properties of graphene-metal contacts. *Scientific Reports* **7,** 5109 (2017).

[148] Safi, I. Recent aspects concerning DC reactive magnetron sputtering of thin films: a review. *Surface and Coatings Technology* **127,** 203–218 (2000).

[149] Draelos, A. W. *et al.* Investigation of Supercurrent in the Quantum Hall Regime in Graphene Josephson Junctions. *Journal of Low Temperature Physics* **191,** 288–300 (2018).

[150] Seredinski, A. *et al.* Quantum Hall–based superconducting interference device. *Science Advances* **5** (2019).

[151] Zhao, L. *et al.* Interference of chiral Andreev edge states. *Nature Physics* **16,** 862–867 (2020).

[152] Schneider, B. H., Etaki, S., van der Zant, H. S. J. & Steele, G. A. Coupling carbon nanotube mechanics to a superconducting circuit. *Scientific Reports* **2,** 599 (2012).

[153] Rickhaus, P., Weiss, M., Marot, L. & Schönenberger, C. Quantum hall effect in graphene with superconducting electrodes. *Nano Letters* **12,** 1942–1945 (2012).

[154] Komatsu, K. *et al.* Superconducting proximity effect in long superconductor/graphene/-superconductor junctions: From specular Andreev reflection at zero field to the quantum Hall regime. *Physical Review B* **86,** 115412 (2012).

[155] Lee, G.-H. *et al.* Inducing superconducting correlation in quantum Hall edge states. *Nature Physics* **13,** 693–698 (2017).

[156] Popinciuc, M. *et al.* Zero-bias conductance peak and Josephson effect in graphene-NbTiN junctions. *Physical Review B* **85,** 205404 (2012).

[157] Haque, M. T. *et al.* Critical current fluctuations in graphene Josephson junctions. *Scientific Reports* **11,** 19900 (2021).

[158] Rout, P. *et al.* Supercurrent mediated by helical edge modes in bilayer graphene. *Nature Communications* **15,** 856 (2024).

[159] Ojeda-Aristizabal, C., Ferrier, M., Guéron, S. & Bouchiat, H. Tuning the proximity effect in a superconductor-graphene-superconductor junction. *Physical Review B* **79,** 165436 (2009).

[160] Rooks, M. J. *et al.* Low stress development of poly(methylmethacrylate) for high aspect ratio structures. *Journal of Vacuum Science & Technology B: Microelectronics and Nanometer Structures Processing, Measurement, and Phenomena* **20,** 2937–2941 (2002).

[161] Seredinski, A. *Interference Effects in Graphene Josephson Junctions Subject to Magnetic Field.* Doctoral thesis (Duke University, 2020).

[162] Foltyn, S. R. *et al.* Influence of deposition rate on the properties of thick YBa2Cu3O7–δ films. *Journal of Materials Research* **12,** 2941–2946 (1997).

[163] Park, S. *et al.* Steady Floquet–Andreev states in graphene Josephson junctions. *Nature* **603,** 421–426 (2022).

[164] Jang, S. *et al.* Engineering Superconducting Contacts Transparent to a Bipolar Graphene. *Nano Letters* **24,** 15582–15587 (2024).

[165] Giazotto, F. *et al.* Opportunities for mesoscopics in thermometry and refrigeration: Physics and applications. *Reviews of Modern Physics* **78,** 217–274 (2006).

[166] Pobell, F. *Matter and Methods at Low Temperatures* (Springer, Berlin, Heidelberg, 2007).

[167] Moya, X. *et al.* Cooling and heating by adiabatic magnetization in the Ni 50 Mn 34 In 16 magnetic shape-memory alloy. *Physical Review B* **75,** 184412 (2007).

[168] Brück, E. Developments in magnetocaloric refrigeration. *Journal of Physics D: Applied Physics* **38,** R381 (2005).

[169] Thalmann, M. *et al.* Comparison of cryogenic low-pass filters. *The Review of Scientific Instruments* **88,** 114703 (2017).

[170] *Principles of Lock-in Detection — Zurich Instruments.* 2019.

[171] Ivanov, D. *Reproducible Superconducting Contacts to Graphene-Based Heterostructures.* MA thesis (Ludwig-Maximilians-University Munich, 2024).

[172] Barrier, J. *et al.* One-dimensional proximity superconductivity in the quantum Hall regime. *Nature* **628,** 741–745 (2024).

[173] Indolese, D. I. *et al.* Signatures of van Hove Singularities Probed by the Supercurrent in a Graphene-hBN Superlattice. *Physical Review Letters* **121,** 137701 (2018).

[174] Fortin-Deschênes, M. *et al.* Uncovering Topological Edge States in Twisted Bilayer Graphene. *Nano Letters* **22,** 6186–6193 (2022).

[175] Shytov, A. V., Rudner, M. S. & Levitov, L. S. Klein Backscattering and Fabry-Pérot Interference in Graphene Heterojunctions. *Physical Review Letters* **101,** 156804 (2008).

[176] Young, A. F. & Kim, P. Quantum interference and Klein tunnelling in graphene heterojunctions. *Nature Physics* **5,** 222–226 (2009).

[177] Rickhaus, P. *et al.* Ballistic interferences in suspended graphene. *Nature Communications* **4,** 2342 (2013).

[178] Handschin, C. *et al.* Fabry-Pérot resonances in a graphene/hBN Moiré superlattice. *Nano Letters* **17,** 328–333 (2017).

[179] Lee, M. *et al.* Ballistic miniband conduction in a graphene superlattice. *Science* **353,** 1526–1529 (2016).

[180] Moriya, R. *et al.* Emergence of orbital angular moment at van Hove singularity in graphene/h-BN moiré superlattice. *Nature Communications* **11,** 5380 (2020).

[181] Chen, S.-C. *et al.* Electrostatic superlattices on scaled graphene lattices. *Communications Physics* **3,** 1–7 (2020).

[182] Wang, Z. *et al.* Open-orbit induced low field extremely large magnetoresistance in graphene/h-BN superlattices. *arXiv Preprint,* arXiv:2312.07004 (2023).

[183] Mreńca-Kolasińska, A., Chen, S.-C. & Liu, M.-H. Probing miniband structure and Hofstadter butterfly in gated graphene superlattices via magnetotransport. *npj 2D Materials and Applications* **7,** 1–9 (2023).

[184] Guarochico-Moreira, V. H. *et al.* Thermopower in hBN/graphene/hBN superlattices. *Physical Review B* **108,** 115418 (2023).

[185] Markiewicz, R. S. Topological interpretation of the Van Hove singularity: Orbital switching. *Journal of Superconductivity* **7,** 803–807 (1994).

[186] De Gennes, P. G. Boundary Effects in Superconductors. *Reviews of Modern Physics* **36,** 225–237 (1964).

[187] Klapwijk, T. M. Proximity Effect From an Andreev Perspective. *Journal of Superconductivity* **17,** 593–611 (2004).

[188] Tafuri, F. *Fundamentals and Frontiers of the Josephson Effect* (Springer International Publishing, 2019).

[189] Ahmadkhani, S. & Hosseini, M. V. Superconducting proximity effect in flat band systems. *Journal of Physics: Condensed Matter* **32,** 315504 (2020).

[190] Pyykkönen, V. A. J. *et al.* Flat-band transport and Josephson effect through a finite-size sawtooth lattice. *Physical Review B* **103,** 144519 (2021).

[191] Li, Z. C. F. *et al.* Flat band Josephson junctions with quantum metric. *Physical Review Research* **7,** 023273 (2025).

[192] Peotta, S. & Törmä, P. Superfluidity in topologically nontrivial flat bands. *Nature Communications* **6,** 8944 (2015).

[193] Hu, X., Hyart, T., Pikulin, D. I. & Rossi, E. Geometric and Conventional Contribution to the Superfluid Weight in Twisted Bilayer Graphene. *Physical Review Letters* **123,** 237002 (2019).

[194] Julku, A. *et al.* Superfluid weight and Berezinskii-Kosterlitz-Thouless transition temperature of twisted bilayer graphene. *Physical Review B* **101,** 060505 (2020).

[195] Xie, F., Song, Z., Lian, B. & Bernevig, B. A. Topology-Bounded Superfluid Weight in Twisted Bilayer Graphene. *Physical Review Letters* **124,** 167002 (2020).

[196] Törmä, P., Peotta, S. & Bernevig, B. A. Superconductivity, superfluidity and quantum geometry in twisted multilayer systems. *Nature Reviews Physics* **4,** 528–542 (2022).

[197] Tian, H. *et al.* Evidence for Dirac flat band superconductivity enabled by quantum geometry. *Nature* **614,** 440–444 (2023).

[198] Törmä, P. Essay: Where Can Quantum Geometry Lead Us? *Physical Review Letters* **131,** 240001 (2023).

[199] Scalapino, D. J., White, S. R. & Zhang, S. C. Superfluid density and the Drude weight of the Hubbard model. *Physical Review Letters* **68,** 2830–2833 (1992).

[200] Liang, L. *et al.* Band geometry, Berry curvature, and superfluid weight. *Physical Review B* **95,** 024515 (2017).

[201] Portolés, E. *et al.* A tunable monolithic SQUID in twisted bilayer graphene. *Nature Nanotechnology* **17,** 1159–1164 (2022).

[202] Jha, R. *et al.* Large Tunable Kinetic Inductance in a Twisted Graphene Superconductor. *Physical Review Letters* **134,** 216001 (2025).

[203] Banerjee, A. *et al.* Superfluid stiffness of twisted trilayer graphene superconductors. *Nature* **638,** 93–98 (2025).

[204] De Vries, F. K. *et al.* Gate-defined Josephson junctions in magic-angle twisted bilayer graphene. *Nature Nanotechnology* **16,** 760–763 (2021).

[205] Rodan-Legrain, D. *et al.* Highly tunable junctions and non-local Josephson effect in magic-angle graphene tunnelling devices. *Nature Nanotechnology* **16,** 769–775 (2021).

[206] Iwakiri, S. *et al.* Tunable quantum interferometer for correlated moiré electrons. *Nature Communications* **15,** 390 (2024).

[207] Lake, E., Patri, A. S. & Senthil, T. Pairing symmetry of twisted bilayer graphene: A phenomenological synthesis. *Physical Review B* **106,** 104506 (2022).

[208] Du, X., Skachko, I. & Andrei, E. Y. Josephson current and multiple Andreev reflections in graphene SNS junctions. *Physical Review B - Condensed Matter and Materials Physics* **77** (2008).

[209] Thoen, D. J. *et al.* Superconducting NbTin Thin Films With Highly Uniform Properties Over a 100 mm Wafer. *IEEE Transactions on Applied Superconductivity* **27,** 1–5 (2017).

[210] Hazra, D. *et al.* Superconducting properties of NbTiN thin films deposited by high-temperature chemical vapor deposition. *Physical Review B* **97,** 144518 (2018).

[211] Ke, C. T. *et al.* Critical Current Scaling in Long Diffusive Graphene-Based Josephson Junctions. *Nano Letters* **16,** 4788–4791 (2016).

[212] Li, C., Guéron, S., Chepelianskii, A. & Bouchiat, H. Full range of proximity effect probed with superconductor / graphene / superconductor junctions. *Physical Review B* **94,** 115405 (2016).

[213] Qin, W., Zou, B. & MacDonald, A. H. Critical magnetic fields and electron-pairing in magic-angle twisted bilayer graphene (2021).

[214] Chen, S. A. & Law, K. T. Ginzburg-Landau Theory of Flat-Band Superconductors with Quantum Metric. *Physical Review Letters* **132,** 026002 (2024).

[215] Hu, J.-X., Chen, S. A. & Law, K. T. Anomalous coherence length in superconductors with quantum metric. *Communications Physics* **8,** 1–7 (2025).

[216] Titov, M. & Beenakker, C. W. Josephson effect in ballistic graphene. *Physical Review B - Condensed Matter and Materials Physics* **74** (2006).

[217] Christos, M., Sachdev, S. & Scheurer, M. S. Nodal band-off-diagonal superconductivity in twisted graphene superlattices. *Nature Communications* **14,** 7134 (2023).

[218] Hu, J., Wu, C. & Dai, X. Proposed Design of a Josephson Diode. *Physical Review Letters* **99,** 067004 (2007).

[219] Nadeem, M., Fuhrer, M. S. & Wang, X. The superconducting diode effect. *Nature Reviews Physics* **5,** 558–577 (2023).

[220] Barone. in *Physics and Applications of the Josephson Effect* 96–120 (John Wiley & Sons, Ltd, 1982).

[221] Krasnov, V. M., Oboznov, V. A. & Pedersen, N. F. Fluxon dynamics in long Josephson junctions in the presence of a temperature gradient or spatial nonuniformity. *Physical Review B* **55,** 14486–14498 (1997).

[222] Chen, S. *et al.* Current induced hidden states in Josephson junctions. *Nature Communications* **15,** 8059 (2024).

[223] Zapata, I., Bartussek, R., Sols, F. & Hänggi, P. Voltage Rectification by a SQUID Ratchet. *Physical Review Letters* **77,** 2292–2295 (1996).

[224] Falo, F. *et al.* Fluxon ratchet potentials in superconducting circuits. *Applied Physics A* **75,** 263–269 (2002).

[225] Shalóm, D. E. & Pastoriza, H. Vortex Motion Rectification in Josephson Junction Arrays with a Ratchet Potential. *Physical Review Letters* **94,** 177001 (2005).

[226] Lee, C.-S., Jankó, B., Derényi, I. & Barabási, A.-L. Reducing vortex density in superconductors using the 'ratchet effect'. *Nature* **400,** 337–340 (1999).

[227] Villegas, J. E. *et al.* A Superconducting Reversible Rectifier That Controls the Motion of Magnetic Flux Quanta. *Science* **302,** 1188–1191 (2003).

[228] Wakatsuki, R. *et al.* Nonreciprocal charge transport in noncentrosymmetric superconductors. *Science Advances* **3,** e1602390 (2017).

[229] Qin, F. *et al.* Superconductivity in a chiral nanotube. *Nature Communications* **8,** 14465 (2017).

[230] Tokura, Y. & Nagaosa, N. Nonreciprocal responses from non-centrosymmetric quantum materials. *Nature Communications* **9,** 3740 (2018).

[231] Rikken, G. L. J. A., Fölling, J. & Wyder, P. Electrical Magnetochiral Anisotropy. *Physical Review Letters* **87,** 236602 (2001).

[232] Rikken, G. L. J. A. & Wyder, P. Magnetoelectric Anisotropy in Diffusive Transport. *Physical Review Letters* **94,** 016601 (2005).

[233] Ando, F. *et al.* Observation of superconducting diode effect. *Nature* **584,** 373–376 (2020).

[234] Baumgartner, C. *et al.* Supercurrent rectification and magnetochiral effects in symmetric Josephson junctions. *Nature Nanotechnology* **17,** 39–44 (2022).

[235] Mazur, G. *et al.* Gate-tunable Josephson diode. *Physical Review Applied* **22,** 054034 (2024).

[236] Bauriedl, L. *et al.* Supercurrent diode effect and magnetochiral anisotropy in few-layer NbSe2. *Nature Communications* **13,** 4266 (2022).

[237] Gupta, M. *et al.* Gate-tunable superconducting diode effect in a three-terminal Josephson device. *Nature Communications* **14,** 3078 (2023).

[238] Coraiola, M. *et al.* Flux-Tunable Josephson Diode Effect in a Hybrid Four-Terminal Josephson Junction. *ACS Nano* **18,** 9221–9231 (2024).

[239] Goldobin, E., Koelle, D., Kleiner, R. & Buzdin, A. Josephson junctions with second harmonic in the current-phase relation: Properties of phi junctions. *Physical Review B* **76,** 224523 (2007).

[240] Buzdin, A. Direct Coupling Between Magnetism and Superconducting Current in the Josephson phi0 Junction. *Physical Review Letters* **101,** 107005 (2008).

[241] Fominov, Y. V. & Mikhailov, D. S. Asymmetric higher-harmonic SQUID as a Josephson diode. *Physical Review B* **106,** 134514 (2022).

[242] Souto, R. S., Leijnse, M. & Schrade, C. Josephson Diode Effect in Supercurrent Interferometers. *Physical Review Letters* **129,** 267702 (2022).

[243] Fulde, P. & Ferrell, R. A. Superconductivity in a Strong Spin-Exchange Field. *Physical Review* **135,** A550–A563 (1964).

[244] Steglich, F. *et al.* Experimental evidence for a generalized FFLO state in clean type-II superconductors with short coherence length and enhanced Pauli susceptibility. *Physica C: Superconductivity. Proceedings of the International Symposium on Frontiers of High - Tc Superconductivity* **263,** 498–504 (1996).

[245] Chen, A. Q. *et al.* Finite momentum Cooper pairing in three-dimensional topological insulator Josephson junctions. *Nature Communications* **9,** 3478 (2018).

[246] Yuan, N. F. Q. & Fu, L. Supercurrent diode effect and finite-momentum superconductors. *Proceedings of the National Academy of Sciences* **119,** e2119548119 (2022).

[247] Pal, B. *et al.* Josephson diode effect from Cooper pair momentum in a topological semimetal. *Nature Physics* **18,** 1228–1233 (2022).

[248] Davydova, M., Prembabu, S. & Fu, L. Universal Josephson diode effect. *Science Advances* **8,** eabo0309 (2022).

[249] Wu, H. *et al.* The field-free Josephson diode in a van der Waals heterostructure. *Nature* **604,** 653–656 (2022).

[250] Jeon, K.-R. *et al.* Zero-field polarity-reversible Josephson supercurrent diodes enabled by a proximity-magnetized Pt barrier. *Nature Materials* **21,** 1008–1013 (2022).

[251] Lin, J.-X. *et al.* Zero-field superconducting diode effect in small-twist-angle trilayer graphene. *Nature Physics* **18,** 1221–1227 (2022).

[252] Scammell, H. D., Li, J. I. A. & Scheurer, M. S. Theory of zero-field superconducting diode effect in twisted trilayer graphene. *2D Materials* **9,** 025027 (2022).

[253] Golod, T. & Krasnov, V. M. Demonstration of a superconducting diode-with-memory, operational at zero magnetic field with switchable nonreciprocity. *Nature Communications* **13,** 3658 (2022).

[254] Uchida, N. *et al.* Flux trapping in Josephson tunnel junctions. *Journal of Applied Physics* **54,** 5287–5292 (1983).

[255] Pippard, A. B. & Shoenberg, D. Trapped flux in superconductors. *Philosophical Transactions of the Royal Society of London. Series A, Mathematical and Physical Sciences* **248,** 97–129 (1997).

[256] Tseng, C.-C. *et al.* Anomalous Hall effect at half filling in twisted bilayer graphene. *Nature Physics* **18,** 1038–1042 (2022).

[257] Hu, J.-X., Sun, Z.-T., Xie, Y.-M. & Law, K. T. Josephson Diode Effect Induced by Valley Polarization in Twisted Bilayer Graphene. *Physical Review Letters* **130,** 266003 (2023).

[258] Jiang, Y. *et al.* Charge order and broken rotational symmetry in magic-angle twisted bilayer graphene. *Nature* **573,** 91–95 (2019).

[259] Bultinck, N. *et al.* Ground State and Hidden Symmetry of Magic-Angle Graphene at Even Integer Filling. *Physical Review X* **10,** 031034 (2020).

[260] Christos, M., Sachdev, S. & Scheurer, M. S. Correlated Insulators, Semimetals, and Superconductivity in Twisted Trilayer Graphene. *Physical Review X* **12,** 021018 (2022).

[261] Mesple, F. *et al.* Heterostrain Determines Flat Bands in Magic-Angle Twisted Graphene Layers. *Physical Review Letters* **127,** 126405 (2021).

[262] Clem, J. R. Josephson junctions in thin and narrow rectangular superconducting strips. *Physical Review B - Condensed Matter and Materials Physics* **81** (2010).

[263] Kroll, J. *et al.* Magnetic-Field-Resilient Superconducting Coplanar-Waveguide Resonators for Hybrid Circuit Quantum Electrodynamics Experiments. *Physical Review Applied* **11,** 064053 (2019).

[264] Kononov, A. *et al.* One-Dimensional Edge Transport in Few-Layer WTe2. *Nano Letters* **20,** 4228–4233 (2020).

[265] Bocquillon, E. *et al.* Gapless Andreev bound states in the quantum spin Hall insulator HgTe. *Nature Nanotechnology* **12,** 137–143 (2017).

[266] Chen, C.-Z. *et al.* Asymmetric Josephson effect in inversion symmetry breaking topological materials. *Physical Review B* **98,** 075430 (2018).

[267] Endres, M. *et al.* Current–Phase Relation of a WTe2 Josephson Junction. *Nano Letters* **23,** 4654–4659 (2023).

[268] Alvarado, M., Burset, P. & Yeyati, A. L. Intrinsic nonmagnetic phi0 Josephson junctions in twisted bilayer graphene. *Physical Review Research* **5,** L032033 (2023).

[269] Sainz-Cruz, H. *et al.* Junctions and Superconducting Symmetry in Twisted Bilayer Graphene. *Physical Review Letters* **131,** 016003 (2023).

[270] Sinko, M. R. *et al.* Superconducting contact and quantum interference between two-dimensional van der Waals and three-dimensional conventional superconductors. *Physical Review Materials* **5,** 014001 (2021).

[271] Díez Mérida, J. *Probing magic-angle twisted bilayer graphene with monolithic gate-defined Josephson junctions.* Doctoral thesis (Universitat Politècnica de Catalunya, 2024).

[272] Luque Merino, R. *Optoelectronic studies of strongly correlated 2D materials.* Doctoral thesis (Universitat Politècnica de Catalunya, 2024).

[273] Zheng, G. *et al.* Gate-defined superconducting channel in magic-angle twisted bilayer graphene. *Physical Review Research* **6,** L012051 (2024).

[274] Zibrov, A. A. *et al.* Tunable interacting composite fermion phases in a half-filled bilayer-graphene Landau level. *Nature* **549,** 360–364 (2017).

[275] Cohen, L. A. *et al.* Nanoscale electrostatic control in ultraclean van der Waals heterostructures by local anodic oxidation of graphite gates. *Nature Physics,* 1–7 (2023).

[276] Randle, M. D. *et al.* Gate-Defined Josephson Weak-Links in Monolayer WTe2. *Advanced Materials* **35,** 2301683 (2023).

[277] Yurgens, A. A. Intrinsic Josephson junctions: recent developments. *Superconductor Science and Technology* **13,** R85 (2000).

[278] Tolpygo, S. K. *et al.* Fabrication Process and Properties of Fully-Planarized Deep-Submicron Nb/Al-AlO/Nb Josephson Junctions for VLSI Circuits. *IEEE Transactions on Applied Superconductivity* **25,** 1–12 (2015).

[279] Kjaergaard, M. *et al.* Transparent Semiconductor - Superconductor Interface and Induced Gap in an Epitaxial Heterostructure Josephson Junction. *Physical Review Applied* **7,** 034029 (2017).

[280] Endres, M. *et al.* Transparent Josephson junctions in higher-order topological insulator WTe 2 via Pd diffusion. *Physical Review Materials* **6,** L081201 (2022).

[281] Moshe, M., Kogan, V. G. & Mints, R. G. Edge-type Josephson junctions in narrow thin-film strips. *Physical Review B - Condensed Matter and Materials Physics* **78** (2008).

[282] Boris, A. A. *et al.* Evidence for Nonlocal Electrodynamics in Planar Josephson Junctions. *Physical Review Letters* **111,** 117002 (2013).

[283] Stepanov, P. *et al.* Competing Zero-Field Chern Insulators in Superconducting Twisted Bilayer Graphene. *Physical Review Letters* **127,** 197701 (2021).

[284] Xie, Y.-M., Efetov, D. K. & Law, K. T. phi0-Josephson junction in twisted bilayer graphene induced by a valley-polarized state. *Physical Review Research* **5,** 023029 (2023).

[285] He, M. *et al.* Competing correlated states and abundant orbital magnetism in twisted monolayer-bilayer graphene. *Nature Communications* **12,** 4727 (2021).

[286] Grover, S. *et al.* Chern mosaic and Berry-curvature magnetism in magic-angle graphene. *Nature Physics* **18,** 885–892 (2022).

[287] Xie, F. *et al.* Twisted bilayer graphene. VI. An exact diagonalization study at nonzero integer filling. *Physical Review B* **103,** 205416 (2021).

[288] Kwan, Y. H. *et al.* Kekulé Spiral Order at All Nonzero Integer Fillings in Twisted Bilayer Graphene. *Physical Review X* **11,** 041063 (2021).

[289] Kim, H. *et al.* Imaging inter-valley coherent order in magic-angle twisted trilayer graphene. *Nature* **623,** 942–948 (2023).

[290] Nuckolls, K. P. & Yazdani, A. A microscopic perspective on moiré materials. *Nature Reviews Materials* **9,** 460–480 (2024).

[291] Ghawri, B. *et al.* Breakdown of semiclassical description of thermoelectricity in near-magic angle twisted bilayer graphene. *Nature Communications* **13,** 1522 (2022).

[292] Paul, A. K. *et al.* Interaction-driven giant thermopower in magic-angle twisted bilayer graphene. *Nature Physics* **18,** 691–698 (2022).

[293] Bhowmik, S. *et al.* Broken-symmetry states at half-integer band fillings in twisted bilayer graphene. *Nature Physics* **18,** 639–643 (2022).

[294] Batlle-Porro, S. *et al.* Cryo-Near-Field Photovoltage Microscopy of Heavy-Fermion Twisted Symmetric Trilayer Graphene. *arXiv Preprint,* arXiv:2402.12296 (2024).

[295] Hesp, N. C. H. *et al.* Observation of interband collective excitations in twisted bilayer graphene. *Nature Physics* **17,** 1162–1168 (2021).

[296] Morissette, E. *et al.* Dirac revivals drive a resonance response in twisted bilayer graphene. *Nature Physics* **19,** 1156–1162 (2023).

[297] Xie, T. *et al.* Long-lived isospin excitations in magic-angle twisted bilayer graphene. *Nature* **633,** 77–82 (2024).

[298] Li, G. *et al.* Infrared Spectroscopy for Diagnosing Superlattice Minibands in Twisted Bilayer Graphene near the Magic Angle. *Nano Letters* **24,** 15956–15963 (2024).

[299] Krishna Kumar, R. *et al.* Terahertz photocurrent probe of quantum geometry and interactions in magic-angle twisted bilayer graphene. *Nature Materials,* 1–8 (2025).

[300] Stauber, T., Low, T. & Gómez-Santos, G. Chiral Response of Twisted Bilayer Graphene. *Physical Review Letters* **120,** 046801 (2018).

[301] Călugăru, D. *et al.* The Thermoelectric Effect and Its Natural Heavy Fermion Explanation in Twisted Bilayer and Trilayer Graphene. *arXiv Preprint,* arXiv:2402.14057 (2024).

[302] Bera, K., Chatterjee, P., Mohan, P. & Saha, A. Thermoelectric properties of magic angle twisted bilayer graphene-superconductor hetero-junction: effect of valley polarization and trigonal warping. *arXiv Preprint,* arXiv:2501.15882 (2025).

[303] Koshino, M. & Nam, N. N. T. Effective continuum model for relaxed twisted bilayer graphene and moiré electron-phonon interaction. *Physical Review B* **101,** 195425 (2020).

[304] Massicotte, M., Soavi, G., Principi, A. & Tielrooij, K.-J. Hot carriers in graphene – fundamentals and applications. *Nanoscale* **13,** 8376–8411 (2021).

[305] Urich, A., Unterrainer, K. & Mueller, T. Intrinsic Response Time of Graphene Photodetectors. *Nano Letters* **11,** 2804–2808 (2011).

[306] Tielrooij, K. J. *et al.* Generation of photovoltage in graphene on a femtosecond timescale through efficient carrier heating. *Nature Nanotechnology* **10,** 437–443 (2015).

[307] Jadidi, M. M. *et al.* Tunable Ultrafast Thermal Relaxation in Graphene Measured by Continuous-Wave Photomixing. *Physical Review Letters* **117,** 257401 (2016).

[308] Song, J. C. W., Reizer, M. Y. & Levitov, L. S. Disorder-Assisted Electron-Phonon Scattering and Cooling Pathways in Graphene. *Physical Review Letters* **109,** 106602 (2012).

[309] MacDonald, D. K. C. & Tuomi, D. Thermoelectricity: An Introduction to the Principles. *Journal of The Electrochemical Society* **110,** 206C (1963).

[310] Cutler, M. & Mott, N. F. Observation of Anderson Localization in an Electron Gas. *Physical Review* **181,** 1336–1340 (1969).

[311] Zuev, Y. M., Chang, W. & Kim, P. Thermoelectric and Magnetothermoelectric Transport Measurements of Graphene. *Physical Review Letters* **102,** 096807 (2009).

[312] Xu, X. *et al.* Photo-Thermoelectric Effect at a Graphene Interface Junction. *Nano Letters* **10,** 562–566 (2010).

[313] Gabor, N. M. *et al.* Hot Carrier–Assisted Intrinsic Photoresponse in Graphene. *Science* **334,** 648–652 (2011).

[314] Song, J. C. W., Rudner, M. S., Marcus, C. M. & Levitov, L. S. Hot Carrier Transport and Photocurrent Response in Graphene. *Nano Letters* **11,** 4688–4692 (2011).

[315] Pyykkönen, V. A. J., Peotta, S. & Törmä, P. Suppression of Nonequilibrium Quasiparticle Transport in Flat-Band Superconductors. *Physical Review Letters* **130,** 216003 (2023).

[316] Efetov, D. K. *et al.* Specular interband Andreev reflections at van der Waals interfaces between graphene and NbSe2. *Nature Physics* **12,** 328–332 (2016).

[317] Van Harlingen, D. J., Wollman, D. A., Ginsberg, D. M. & Leggett, A. J. Phase-sensitive tests of the symmetry of the pairing state in the high temperature superconductors — evidence for dx2-y2 symmetry in YBCO. *Physica C: Superconductivity and its applications* **235-240,** 122–125 (1994).

[318] Inbar, A. *et al.* The quantum twisting microscope. *Nature* **614,** 682–687 (2023).

[319] Alicea, J. & Fendley, P. Topological Phases with Parafermions: Theory and Blueprints. *Annual Review of Condensed Matter Physics* **7,** 119–139 (2016).

[320] Akiho, T. *et al.* Andreev Reflection in the Quantum Hall Regime at an Al/InAs Junction on a Cleaved Edge. *Nano Letters* **24,** 14790–14796 (2024).

[321] Tang, Y. *et al.* Simulation of Hubbard model physics in WSe2/WS2 moiré superlattices. *Nature* **579,** 353–358 (2020).

[322] Zhao, W. *et al.* Realization of the Haldane Chern insulator in a moiré lattice. *Nature Physics* **20,** 275–280 (2024).

[323] Kang, K. *et al.* Evidence of the fractional quantum spin Hall effect in moiré MoTe2. *Nature* **628,** 522–526 (2024).

[324] Zhao, W.-M. *et al.* Moiré enhanced charge density wave state in twisted 1T-TiTe2/1T-TiSe2 heterostructures. *Nature Materials* **21,** 284–289 (2022).

[325] Wang, Y. & Chhowalla, M. Making clean electrical contacts on 2D transition metal dichalcogenides. *Nature Reviews Physics* **4,** 101–112 (2022).

[326] Ma, L., Wang, Y. & Liu, Y. van der Waals Contact for Two-Dimensional Transition Metal Dichalcogenides. *Chemical Reviews* **124,** 2583–2616 (2024).

[327] Jia, Y. *et al.* Superconductivity from On-Chip Metallization on 2D Topological Chalcogenides. *Physical Review X* **14,** 021051 (2024).

[328] Jia, Y. *et al.* Anomalous superconductivity in twisted MoTe2 nanojunctions. *Science Advances* **11,** eadq5712 (2025).

[329] Cai, J. *et al.* Signatures of fractional quantum anomalous Hall states in twisted MoTe2. *Nature* **622,** 63–68 (2023).

[330] Park, H. *et al.* Observation of fractionally quantized anomalous Hall effect. *Nature* **622,** 74–79 (2023).

[331] Xu, F. *et al.* Observation of Integer and Fractional Quantum Anomalous Hall Effects in Twisted Bilayer MoTe2. *Physical Review X* **13,** 031037 (2023).

[332] Lu, Z. *et al.* Fractional quantum anomalous Hall effect in multilayer graphene. *Nature* **626,** 759–764 (2024).

[333] Chang, C.-Z., Liu, C.-X. & MacDonald, A. H. Colloquium: Quantum anomalous Hall effect. *Reviews of Modern Physics* **95,** 011002 (2023).

[334] Lu, Z. *et al.* Extended quantum anomalous Hall states in graphene/hBN moiré superlattices. *Nature* **637,** 1090–1095 (2025).

[335] Xie, J. *et al.* Tunable fractional Chern insulators in rhombohedral graphene superlattices. *Nature Materials,* 1–7 (2025).

List of Abbreviations and Symbols

Abbreviations

2D	Two-dimensional
ABS	Andreev Bound state
AFM	Atomic force microscope
CNP	Charge neutrality point
CPR	Current-phase relation
DIW	De-ionized water
DOS	Density of states
EBL	Electron beam lithography
FP	Fabry-Pérot
hBN	Hexagonal boron nitride
IPA	Isopropyl alcohol
JDE	Josephson diode effect
JJ	Josephson junction
LL	Landau level
MIBK	Methyl isobutyl ketone
PC	Polycarbonate
PDMS	Polydimethylsiloxane
PMMA	Polymethyl methacrylate
RIE	Reactive ion etching
SEM	Scanning electron microscope

SC	Superconducting
SNS	Superconductor / Normal metal / Superconductor
SQUID	Superconducting quantum interference device
TBG	Twisted bilayer graphene
TRS	Time-reversal symmetry
PID	Proportional-integral-derivative
vdW	van der Waals
vHs	van Hove singularity

Symbols

h	Planck constant
$\hbar$	Reduced Planck constant
e	Electron charge
B	Magnetic field
λ_L	London penetration depth
Φ_0	Magnetic flux quantum
ξ_N	Superconducting coherence length in the weak link
Δ	Superconducting gap
I_c	Critical current of a Josephson junction
R_N	Normal state resistance
G_N	Normal state conductance
l_{mfp}	Electron mean-free-path in a metal
D	Diffusion constant
r_c	Cyclotron radius
E_F	Fermi energy/level
v_F	Fermi velocity
ν	Filling factor of the electronic bands
ν_{LL}	Landau level filling factor
n	Carrier density
V_g	Gate voltage